UNIVERSITY OF THE WITWATERSRAND

A critical analysis using remote sensing and GIS techniques for spatial distribution and macro-morphological analyses of rockfalls in the Golden Gate Highlands National Park, South Africa

---

A dissertation submitted to the Faculty of Science, University of the Witwatersrand, in fulfilment of the requirements for the degree of Master of Science

Hugo Jose De Lemos

11/30/2013

Declaration

I declare that this dissertation is my own, unaided work. It is being submitted for the Degree of Master of Science in the University of the Witwatersrand, Johannesburg. It has not been submitted before for any degree in any other University.

____

(Signature of candidate)

_______________day of_______________2013

Abstract

A variety of mass movement and depositional geomorphic phenomena in the Golden Gate Highlands National Park have been described in the literature over the past few decades, yet notably, the prominent rockfalls remain understudied. The objective of the MSc study is to undertake detailed mapping of the GGHNP rockfalls, and in so doing ascertain a better understanding of their macro-morphologies, associated spatial-size dynamics and relationships to lithology, using both field-based and desktop image processing techniques.

Ground truthing, using the highest possible resolution achievable through differential GPS (DGPS) and field measurements with an accuracy of cm to mm, serves to quantify the accuracy of mapping rockfall phenomena through 0.5 m GSD colour aerial imagery. In addition, field measurements are used as inputs for feature extraction, such that rockfalls associated with the Clarens, Elliot and Molteno Formation Sandstones may be defined using object orientated classification techniques. The dimensions, orientation and absolute coordinates of rockfalls for select representative sites were captured using both field based and desktop techniques. The rockfall coordinates were taken at the midpoint of each measured rock using a DGPS, with an accuracy of ~ 2 cm on the x, y and z axis.

Object Based Image Analysis (OBIA) of Clarens and Molteno Fm. rockfalls was performed successfully using ground-truthed rockfall measurements to guide the creation of segmentation and classification rulesets. Multiple linear regression modelling can be used to model rockfall characteristics from ground-truthing with remotely sensed imagery, albeit to a very limited extent. Elliot Formation rockfalls could not be mapped and analysed mainly due to resolution limitations. Uni- and bi-variate statistics show promise in interpreting rockfall distribution and weighting with environmental variables derived from a DEM and geological vector.

Point density analyses found that for the entire GGHNP ~2 and ~4 rockfalls are found per Km² of Clarens and Molteno Formation rockfall areas

respectively. Park infrastructure and anthropogenic activities at Wilgerhof show potential risk to Clarens Fm. rockfalls. Overall, infrastructure at the GGHNP possesses no real danger from Clarens and Molteno Fm. rockfalls, however anthropogenic outdoor activities such as hiking, which are more difficult to measure, could possess a high degree of rockfall hazard, especially where they are found occurring in very high density Clarens Fm. rockfall regions.

The frequency distribution of Clarens and Molteno Fm. rockfalls in the GGHNP compares well with the frequency distribution of rockfalls in the Bushmen's Nek region of the southern Drakensberg for rockfalls 0 – 25 m of rock exposures, on slopes with an altitude between 1800 and 2000 m a.s.l with slope gradients of 18° - 29°. The observed mean distance between Clarens and Molteno Fm. rockfalls was observed to increase with a decrease in altitude, slope gradient, and distance to rock exposures and drainage lines. The observed mean distance between Clarens and Molteno Fm. rockfalls was also notably higher on south-facing slopes. The InfoVal weights for the Clarens Fm. rockfalls indicate that rockfalls are most greatly influenced by very steep slope gradients.

Acknowledgements

The writing of this dissertation has been some years in the making and is one of the most significant academic challenges I have had to face. This dissertation would not have been possible without the mentorship of my supervisor, Prof. Stefan Grab, who always provided me with excellent guidance, and motivation. I would also like to express my gratitude toward Dr Devlyn Hardwick, who provided me with brilliant GIS knowledge and guidance along the way. A big thank you to Dr Nichola Knox, whose support in statistics and remote sensing has been invaluable. A very heartfelt thank you goes to my family for without their belief in me, this dissertation would not have been possible.

Finally, I would like to acknowledge the South African National Space Agency Earth Observation Directorate for providing me with bursary funding to pursue this dissertation, and members of GGHNP management for the assistance I received during my field work.

Table of Contents

Figures

Tables

Abbreviations

A	Aspect
ANN	Average Nearest Neighbour
ASTER	Advanced Spaceborne Thermal Emission and Reflection Radiometer
B1	Band 1 (red)
B2	Band 2 (green)
B3	Band 3 (blue)
C	Curvature
CC	Concave concave slope unit
CCx	Concave Convex slope unit
CD: NGI	Chief Directorate: National Geo-spatial Information
Circum.	Circumference
CxC	Convex Concave slope unit
CxCx	Convex Convex slope unit
DEM	Digital Elevation Model
DTM	Digital Terrain Model
E	Elevation
ESRI	Environmental Systems Research Institute
Fm.	Formation
GGHNP	Golden Gate Highlands National Park
GIS	Geographic Information Systems
LA	Longest Axis
m a.s.l	meters above sea level
Max.	Maximum
Min.	Minimum
NSV	No significant variables
OBIA	Object Based Image Analysis
PA	Perpendicular Axis
Pr	Profile
R	Roughnes
RMSE	Root Moean Square Error
S	Slope
SANSA	South African National Space Agency
SRTM	Shuttle Radar Topography Mission
TC	Total curvature
TEGP	Topographic Environmental GIS Proxies
TPI	Topographic Position Index
TRI	Topographic Ruggedness Index

Chapter 1 - Introduction

1.1. Rockfalls within a southern African context

Mass movement phenomena such as landslides are the 7th largest killer among natural disasters (Herath & Wang, 2009). The socio-economic impacts of mass movements are usually severe (Schuster, 1996). In, Japan, annual losses associated with mass movements were reported to be between 4 and 6 billion US$ in 2008 (Herath and Wang, 2009). The estimated cost for the prevention and rehabilitation of mass movements in southern Africa is about 20 million US$ a year (Paige-Green, 1989), however this outdated figure is likely an underestimate, given that no new estimates have been made (Paige-Green & Leyland, 2009). In South Africa, the socio-economic impacts of mass movements are gaining attention. For instance, the Council for Geosciences (CGS) has identified the need of local and provincial authorities to effectively manage strategies for reducing economic and social losses due to mass movements (Diop et al., 2010). Consequently, the CGS has embarked on the systematic inventorisation and susceptibility mapping of zones prone to slope instability in South Africa (Diop et al., 2010). The first synoptic landslide hazard map for South Africa was first developed by Paige-Green (1985) and modified and updated by Garland & Olivier (1993) and then revised again by Paige-Green & Croukamp (2004). Synoptic mass movement hazard maps are valuable at raising public and governmental awareness of geohazards such as landslides.

Many regions of the world are experiencing increases in mean, maximum, and minimum air temperatures, as also more frequent heavy precipitation (IPCC, 2007). Studying of the effects of climate change on mass movements in mountain environments such as the European Alps, has become increasingly relevant, since climatic changes affect the frequency and magnitude of mass movements, such as shallow landslides, debris flows, rock slope failures, or ice avalanches (Stoffel & Huggel, 2012). For instance, the frequency of rock slope failures is likely to increase in the European Alps, as excessively warm air temperatures, glacier shrinkage, as well as permafrost warming and thawing will affect and reduce rock slope stability in the direction that adversely affects rock slope stability (Stoffel et al., 2014). In southern Africa disastrous rainfall-triggered mass movements have been recorded in the Western Cape (Blight et al., 1970) and KwaZulu Natal (Thomas and van Schalkwyk, 1993). It has been suggested that climate change will indirectly result in an increase in the number of catastrophic mass movements (Petley, 2010). Thus, there is a growing need for South African earth scientists to increase their understanding of mass movements, particularly for improving spatial and temporal predictions of their likely future occurrences (Hardwick, 2012).

In South Africa, studies commonly focusing on rockfalls and rockbursts are associated with anthropogenic activities such as mining and blasting (Esterhuizen & Streuders, 1998; Gumede & Stacey, 2007; Vogt et al., 2010). Naturally occurring rockfalls within South Africa are usually localised to the cliffs along the Great Escarpment, however there have been few geomorphological studies (Boelhouwers & Meiklejohn, 2002; Grab, 2010; Grab & Mills, 2011; Hardwick, 2012).

In the Ceres Mountains (Western Cape), rockfall activity has been associated with earthquakes (Green & Bloch, 1971). At Chapman's Peak Drive in the Western Cape, the famous 10 Km scenic road had to be closed and reopened to the public in 2004 following extensive reconstruction works and assessments of rockfall hazards using innovative numerical and geotechnical methods which included a special GIS-based mapping of all potential rockfalls together with a corresponding 3D-trajectory analysis, and an additional probabilistic analysis of the expected rockfalls and the design of the protective structures (Volkwein et al., 2005). Rockfalls along the Drakensberg Lesotho mountains occur as falling and toppling movements along the horizontally-bedded rock outcrops of the Karoo Supergroup (Hardwick, 2012). In the Drakensberg-Maluti Mountains, field evidence of massive Basalt and Clarens Formation boulders on the scree slopes below the cliffs formed by the resistant Drakensberg basalt and Clarens Formation are primarily controlled by the detachment of large blocks along joints and other lines of weakness by processes such as undercutting and ice-wedging (Figure 1) (Moore & Blenkinsop, 2006). In southern Africa, little is understood regarding the spatial and macro-morphology of rockfalls, particularly those pertaining to the Clarens, Molteno and Elliot Formations.

Traditionally, rockfall activity has been measured by collecting data from the clasts detached from cliffs in natural embayments or by artificial means (Matsuoka and Sakai, 1999). This activity usually required that a great number of samples be obtained and long time spent collecting the data, and together with the complexity of the sampling devices, made it difficult to obtain information on rockfall activity in wide geographic areas, thus hindering interpretation at the regional scale (Menéndez Duarte & Marquinez, 2002). Remote sensing techniques, such as Aerial Photo Interpretation (API), offer a cheaper and quicker approach for regional mass movement feature identification than field-based methods (Brardinoni et al., 2003). In southern Africa, API has been successfully adopted to investigate and map mass movement phenomena (Bijker, 2001; Singh, 2008; Hardwick, 2012).

1.2. Aims and objectives

In the Bushmen’s Nek region of the southern Drakensberg, site-specific classification for mass movement features and analyses of a large variety of environmental factors leading to mass movement activity have been assessed (Hardwick, 2012). Using similar approaches, this study aims to better understand the spatial distribution and macro-morphology of rockfalls originating from the Clarens and Molteno Formation sandstones and Elliot mudstone, in relation to a variety of environmental variables in the Golden Gate Highlands National Park (GGHNP), Eastern Free State. The GGHNP which forms part of the Maloti Drakensberg Transfrontier Conservation Area (MDTFCA), was established to conserve these geological formations and as such was chosen as the study area. The park, which is currently managed by SanParks, is best known for its geological, paleontological and geomorphological heritage.

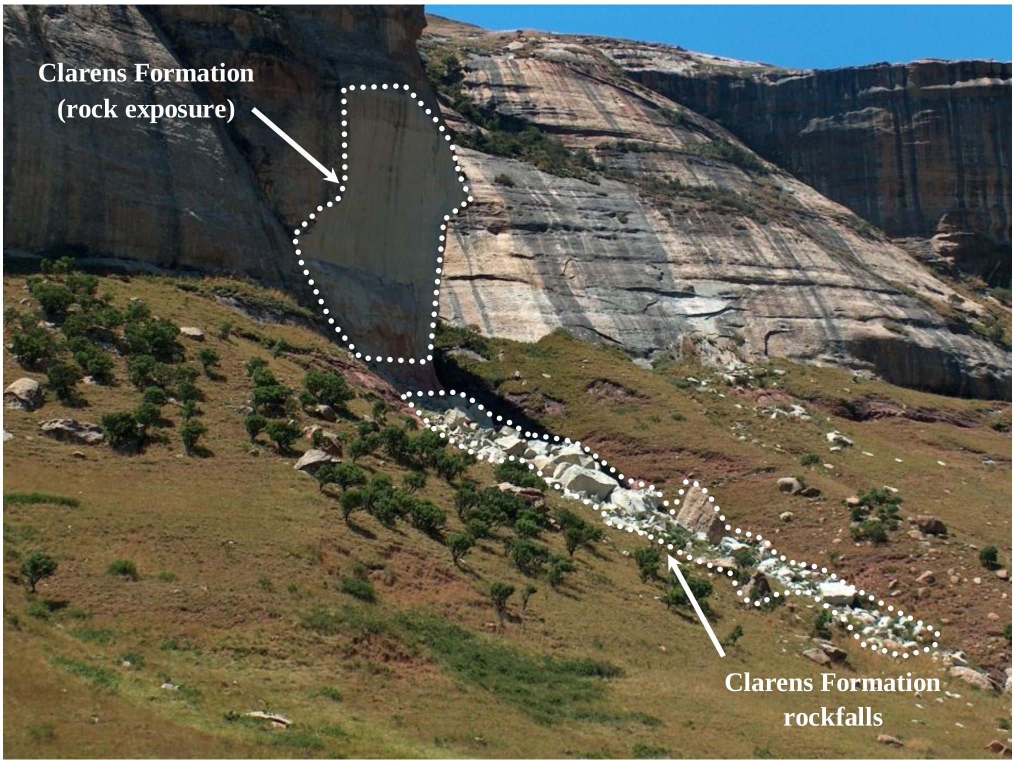

Figure 1: Massive Clarens Formation boulders strewn across the slopes of the Drakensberg-Maluti mountainland.

Although the diversity of sandstone geomorphological phenomena in the park has been highlighted (Grab et al., 2011), little is known about the spatial distribution and macro-morphology of rockfalls originating from the Clarens and Molteno Formation sandstones and Elliot mudstone. The environmental variables of altitude, slope aspect, slope gradient, slope unit, and distance to drainage lines and lithology (rock exposure) were selected, as they are the typical variables used in landslide and rockfall hazard zonation studies (Nefeslioglu et al., 2008; Pandey et al., 2008). The environmental variables were selected to examine the spatial distribution of rockfalls in relation to topography.

The GGHNP is suited to studies focusing on the environmental, rather than anthropogenic effects on rockfalls, as only a small percentage of the GGHNP is accessible to visitors and most of the human impacts are concentrated along footpaths or hiking trails, camp sites, and hotels or tourist attractions, such as rock overhangs.

The primary objectives of this study include:

1. Using ground-truthed rockfalls to develop and validate a remote sensing based classification approach for rockfalls originating from the Clarens and Molteno Formation sandstones and Elliot Formation mudstone.
2. To examine whether or not Clarens, Molteno and Elliot Formation rockfall characteristics measured during ground-truthing can be modelled with Topographic Environmental GIS Proxies (TEGP) using multiple linear regression.
3. To understand the spatial and macro-morphology of rockfalls originating from the Clarens and Molteno Formation sandstones and Elliot Formation mudstone.
4. To compare the findings of rockfalls originating from the Clarens and Molteno Formation sandstones and Elliot Formation mudstone in the Drakensberg-Maluti mountains to those of a previous study in the southern Drakensberg. This was done to examine whether or not the rockfalls originating in the southern Drakensberg share trends with rockfalls originating in the GGHNP.

1.3. Structure of the dissertation

This dissertation is structured into eight chapters. Chapter 1 is the introduction, which describes the relevance of mass movement studies, such as landslides and rockfalls, presenting the current state of rockfall studies in a southern African context, and the aims and objectives of the research. Chapter 2 discusses the characteristics of rockfalls, rockfall susceptibility and modelling research, and the potential for classifying rockfalls through the use of object-oriented approaches. Chapter 3 describes the environmental setting of the GGHNP. Chapter 4 presents the methodology used for ground-truthing rockfalls, processing remotely sensed data to meaningful environmental variables, and the approach for modelling rockfall characteristics using multiple linear regression modelling. Chapter 5 discusses the results of the ground-truthing work. Chapter 6 presents the results and discussion of the multiple linear regression models, which test whether or not rockfall characteristics gathered from ground-truthed measurements, can be detected using TEGP. The results of chapter 5 and 6 were then used to develop an object-oriented approach for mapping rockfall points in the GGHNP, presented in chapter 7. The spatial distribution and macro-morphology of rockfalls extracted through object-oriented approaches was then critically analysed in chapter 7 using a number of GIS, and statistical approaches. Chapter 8 provides a summary of all the findings for rockfalls in the GGHNP originating from the sandstone Formations.

Chapter 2 - Rockfall Characteristics, Modelling, and Mapping

2.1. Rockfall characteristics

Varnes (1978) defines a rockfall as a fragment of rock (a block) detached by sliding, toppling, or falling, which fails along a vertical or sub-vertical cliff, proceeding down slope by bouncing and flying or by rolling on talus or debris slopes. Antoniou & Lekkas (2010) define a rockfall as small cobble stones, to large boulders hundreds of cubic meters in size, which travel at speeds ranging from few to tens of meters per second. Rockfalls are a natural hazard that usually impact small areas, however, the damage to infrastructure or persons directly affected can be high with serious consequences (Volkwein et al., 2011: 2617). Rockfalls come to rest in what is termed the "rockfall runout zone", these occur at or near the base of a slope. When a rockfall triggers a large-scale mass movement of rock material, it is defined as a rock-slide or –avalanche (Dorren, 2003). Rock cuttings for highways and railways, and developments in mountainous terrain are most at risk to rockfall events.

Figure 2 and Table 1 illustrate and list the external forces and internal factors which initiate rockfalls respectively. Internal parameters refer to the intrinsic features of slopes, and with time evolve due to external forces such as climate (Volkwein et al., 2011). Rockfalls are generally initiated by some climatic or biological event that causes a change in the forces acting on a rock. The potential for rockfalls is dependent on a number of environmental factors causing physical or chemical weathering, and the geological and geotechnical properties of the rockfall source (Day, 1997). These factors may include pore pressure increases due to rainfall infiltration, erosion of surrounding material during heavy rain storms, freeze-thaw processes in cold climates, chemical degradation or weathering of the rock, and plant root growth, to name a few. Luckman (1976) also attributes rockfalls to the morphological and geological characteristics of the cliff and rock surface temperature fluctuations. Freeze-thaw activity is probably one of the most frequently documented promoters and causes of rockfalls (McCarol et al., 1998; Masuoka & Sakai, 1999; Peila et al., 2011; Kenner et al., 2011; Kellerer-Pirklbauer et al., 2012; Šilhán et al., 2013), especially in cold environments. The diversity of rockfall promoting factors have been investigated in the Yosemite valley (USA), where rockfalls have been attributed to factors such as seismic activity, rain storms, rapid snow melt, freeze-thaw cycles, root penetration, wedging, and stress relief followed by deglaciation (Stock et al., 2011; Stock et al., 2012; Zimmer et al., 2012; Cordes et al., 2013).

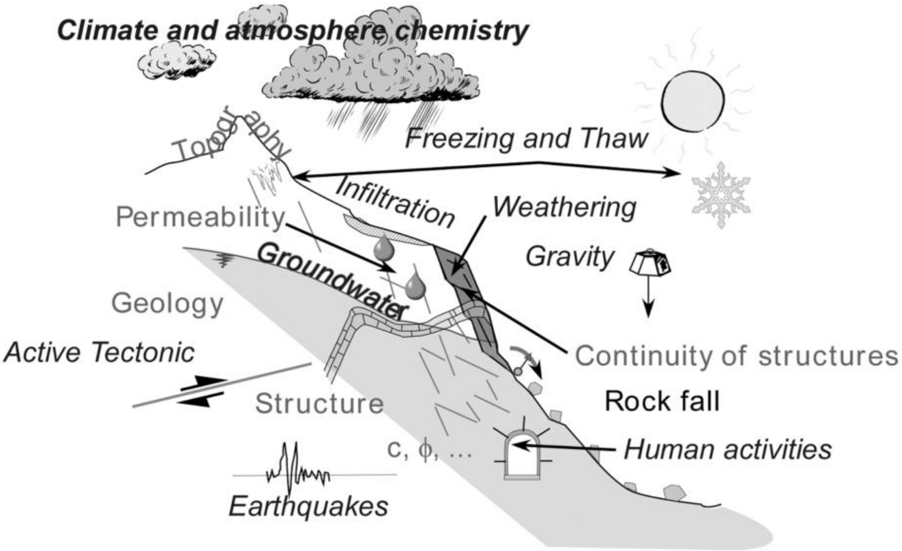

Figure 2: Illustration of the internal parameters and external forces, which initiate rockfalls (after Jaboyedoff & Labiouse, 2003; Jaboyedoff & Derron, 2005).

A rockfall can experience four types of motion along its path; free fall, rolling, bouncing and sliding (Basson, 2012). Figure 3 shows the type of motions during a rockfall. The freefall of rocks occurs on steep slopes which exceed 70°. As the slope gradient decreases towards 45°, the rockfalls have a movement which is at or near the slope surface. If the mean slope gradient decreases in the down-slope section, rocks begin colliding with the slope and are then said to be bouncing (Dorren, 2003: 72). At 45° and less, the rockfall movement gradually transforms its motion to rolling. Retardation of moving

Internal Parameters	Morphology	Slope types (slope angle, height of slope, profile, etc.), exposure, type of relief (depends on the controlling erosive processes), etc.
	Geology	Rock types and weathering, variability of the geological structure, bedding, type of deposit, folded zone, etc.
	Fracturing	Joint sets, trace lengths, spacing, fracturing intensity, etc.
	Mechanical properties of rocks and soil	Cohesion, friction angle, etc.
	Activity	Movements or rockfalls, etc.
	Hydrogeology	Permeability, joint permeability, etc.
External Forces	Gravitational effects	Geology and hydrogeology, climate, precipitation in the form of rainfall or snow, infiltration rates, ground water.
	Water circulation	
	Weathering	
	Erosion	
	Seismicity	
	Active tectonics	
	Microclimate	Including freezing and thawing, sun exposure, permafrost.
	Nearby instabilities	
	Human activities	Anthropogenic factors (eg. Mining).

Table 1: Internal parameters and external forces which initiate rockfalls (adapted from Volkwein et al., 2011).

rocks refers to the factors acting to bring the rock to discontinue moving. The velocity and eventual stoppage of a rockfall depend on the mean slope gradient, since falling rocks generally accelerate on a steeper slope gradient and decelerate on flatter slopes (Dorren, 2003).

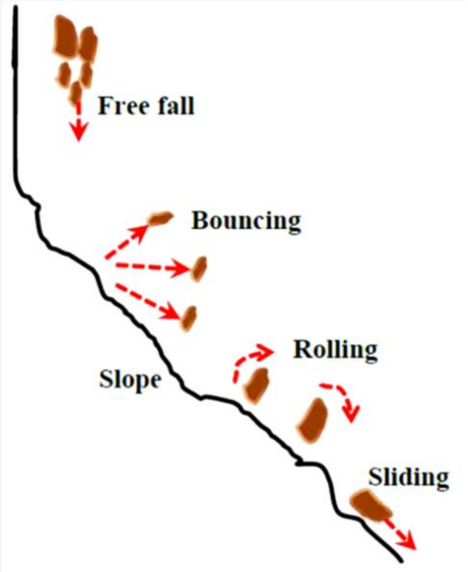

Figure 3: Types of motion during a rockfall (from Basson, 2012).

2.2. Rockfall susceptibility mapping

Rockfalls are one of the more extensively studied geomorphic phenomena due to the fact that they have catastrophic consequences, particularly in mountainous regions (Ballifard et al., 2003; Dorren, 2003; Erener & Düzgün et al., 2010; Jiménez-Perálvarez et al., 2011; Jaboyedoff et al., 2012a; Jaboyedoff et al., 2012b). Traditional approaches for studying rockfall activity consist of measuring and gathering data from the clasts detached from cliffs (Hardwick, 2012). The development of mass movement classifications (Hutchinson 1968; Varnes, 1978) has enabled innovative technologies such as GIS and remote sensing to interpret mass movement phenomena such as rockfalls more effectively and extensively (Guzzetti et al., 1999; Temesgen et al., 2001; Dorren & Seijmonsbergen., 2003; Chau et al., 2004; Ayalew & Yamagishi, 2004; Pradhan et al., 2009). In particular, GIS analyses enabling the production of susceptibility maps have become popular in recent years (Wieczorek et al., 1999; Dai & Lee, 2002; Ballifard et al., 2003; Antoniou & Lekkas, 2010; Erener & Düzgün et al., 2010; Jiménez-Perálvarez et al., 2011; Jaboyedoff et al., 2012a; Jaboyedoff et al., 2012b). Probabilistic, heuristic and deterministic methods are some of the approaches which have been developed to study mass movement phenomena. Examples of studies using the aforementioned approaches are described in further detail.

2.2.1. Probabilistic methods

Probabilistic methods compare the distribution of observed mass movements with the distribution of physical factors thought to cause mass movements, either directly or indirectly (Hagos, 2013; Cirella et al., 2014). The Probabilistic methods rely on quantitative techniques and are the most frequently used. A great deal of statistical analysis has been used for quantitatively understanding mass movement phenomena and these range from methods based on the inventorying of mass movements, qualitative and statistical bivariate analysis (Chung & Fabbri, 1999; Yilmaz & Yildirim, 2006; Pradhan & Lee, 2010; Yalcin et al., 2011), multiple regression analysis, and discriminant analysis (Pradhan, 2010; Rossi et al., 2010; Yilmaz, 2010). Logistic regression is a popular probabilistic statistical classification model which has been used for exploring the relationships between mass movement occurrence and topographic variables for the prediction of slope instability (Carrara et al., 1991; Rowbotham & Dudycha, 1998; Das et al., 2010; Prabhan, 2010; Yilmaz, 2010; Dong et al., 2011).

Multivariate models for landslide hazard evaluation were first explored as part of a long-term project aimed to better understand the geological and geomorphological factors that control slope instability in southern Italy (Carrara, 1983). Mappable geological and geomorphological variables have been shown to differentiate between mass movements on stable and unstable slope units, using multiple regression analysis to predict actual and potential mass movement hazards (Carrara, 1983). Multivariate statistics has proven popular in studies demonstrating hypothetical correlations between instability factors and mass movement occurrence (Carrara, 1983; Carrara et al., 1991; Dai & Lee, 2002; Ayalew & Yamagishi, 2004; Yilmaz, 2009). However, multiple regression is limited in that it generalises and over simplifies causal factors, does not take into account the temporal aspects of mass movements, and is not able to predict the impact of changes in the controlling conditions (Yilmaz, 2009).

Probabilistic methods depend on the collection of large amounts of data for reliable results. Such data sets include mass movement inventory maps, land component maps, DEMs, topographic variables derived from a DEM, rainfall data, geological data, and land use data, to name a few. For instance, the GIS modelling of mass movements and slope instability in Lantau Island (Hong Kong), demonstrates how DEM elevation data, topographic variables derived from a DEM, lithological layers from geological data, and land use data are statistically significant in predicting slope instability, using logistic multiple regression analysis (Dai & Lee, 2002).

2.2.2. Heuristic methods

In contrast to probabilistic methods, heuristic methods are qualitative and rely on the expert knowledge of the analyst to associate weights to various mass movement instability factors (Ballifard et al., 2003). The heuristic method makes use of mass movement inventory maps which can be combined with maps which express various terrain parameters, such as topography, geology or drainage to produce mapping units that are ranked into mass movement susceptibility classes (Casadei et al., 2003). Two different types of heuristic analysis are recognised: geomorphological analysis and qualitative map combinations. In geomorphological analysis, mass movement susceptibility is directly established by researchers in the field, and in qualitative map combinations, expert knowledge is used to assign weights to a series of thematic layers (Yilmaz, 2009: 1126). There are many examples of studies which have applied the heuristic method for mass movement risk assessment (Ives & Messerli, 1981; Barredo et al., 2000, Van Westen, 2000; Ballifard et al., 2003; Ruff & Czurda, 2008; Bijukchhen et al., 2012; Blais-Stevens et al., 2012; Kayastha et al., 2012; Soomro et al., 2012).

In Switzerland, the heuristic method has been effective in determining rockfall hazards along mountainous roads with high sensitivity to rockfall instability by taking into consideration instability factors related to topographic, geomorphological, and geological settings where rockfalls might occur (Ballifard et al., 2003). Being a qualitative approach, heuristic methods are limited in that they provide insufficient knowledge about the area of interest, leading to unacceptable generalizations and subjectivity in the weighting of variables (Barredo et al., 2000; Yilmaz, 2009).

2.2.3. Deterministic methods

Deterministic or physically-based models evaluate landslide instability, using physical laws of conservation of mass, energy or momentum (Dias & Gunathilake, 2012), and involve the estimation of quantitative values of stability variables, known as safety factors, over a defined area (Yilmaz, 2009). There are many examples of studies which have applied the deterministic method for landslide risk assessment (Terlein & Van Westen, 1995; Haneberg. 2000; Gomez & Kavzoglu, 2005; Yilmaz, 2009; Chiessi et al., 2010; Dahal et al., 2010; Mergili et al., 2011; Iverson, 2014), although this remains less popular than the probabilistic methods. The required data for the deterministic method typically include soil strength, depth below the terrain surface, soil layer thickness, slope angle and pore water pressure (Yilmaz, 2009).

The artificial neural networks technique is an example of deterministic methods which have been successfully used to create landslide susceptibility maps with satisfactory accuracies (Gomez & Kavzoglu, 2005; Yilmaz, 2009; García-Rodríguez et al., 2010; Pradhan & Lee, 2010; Xu et al., 2013). Gomez and Kavzoglu (2005) used a DEM and remotely sensed image data to derive nine parameters related to landslide phenomenon, and together with a ground-truthed image, employed an artificial neural network to successfully delineate the underlying relationship between the nine parameters related to landslide phenomenon. A comparison of probabilistic and deterministic methods shows that the deterministic method produces slightly more accurate results than the probabilistic method (Yilmaz, 2009). However, one of the main drawbacks of the deterministic method is the large extent of oversimplification when the data for the variables is incomplete, and too expensive (Gomez & Kavzoglu, 2005).

2.3. Rockfall runout modelling

Rockfall simulation models are capable of producing reasonably accurate predictions of rockfall trajectories and runout zones. Dorren (2003) categorises rockfall runout models into three main groups: (1) empirical models, (2) process-based models and (3) GIS-based models. Currently, a large variety of empirical and process-based rockfall models exist. Empirical models are usually based on relationships between topographical factors and the length of the rockfall runout zone of one or more rockfall events (Shirzadi et al., 2012). Process-based models describe or simulate the modes of motion of falling rocks over slope surfaces, thus providing more accurate predictions of runout zones (Loye & Jaboyedoff, 2009). GIS-based models offer the latest methods for determining rockfall runout zones and consist of three procedures: the first identifies the rockfall source areas in the region of interest, the second determines the falltrack, and the third calculates the length of the runout zone (Shirzadi et al., 2012). Each of the modelling approaches has strengths and weaknesses. Empirical models provide quick and simple approximations of rockfall runout zones, whereas process-based models produce more accurate predictions of runout zones (Dorren, 2003: 84). The integration of process-based models with a GIS has proven useful in the identification of rockfall source areas, the determination of falltracks, and the prediction of rockfall runout zones at a regional scale (Dorren & Seijmonsbergen, 2003).

2.3.1. Empirical models

Empirical models, also referred to as statistical models, are defined as the relationship between topographic factors and the length of the runout zone for one or more rockfall events (Shirzadi et al., 2012). Statistical models are advantageous in that they quickly and effectively allow the determination of rockfall hazards over a broad area (Keylock & Domaas, 1999). The favoured statistical model is guided by the data available for the study area. A process based model called the ‘simple dynamics rockfall model’, and three empirical models namely; the ‘height function model’, the ‘α-β model’, and the ‘runout ratio model’ were tested in a study of rockfall runout which concluded that the ‘runout ratio model’ appeared to be the most accurate of the models used (Keylock & Domaas, 1999). Table 2 describes the ‘height function model’, the ‘α-β model’, and the ‘runout ratio model’ in further detail. A considerable number of studies have demonstrated the development and application of different empirical models for simulating and predicting rockfall (Van Dijke & Van Westen, 1990; Guzzetti et al., 2002; Stoffel et al., 2006; Lan et al., 2007; Jaboyedoff & Labiouse, 2011; Bell et al., 2013).

Model	**Type**	**Description**
Height Function Model	Empirical	Assumes that runout distance beyond the foot of the talus slope can be derived from the combined vertical height of the free rock face and the talus slope.
α-β model	Empirical	Based on the correlation between the average energy of an extreme rockfall event, where a boulder stops beyond the foot of the talus slope and the energy of an average event, where the boulder stops at the foot of the talus slope.
Runout ratio model	Empirical	Describes the ratio between the horizontal length of the runout zone to the combined horizontal length of the talus slope and the free rock face.

Table 2: The three empirical models, as used by Keylock & Domaas (1999).

2.3.2. Process-based models

Process-based models express or simulate the models of motion of rockfall over slope surfaces (Dorren, 2003). The work was pioneered by Kirkby and Statham (1975), and Statham (1976), who developed a process-based rockfall model for the transport of rock over talus slopes. This process-based model assumed that rocks only slide over a talus slope surface. A similar process-based model known as ‘the simple dynamics rockfall model’ scrutinised the transport of rock over talus slope surfaces and concluded that it did not appear to hold a significant advantage over empirical models (Keylock & Domaas, 1999). Process-based rockfall models share the following three common characteristics (Dorren, 2003):

1. Two-dimensional slope-scale models that ignore the lateral movements of rockfall.
2. Rockfall track is defined as a composite of connected straight lines with slope angle equal to the measured slope gradient.
3. Rockfall motions are simulated as a succession of flying phases and contact phases.

Table 3 refers to studies which were significant in contributing to the development of the process-based rockfall runout model. Although process-based rockfall runout models are advantageous for describing and simulating the models of motion for falling rocks, they are limited in their ability to simulate multiple falling rocks and the complex interactions between them.

2.3.3 GIS-based models

During more recent times, the development of GIS has allowed for the contribution of models that identify the coordinates, velocity, and angular velocity for multiple particles in a three dimensional space. GIS-based models can be raster-based (2D) or 3D models where a raster neighbourhood analysis using a roaming window is used to calculate fall directions (van Dijke & van Westen, 1990; Meissi, 1998; Lan et al., 2007; Loye & Jaboyedoff, 2009; Antoniou & Lekkas, 2010; Antoniou, 2013). RockFall Analyst is an example of a GIS extension used in the software package ArcGIS, which uses particle-based rockfall process modelling and geostatistics-based rockfall raster modelling to simulate the 3D trajectory of rockfalls and also interprets the spatial distribution of rockfalls (Lan et al., 2007). Rockfall modelling software packages such as Rockfall Analyst are usually proprietary and expensive. However, Open Source software alternatives such as GRASS GIS for rockfall analysis is freely available and allow users to develop and adapt it to suit their purposes (Filipello & Mandrone, 2013). One of the major advantages of a GIS-based rockfall analysis is that it allows for the modelling and analysis of the spatial distribution of rockfalls using multiple parameters, which include climate and presence of water on slopes as well as rockfall history, and various indices relating to geology, blockiness of rock masses and orientation of joints with their weathering condition and roughness (Antoniou, 2013).

Author(s)	**Contribution**
Azzoni et al., 1995	Developed a model based on the coefficient for the efficiency of collision.
Kobiyashi et al., 1990	Developed a model that simulated the contact phases with different characterisations for bouncing and rolling.
Pfeiffer and Bowen, 1989	Developed a model using both a tangential and normal coefficient for the efficiency of collision.
Evans & Hungr, 1993	Applied a lumped mass model to three test cases in British Columbia.
Descoudres & Zimmermann, 1987	Developed a three-dimensional process based rockfall model using a high resolution DEM.
Lan et al., 2007	Rockfall Analyst: Raster and 3D rockfall modelling to ascertain distribution and trajectories in a GIS.
Filipello & Mandrone, 2013	Open Source GIS for rockfall analysis. Modules examine both the potential failure detection (rockfall susceptibility) and the area of potential propagation. The study investigate three different mechanisms of failure: planar sliding, wedge sliding and toppling.

Table 3: Key contributions in the development of the process based rockfall, runout model (adapted from Dorren, 2003).

The ‘fall track model’ was a key contribution towards GIS-based rockfall runout modelling which also used an empirical model to calculate the fall track of a rockfall source area using a raster-based neighbourhood analysis (Meissi, 1998). This raster-based neighbourhood analysis was developed into a module referred to as the “D-16 method”. The D-16 method used a 5x5 roaming window allowing for 16 fall directions from a central raster cell to be simulated (illustrated in Figure 7). The fall track model was advantageous for calculating the maximum height difference between a central raster cell and its 16 surrounding cells divided by the distance of the two cells (Dorren, 2003).

The increased use of GIS has meant that current research is able to use the production of rockfall susceptibility maps as a basic methodological tool combined with geomorphic inventories and DEMs (Copons & Vilaplana, 2008; Melzner et al., 2009; Antoniou & Lekkas, 2010; Chiessi et al., 2010; Tanarro & Muñoz, 2012; Antoniou, 2013). DEM modelling is a powerful tool for describing the physical characteristics of a surface including topography and its derivatives (e.g., slope, aspect, curvature, etc.), thereby offering the ability to delineate the physical rock fall process (Lan et al., 2007). However, the modelling of rockfall behaviour is challenging, and one of the main difficulties is that source areas are often not well identified (Agliardi & Crosta, 2003) and the behaviour of rockfall fragments is very uncertain as most of the important parameters required are difficult to measure (Frattini et al., 2008; Straub & Schubert, 2008). However, the issues regarding the difficulties in identifying potential rockfall source areas can be addressed with DEM-based geomorphometric analysis in combination with geological and topographic information in a GIS (Loye et al., 2009).

2.4 Object-oriented landform mapping

Remote sensing image classification techniques have been used effectively to extract extensive mass movement features for comparing to known mass movement locations (Park & Chi, 2008; Martha et al., 2010; Pradhan, 2010; Stumpf & Kerle, 2011; Martha et al., 2012). Traditionally, this has been done using pixel-based image classification techniques (Borghuis et al., 2007). Pixel-based image classification uses the spectral values of pixels (digital number or DN) stored in the remotely sensed image’s pixels to categorise pixels into classes by considering the spectral similarities within pre-defined land cover classes (Casals-Carrasco et al., 2000). Although pixel-based techniques are well developed and have sophisticated variations such as soft classifiers, sub-pixel classifiers and spectral un-mixing techniques, it is argued that they do not make use of the spatial concept (eg. shape and size) (Blaschke et al., 2000). The short-comings of pixel-based landform classifications pertain to their limitations in tying the scale analysis to the raster resolution, difficulties in including topological relationships in classification and also in developing hierarchies of landforms (Drăguţ & Eisank, 2011: 184). In contrast, object-oriented approaches offer an alternative to traditional pixel-based classifications as they consider pertinent contributions to scale and object representation from remotely sensed imagery (Deng, 2007; Minár & Evans, 2008; Hengl & Reuter, 2009). Change detection for rapid landslide mapping in Messina (southern Italy), has demonstrated how object-oriented classification is superior in delineating landslides as opposed to pixel-based classifications which were found to have fundamental limitations in addressing particular landslide characteristics due to their finite spatial extent (Lu et al., 2011).

Image segmentation is the most fundamental aspect of OBIA and its worth has been demonstrated in a useful review on object ontology, showing the limitations of the pixel-based approach in mapping landforms followed by the introduction of segmentation of elementary forms as an alternative (Drăguţ & Eisank, 2011). Image segmentation is the process of partitioning a digital image into multiple segments, also known as super-pixels or image objects (Shapiro & Stockman, 2000), and has its roots in industrial image processing which was not used extensively in Geospatial applications throughout the 1980s and 1990s (Blaschke et al., 2004). In OBIA, image segmentation is generally seen as a means of simplifying an image into more meaningful image objects. Super-pixels or image objects are created through the process of image segmentation, which assigns a label to every pixel in an image, so that pixels with the same label share certain visual characteristics, such as spectral behaviour, shape and context. Thus, unlike pixel based methods, OBIA techniques reach beyond the spectral characteristics of pixels.

One of the reasons for grouping pixels into image objects is to overcome the so-called ‘salt-and-pepper effect’ inherent with traditional pixel-based techniques (Blaschke et al., 2000). The information available from image objects includes the mean, median, minimum, and maximum value per raster band, texture, shape (e.g. length, number of edges), topological features (neighbour, super-object) and the close relation between real-world objects and image objects (Benz et al., 2004). OBIA brings together the spectral capabilities of remote sensing and the geo-spatial tools of GIS into one desktop environment, allowing for more robust methods for mapping surface features (Flanders et al., 2003).

OBIA is well suited for high spatial resolution imagery. Figure 4 shows the relationship between actual ground truthed objects and spatial resolution. In Figure 4, (a) represents a low spatial resolution image, (b) a medium spatial resolution image, and (c) a high spatial resolution image. The low and medium spatial resolution imagery in (a) and (b) do not leave much choice when the task is to identify, classify and characterise objects. However, the high spatial resolution image in (c) is ideal for OBIA analysis as the pixels are significantly smaller than the objects.

Much of the work on OBIA in remote sensing originated around the software known as “eCognition”. eCognition previously known as Definiens, is a powerful software development environment for object-based image analysis which is commonly used in earth sciences to develop rule sets for the automatic analysis of remote sensing data (Blaschke, 2010). DEMs, thematic layers such as geomorphological inventory maps, and medium and high-resolution optical aerial and satellite imagery, have been well integrated in studies using OBIA to extract mass movements (Barlow et al., 2003; Martin & Franklin., 2005; Barlow et al., 2006; Martha et al., 2010; Lu et al., 2011). Studies which have utilised OBIA techniques for mapping geomorphological landforms, and mass movements, are further described.

One of the major benefits of an OBIA is the ability to semi-automate the extraction of landforms and terrain units from optical aerial and satellite imagery. OBIA semi-automated approaches have proven valuable at detecting and classifying landslides rapidly to aid in risk analysis, disaster management and decision making processes in the aftermath of a landslide event (Martin & Franklin, 2005). Barlow et al. (2006) were the first to further the development of a successful OBIA approach using high-spatial resolution SPOT-5 satellite

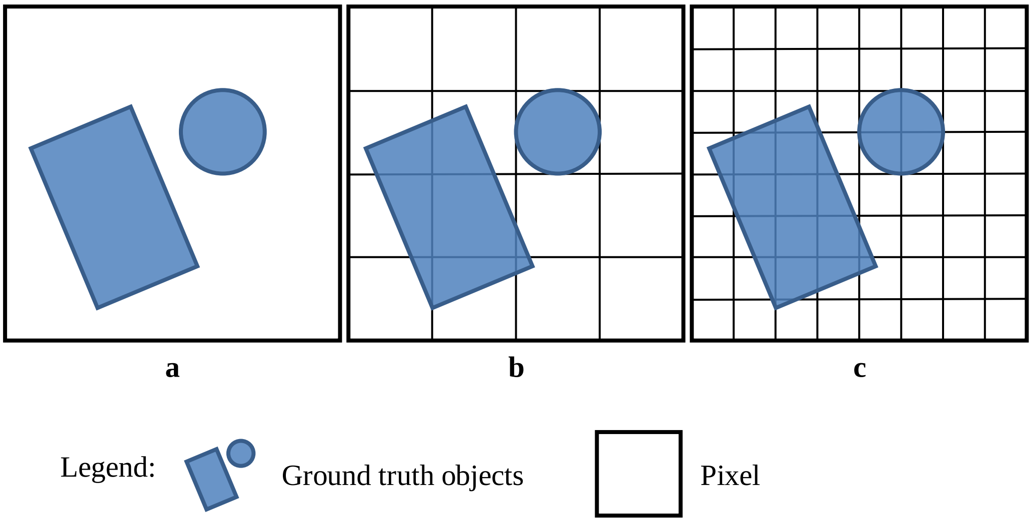

Figure 4: Relationships between objects under consideration and spatial resolution: (a) Low spatial resolution image: the image pixels are significantly larger than the ground truthed objects; sub pixel techniques are appropriate; (b) Medium spatial resolution image: image pixels and ground truth objects of the same order, pixel-based techniques are appropriate; (c) high spatial resolution image: the pixels are significantly smaller than the ground truth objects, OBIA would be ideal (adapted from Blaschke, 2010).

imagery, and geomorphic variables derived from a DEM to automatically detect landslide hazards. Expert-driven multilevel OBIA has been effective at semi-automating the delineation of geomorphological units in mountainous forested ecosystems (Figure 5) (Van Asselen & Seijmonsbergen, 2006). Multi-temporal object based segmentation of high-spatial resolution remote sensing data has proven highly effective at predicting 83% of actual landslide occurrences in Korea (Park & Chi, 2008). A similar study conducted by Schneevoigt et al. (2008), investigated the suitability of remote sensing for detecting rock and sediment storage areas in the Reintal subcatchment, east of Zugspitze (Germany) using a multi-scale OBIA comprising four differently scaled segmentation levels. Their results show that classification of geomorphological units using OBIA constitutes a promising scientific approach, especially with regards to the enhanced spatial and spectral resolution of modern satellite systems (Figure 6). In the Himalayas, OBIA intergrated with spectral, spatial and morphometric features was able to recognise and classify five different types of landslides on difficult terrain with an overall success rate of 70% (Martha et al., 2010). A similar study in Messina (southern Italy) went a step further, constructing an event-related landslide inventory by applying OBIA to automatically detect and classify landslides from high-spatial resolution optical satellite imagery acquired prior to and after landslide events (Lu et al., 2011).

One of the main objectives of this MSc study is to develop an OBIA methodology similar to the ones described in the literature for extracting landslides and landforms. Ground-truthed rockfall measurements taken in the field were used in this study as an input for defining the thresholds for the OBIA’s segmentation and classification, adopting a similar approach used for extracting landslide areas (Martha et al., 2010). The ground-truthed rockfall measurements were also used to examine whether or not rockfall characteristics can be modelled with TEGP using linear regression modelling, and for validating the results of the OBIA. Univariate and bivariate statistical techniques discussed in the literature are applied in this study to describe the spatial distribution of the rockfalls extracted from the OBIA in conjunction with various environmental variables. The spatial patterns of rockfalls in the study area are analysed using average nearest neighbour statistics. One of the initially intended goals of this study was to examine rockfall probability using multivariate statistics as discussed in the literature. However, rockfall probability was not examined in this study in the interest of keeping to the original MSc level scope the study, which is to better understand the rockfalls of the GGHNP. The results of this study could, however, feed into further studies examining rockfall probability in the GGHNP.

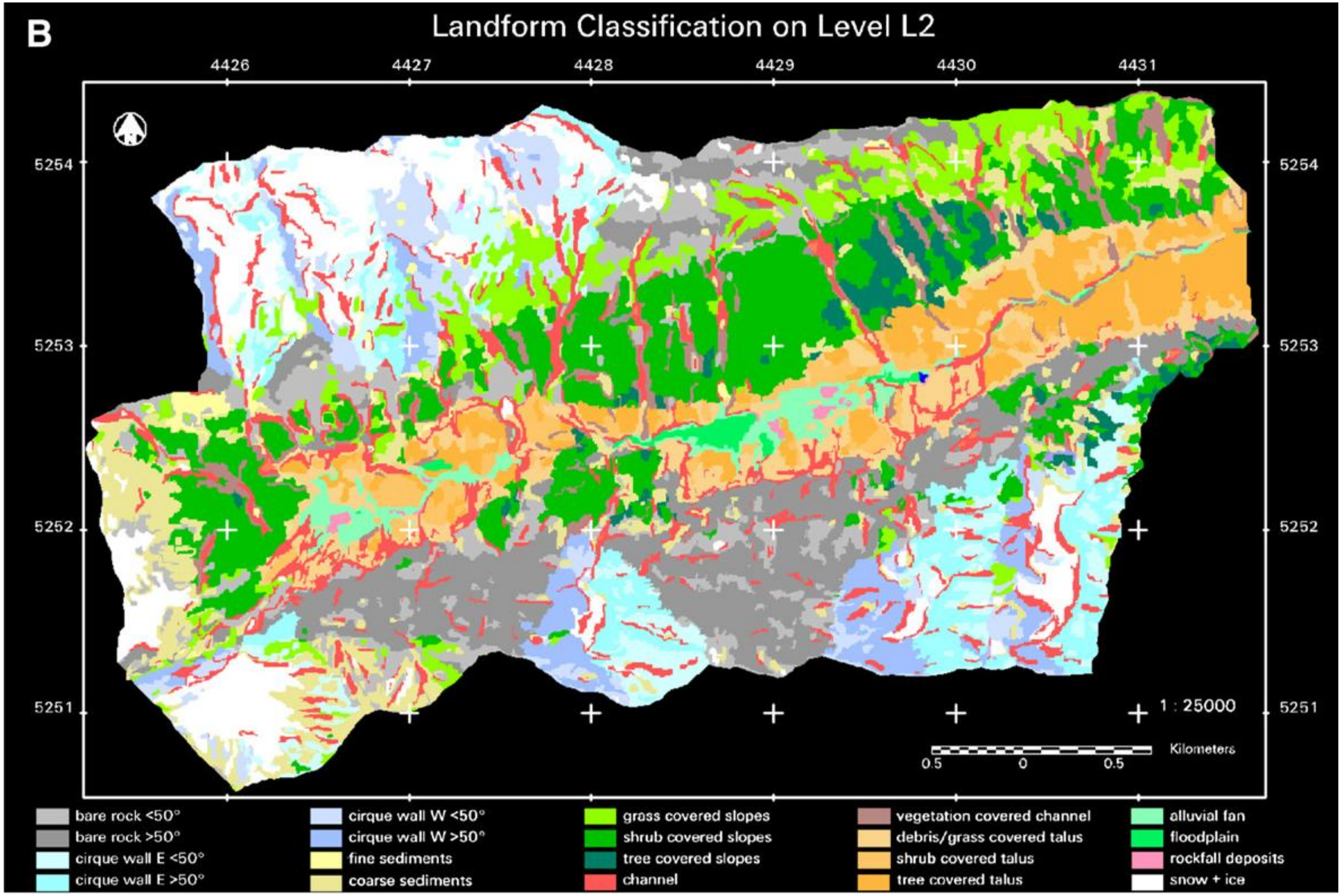

Figure 5: Classification results, showing 20 landform classes and in blue the lake of Vordere Gumpe (from Schneevoigt et al., 2008).

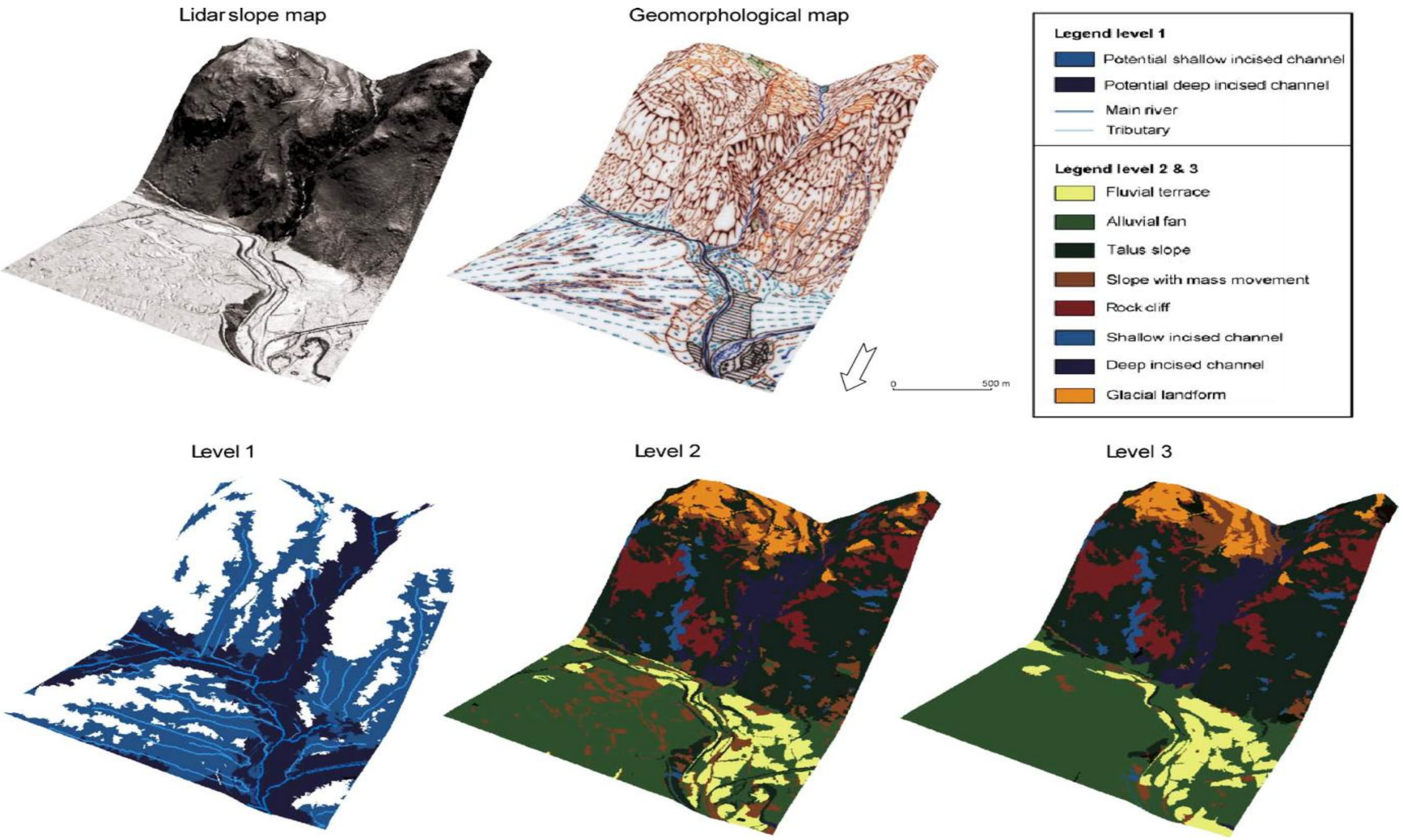

Figure 6: LIDAR slope map, geomorphological map, and classification results of levels 1, 2 and 3, draped over the LIDAR DTM representing part of the study area (from Asselen and Seijmonsbergen, 2006). Levels refer to the segmentation levels used in the OBIA.

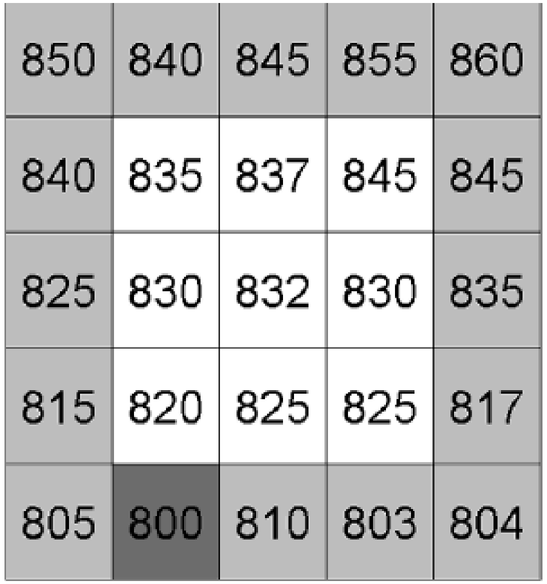

850	840	845	855	860
840	835	837	845	845
825	830	832	830	835
815	820	825	825	817
805	800	810	803	804

Figure 7: The D-16 method. A 5x5 roaming window allowing for 16 fall directions from a central raster cell to be simulated (adapted from Dorren, 2003).

Chapter 3 - Environmental Setting of the GGHNP

3.1. Geographic setting of the study area

GGHNP is located in the north-eastern Free-State province of South Africa, in the foothills of the Maluti Mountains (28°27’S – 28°37’S and 28°33’E – 28°42’E), between the towns of Clarens and Phutadithaba (Figure 8). The park consists of a number of former farms, the first of which (Glen Reenen, Wodehouse and Melsetter) were proclaimed for conservation on the 13th September 1963 (1,792 ha). In 1981, Noord Brabant farm was added, contributing a substantial 6,241 ha to the park (SANPARKS, 2012). Between 1988 and 1989, an additional 8 farms were added, thus extending the park’s boundaries to the QwaQwa National Park and Lesotho, and expanding the park to 11,630ha. On the 21st November 2008, the QwaQwa National park was included to the GGHNP, further increasing the park to its current size of 32,690ha (SANPARKS, 2012). The GGHNP lies between 1,892 m and 2,829 m above sea level, the highest point being Ribbokkop (2,829 m) (Grab et al., 2011).

3.2. Climate

The GGHNP is situated in the summer-rainfall region, characterised by summer rainfall, temperate summers and cold winters with frost and occasional snow on the peaks. Summer temperatures have a mean range of 13°C to 26°C, and winters between 1°C to 15°C (Cooks & Pretorius, 1987). Maximum daily temperatures average 27°C in summer, but daily minimum temperatures average −2°C during the coldest winter months (Norstrom et al., 2009). Frost is usually widespread during the winter months with snow occasionally falling on the higher peaks in the park (Grab et al., 2011). The region is dry sub-humid and receives ~700 mm per annum, primarily in summer. Precipitation may be highly variable, with amounts of up to 1400 mm per annum just 80 Km to the west (Norstrom et al., 2009). Most precipitation in the GGHNP falls between November and April (Groenewald, 1986).

3.3. Vegetation

The vegetation in the GGHNP falls within the Drakensberg Grassland Bioregion and Mesic Highland Grassland Bioregion (Mucina & Rutherford, 2006). The valleys of the park are characterised by grasslands, herbs and only occasional trees and shrubs (Telfer et al., 2012). The five vegetation types typically recognised are the Eastern Free State Sandy Grassland, Basotho Montane Shrubland, Northern Drakensberg Highlands Grassland, Drakensberg-Amathole Afromontane Fynbos, and Lesotho Highland Basalt (Mucina & Rutherford, 2006). Shrubland vegetation is concentrated on sandstone of the Clarens Formation, in gullies, on scree slopes, mobile boulder beds, and on rocky ridges (Brand et al., 2010). The montane grassland species (e.g. Bromus, Festuca, and Danthonia) stabilise the steep slopes of the upper catchments in the park against erosion. However, the sandstone formations have characteristically shallower sandy soils with less vegetation, thus making them more prone to erosion (Roberts, 1969).

3.4. Geological setting

The park is well known for its geological heritage. The geology of the park is underlain by stratigraphic units belonging to the upper part of the Karoo sequence, which includes part of the Beaufort group, and the Molteno, Elliot, Clarens and Drakensberg Formations (Groenewald, 1986). The geology consists of four sedimentary formations (Tarkastad, Molteno, Elliot, and Clarens formations) and one igneous formation (Drakensberg formation) that dates back to 195-210 million years ago. The rockfall mapping effort for this study focuses on sandstone, siltstone and mudstone formations in the park. These formations include the Clarens, Elliot and Molteno Formations which collectively form the Stormberg Group. Table 4 summarises the stratigraphic units of the Stormberg Group. The GGHNP geology was first mapped by Van Eeden (1937), followed by Visser & van Riet Lowe (1956) and Spies (1969).

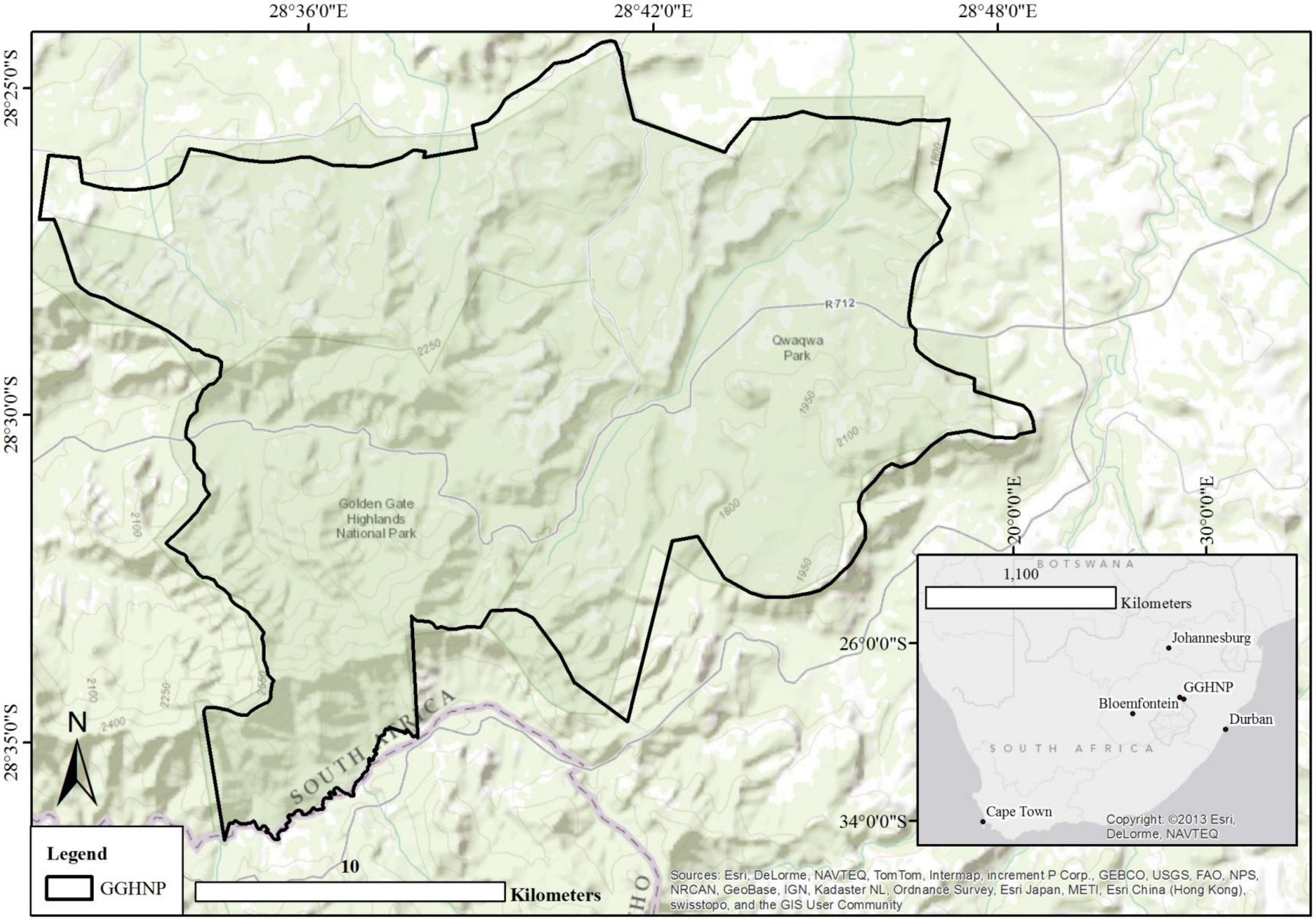

Sources: Esri, DeLorme, NAVTEQ, TomTom, Intermap, increment P Corp., GEBCO, USGS, FAO, NPS, NRCAN, GeoBase, IGN, Kadaster NL, Ordnance Survey, Esri Japan, METI, Esri China (Hong Kong), swisstopo, and the GIS User Community

Copyright: ©2013 Esri, DeLorme, NAVTEQ

Figure 8: Geographic location and extent of the GGHNP.

Eriksson (1983) postulated the possible paleoenvironment of the Drakensberg and north-eastern Free State by studying the Clarens, Elliot and Molteno sandstone Formations, whilst the first sedimentalogical investigations of this formation were carried out by Beukes (1969, 1970).

The Clarens Formation overlies the Elliot Formation, which has an upper contact with the Molteno Formation. These sandstone formations are believed to have been deposited ca. 228 to 200 million years ago during the late Triassic Epoch (Groenewald, 1986). Deposition of the Clarens, Elliot and Molteno Formation indicates changing paleoenvironmental conditions from dominantly fluvial (Molteno Formation) to increasingly aeolian (Clarens Formation) (Eriksson 1984; Groenewald, 1986; Bordy et al., 2004). The ever-changing landscape of the GGHNP is believed to have undergone its greatest change during the Quaternary period when there were cold climatic processes and associated changes in vegetation (Henderson, et al, 2006). The GGHNP is situated on the watershed between the Vaal and Orange River systems forming part of the Maluti Drakensberg Catchment Complex. Thirty percent of the total water supply in southern Africa is derived from this catchment (GGHPMP, 2012).

Formation	**Period**	**Sequence**	**Group**	**Lithology**	**Origin**
Drakensberg	Jurassic	Karoo	Stormberg	Basalt	Volcanic
Clarens	Triassic			Sandstone	Aeolian
Elliot				Mudstone, Siltstone	Fluvial
Molteno				Sandstone, Mudstone	

Table 4: Summary of the geological stratigraphic units of the Clarens, Elliot and Molteno Formations (modified after Groenewald, 1986).

3.4.1. Drakensberg Formation

A prominent formation in the GGHNP is the Drakensberg basalt formation, an igneous formation which dates back 195-210 million years (Groenewald, 1986). This Formation is characterised by numerous superimposed outflows of basaltic lava which over the course of time have led to the higher mountains visible in the GGHNP (Groenewald, 1986) and the Lesotho Mountains (Boelhouwers & Meiklejohn, 2002). These basaltic rocks are very dark in colour, fine to coarse crystalline, and contain mineral-filled amygdales of various sizes and shapes (Visser & van Riet Lowe, 1956; Groenewald, 1986).

3.4.2. Clarens Formation

The Clarens Formation is made up of fine to very fine-grained light yellow-brown sandstone, which is generally uniform and consists of mainly angular to sub-rounded quartz and a few feldspar grains (Groenewald, 1986: 174). The Clarens Formation is very visible in the park and is considered the primary geological attraction in the park (Grab et al., 2011). This sandstone Formation forms the characteristic cliffs seen at the GGHNP and is typically between 115 m to 195 m in thickness (Eriksson, 1981). The park management has developed hiking trails accessible from the accommodation sites which extend along large cliff overhangs and outcrops of this formation.

The impressive overhangs are a product of sandstone weathering. One such weathering process is exudation or salt weathering, the process whereby rock surfaces are scaled off due to the growth of salt crystals by capillary action (Groenewald, 1986: 175). Undercutting of the formation is believed to be responsible for the formation of rock overhangs (‘caves’). The red or orange hollow marks on the surface of the Formation are apparently due to the oxidation of pyrite (Eriksson, 1983).

The earliest postulations suggested that the Clarens Formation was laid down by aeolian processes (Du Toit, 1981). Investigations of the Clarens sedimentary sequence suggested the Formation may be the product of a semi-arid to arid paleoclimate characterised by an aeolian (wind-blown) aqueous desert where dune deposition occurred (Beukes, 1970; Bigarella & van Eden, 1970; Eriksson, 1979, 1983). The fossil assemblage of the Clarens Formation also supports the hypothesis of a semi-arid to arid paleoenvironment (Jubb, 1973; Kitching, 1977). Groenewald (1986) places the deposition of the Formation somewhere in the late Triassic Epoch.

3.4.3. Elliot Formation

The Elliot Formation consists of red mudstone and siltstone with subordinate red and light yellow medium- to fine-grained sandstone beds (Groenewald, 1986: 171), usually from ca. 28 m to over 150 m in thickness (Eriksson, 1985). The characteristic red colour of the Elliot Formation is due to the oxidation of mudstones and siltstones after they were deposited. The Elliot formation breaks down easily with mudstones and siltstones weathering rapidly to a poor soil which forms the negative slopes on the mountain sides (Groenewald, 1986). This formation is well known in the GGHNP for its vertebrate fossil remains (Kitching, 1979; Kitching & Raath, 1984; Reisz et al, 2005).

Early scientific work suggests that the Elliot Formation was laid down by predominantly fluvial processes in a semi-arid climate which gradually became more arid (Botha, 1968; le Roux, 1974), which is supported by the fossil fauna records (Eriksson, 1983). The presence of fining-upward cycles, trough cross-bedded sandstone and red mudstones are believed to be indicators of fluvial deposition (Groenewald, 1986). The Elliot Formation is rich in dinosaur fossils and these include the discovery of a cluster of six dinosaur eggs with embryonic preservation at the bottom half of five of these eggs (Reisz et al., 2005).

3.4.4. Molteno Formation

The light-coloured Molteno Formation consists mainly of medium- to coarse grained slightly feldspathic sandstone (Groenewald, 1986: 170) and varies in thickness from less than 10 m to over 100 m (Erikson, 1984). This formation crops out in the north and north-eastern parts of the GGHNP.

The Molteno Formation is understood to originate from deposition associated with a braided river deposit. Sedimentological studies ascribe it to shallow water deposition (Rust, 1962), as it consists of mainly thick beds of cross-bedded sandstone with very little interlayered mudstone in the upward-fining cycles (Groenewald, 1986). This Formation is postulated to have been deposited by low sinuosity fluvial processes in which a cool, humid paleoclimate would have prevailed (Eriksson, 1983).

3.5. Geomorphology

The GGHNP is renowned for its impressive sandstone formations belonging to the Drakensberg World Heritage region. A variety of sandstone geomorphological phenomena have been documented through the use of geomorphological maps, highlighting prominent and interesting micro- and macro-scale sandstone landforms for portions of the GGHNP, and placed in a global context with other sandstone geomorphological landforms (Grab et al., 2011).

The GGHNP, which is nestled in the Drakensberg-Maluti mountains, falls within the 'African Surface' of Partridge and Maud (1987). Lester King's model first hypothesised that the dramatic basalt-capped section of the Great Escarpment forming the Drakensberg-Maluti mountainland is the product of multiple erosion cycles, arguing that scarp retreat is the dominant control in the planation of successive land surfaces and that episodic continental uplift provided the mechanism for initiating new erosion cycles (King 1955; King 1963; King 1972). Similar studies presented findings which endorsed King's model (Ollier & Marker, 1985; Partridge & Maud, 1987). However, more recent studies have criticised King's model based on findings which suggest that the evolution of the Drakensberg escarpment was controlled primarily by a pre-existing drainage divide, inland of the coastal margin, which formed as a result of continental break-up, rather than by scarp retreat (Fleming et al., 1999; van der Beek et al., 2002). The Drakensberg basalts cap the Clarens Formation sandstone to form the highly resilient scarps observed in the Drakensberg-Maluti Mountains. The presence of massive basalt and Clarens Formation sandstone boulders on the scree slopes below the cliffs formed by the resilient Basalt-Clarens Formation scarps suggests that the Basalt-Clarens Formation scarps in the Drakensberg-Maluti region are above all lithologically controlled and that the development of the Drakensberg section of the Great Escarpment, and slow Cenozoic rates of retreat, are primarily linked to the armouring effect of the resistant capping formed by massive lava flows, and underlying massive Clarens Formation sandstones (Moore & Blenkinsop, 2006: 604).

The Clarens Formation possesses particularly interesting tafoni landforms (Figure 9). Tafoni are large cavernous landforms which through weathering have developed overhangs, arch-shaped entrances, and concave inner walls (Mellor et al., 1997). Weathering and erosion of the structurally weaker lower sections of the Clarens Formation create overhanging shelters or 'caves' (see Figure 9) within which numerous examples of San rock art (see Figure 10) are found (Sumner et al., 2009). Despite the presence of good strategies and initiatives in the GGHNP management plan, it has been noted that there are areas of concern that may compromise the conservation of heritage resources such as the San rock art paintings in the park, even though the park was proclaimed to conserve them (Taru et al., 2013). Recent studies analysing a selection of mega-tafoni features in the park, which have formed huge overhangs in the Clarens Formation sandstone, have shed new light on the complex interactions between case hardening and internal moisture regimes (Mol & Viles, 2012; Mol, 2013). Tafoni features commonly develop in sandstone, however, their development through time is contentious. Case hardening refers to the development of a surface crust on sandstone which makes them more resistant to weathering (Dorn, 2004). Case hardening has been observed to play a significant role in the internal moisture regime of the Clarens sandstone and that in its absence, evaporation from the surface of the sandstone increases, leading to a weakening of the sub-surface, and in turn an increase in the weathering of sandstone material (Mol & Viles, 2012). A follow-up study confirmed a direct relationship between rock hardness and moisture regimes, adding further detail such as temperature to ultimately show the importance of annual variation in moisture regimes as a driver of Clarens sandstone deterioration (Mol, 2013).

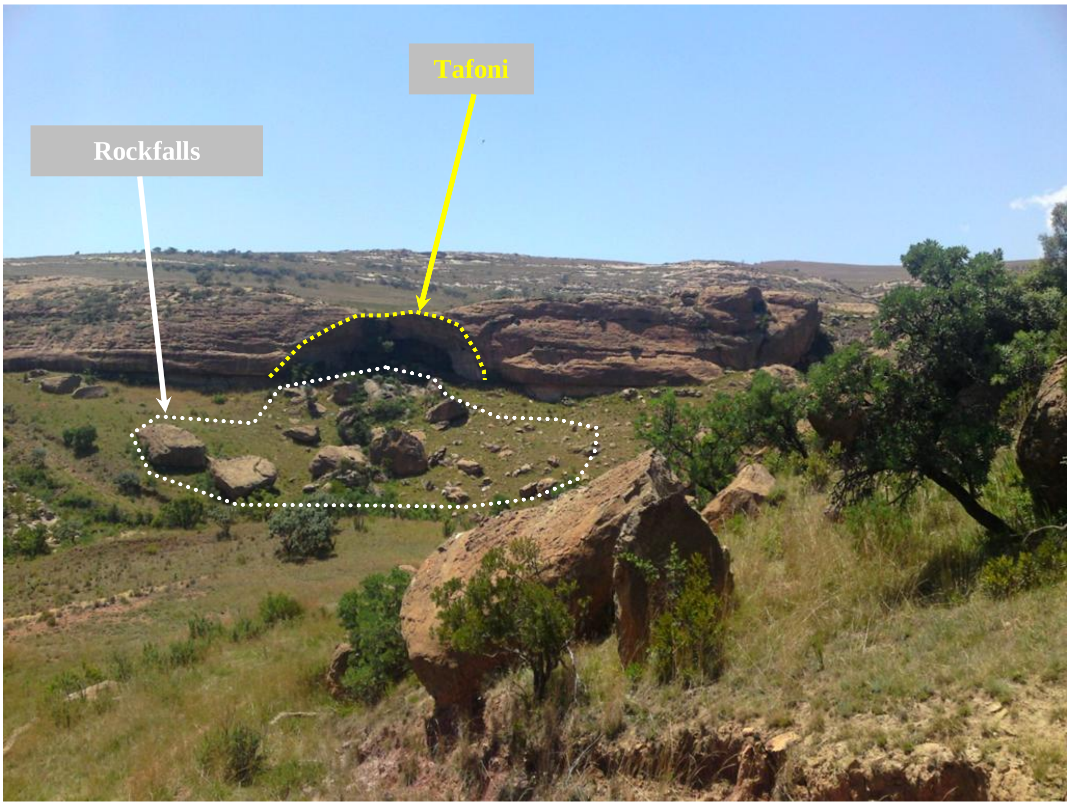

Figure 9: An example of tafoni at Glen Reenen camp.

A number of studies in the GGHNP have examined biogenic weathering (Wessels & Schoeman, 1988; Wessels & Wessels, 1991; Wessels & Büdel, 1995; Wessels et al., 1995; Büdel et al., 2004). For instance, some studies have been able to show that depressions on the rock surfaces may form due to the combined actions of chemical weathering and expansion of hyphae into the rock surface (Wessels & Schoemann, 1988; Wessels et al., 1995; McKechnie et al., 2007). The importance of microbial communities growing on the rock surface cannot be overlooked, and contribute to the stability of the rock surface for friable sandstones by cementation (Mellor et al., 1997; Kurtz & Netoff, 2001). Microbial communities on Clarens Formation sandstone contribute considerably to case hardening by helping to cement the rock surface and in turn influencing the interactions between surface hardness and internal moisture (Mol & Viles, 2012).

The recent discovery of an 11 m sand ramp deposit in the GGHNP has shown the potential for using geomorphic deposits as a proxy to better understand the past paleoenvironment of the region (Telfer et al., 2012). Significant Last Glacial Maximum (LGM) and late glacial pollen sequences in Braamhoek have revealed Late Quaternary vegetation shifts in the eastern part of central southern Africa (Norstrom et al., 2009). However, the accumulation of sand ramps in the GGHNP during the LGM (dated at 45 to 16 ka using Optically-stimulated luminescence) bares testament to former aeolian conditions consistent with a periglacial environment (Telfer et al., 2012).

Figure 10: Rockart at Glen Reenen camp, GGHNP.

Chapter 4 - Methodology

4.1. Introduction

A variety of sandstone geomorphological landforms have been described and mapped in the GGHNP, however rockfalls in the GGHNP remain unmapped and un-characterised (Grab et al., 2011). The methodological approach adopted for mapping rockfalls in the GGHNP is shown in Figure 11. The first part of the approach involves the creation of environmental variables which describe the GGHNP, through the manipulation of remotely sensed datasets. Rockfalls were physically measured and ground-truthed with a Differential Global Positioning System (DGPS) in order to establish parameters for characterising rockfalls using remote sensing and GIS techniques. The ground-truthed samples were restricted to the three sandstone formations responsible for rockfall deposition in the GGHNP, namely the Clarens, Elliot, and Molteno Formation (Fm.) sandstones. An Object Based Image Analysis (OBIA) was chosen for classifying rockfalls in the GGHNP, as unlike traditional pixel-based approaches, OBIA groups pixels into segments according to their spectral similarity and other criteria such as shape, area, and position (Schoffer et al., 2010). The ground-truthed data were not only used as an input for characterising rockfalls, but also for validating rockfalls mapped with an OBIA. The centroids for the OBIA were then determined and analysed in combination with environmental variables. This permitted the spatial and macro-morphological analyses of rockfalls in the GGHNP.

4.2. Data Sources

4.2.1. Aerial imagery

The core remote sensing interpretation of this study was conducted with 0.5 m spatial resolution colour aerial imagery. The aerial imagery was provided by Chief Directorate: National Geo-spatial Information (CD: NGI). CD: NGI has the largest and most extensive archive of aerial photography and imagery dating back to 1926 with numerous national coverages, and are responsible for

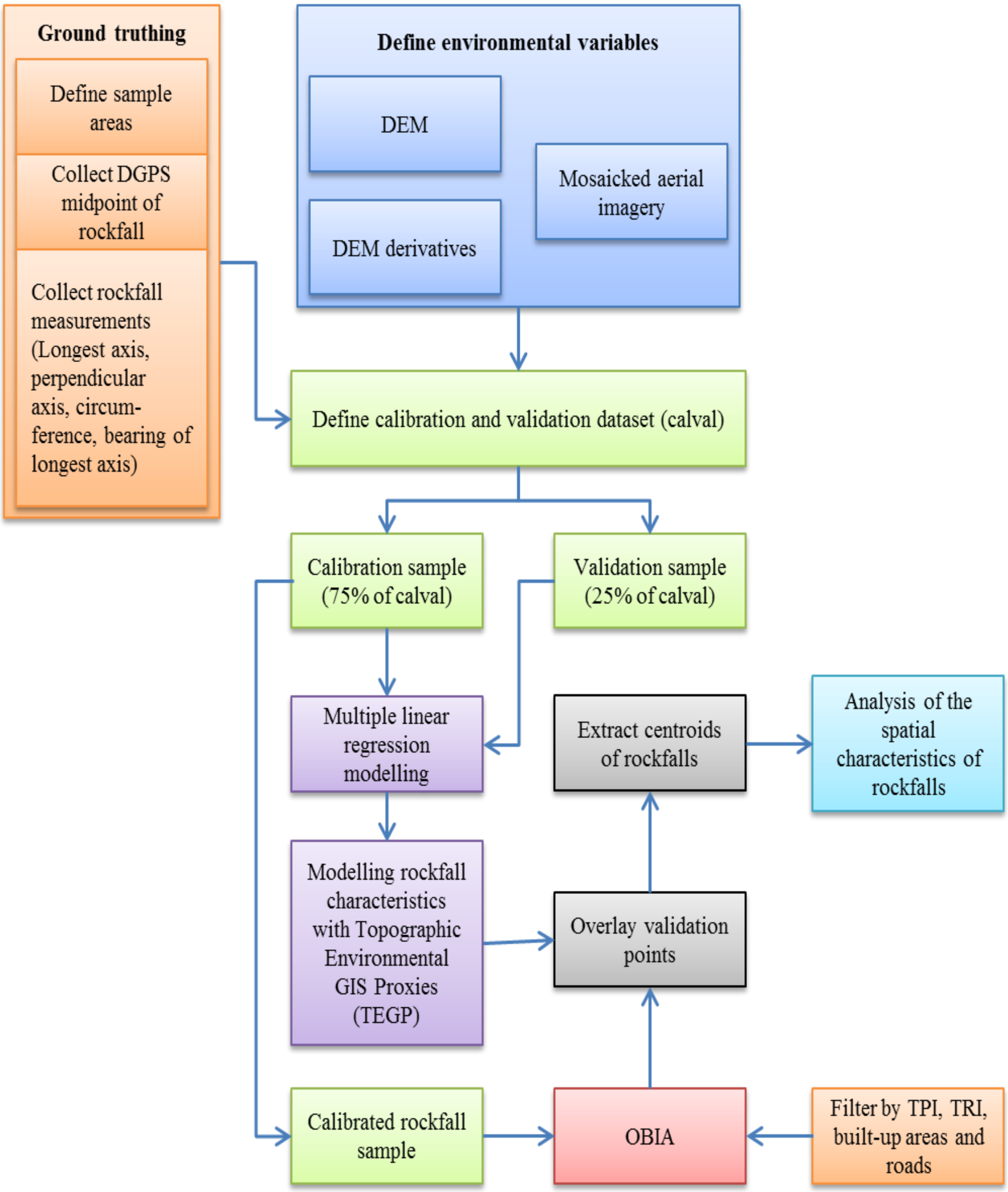

Figure 11: Methodology for mapping and characterising rockfalls in the GGHNP.

land surveys and the provision of a spatial data infrastructure. The aerial imagery has evolved significantly over time, and, since 2008, all imagery is acquired with high resolution digital sensors in both colour (RGB) and CIR (colour infra-red). The 2009 colour aerial imagery was captured using Intergraph's DMC II camera technology. The aerial imagery is delivered fully orthorectified from NGI, thus no geometric image correction was necessary. NGI, thus no geometric image correction was necessary.

The 0.5 m aerial imagery delivered by CD: NGI, previously Chief Directorate: Surveys and Mapping (CDSM)) is packaged as 1:10,000 scale tiles. A total of 23 tiles were acquired for full coverage of the GGHNP. In order to optimise the OBIA approach, the aerial imagery was mosaicked in the software package "PCI Geomatica 10". PCI Geomatica 10 was chosen, as its award winning algorithms preserve the spectral integrity of the image during mosaicking. The mosaicked aerial imagery was then clipped with the boundary of the GGHNP so that rockfalls located outside of the GGHNP would be excluded from the OBIA (Figure12). A major source of error (inaccuracies) in the planimetric position of objects in an orthorectified image lies with the accuracy of the DEM. However, the DEM is necessary for converting from a central projection to an orthogonal projection. (Department: Rural Development and Land Reform, 2009A). The CD: NGI used a 20 m DEM derived from 20 m contour data to orthorectify the digital aerial imagery and found that such DEM's posses a bias of 10.5 m (Department: Rural Development and Land Reform, 2009B). Digital aerial imagery orthorectified with a 10.5 m DEM bias was determined to result in an accuracy range of 1 to 11 m from vectorised 20 m contours (Department: Rural Development and Land Reform, 2009A).

4.2.2. Digital Elevation Model (DEM)

The 20 m DEM for the study was provided by SANSA Earth Observation directorate. The 20 m spatial resolution DEM is a Digital Terrain Model (DTM) which was compiled by ComputaMaps. The terrain model was interpolated (bilinear) from digitised map data captured from 1:50,000 scale topographic maps supplied by CD: NGI. The 20 m contours and spot heights digitised off of the 1:50,000 topographic maps were originally captured in the field by surveyors using a Geodesy survey instrument. As such, the vertical and horizontal plainimetric accuracy of the DEM is related to the accuracy of the surveyed contours and spot heights. The DEM was visually inspected for artefacts and errors by producing a hillshade raster of the DEM using the

HILLSHADE function in ArGIS 10 Spatial Analyst Surface tools. Artefacts or errors are more easily identifiable from a hillshade of the DEM than the original DEM raster (Hayakawa et al., 2008). No artefacts or errors were observed in the hillshade raster. Although the DEM and aerial imagery differ by a factor of 10, the 20 m DEM was deemed the most suitable for the study area to date; no higher spatial resolution DEMs exist for the GGHNP. Other available DEM options which currently exist are the freely available ASTER GDEM and SRTM DEM. ASTER GDEM is a global DEM based on ASTER satellite imagery offering a spatial resolution of 30 m or horizontal resolution of 1 arc second. SRTM (Shuttle Radar Topography Mission) DEM is a 30 m DEM resampled to 90 m for areas outside North America that was created by NASA using the mean difference between laser heights and Synthetic Aperture Radar (SAR) heights. Statistical analysis measuring the accuracy of GDEM against LiDAR data has found GDEM’s 30 m resolution to be over-optimistic and not more detailed and accurate than 90 m SRTM DEM (Hengl & Reuter, 2011). Subsequently, GDEM has been found to be unsuitable for terrain analysis at 30 m spatial resolution (Reuter et al., 2009). However a study comparing ASTER GDEM and SRTM-3 has found terrain representation by GDEM to be superior to that of SRTM-3 for most landform elements, including hilly lowlands and steep mountains (Hayakawa et al., 2008). The interpolated 20 m DEM produced from 1:50,000 contour and spot height data was chosen as it firstly offers a higher horizontal and vertical spatial resolution than ASTER GDEM and SRTM DEM, and represents survey quality measurements which the CD: NGI are mandated with providing for the whole of South Africa (LAND SURVEY ACT 8 OF 1997 and SPATIAL DATA INFRASTRUCTURE ACT 54 OF 2003).

The creation of DEM’s from digital photogrammetrically derived data (i.e. contours) can possess error which is typically inherent with interpolation (the filling of gaps) (Höhle & Höhle, 2009). In order to assess the vertical accuracy of the 20 m DEM with accurate reference values, statistical measures like the Root Mean Square Error (RMSE), mean error and the standard deviation could be used. The vertical accuracy of the 20 m DEM was calculated using the RMSE as the RMSE has been shown to be a good measure of the differences between predicted values and the actual values observed values (Aguilar et al., 2005). Spot heights were acquired from CD: NGI for the study area. The Spot heights represent actual ground truthed heights which were digitised off 1:50,000 topographic maps. A total of 183 spot heights covering the study area were used for the vertical accuracy assessment of the 20 m DEM (Figure 13). The equation for the RMSE is defined as:

$$RMSE = \sqrt{\frac{1}{n}\sum_{j=1}^{n}(P_j - A_j)^2}$$

Where P is the predicted value, A the actual value and n the number of expected values. The RMSE was calculated for the spot heights layer using the RASTER CALCULATOR tool in ArcGIS. A total of 183 spot height values were substituted as the actual values (A) and 183 predicted values (P) were derived by extracting the interpolated DEM pixel values to a separate field in the spot heights layer using the GIS function EXTRACT VALUES TO POINTS. The RMSE formula was determined in a separate field using RASTER CALCULATOR. The sum of the final RMSE for 183 observed points was 1.23 m.

The bias with using this method for assessing the vertical accuracy of the 20 m DEM using spot heights is if the spot heights were also considered in the bilinear interpolation process used to create the DEM, in which case the validation dataset would not be independent of the interpolation model. The consequence would be that the RMSE’s reported would be higher than their true value. The 20 m DEM was reclassed to an altitude thematic layer with the following thematic classes (Figure 13):

1600 – 1800 m a.s.l
1800 – 2000 m a.s.l
2000 – 2200 m a.s.l
2200 – 2400 m a.s.l
2400 – 2600 m a.s.l
2600 – 2800 m a.s.l

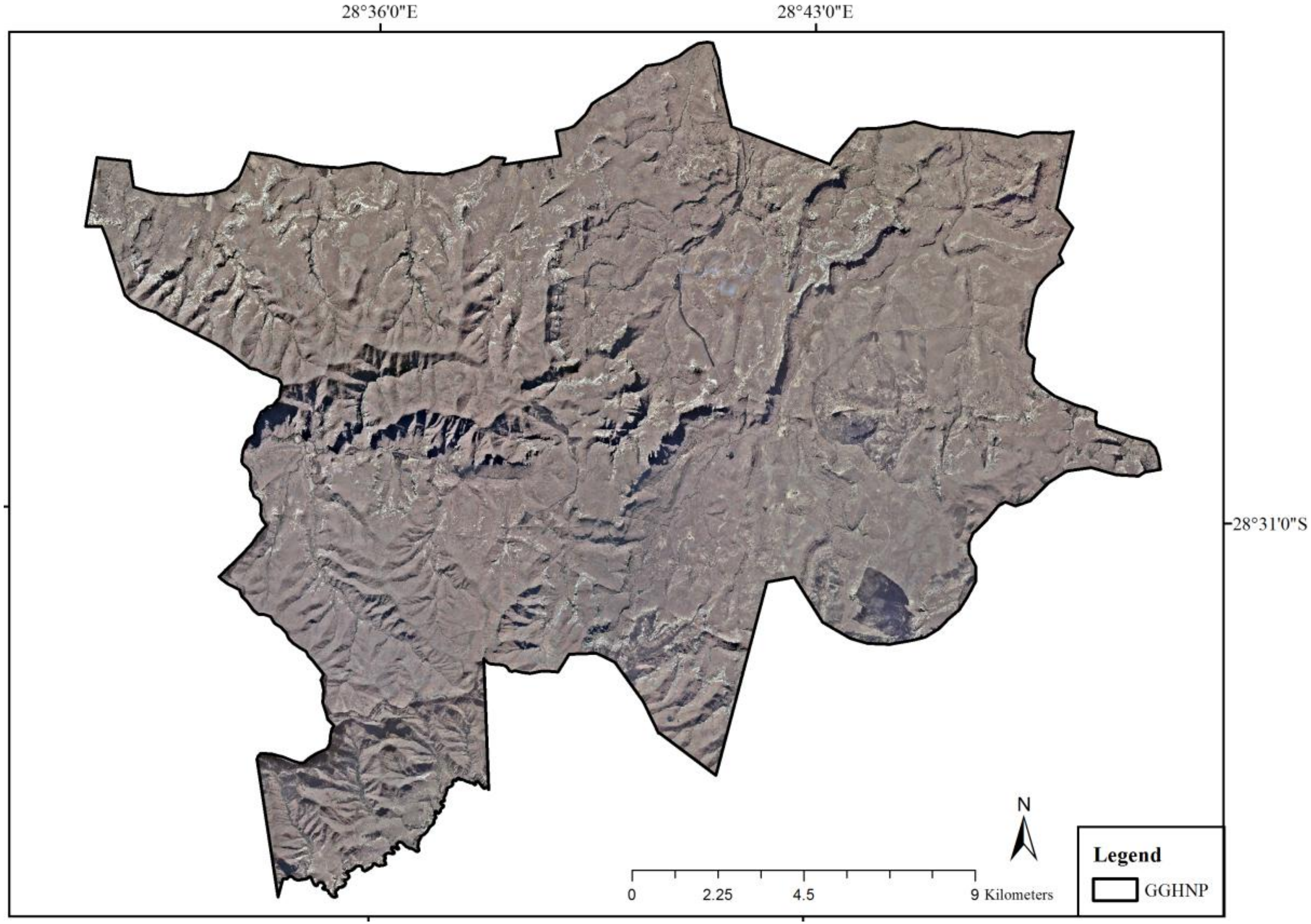

Figure 12: Mosaicked 0.5 m aerial imagery for the GGHNP.

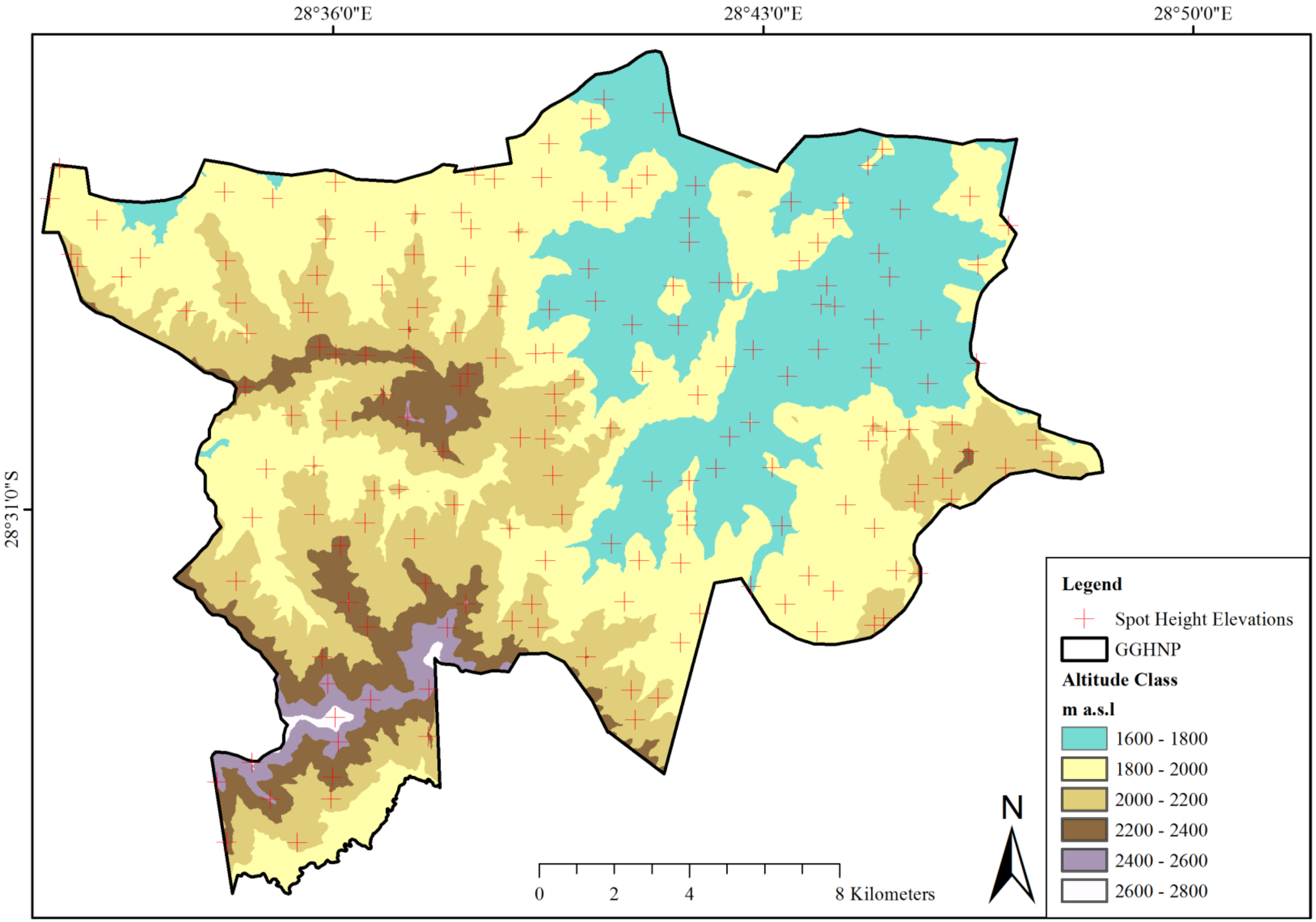

Figure 13: Altitude thematic layer for the GGHNP.

4.2.3. Geological data

Geological data describing the lithology of the GGHNP were provided by the Council for Geosciences at a 1: 250,000 scale, in vector form. The geological vector layer was clipped to the boundary of the GGHNP (Figure 14).

4.2.4. Infrastructure

All infrastructures within the GGHNP, such as building structures and tarred/dirt roads were digitised to polygon features using the 0.5 m spatial resolution mosaicked aerial imagery (Figure15).

4.3. Defining the remote sensing and environmental variables

The environmental variables refer to the input independent variables which the dependent variables (rockfalls) are analysed alongside. Environmental variables can be derived through a number of sources, as has been shown by previous mass movement studies (Yin & Yan, 1988; Carrara et al., 1991, 2003; Guzzetti et al., 1999, 2005; Santacana et al., 2003; Ayalew et al., 2004; Liu et al., 2004; Singh et al., 2005; Vijith et al., 2009; Hardwick, 2012; Catani et al., 2013). In this study, six environmental variables were identified for analysis with the dependent variables or rockfalls. They include the topographic variables: altitude, slope aspect, slope gradient, slope unit and distance to the Clarens/Molteno Fm. sandstones (lithology) and drainage lines. The environmental variables were derived through various surface models applied using the 20 m DEM. Thematic layers of the environmental variables were reclassed into specific thematic classes. In addition to this, total curvature, plan, profile, Topographic Position Index (TPI), and Topographic Roughness Index (TRI) rasters were created for other purposes such as filtering out misclassification, and for input as TEGP for characterising rockfalls using multiple linear regression modelling.

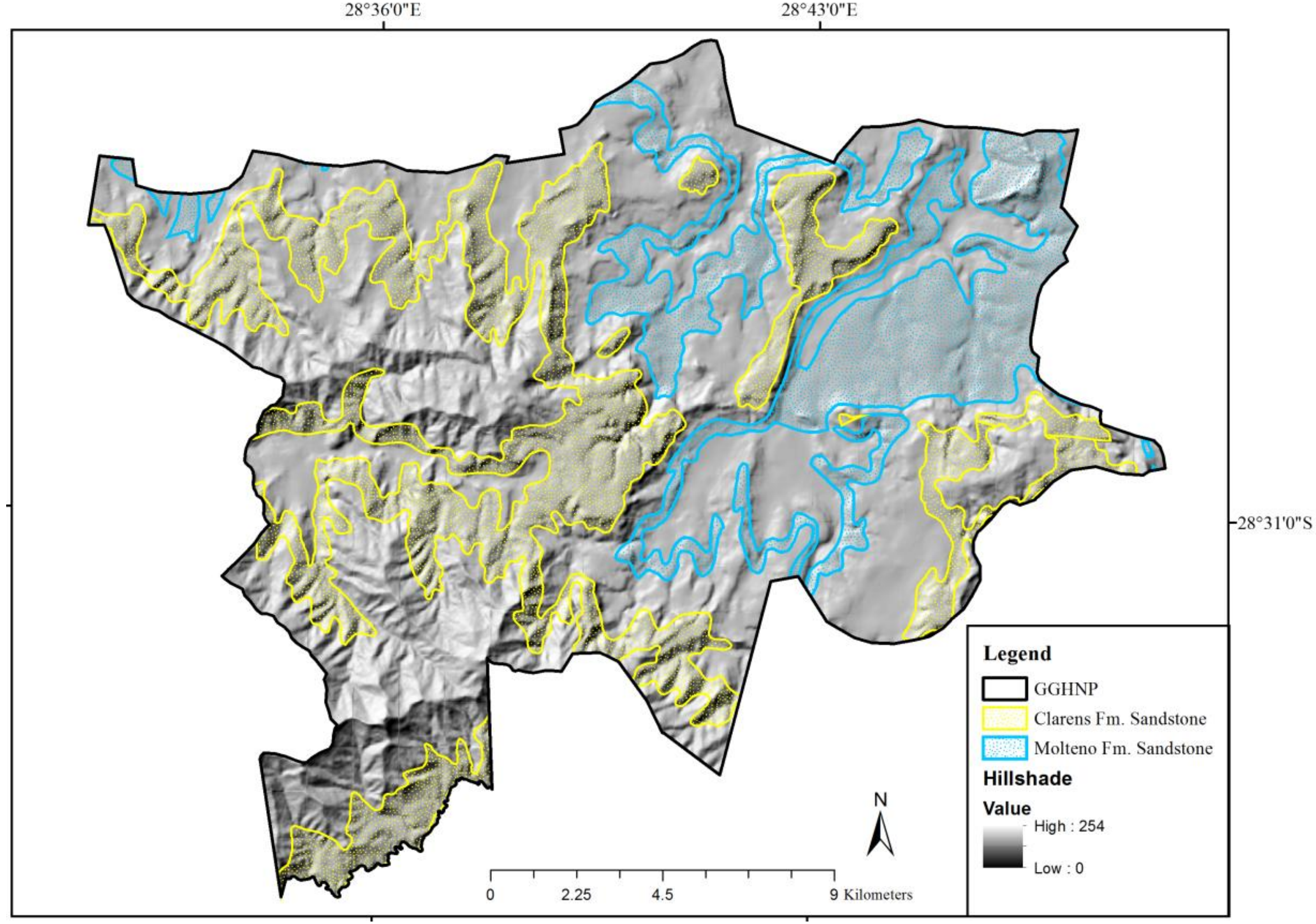

Figure 14: 1:250,000 geological vector layer for the GGHNP.

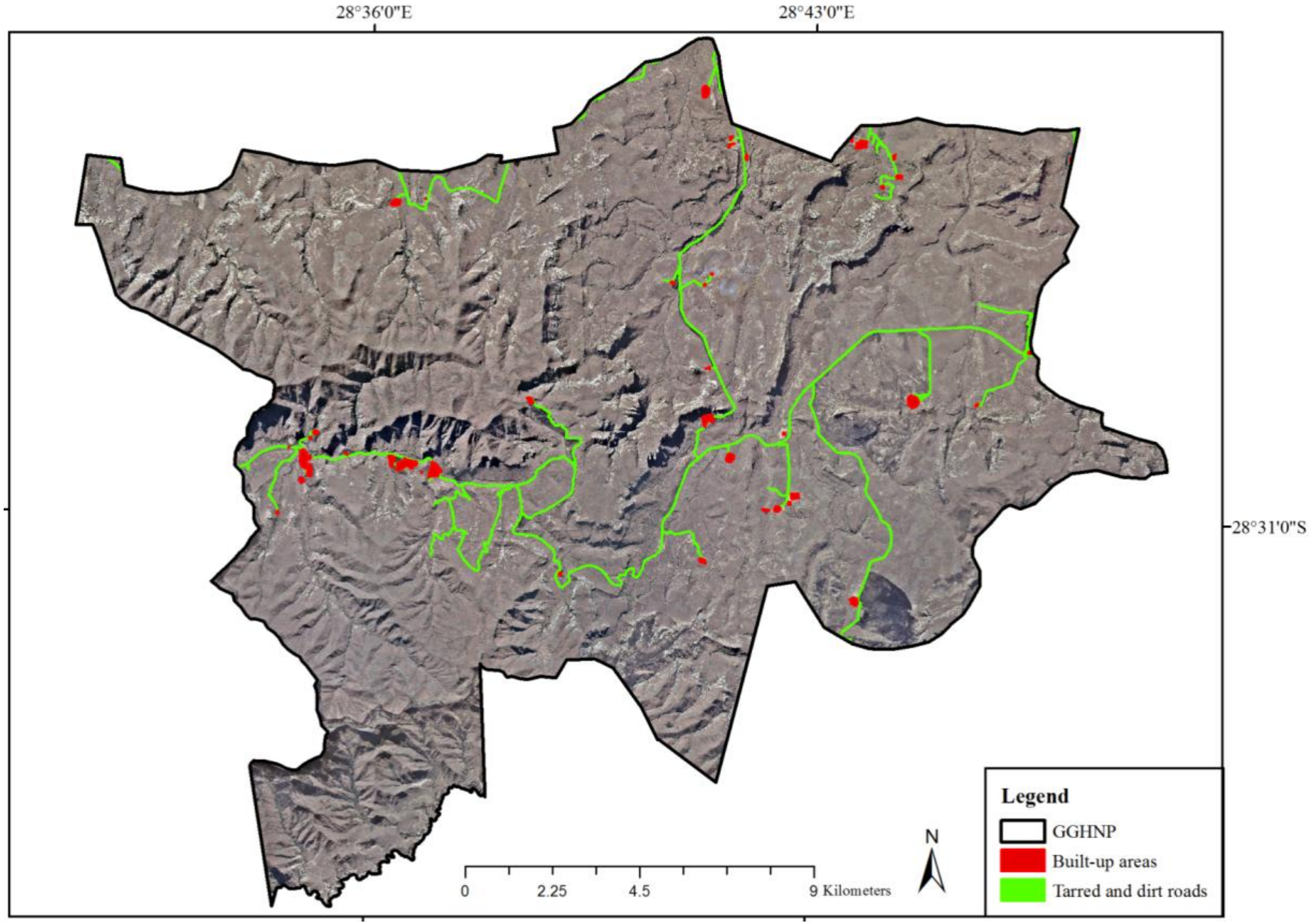

Figure 15: Digitised roads, dirt roads and built-up areas in the GGHNP.

Elevation models can be used to generate surface models such as slope, aspect, curvature, plan, profile, and roughness. DEM derivatives provide important topographic variables which characterise the environment of the study area. Aspect and slope rasters created from DEMs themselves are used to model important surface topography, critical to calculating the rockfall process and its physical characteristics (Lan et al., 2007). The ArcGIS Spatial Analyst extension and QGIS's raster based terrain analysis tool were used to produce the DEM derivatives. The DEM is used as the primary input in these tools. The advantage of DEM derivatives is that one can derive patterns that were not readily apparent in the original DEM, such as contours, slope gradient, steepest downslope direction (aspect), shaded relief (hillshade), and viewshed. The DEM derivatives for this study were derived to create environmental variables for inputs in the analysis of rockfall characteristics with TEGP, the analysis of the spatial pattern of rockfall points, and the frequency distribution of rockfall points in relation to thematic classes defined with the environmental variables. The DEM derivatives are described in further detail.

4.3.1. Slope

Figure 16 shows the reclassified slope raster for the GGHNP, derived using the 20 m DEM. Slope refers to the slope gradient, or rate of maximum change in the z-value from each cell of a raster surface, and the range of values for a slope output is typically reported in degrees (ESRI, 2011). For degrees, the range of slope values is 0 to 90. Slope was derived in ArcMap using Spatial Analyst's surface tools. The slope thematic layer was then reclassified into the following thematic classes:

0° – 8° = Flat to near flat surfaces
8° – 18° = Gentle slope
18° – 29° = Steep slope
29° – 62° = Very steep slope

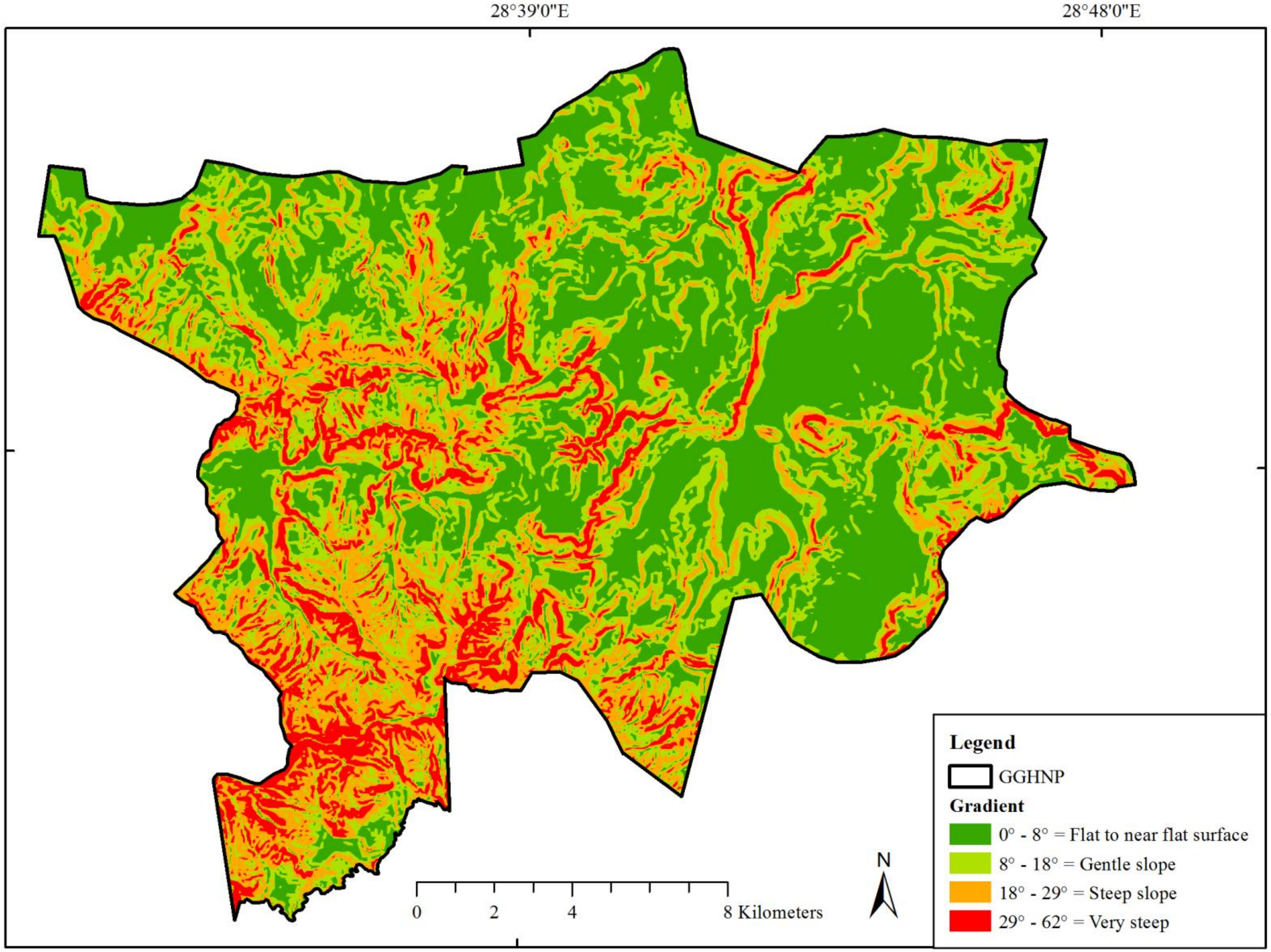

Figure 16: Reclassed slope thematic layer for the GGHNP derived using the 20 m DEM.

4.3.2. Slope aspect

Figure 17 shows the aspect raster for the GGHNP. Aspect or slope direction, derived from a DEM, identifies the downslope direction of the maximum rate of change in value from each raster cell to its neighbours (ESRI, 2011). The cell values for the aspect derivative are expressed in positive degrees from 0 to 359.9, measured clockwise from north. Slope aspect was derived in ArcMap using Spatial Analyst's surface tools. The slope aspect thematic layer was reclassified into the following thematic classes:

Flat = -1°
North = 0° – 22.5°
North-east = 22.5 – 67.5°
East = 67.5 – 112.5°
South-east = 112.5 – 157.5°
South = 157.5 – 202.5°
South-west = 202.5 – 247.5°
West = 247.5 – 292.5°
North-west = 292.5 – 337.5°
North = 337.5 - 360°

4.3.3. Curvature, profile, and plan (ESRI, 2011)

Curvature is calculated from the second derivative of the surface or slope-of-the-slope. Profile and plan curvatures are optional outputs of curvature which were calculated using Spatial Analyst's curvature tool. This is determined on a cell by cell basis and a fourth-order polynomial is fit to a surface composed of a 3x3 pixel moving window. Profile curvature is in the direction of the maximum slope, and plan curvature is perpendicular to the direction of the maximum slope. Positive curvature indicates that the surface is upwardly convex at that cell, and negative curvature indicates that the surface is upwardly concave at that cell. A zero curvature value indicates that the surface is flat. A negative profile curvature value indicates that the surface is upwardly convex at that cell, and a positive profile curvature value indicates that the surface is upwardly concave at that cell.

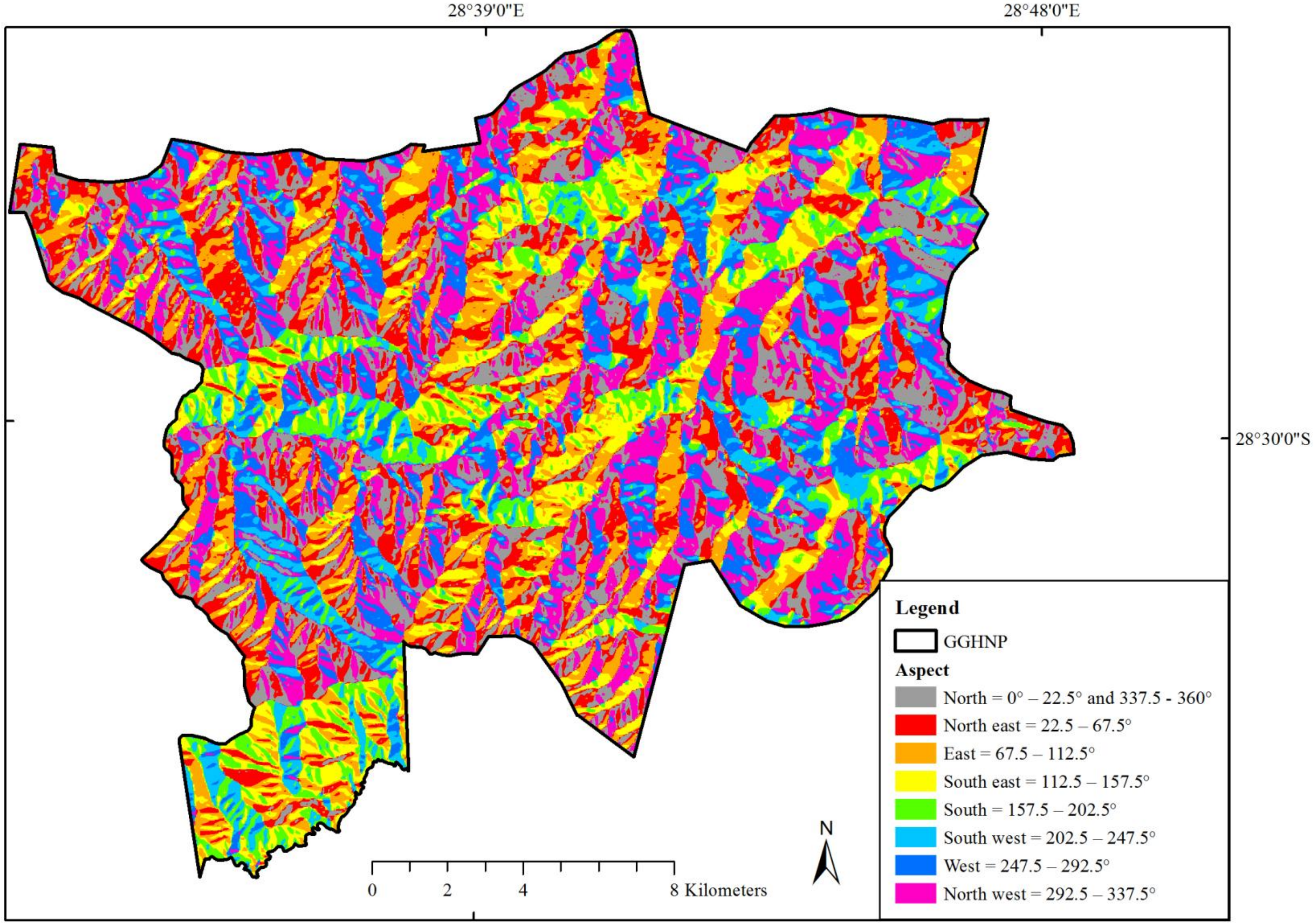

Figure 17: Slope aspect thematic layer of the GGHNP derived from the 20 m DEM.

A zero profile curvature value indicates that the surface is flat. For plan curvature, a positive value indicates the surface is upwardly convex at that cell, and a negative value indicates that the surface is upwardly concave at that cell. A zero plan curvature value indicates the surface is flat. Curvature, and plan and profile curvature, is reported in units that are one hundredth of an elevation unit. Moderate relief values vary from -0.5 to 0.5, while extreme relief can vary between – 4 and 4. Curvature, profile, and plan were derived in ArcMap using Spatial Analyst’s surface tools.

4.3.4. Slope units

Figure 20 shows the composite raster of the four GGHNP slope units created using profile and plan rasters. Slope units refer to the Hypothetical Nine-Unit Land-Surface Model, which is used to show how mass movement types could be classified according to their occurrence on slope forms, with particular combinations of vertical (profile curvature) and lateral (plan curvature) curvatures (Dalrymple et al., 1968). Ayalew & Yamagishi (2004) adopted a similar approach to show how rockfalls occur on concave-planar slopes in the Blue Nile Basin. To better understand how slope form affects mass movement distribution, the plan and profile curvature rasters were multiplied to produce nine layers (Figure 18) that matched the nine landforms identified by Ayalew & Yamagishi (2004).

Slope units are useful for representing landscapes which are widely described as convex, concave, or planar surfaces. Regional investigations of landforms on landscapes are usually limited to describing the outline of the topography in 2D. Slope units developed from the hypothetical landscape model, offer the ability to analyse topography in 3D. For instance, Dikau (1989) demonstrated this by classifying landform elements by plan and profile curvature to define basic relief units in 3D for soil mapping purposes.

Figure 19 shows the raster calculations used in ArcMap to derive the slope units associated with rockfalls in the GGHNP; namely sloping recessing hills which have a concave lateral profile and convex vertical profile (concave–

convex or CCx), sloping closed basins which have a concave lateral and vertical profile (concave-concave or CC), sloping inflated hills which have a convex lateral and vertical profile (convex-convex or CxCx), and sloping protuberant basins which have a convex lateral profile and concave vertical profile (convex-concave or CxC).

The four slope units were combined to create a composite of the four landscape units present in the GGHNP (Figure 20). The RECLASSIFY tool was used to create binary rasters according to profile/plan curvature greater than zero, less than zero and equal to zero. A surface with profile and plan equal to 0 is the same as a flat slope unit. Combinations of positive and negative profile/plan rasters were multiplied using RASTER CALCULATOR to produce the different slope units.

4.3.5. Topographic ruggedness index (TRI)

Figure 21 shows the TRI raster created for the GGHNP using the 20 m DEM. The TRI is defined as the mean between a central cell and its surrounding cells (Wilson et al., 2007). Riley et al. (1999) show how the TRI quantifies topographic heterogeneity. Measurement of terrain ruggedness is important for a number of scientific disciplines, and complex methods of quantifying surface characteristics have been evolving within fields such as geomorphology and wind engineering (Sappington et al., 2007: 1419). The TRI is one such method which, using a DTM and GIS, quantifies the total elevation change across a given area (Riley, 1999). The TRI was derived with QGIS's raster based terrain analysis tool using the 20 m DEM as an input. Ruggedness index values can be classified into categories to describe the different types of terrain (Riley, 1999). The thematic classes are as follows (Riley, 1999):

Level = 0 - 80 m
Nearly level = 81 – 116 m
Slightly rugged = 117 – 161 m
Intermediately rugged = 162 – 239 m

Moderately rugged = 240 – 497 m

Highly rugged = 498 – 958 m

Extremely rugged = 959 – 4367 m

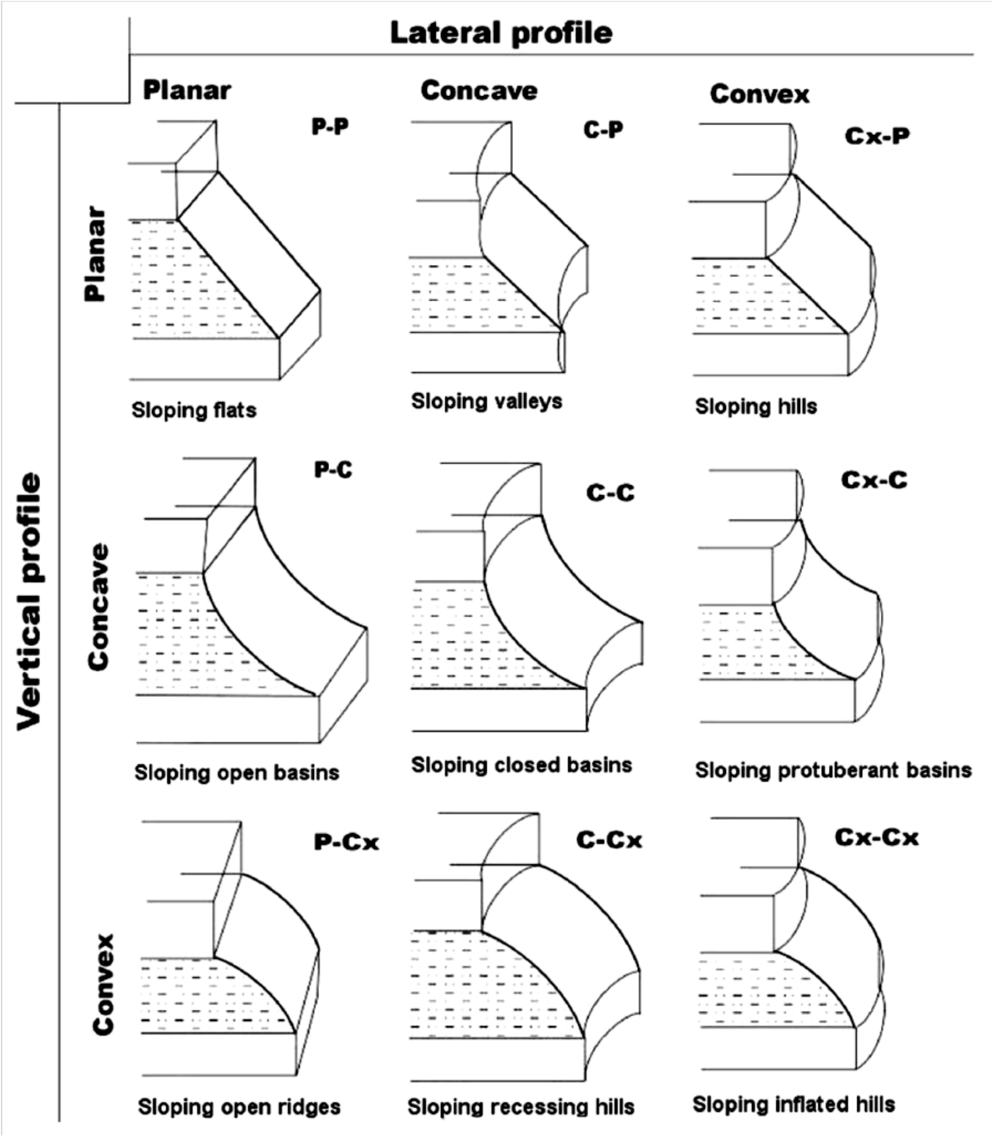

Figure 18: The hypothetical landscape model (after Ayalew & Yamagishi, 2004).

	Profile	**Plan**
Positive	C	Cx
Negative	Cx	C
0	Flat	Flat

Thematic classes:

CCx = Profile x Plan = Sloping recessing hills
CC = Profile x -(Plan) = Sloping closed basins
CxCx = -(Profile) x Plan = Sloping inflated hills
CxC = -(Profile) x -(Plan) = Sloping protuberant basins

Legend:

C - Concave	Cx - Convex

Figure 19: The raster calculations used in ArcMap to derive the slope units associated with rockfalls in the GGHNP include sloping recessing hills (concave–convex or CCx), sloping closed basins (concave-concave or CC), sloping inflated hills (convex-convex or CxCx), and sloping protuberant basins (convex-concave or CxC).

4.3.6 Topographic position index (TPI)

Figure 22 shows the TPI thematic layer derived from the 20 m DEM for the GGHNP. The TPI is defined as the difference between a cell elevation value and the average elevation of the neighbourhood around that cell (Jenness, 2006). Using the TPI at different scales and slope, allows for the classification of landscape into both topographic position (i.e. ridgetop, depressions, and mid-slope) and landform category (i.e. steep narrow depressions, gentle valleys, open slopes, etc.). The TPI was calculated using Land Facet Corridor Designer, an open source ArcGIS toolbox which identifies the geographic portion of a region that maximizes continuity and diversity of landscape units

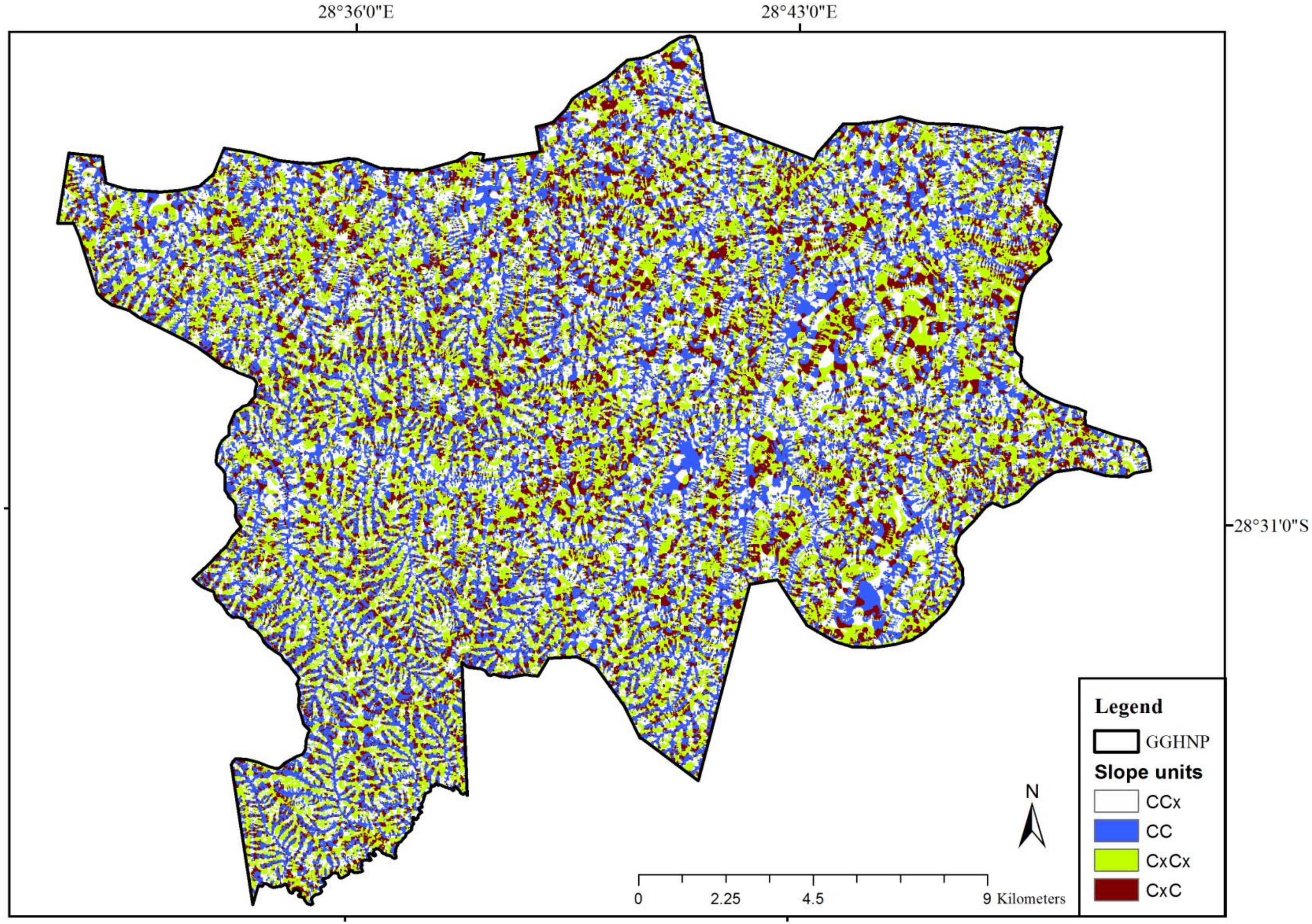

Figure 20: Slope unit thematic layer for the GGHNP.

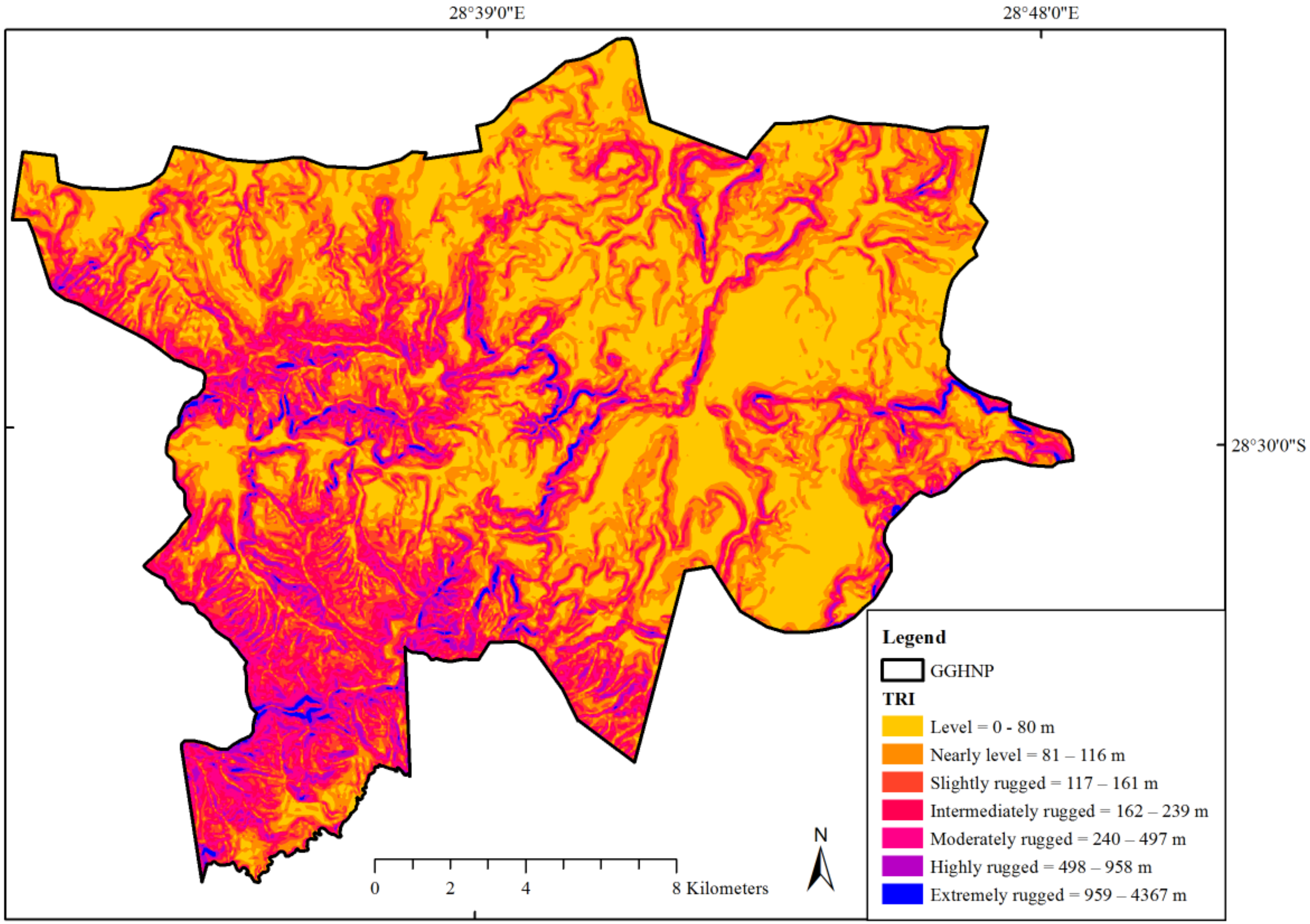

Figure 21: TRI thematic layer for the GGHNP derived using the 20 m DEM.

defined by topographic and soil traits that are expected to facilitate wildlife movement. TPI is an inherently scale-dependent phenomenon, and the classification produced depends entirely on the scale specified by the user analysing the landscape (Jenness, 2006). A scale parameter of 250 m was found to best represent ridgetops (Guisan et al., 1999), which was confirmed through visual interpretation of the output with the aerial imagery. Positive TPI values mean the cell is higher than its surroundings, while negative values mean it is lower. If the TPI cell values are negative, then they are likely to indicate valley and canyon bottoms. If the TPI cell values are positive, they indicate ridgetops and hilltops. A TPI value of zero is indicative of mid-slope areas. The TPI was then reclassified into the following thematic classes (Jenness et al., 2010):

Depressions (negative TPI values)
Flat-gentle slope
Steep slope
Ridgetop (positive TPI values)

4.3.7. Drainage lines

Drainage lines were derived from the hydrological DEM derivative, flow accumulation. Using Spatial Analyst's HYDROLOGY toolbox, a flow accumulation raster was created. The flow accumulation raster was then reclassed to 7 classes (Figure 23) to delineate stream order using Strahler's method (Strahler, 1952). The reclassed flow accumulation raster contains 7 stream orders. The reclassed flow accumulation raster was then converted to a vector layer using the RASTER TO POLYLINE function (Figure 24). Table 5 shows the percentage of river length for each stream order within the 322.032 Km² study area. A 1: 500,000 drainage layer produced by the South African Department of Water and Sanitation (previously Department of Water Affairs and Forestry) was overlaid with the drainage lines derived from the 20 m DEM to act as a means for visually validating the derived drainage lines. The highest stream orders compare well between the 1: 500,000 drainage vector and derived drainage vector however, the lower stream orders cannot be validated due to the coarser scale of the 1: 500,000 drainage vector.

4.4. Defining the ground-truthed sites

Accessibility to rockfalls was the main constraint for the sampling selection procedure. For the purpose of collecting DGPS coordinates, it is very important to be as close to a trigonometric beacon as possible, as the trigonometric beacons provide the only accurate known geographic locations within the Park. Accessing the trigonometric beacons to set up DGPS base stations was a difficult task in itself, as the beacons are located on top of the koppies throughout the Park. The Rietspruit trigonometric beacon located on the Silasberg (Figure 25) is the most accessible of all the beacons within the representative sample area. An investigation of the aerial imagery revealed it to be the most accessible of all the trigonometric beacons within the representative sample area. As such, the selection of sampling sites was closely influenced by the location of the Rietspruit trigonometric beacon. The first reference point (i.e. A0) was determined using this beacon and subsequent reference points were then determined from one another as follows:

Rietspruit Beacon ⇨ A0 ⇨ H3 ⇨ H4 ⇨ H6 ⇨ H7 ⇨ H8

Many areas of the GGHNP are inaccessible by vehicle and could potentially take over a day to reach by foot, thus, for the scope of this study, it was essential to keep the sampling sites within reasonable walking distance. For this purpose, the sampling sites were constrained to a 1 Km radius from the main road, dirt roads and foot paths (Figure 25). The selection of the 1 Km buffer radius was influenced by preliminary observations on the abundance of accessible rockfalls from the main road. The main and secondary road (i.e. dirt roads and footpaths) layers were created by digitising off the aerial imagery. The main road and secondary road layers were then merged and buffered to a 1 Km radius to define the representative sample area.

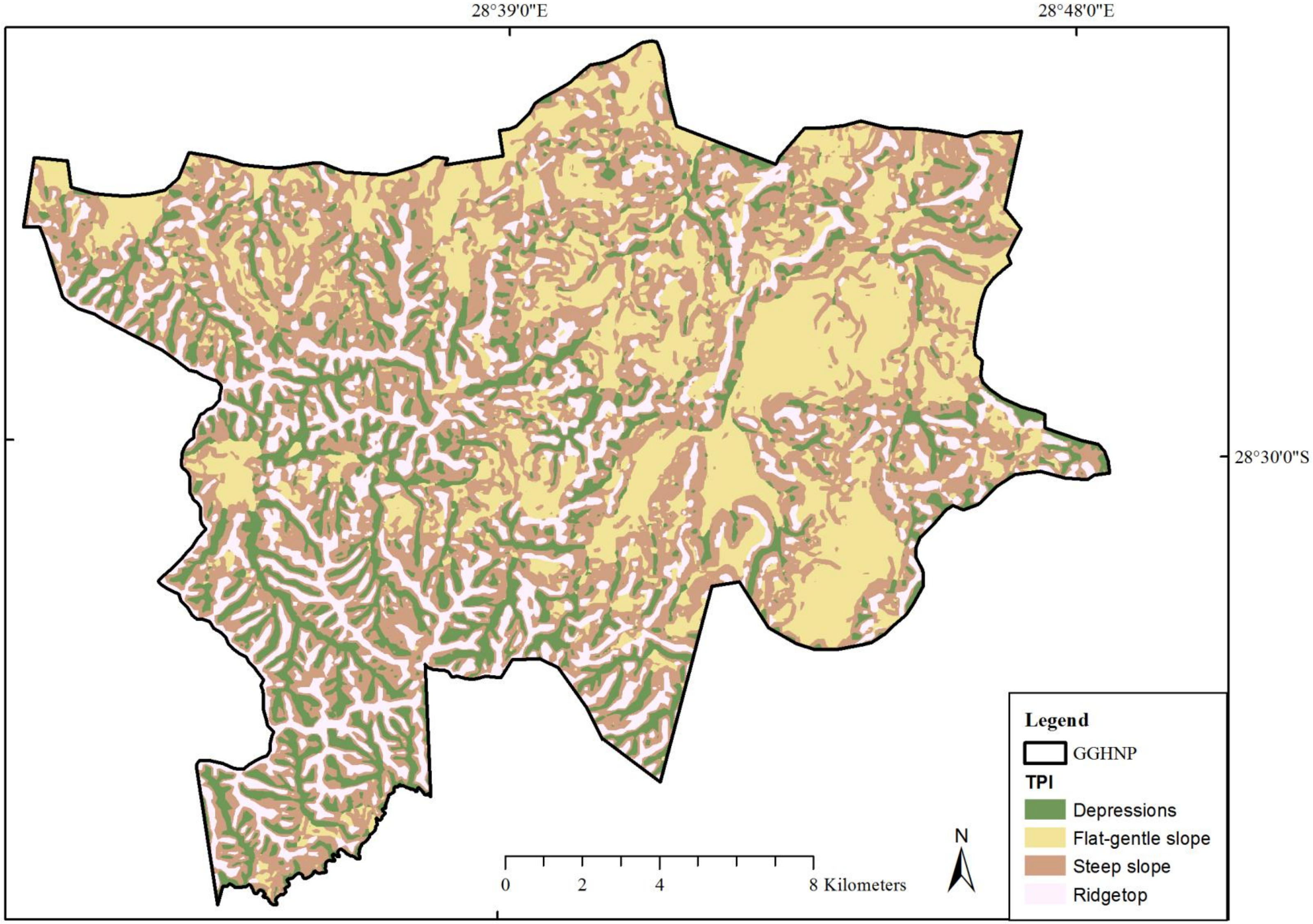

Figure 22: TPI for the GGHNP.

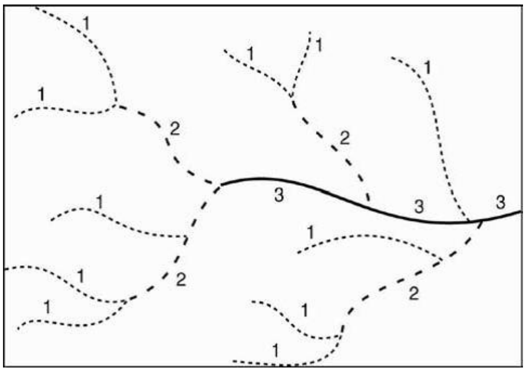

Figure 23: Strahler's method for categorising stream order (adapted from Strahler, 1952).

Stream Order	Length (Km)	Length %
1	99.42	49.9975
2	45.99	23.128
3	22.49	11.31
4	9.58	4.8177
5	9.62	4.83782
6	8.69	4.37013
7	3.06	1.53885

Table 5: Total and percentage length of drainage line by stream order.

The geology of the GGHNP was the next most important criterion for determining representative rockfall sites. As already discussed, only Clarens, Elliot and Molteno Fm. sandstones were selected for inclusion in the sample. A 1:250,000 geological vector layer was then clipped to the 1 Km representative sample area to aid in the selection of representative ground-truthed sites. The last sampling constraint was the presence of rockfalls. Small to large groups of rockfalls were manually digitised as polygons using the aerial imagery. The digitisation procedure ignored large outcrops, especially of the Clarens and Molteno Fm. sandstones, which show up very clearly in the aerial imagery. It is important to note that the digitised clusters possess a bias as they are a subjective interpretation of what is considered a rockfall, however, this process served to provide a general indication of rockfall densities.

Fishnet grids of 500 m by 500 m were created and clipped to the 1 Km representative sample area in order to assist in tracking progress made with the digitisation of potential rockfalls. The rockfall polygons were only digitised within the representative sample area. The centroids of the digitised rockfall polygons were then determined and overlaid with the aerial imagery and clipped geological vector data to provide a basic visualisation of the density of rockfalls within the representative sample area (Figure 26).

For the purpose of this research, it was necessary to sample at least one site per lithology; hence at least one rockfall ground-truthed site was required for each of the Clarens, Elliot and Molteno sandstone Formations. Figure 27 demonstrates the GIS workflow of the methodology used for selecting the ground-truthed sites. The representative ground-truthed sites were selected to include each of the sandstone lithologies present in the region. The Clarens, Elliot and Molteno Fm. Sandstone sample sites (1-3) were selected where points representing rockfall of the interested lithology were isolated from the other lithologic groups, based on the overlaid 1:250,000 geological vector layer. The sample ground truth sites were selected where rockfall densities are closest to the Rietspruit trigonometric beacon, with the highest densities for each of the Formation sandstone groups.

4.5. Field data collection

All of the field work was undertaken during two visits to the Park. The majority of the field work was undertaken from the 15th to the 22nd of December 2011. During this time, the focus was on setting up base stations and locating the ground-truthed sites. Table 6 outlines the field work activities in more detail. The Rietspruit trigonometric beacon, which is the most accessible of the trigonometric beacons within the representative sampling area, was used to set up a DGPS base station (Figure 30), so that the first reference point could be established. This trigonometric beacon is located

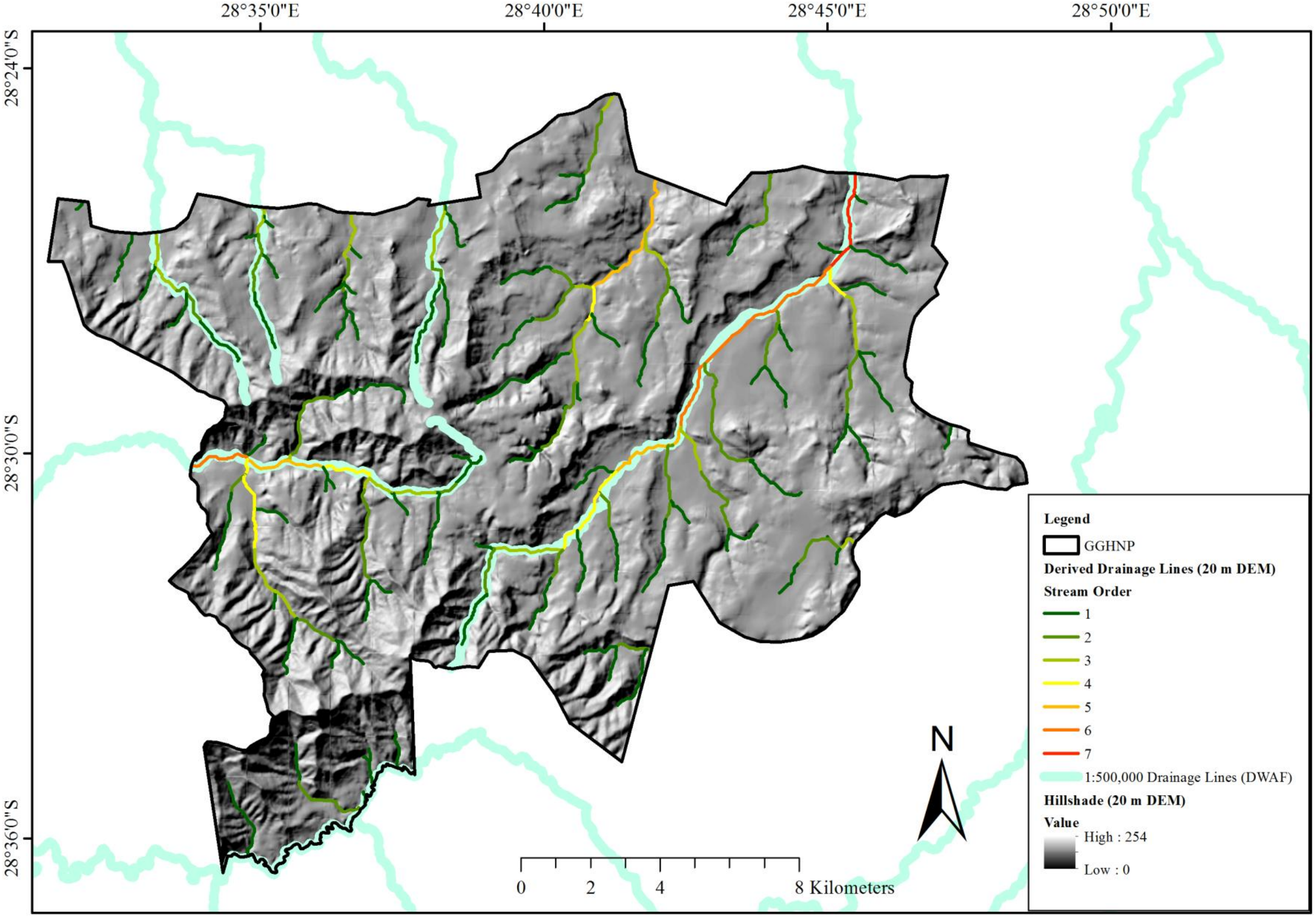

Figure 24: Vector layer of drainage lines for the GGHNP.

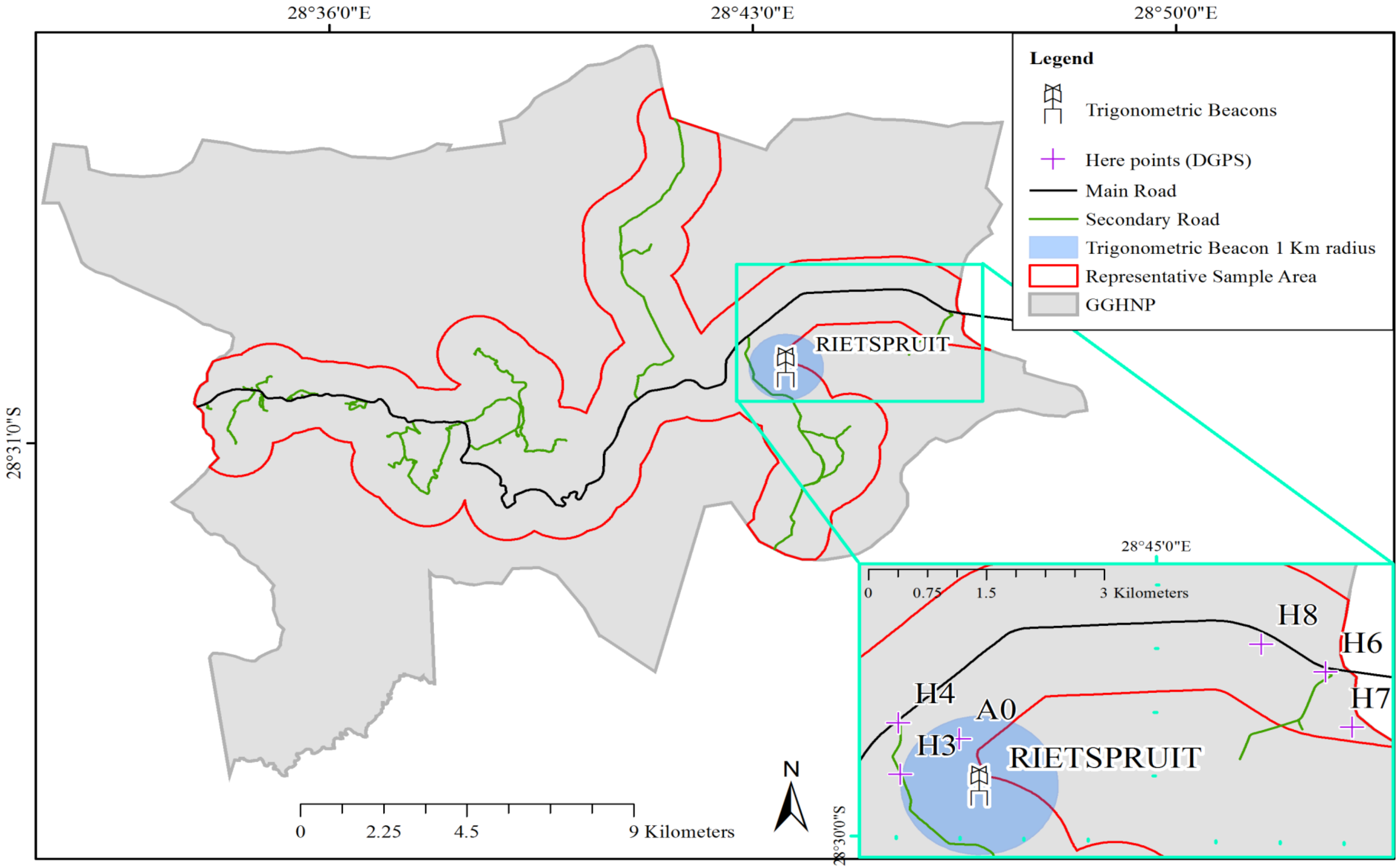

Figure 25: The representative sample area also indicating the locations of the DGPS here points.

at the summit of the Silasberg and was only accessible by hiking along the crests of hills near the Basotho cultural village located ~ 1.5 Km east of the Silasberg (Figure 31). Once the DGPS base station was established at the Rietspruit trigonometric beacon, some field assistants stayed to watch over the base station whilst other members of the team hiked back down the Silasberg for ~ 800 m northward along the slope to locate the Clarens Fm. ground-truthed site. The Clarens Fm. ground-truthed site was located by tracking the coordinates from one of the 5 m grids at the Clarens Fm. ground-truthed site using the stakeout points feature on the DGPS's rover (see fig 30, b). Once the coordinate point was located, a steel rod was placed into the ground as a marker (see Figure 32). This marker then served as a reference point. The DGPS base station was then set up at the newly located reference point known as A0.

Visible rockfalls were subsequently mapped with the establishment of further reference points (H3 and H4). Reference points H3 and H4 were conveniently set up near the main road (R712). Reference points were established for the Elliot and Molteno Fm. ground-truthed sites. Reference point H6 was determined using reference point H4 as a base station. Reference point H6 was then used to locate reference point H7 which was consequently used as a base station for collecting coordinate measurements at the Elliot Fm. ground-truthed site (Figure 33). The Molteno Fm. ground-truthed site (Figure 34) was located using reference point H6, so as to set up reference point H8, which served as the base station for collecting DGPS readings at the Molteno Fm. ground-truthed site. An additional field visit from 1 - 3 June 2012 was undertaken to complete data collection at the Molteno Fm. ground-truthed site.

4.5.1. Rockfall position

The position of every rock sample was measured at approximately the mid-point of the rock using the DGPS. The DGPS collects coordinates with accuracies of at least 10 cm. The point nomenclature for every rockfall was named according to three attributes: their grid occupancy, site occupancy (i.e. abbreviated to the first letter of the ground-truthed sites name) and feature number (Figure 35). Each attribute is separated by a hyphen, for example the 12th rockfall occupying grid C1 at the Molteno site would have a point identification (point ID) C1-M-12. The ground-truthed sample sites were named as follows:

1- Clarens Fm. ground-truthed site
2- Elliot Fm. ground-truthed site
3- Molteno Fm. ground-truthed site

The GIS methodology for creating the five meter by five meter ground truth grids is shown in Figure 28. Rockfalls within each representative sample site were selected using a polygon. This polygon defined the extent of the grid. Vector grids with five meter spacing for both the X and Y axis were then created. A total of three columns by four rows were chosen for sampling. This sample size was deemed sufficient for mapping features, both down slope and across the slope. At the Clarens and Elliot ground truth sites, the three columns were labelled A – C, and the four rows 1 – 4. At the Molteno ground truth site, the four columns were labelled A – D, and the three rows 1 – 3. In order to find coordinates for the corners of each grid, the nodes for the grids needed to be extracted using the extract nodes tool in QGIS. An X and a Y attribute field were then created for the extracted points nodes. The X field and Y field represent degree values for longitude and latitude respectively. The extracted nodes were then used to locate and mark actual grid points within the field. The sampling grids and points for the sample ground-truthed sites are depicted in Figure 29.

4.5.2. Rockfall measurements

Figure 36 is a graphic representation of how the rock measurements were taken in the field using a measuring tape. The rock measurements refer to the actual physical dimensions of the measured rock. Tables were produced in the field to record the measured longest Axis (LA), the perpendicular axis (PA), height, and circumference of each rock. The readings were recorded in millimetres using a 50 m measuring tape and measured and labelled according to their DGPS point id.

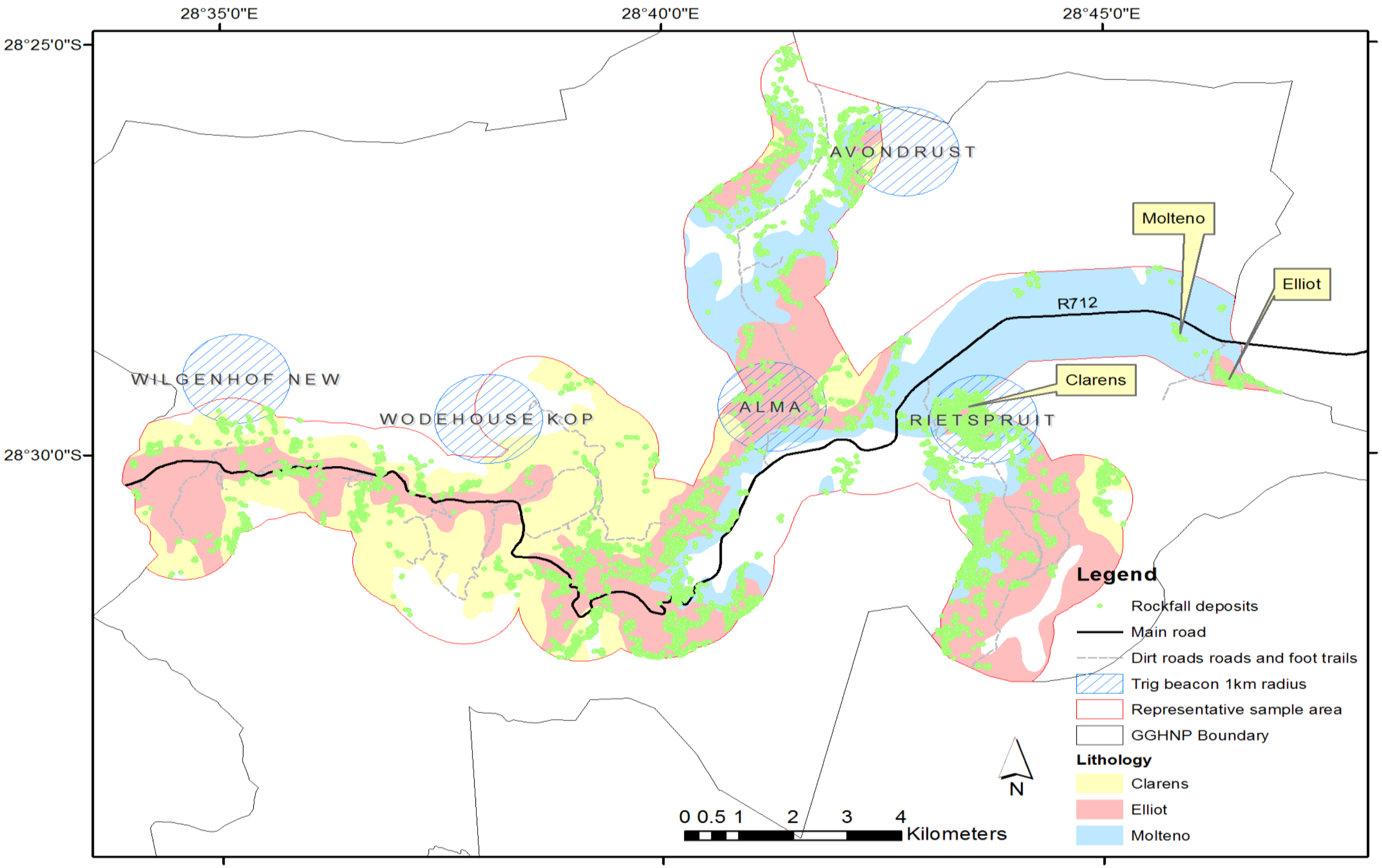

Figure 26: Image showing the density of rockfalls within the representative sample area. The Clarens, Elliot and Molteno Formation Ground-truthed sites were selected using the overlayed information and are indicated by the callouts.

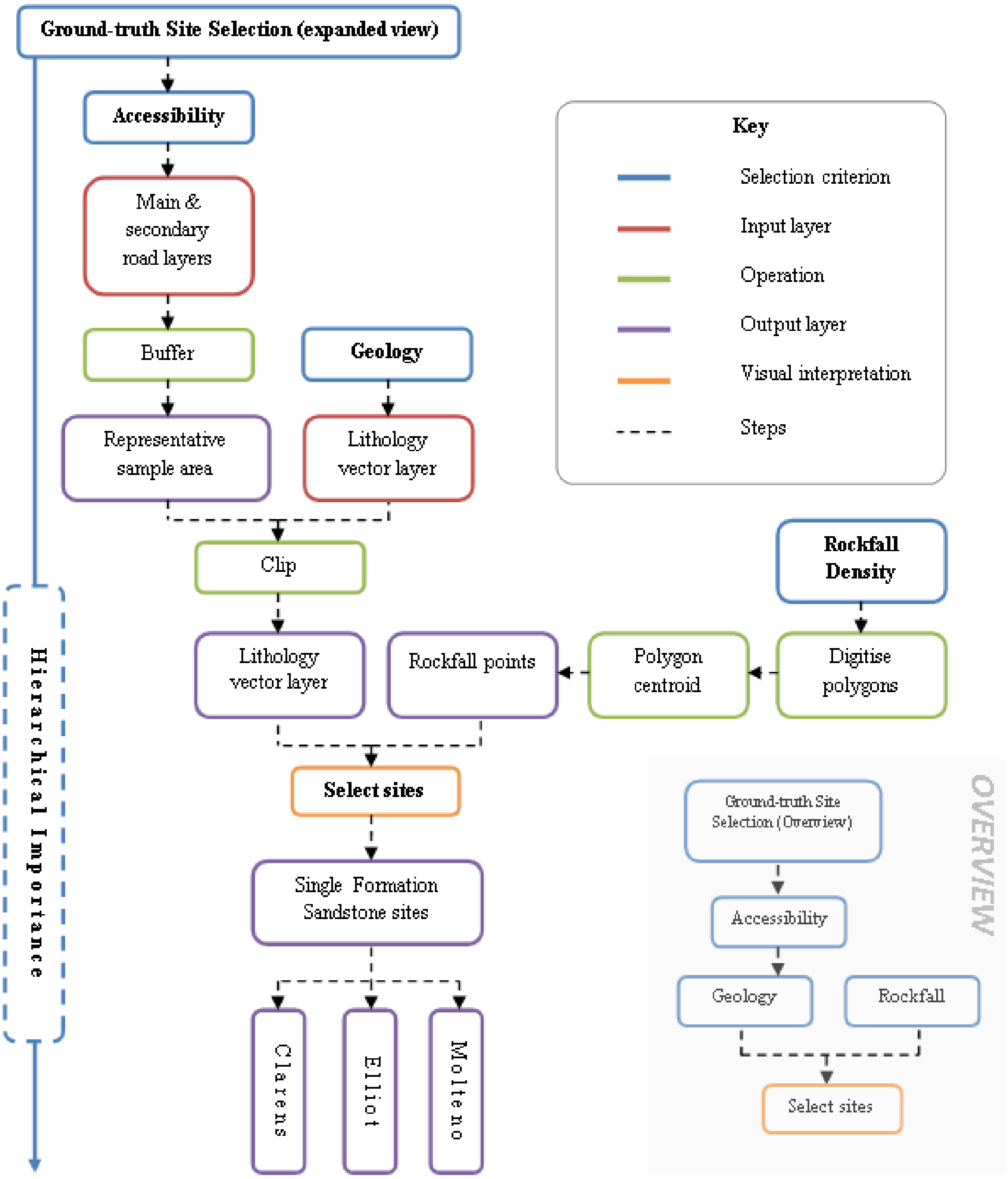

Figure 27: GIS workflow depicting the steps taken for selecting the representative ground-truthed sites. Heirarchical importance is highest for accessibility, followed by geology and the prescence of a rockfall.

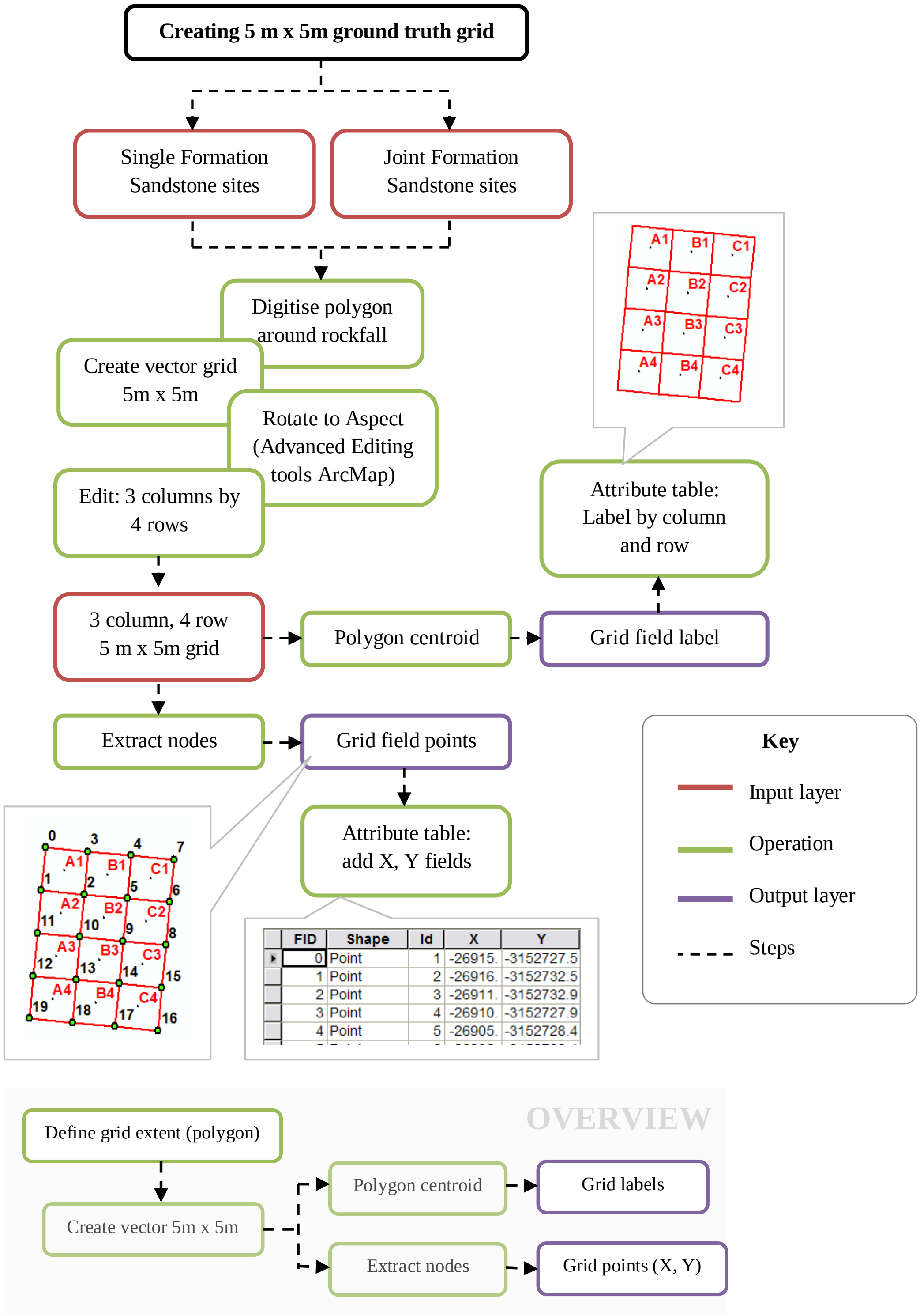

FID	Shape	Id	X	Y
0	Point	1	-26915.	-3152727.5
1	Point	2	-26916.	-3152732.5
2	Point	3	-26911.	-3152732.9
3	Point	4	-26910.	-3152727.9
4	Point	5	-26905.	-3152728.4

Figure 28: GIS workflow depicting the steps taken for creating the 3 column ground-truthed grids.

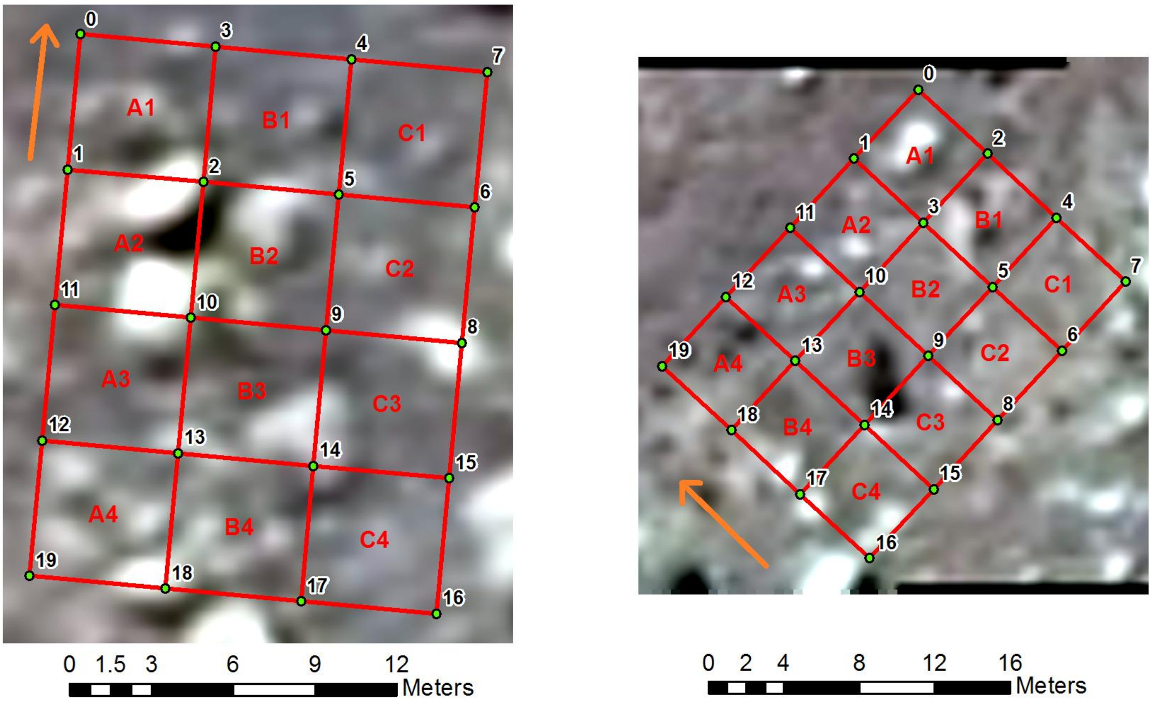

a. Clarens ground truth site

b. Elliot ground truth site

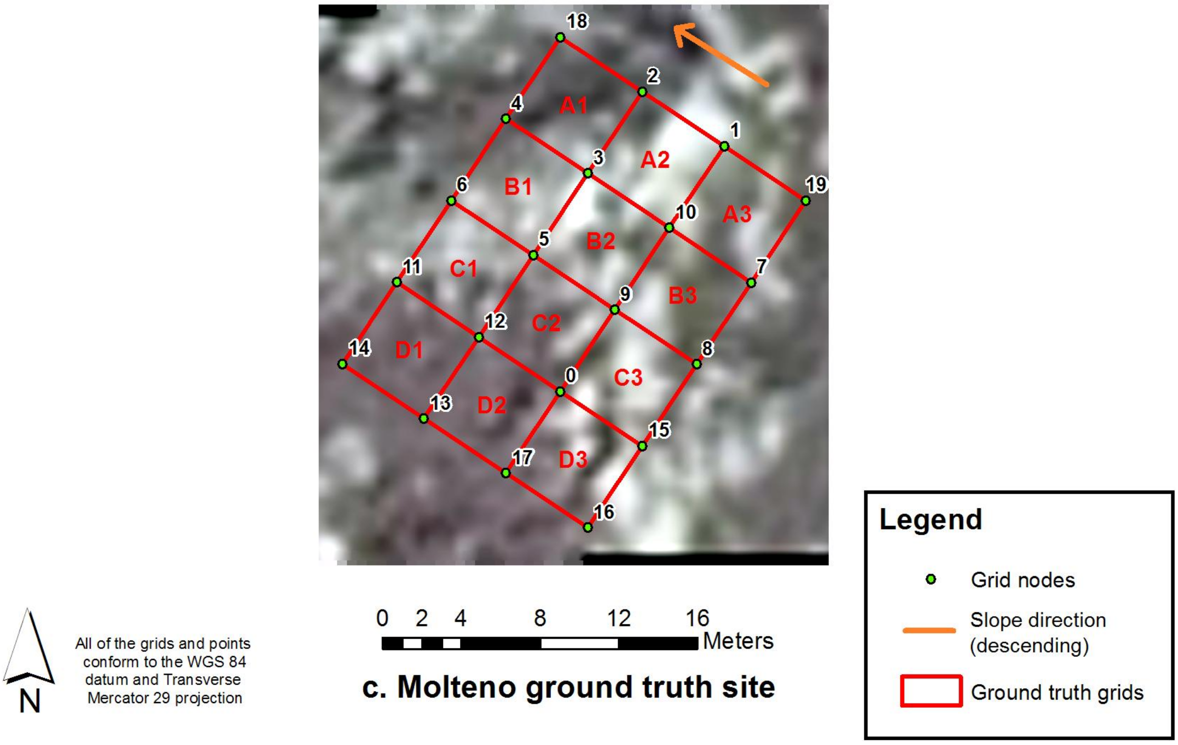

All of the grids and points conform to the WGS 84 datum and Transverse Mercator 29 projection

c. Molteno ground truth site

Figure 29: The 5 m by 5 m grids for the three ground-truthed sites. The grid columns are labelled A – C and the rows 1 - 4.

Field work dates	Field work activities
15-Dec-11	- Reach the Rietspruit trigonometric beacon and set up a base station. - Stake out the Clarens Fm. ground-truthed site. - Set up a base station at the Clarens station - Set up grids and measure rockfalls at the Clarens ground-truthed site. - Set up reference points H3 and H4.
16 - 17 Dec 2011	- Measure rockfalls at the Clarens Fm. ground-truthed site.
18 - 21 Dec 2011	- Set up reference point H6. - Stake out Elliot Fm. ground-truthed site. - Set up reference point H7 at the Elliot Fm. ground-truthed site. - Collect measurements for rockfalls at the Elliot ground-truthed site.
22-Dec-11	- Set up reference point H6. - Stake out the Molteno Fm. ground-truthed site. - Set up reference point H8 at the Molteno Fm. ground-truthed site. - Collect measurements for rockfalls at the Molteno ground-truthed site.
1 -3 June 2012	- Set up reference point H8. - Collect measurements for rockfalls at the Molteno ground-truthed site.

Table 6: A detailed description of the field work activities that took place on specific field work dates.

Figure 30: (a) DGPS base station and (b) rover.

Figure 31: The Silasberg (Clarens Fm. ground-truthed site).

Figure 32: Steel rod marker used as a reference coordinate.

Figure 33: Elliot Fm. ground-truthed site.

Figure 34: Molteno Fm. ground-truthed site.

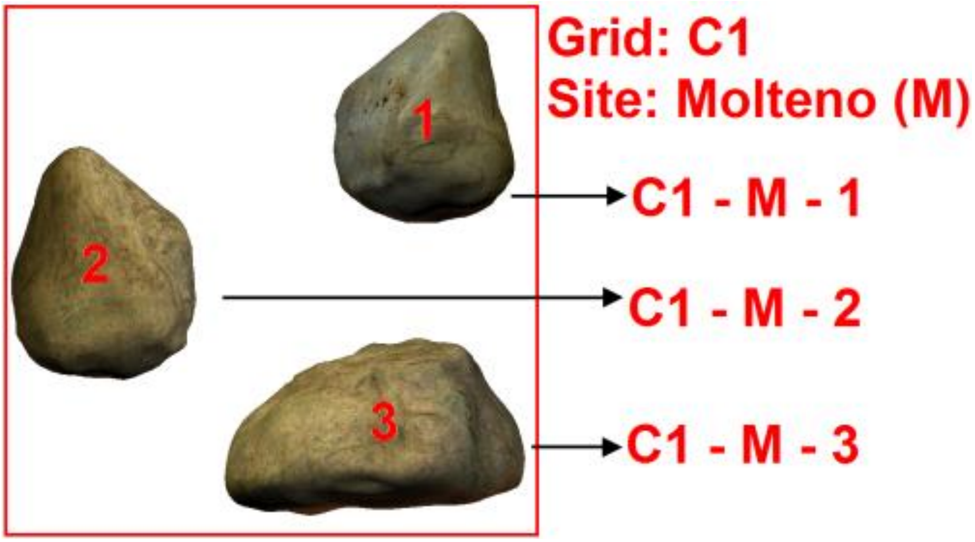

Figure 35: Rockfall nomenclature derived by grid occupancy, site occupancy, and rockfall feature number.

4.5.3. Orientation of the rock

The rock orientation refers to the bearing of the rocks' longest axis. The bearing of the longest axis (bearing of LA) was determined using a map compass with bearing.

4.6. Mapping the field data in a GIS

Once the DGPS field points were collected, it was necessary to export them from the DGPS controller unit to the desktop for analysis. This was done using Trimble Business Centre software, which comes packaged with the R6 DGPS. The points for all the ground truth sites were exported using the WGS84 datum and UTM 35 south conformal projection. The point data were exported to a comma-separated values file format (i.e. .csv). The .csv file was edited and headers added, namely Point ID, X, and Y.

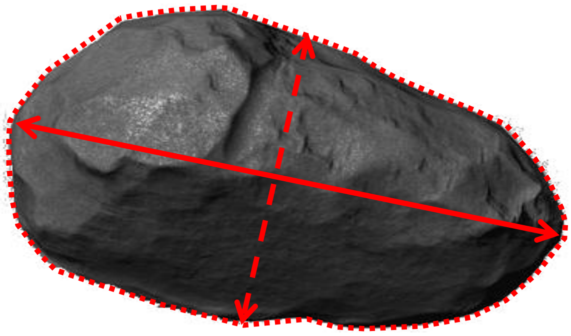

Longest axis
The longest axis is measured and recorded by standing above the rock with a bird's eye view and measuring with tape, the longest length of the rock in millimetres.

Perpendicular axis
The perpendicular axis is measured and recorded by standing above the rock with a bird's eye view and measuring with tape, the width or length perpendicular to the longest axis of the rock in millimetres.

Circumference
The circumference is measured and recorded by standing above the rock with a bird's eye view and measuring with tape, the length around the rock in millimetres.

Figure 36: Ground-truthed measurements taken for individual rocks at the ground-truthed sites.

The next step was to prepare the data for use in a GIS environment. To do this, the .csv files were added to ArcMap. The X Y data were displayed and then exported to shapefile format. The field measurements for each rockfall were associated to its point ID. Attribute fields for the LA, PA, height, bearing of LA, circumference and DGPS base height were physically input for every point ID. In addition to this, an area field was created and populated by multiplying the LA (length) and PA (breadth) for every rock using the field calculator in ArcMap.

4.6.1. Bounding containers

Once the rock measurements were captured in the field for all the point ID's, it was possible to create bounding containers to represent the extents of ground-truthed rockfalls. To create the bounding containers required the LA (length) and the bearing of the LA (direction), the PA, and the angle perpendicular to the bearing of the LA, and then finally, the parallel LA and inverse angle of the bearing of the LA. The LA, bearing of the LA, and PA were determined through ground-truthing, whereas the angle perpendicular to the bearing of the LA, parallel LA and inverse angle of the bearing of the LA are derived from the given measurements. The bounding containers were achieved using advanced digitising in ArcMap. The bounding containers were used to help identify image objects during the OBIA. The methodology for creating the bounding containers is described (Figure 37).

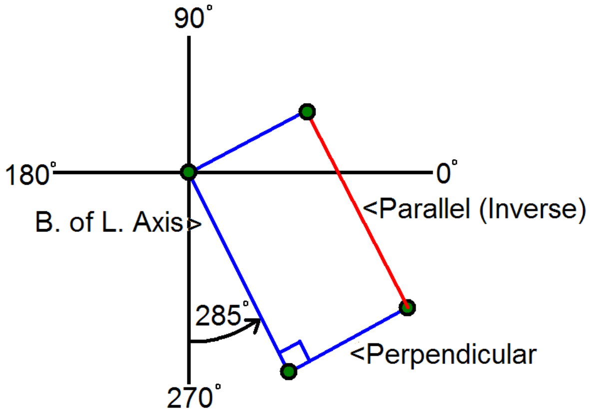

Figure 37: Bounding container showing the perpendicular angle calculated off the bearing of the LA and the parallel line which is the inverse angle of the bearing of the LA.

4.7. Modelling rockfall characteristics with TEGP

One of the objectives of this dissertation was to determine if a relationship between ground-truthed rockfalls (i.e. rockfall characteristics) could be established with remotely sensed imagery. If a relationship between rockfall characteristics and rockfalls in remotely sensed imagery exists, then rockfall characteristics could be modelled by using variables extracted from assumed rockfalls in remotely sensed imagery. The goal was thus to model rockfall characteristics with TEGP (from DEM) and remote sensing variables (from aerial image). Linear regression was chosen for this purpose. In order to answer whether or not TEGP and remote sensing variables can be used to characterise rockfall characteristics (i.e. ground-truthed rockfall measurements), step-wise multiple linear regression modelling was used. A calibration and validation dataset (calval) was created and used as the input for the step-wise multiple linear regression models. Multiple linear regression attempts to model the relationship between two or more explanatory variables and a response variable by fitting a linear equation to the observed data (Multiple linear regression, 1997). Step-wise regression throws out the independent variables which do not show a significant relationship with the dependent variable. Every value of the independent variable *x* is associated with a value of the dependent variable *y* (Multiple linear regression, 1997). In this instance, the dependent variable or *y* is the rockfall characteristic (i.e. ground-truthed rockfall measurement; LA, PA, bearing of LA, circumference, and area), and the independent variable or *x* is the TEGP extracted from remote sensing imagery. The TEGP were extracted to the calval using the derivatives derived from the 20 m DEM, and band 1, band 2, and band 3 of the mosaicked aerial imagery. The TEGP and remote sensing variables essentially represent the environmental variables of the GGHNP. For brevity the TEGP will from here on out also refer to the remote sensing variables extracted from the aerial imagery (i.e. image bands). The extracted TEGP include:

> Aspect – Values extracted to calval from the slope aspect raster derived from the 20 m DEM.
>
> Slope – Values extracted to calval from the slope gradient raster derived from the 20 m DEM.
>
> Curvature – Values extracted to calval from the curvature raster derived from the 20 m DEM.
>
> Plan – Values extracted to calval from the plan raster derived from the 20 m DEM.
>
> Profile – Values extracted to calval from the profile raster derived from the 20 m DEM.

Roughness – Values extracted to calval from the roughness raster derived from the 20 m DEM.

Elevation – Values extracted to calval from the 20 m DEM.

TPI – Values extracted to calval from the topographic position index raster derived from the 20 m DEM.

TRI – Extracted to calval from the topographic roughness index raster derived from the 20 m DEM.

Band 1 – Values extracted to calval from the red band of the mosaicked aerial imagery.

Band 2 – Values extracted to calval from the green band of the mosaicked aerial imagery.

Band 3 – Values extracted to calval from the blue band of the mosaicked aerial imagery.

4.7.1. Defining the multiple linear regression model

The model for multiple linear regression, given *n* observations, is:

$$y_i = \beta_0 + \beta_1 x_{i1} + \beta_2 x_{i2} + \dots \beta_p x_{ip} + \varepsilon_i \text{ for } i = 1, 2, \dots n.$$

Where y_i is the dependent variable (i.e. ground-truthed rockfall measurement; LA, PA, Bearing of LA, circumference, and area)

β_0 the intercept, and $\beta_1 x_{i1} + \beta_2 x_{i2} + \dots \beta_p x_{ip} + \varepsilon_i$ for $i = 1, 2, \dots n$, the independent variables (i.e. the TEGP)

In the statistical software package “R”, the model is expressed as:

DATA = FIT + RESIDUAL

Where the "FIT" term represents the expression $\beta_0 + \beta_1 x_1 + \beta_2 x_2 + \dots \beta_p x_p$. The "RESIDUAL" term represents the deviations of the observed values *y* from their means μ_y, which are normally distributed with mean 0 and variance σ (Multiple linear regression, 1997). Thus the multiple linear regression takes on the following form in R:

Rockfall characteristic ~ Aspect + Curvature + Plan + Roughness + Profile + Slope + Elevation + Total curvature + TPI + TRI + band1 + band2 + band3

Where Rockfall characteristic is either the LA, PA, bearing of LA, circumference or area.

4.7.2. Defining the calibration and validation dataset

The calval was created from the DGPS midpoints ground-truthed dataset. In order for the multiple linear regression models to discern rockfall from features with no rockfall characteristics, it was necessary to collect sample data of features which are not rockfalls. A total 151 points comprising of bare soil, vegetation, water, road, dirt road, shadow, and building roofs were digitised off the mosaicked aerial imagery to the DGPS mid-point ground-truthed dataset and assigned an attribute “N” for ‘not rockfall’. This was done to differentiate rockfall from non-rockfall which consist of ~28% of the points in the calval. In contrast, measured rockfalls were assigned a “Y” attribute. Fields for the aforementioned independent variables (TEGP and remote sensing variables) were created and populated using the ‘extract multiple values to points’ tool on the DEM derivatives, and band 1, band 2, and band 3 of the mosaicked aerial imagery. This brought the population of the DGPS midpoints ground-truthed dataset to 544.

The DGPS midpoints ground-truthed dataset was imported into R as a comma delimited table and named calval. A field called calval was created so that a calibration and validation samples could be allocated within the dataset. The calibration sample was defined as 75% of the calval population whilst the validation sample was allocated the remaining 25% of the calval. It was important to assign 25% of the calval as a validation sample set, as validation is a component of the multiple linear regression models. Generated models can only be validated with an independent validation sample. In essence, the validation sample was used to validate the calibration sample. The calibration sample used in the multiple linear regression models could only be validated with an independent sample (i.e. the validation sample). In addition to validating the multiple linear regression models, the validation sample was also used to validate rockfalls mapped using the OBIA approach.

Chapter 5 - Ground-truthed site results

5.1. Survey results

A total of 21, 5-meter by 5-meter ground truthed grids were sampled (Figure 38), bringing the success rate of the originally planned survey to 58.3%. A total of nine grids were sampled at the Clarens Fm. ground-truthed site, three at the Elliot Fm. ground-truthed site and nine at the Molteno Fm. ground-truthed site. A total of 75% of the ground-truthed grids were sampled for the Clarens and Molteno Fm. ground-truthed sites. In contrast, only 25 % of the Elliot Fm. ground-truthed site was surveyed successfully, hence bringing down the overall success rate of the initially planned survey.

The major factor limiting full survey coverage at the Clarens and Molteno Fm. ground-truthed sites was vegetation cover. The presence of vegetation in some of the grids made collecting measurements for rockfalls difficult, if not impossible in some situations (Figure 39). The major factor limiting survey at the Elliot Fm. ground-truthed site was time constraints. The rockfalls measured at the Elliot Fm. ground-truthed site were the smallest and most abundant per survey grid (Figure 40). It took an entire day to measure rockfalls within two grids at the Elliot Fm. ground-truthed site. Elliot Fm. sandstone deposits are small, with a compressed mud like composition. Many deposits broke easily while surveying, and were difficult to mark, which made monitoring progress even more difficult but especially time consuming. A total of 62 rocks were ground-truthed at the Clarens Fm. ground-truthed site, 141 rocks at the Molteno Fm. ground-truthed site, and 190 rocks at the Elliot Fm. ground-truthed site.

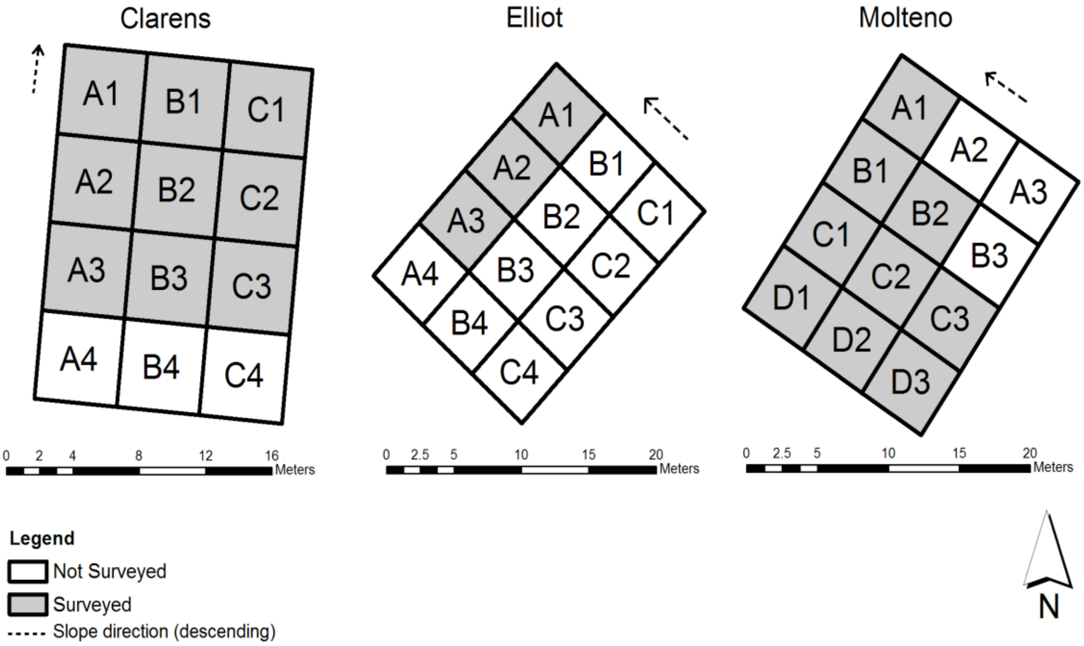

Figure 38: Image showing the surveyed grids at the Clarens, Elliot, and Molteno Fm. ground-truthed sites.

Figure 39: Vegetation cover at the Clarens Fm. ground-truthed site.

Figure 40: Example of the abundant rock deposits measured at the Elliot Fm. ground-truthed site.

5.2. Ground-truthed rockfall statistics

Table 7 provides a summary of statistics for the LA, PA, and circumference of rockfalls ground-truthed at the Clarens, Elliot, and Molteno Fm. ground-truthed sites. The mean LA for all ground-truthed sites is 0.5 m, whilst those for the Clarens, Elliot and Molteno Fm. ground-truthed sites is 0.97 m, 0.2 m, and 0.71 m respectively. The smallest LA for an individual rockfall is 0.06 m and recorded at the Elliot Fm. ground-truthed site. In contrast, the largest LA for an individual rockfall is 5.44 m, recorded at the Clarens Fm. ground-truthed site. The mean PA for all ground-truthed sites is 0.33 m. The mean PA for the Clarens, Elliot, and Molteno Fm. ground-truthed sites is 0.67 m, 0.15 m, and 0.42 m respectively. The smallest PA for an individual rockfall is 0.04 m, recorded at the Elliot Fm. ground-truthed site, whilst the largest PA for an individual rockfall is 3.90 m, recorded at the Clarens Fm. ground-truthed site. The mean circumference for all ground-truthed rockfalls is 1.33 m. The mean circumference for rockfalls measured at the Clarens, Elliot, and

Molteno Fm. ground-truthed sites is 2.52 m, 0.57, and 1.83 m respectively. The smallest circumference for an individual rockfall is 0.16 m, recorded at the Elliot Fm. ground-truthed site. In contrast, the largest circumference for an individual rockfall is 15.14 m, recorded at the Clarens Fm. ground-truthed site. The summary statistics for the LA, PA, and circumference show that on average the largest rockfalls were recorded at the Clarens Fm. ground-truthed site, followed by the rockfalls measured at the Molteno Fm. ground-truthed site. The summary of LA, PA, and circumference statistics also show that the Elliot Fm. ground-truthed site recorded on average the smallest rockfalls.

		Clarens (m)	**Elliot (m)**	**Molteno (m)**	**All sites (m)**
Longest Axis	Mean	0.97	0.2	0.71	0.5
	Median	0.6	0.12	0.58	0.27
	Mode	0.4	0.1	0.17	0.09
	Std. dev.	1.02	0.27	0.57	0.64
	Min	0.2	0.06	0.09	0.06
	Max	5.44	2.18	3.21	5.44
Perpendicular Axis	Mean	0.67	0.15	0.42	0.33
	Median	0.4	0.09	0.35	0.18
	Mode	0.31	0.07	0.19	0.08
	Std. dev.	0.82	0.19	0.32	0.44
	Min	0.15	0.04	0.08	0.04
	Max	3.9	1.46	1.48	3.9
Circumference	Mean	2.52	0.57	1.83	1.33
	Median	1.6	0.34	1.6	0.69
	Mode	1.11	0.23	0.43	0.23
	Std. dev.	2.73	0.77	1.39	1.66
	Min	0.54	0.16	0.25	0.16
	Max	15.14	5.72	7.32	15.14

Table 7: Summary statistics of the LA, PA and circumference of rockfalls ground-truthed at the Clarens, Elliot, and Molteno Fm. ground-truthed sites.

The standard deviation values for the LA, PA, and circumference measurements at the Clarens and Elliot Fm. ground-truthed sites were larger than their respective means. In contrast, the standard deviation values for the LA, PA, and circumference measurements at the Molteno Fm. ground-truthed site were lower than their respective means. Lower standard deviation values indicate less disparity in the LA, PA, and circumference of rockfall measurements, showing that the measured rockfalls are more alike with respect to their means, whereas higher standard deviation values indicate high disparity in the LA, PA, and circumference rockfall measurements showing that the measured rockfalls are less alike with respect to their means.

In summary, the descriptive statistics for the LA, PA and circumference of ground-truthed rockfalls show that the Clarens Fm. ground-truthed site has the largest rockfalls, followed by the Molteno Fm. ground-truthed site. The rockfalls measured at the Elliot Fm. ground-truthed site are the smallest. The standard deviation values for the LA, PA and circumference show that the rockfalls for the Clarens and Elliot Fm. ground-truthed sites vary significantly in contrast to their respective means and the difference between measurements is highly variable. In contrast, the LA, PA and circumference rockfalls for the Molteno Fm. ground-truthed site show little variation between measurements and are more alike with respect to their means.

5.2.1. Analysis of variance

An important step in determining whether remote sensing technologies can practically be used to identify rockfall sites is to evaluate the characteristics of rockfalls irrespective of geology. Prior to evaluating mapping techniques, it was determined whether the rockfall properties are geologically controlled. Analysis of variance (ANOVA) tests were performed to determine if mean rockfall parameters (i.e. LA, PA, circumference and area) differ significantly between the three ground-truthed geologies. The ANOVA F-test shows whether or not there is a significant difference in average values between groups. In this instance, the groups refer to the three ground-truthed sites, highlighted by their geologies (i.e. Clarens, Elliot and Molteno Fm.

sandstones), and the variables used were the LA, PA, circumference and area, all of which were represented in meters.

The H_O for each of these tests were that the mean values for the variables do not differ, for example $LA_{Clarens}=LA_{Elliot}=LA_{Molteno}$. Table 8 summarises the ANOVA statistics for the average of the longest axis, perpendicular axis, circumference, and area ground-truthed measurements. Based on these findings, $H_{O,}$ indicating no statistical difference in rockfall properties with respect to the three measured geological formations, is rejected. The $H_{A,}$ that there are significant differences in rockfall properties with respect to geology, is thus accepted.

ANOVA - Longest Axis

	Df	F value	Pr(>F)
Geology	2	14.55	1.37E-06
Residuals	183		

ANOVA - Perpendicular Axis

	Df	F value	Pr(>F)
Geology	2	12.46	8.42E-06
Residuals	183		

ANOVA - Circumference

	Df	F value	Pr(>F)
Geology	2	13.68	2.92E-06
Residuals	183		

ANOVA - Area

	Df	F value	Pr(>F)
Geology	2	5.4	5.27E-03
Residuals	183		

Significant codes: 0 '***' 0.001 '**'

Table 8: ANOVA statistics for ground-truthed measurements: longest axis, perpendicular axis, circumference and area.

5.2.2. Tukey honestly significant test

The ANOVA test enabled the verification that the average values differ significantly between the three geological formations, but is unable to reveal specifically if each of the three geological rockfall properties differ from one another. The ANOVA test was thus followed by applying the post hoc Tukey Honestly Significant Difference (HSD) test. The TukeyHSD test performs multiple pairwise comparisons between the three formations, for each rockfall property. For each comparison, the null hypothesis is that the average values are equal. Table 9 summarises the results for the TukeyHSD. Padj. values falling below 0.05 indicate that the rockfall properties being compared are significantly different (i.e. that the H_O is rejected and the H_A is accepted).

Tukey multiple comparisons of means test
95% family-wise confidence level

	Geology	**Diff**	**Lower**	**Upper**	**Padj.**
LA	Elliot - Clarens	-0.7	-1.02	-0.39	1.1E-06
	Molteno - Clarens	-0.22	-0.54	0.09	0.23
	Molteno - Elliot	0.48	0.17	0.8	0.001
PA	Elliot - Clarens	-0.48	-0.71	-0.25	4.2E-06
	Molteno - Clarens	-0.25	-0.48	-0.026	0.025
	Molteno - Elliot	0.23	-0.0007	0.45	0.051
Circum.	Elliot - Clarens	-1.78	-2.6	-0.96	0.000002
	Molteno - Clarens	-0.61	-1.43	0.2	0.18
	Molteno - Elliot	1.17	0.35	1.98	0.003
Area	Elliot - Clarens	-1.22	-2.12	-0.32	0.0045
	Molteno - Clarens	-0.85	-1.75	0.05	0.07
	Molteno - Elliot	0.37	-0.53	1.27	0.59

Table 9: TukeyHSD test showing the results for the pair-wise comparisons of means for ground-truthed measurements at the Clarens, Elliot and Molteno Fm. ground-truthed sites.

5.2.3. Rockfall measurements and spatial resolution

Box plots were created for graphically comparing the means of the variables across the groups, relative to the minimum rockfall size that could theoretically be detected by the aerial imagery. Figure 41 contains box plot graphs for the longest axis, perpendicular axis, circumference, and area ground-truthed measurements for the Clarens, Elliot and Molteno Fm. ground-truthed sites. In the box plot graphs for the longest axis, perpendicular axis and circumference, a threshold line is plotted on the y-axis at 0.5 meters. This threshold line corresponds to the spatial resolution of the aerial imagery. If the mean for the longest axis, perpendicular axis and circumference is equal to or above the spatial resolution of the aerial image, it would suggest that the majority of ground-truthed rockfalls should be visible in the aerial image, as the majority of measurements fall above or equal the spatial resolution. The threshold line for the area box plot was plotted at 0.25 meters to correspond to the area of a pixel (i.e. area of a pixel = length of pixel x breadth of pixel).

The box plot graphs for the longest axis and circumference indicate that the mean values for the Clarens and Elliot Fm. ground-truthed sites fall well above the 0.5 meter threshold line, whereas the mean values for the Elliot Fm. site falls below the threshold line. Thus, one would expect to find the majority of ground-truthed rockfalls visible in the aerial imagery, based on longest axis and circumference measurements. The box plot for the perpendicular axis and area show that the mean values for all of the ground-truthed sites fall below the threshold line for the spatial resolution and pixel area of the aerial image. Thus, one would expect the majority of ground-truthed rockfalls not to be visible in the aerial imagery, based on the perpendicular axis and area measurements.

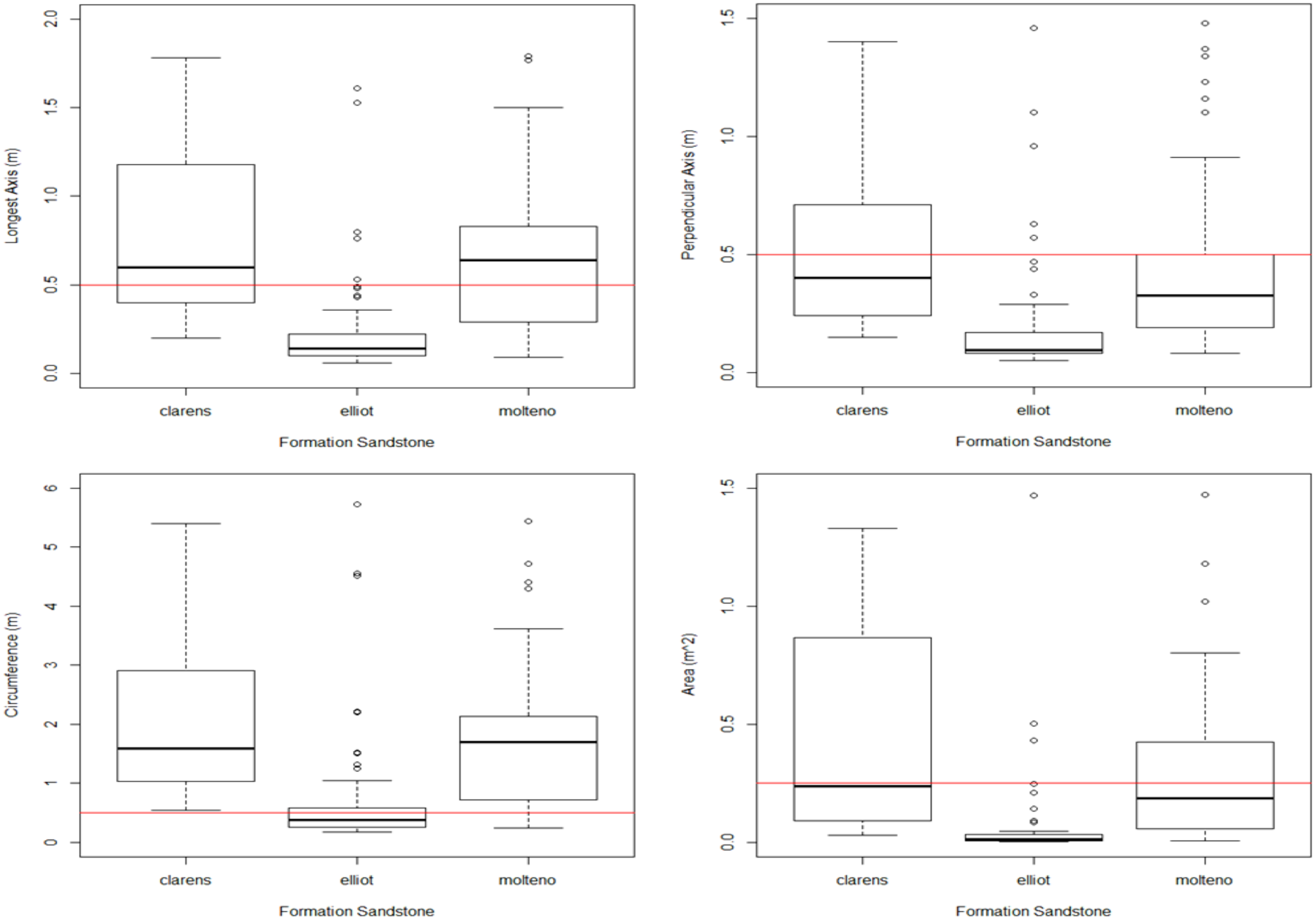

Figure 41: Box plot graphs for the ground-truthed measurements, longest axis, perpendicular axis, circumference and area. The thick black line represents the mean for the ground-truthed variable and the red line (y axis threshold) corresponds to the spatial resolution of the aerial image.

5.2.4. Frequency and gradient

In Figure 43, the gradient for each row of the ground-truthed sites is depicted. The slope gradient at each of the ground-truthed sites was calculated by finding the angle of the tangent using the following equation:

$$\boldsymbol{tanA = \frac{opposite}{adjacent}}$$

Where *A* is the angle (gradient). The *opposite* is the difference in elevation. and the *adjacent* the distance between two point.

Figure 42 shows how the slope gradient was determined using tanA. The ‘opposite’ (Y) represents the elevation (meters). The ‘opposite’ is determined by finding the difference in elevation between two points ($Y = Z_2 - Z_1$). The ‘adjacent’ (X) is the distance in meters between two points. The slope gradient was calculated for each row of the ground-truthed grids. Calculations could only be made for surveyed grids. For instance, in row A of the Clarens Fm. ground-truthed site, point A1-C-1 from grid A1 and point A3-C-13 from grid A1 were selected to calculate the slope gradient for row A. These points were the furthest apart from each other for row A of the Clarens Fm. ground-truthed site. The points with the furthest distance from each other were selected to ensure that the gradient for the entire row could be determined. Each DGPS point recorded an elevation attribute. The difference in elevation is calculated by subtracting the higher elevation from the lower elevation point. The adjacent requirement for the equation was satisfied by finding the distance between the DGPS points. All inputs were used in the tanA equation to ultimately determine the slope gradient (A). This was done for each row of the ground-truthed sites where there were DGPS point data.

The results for the slope gradient are summarised in Table 10. The Clarens Fm. ground-truthed site had the steepest average slope gradient, followed by the Molteno Fm. ground-truthed site. The Elliot Fm. ground-truthed site had the gentlest slope gradient of only ~ 1° or is near level. Figure 44 depicts the frequency of ground-truthed rockfalls against slope gradient for the ground-truthed sites. Slope gradient decreases, so rockfall frequency increases. This may account for the higher rockfall count observed at the Elliot Fm. ground-truthed site in row A, as opposed to the ground-truthed rows at the Clarens and Molteno Fm. ground-truthed sites. Rockfall frequency at the Molteno Fm. ground-truthed site is higher than the rockfall frequency at the Clarens Fm. ground-truthed site, but still lower than the rockfall frequency at the Elliot Fm. ground-truthed site.

Site	Clarens	Molteno	Elliot
Row A	63.66°	4.19°	0.96°
Row B	30.17°	14.36°	
Row C	27.07°	19.56°	
Row D		23.88°	

Table 10: Slope gradient for the sampled rows at the ground-truthed sites.

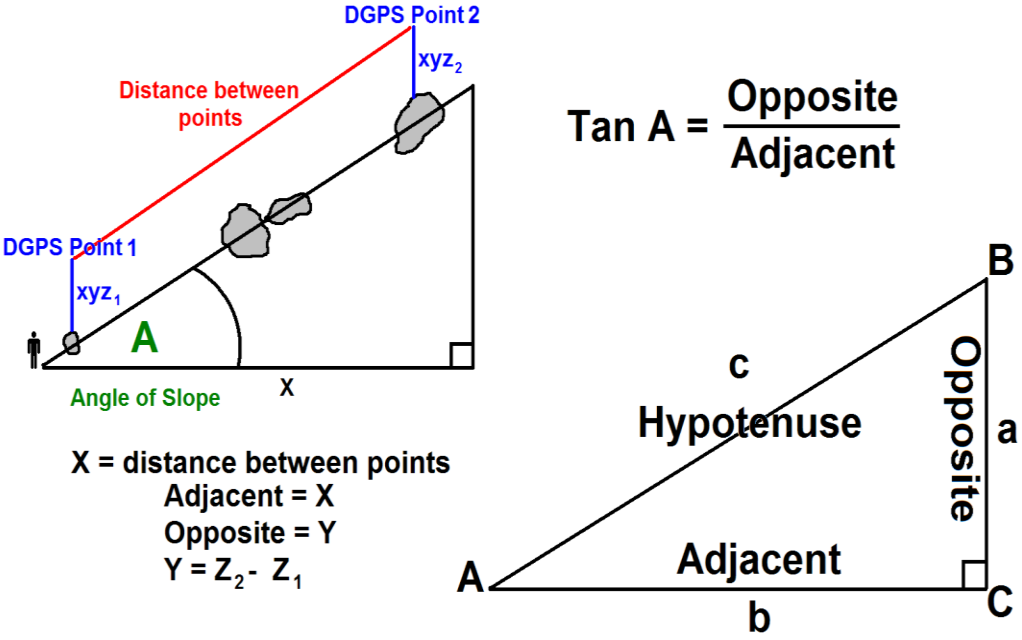

Figure 42: Illustration of the trigonometric technique used for determining the degree of slope for each of the rows of the ground-truthed sites.

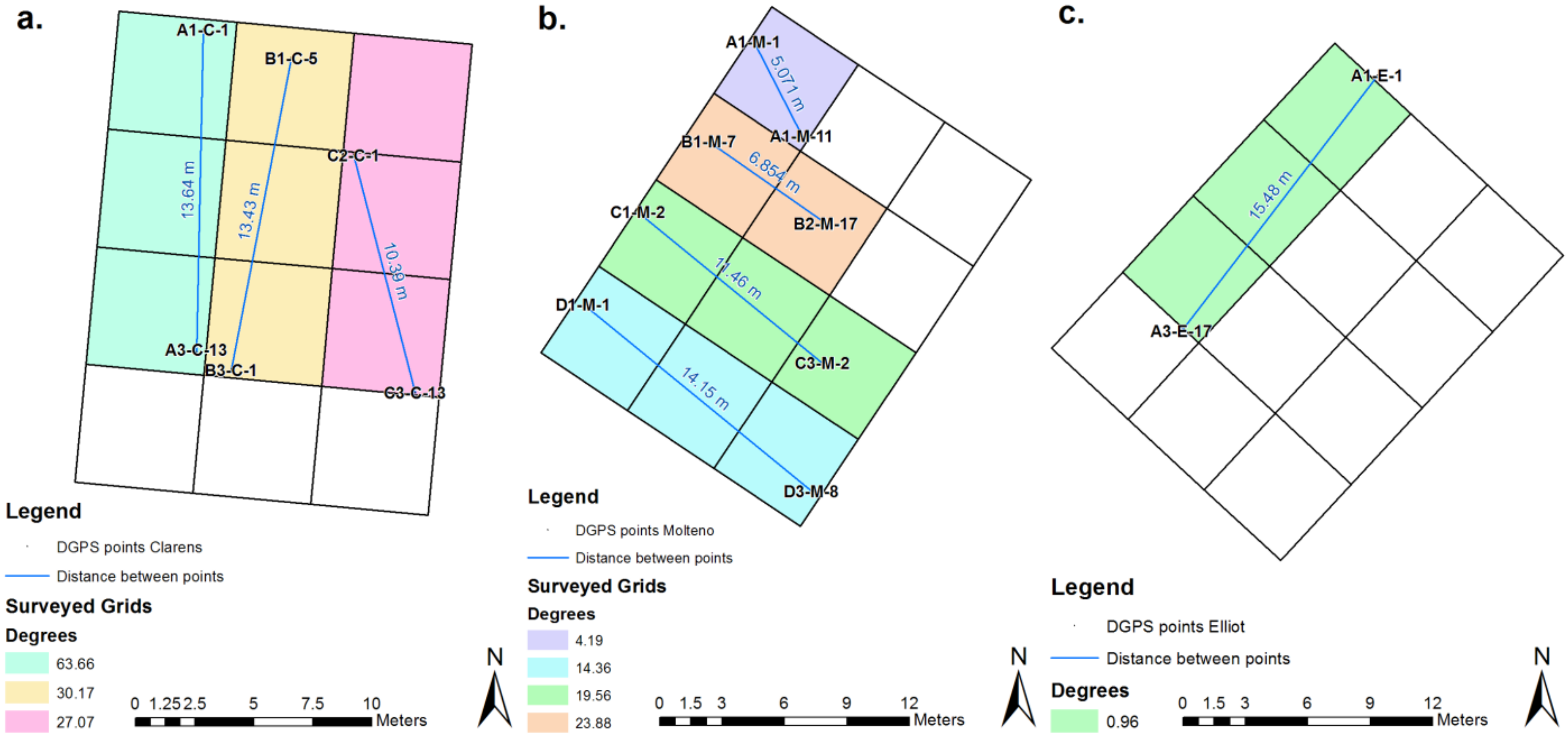

Figure 43: Slope gradient for (a) Clarens ground-truthed site, (b) Molteno ground-truthed site, and (c) Elliot ground-truthed site.

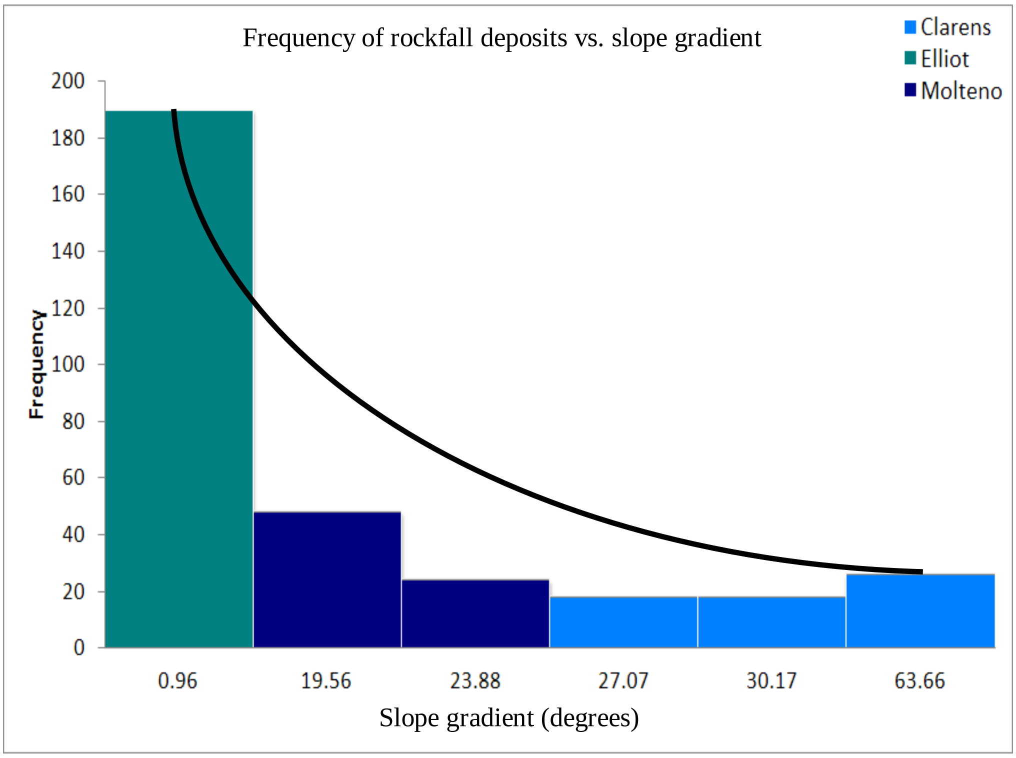

Figure 44: Ground-truthed rockfalls vs. slope gradient.

5.2.5. Bearing of LA and slope aspect

The orientation of ground-truthed rockfalls refers to the bearing of the longest axis measurements. In order to determine the mean orientation of ground-truthed rockfalls, rose diagrams were drawn for each of the ground-truthed sites so that the mean ray of the orientation of ground-truthed rockfalls could be shown. These rose diagrams are linear functions which plot bearing values of 0˚ - 360˚. The rose diagrams were created by importing the bearing of the longest axis measurements into the software "RockWorks" as a table (Figure 45, 46, and 47). The plotted mean ray (or linear directional mean), symbolises the highest incidence of ground-truthed rockfalls occurring at a particular bearing. The slope orientation (i.e. slope aspect) ray was plotted on the rose diagrams to check whether or not there is a relationship between the incidence of ground-truthed rockfalls occurring at a particular bearing with slope aspect. The slope orientation for each ground-truthed site was plotted on the rose diagram by determining the mode of the degree value from a slope aspect raster derived from the 20 m DEM.

In Figure 45, the mean ray for 62 ground-truthed rockfalls recorded at the Clarens Fm. ground-truthed site was 317.73˚ north-west or 137.7˚ south-east in relation to a predominant north-facing slope. The mean ray for 190 ground-truthed rockfalls recorded at the Elliot Fm. ground-truthed site was 278.35˚ west or 98.4˚ east in relation to a predominant north-west-facing slope (Figure 46). In Figure 47, the mean ray for 141 ground-truthed rockfalls recorded at the Molteno Fm. ground-truthed site was 28.2˚ north north-west or 208.21˚ south south-west in relation to a predominant west-facing slope. A comparison of the mean ray with the slope orientation suggests that the rockfalls at all of the ground-truthed sites except the Clarens site have a near perpendicular orientation to the slope orientation. Hardwick (2012) found that the linear directional mean and frequency of digitised rockfalls suggests that the rockfalls are oriented perpendicularly to the rock exposure which compliments the observation that most rockfalls originate from horizontally bedded rock exposures which are oriented parallel to the slope contour.

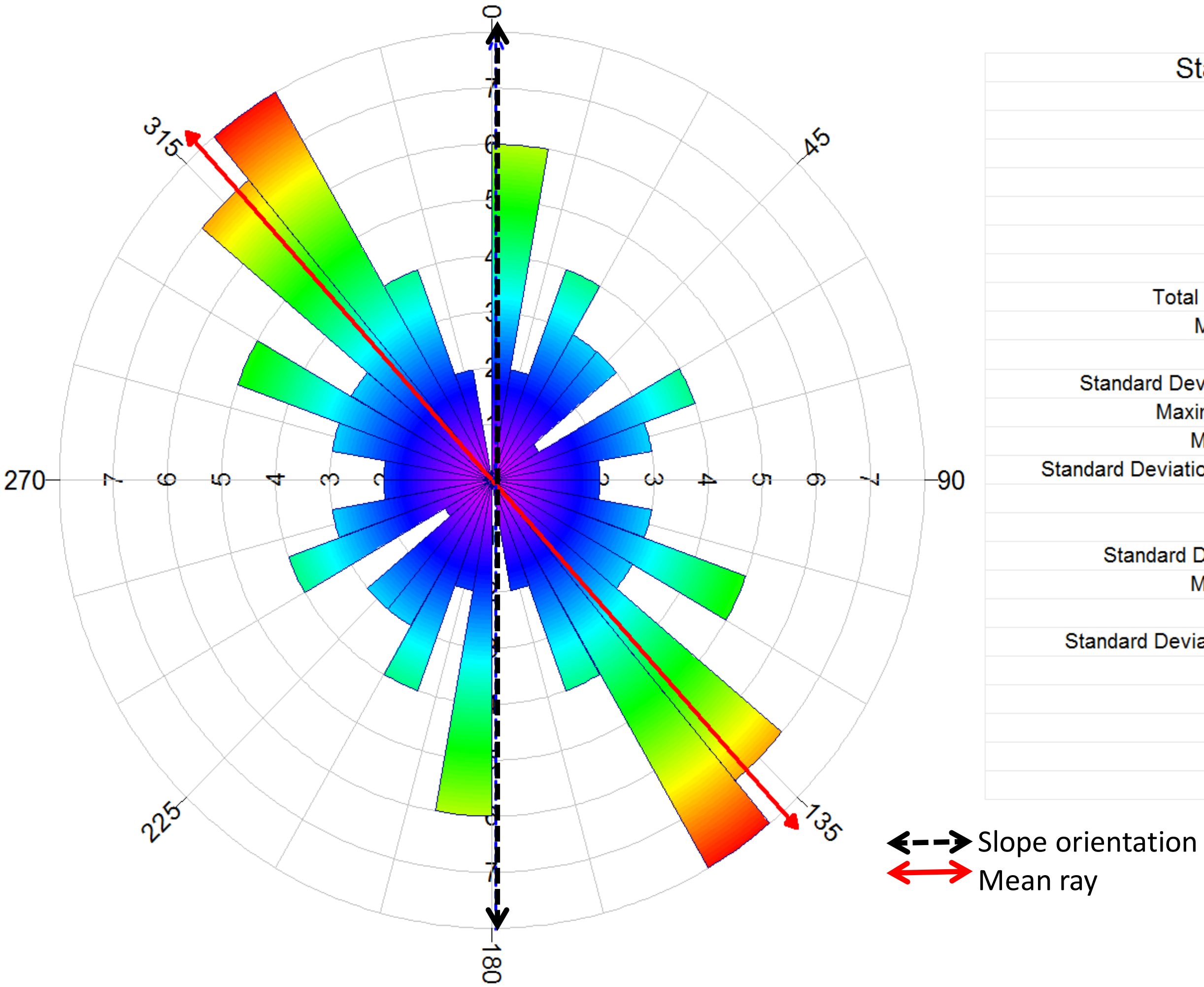

Statistical Summary

Calculation Method:	Frequency
Class Interval:	10.0 Degrees
Azimuth Filtering:	Activated
Minimum Azimuth #1:	0.0 Degrees
Maximum Azimuth #1:	360.0 Degrees
Data Type:	Bidirectional
Population:	62
Total Length of All Lineations:	124.0
Maximum Bin Population:	8.0
Mean Bin Population:	3.65
Standard Deviation of Bin Population:	1.87
Maximum Bin Population (%):	6.45
Mean Bin Population (%):	2.94
Standard Deviation of Bin Population (%):	1.51
Maximum Bin Length:	8.0
Mean Bin Length:	3.65
Standard Deviation of Bin Lengths:	1.87
Maximum Bin Length (%):	6.45
Mean Bin Length (%):	2.94
Standard Deviation of Bin Lengths (%):	1.51
Vector Mean:	137.7 Degrees
	317.73 Degrees
Confidence Interval:	62.3 Degrees
	(95 Percent)
R-mag:	0.16

Figure 45: Rose diagram showing the mean orientation of 62 rockfalls (mean ray) measured at the Clarens Fm. ground-truthed site.

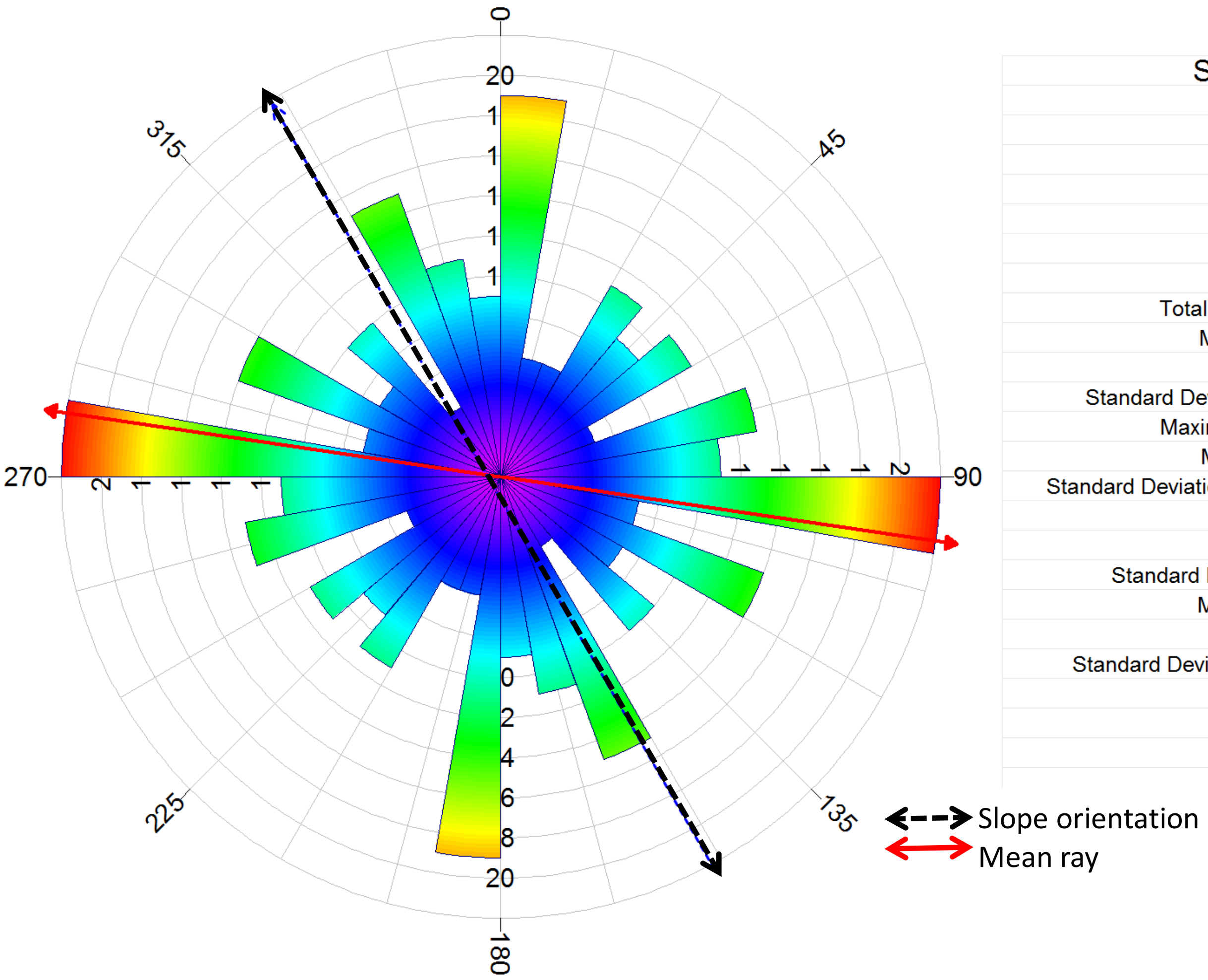

Statistical Summary	
Calculation Method:	Frequency
Class Interval:	10.0 Degrees
Azimuth Filtering:	Activated
Minimum Azimuth #1:	0.0 Degrees
Maximum Azimuth #1:	360.0 Degrees
Data Type:	Bidirectional
Population:	190
Total Length of All Lineations:	380.0
Maximum Bin Population:	22.0
Mean Bin Population:	10.56
Standard Deviation of Bin Population:	4.7
Maximum Bin Population (%):	5.79
Mean Bin Population (%):	2.78
Standard Deviation of Bin Population (%):	1.24
Maximum Bin Length:	22.0
Mean Bin Length:	10.56
Standard Deviation of Bin Lengths:	4.7
Maximum Bin Length (%):	5.79
Mean Bin Length (%):	2.78
Standard Deviation of Bin Lengths (%):	1.24
Vector Mean:	98.4 Degrees
	278.35 Degrees
Confidence Interval:	118.2 Degrees
	(95 Percent)
R-mag:	0.05

Figure 46: Rose diagram showing the mean orientation of 190 rockfalls (mean ray) measured at the Elliot Fm. ground-truthed site.

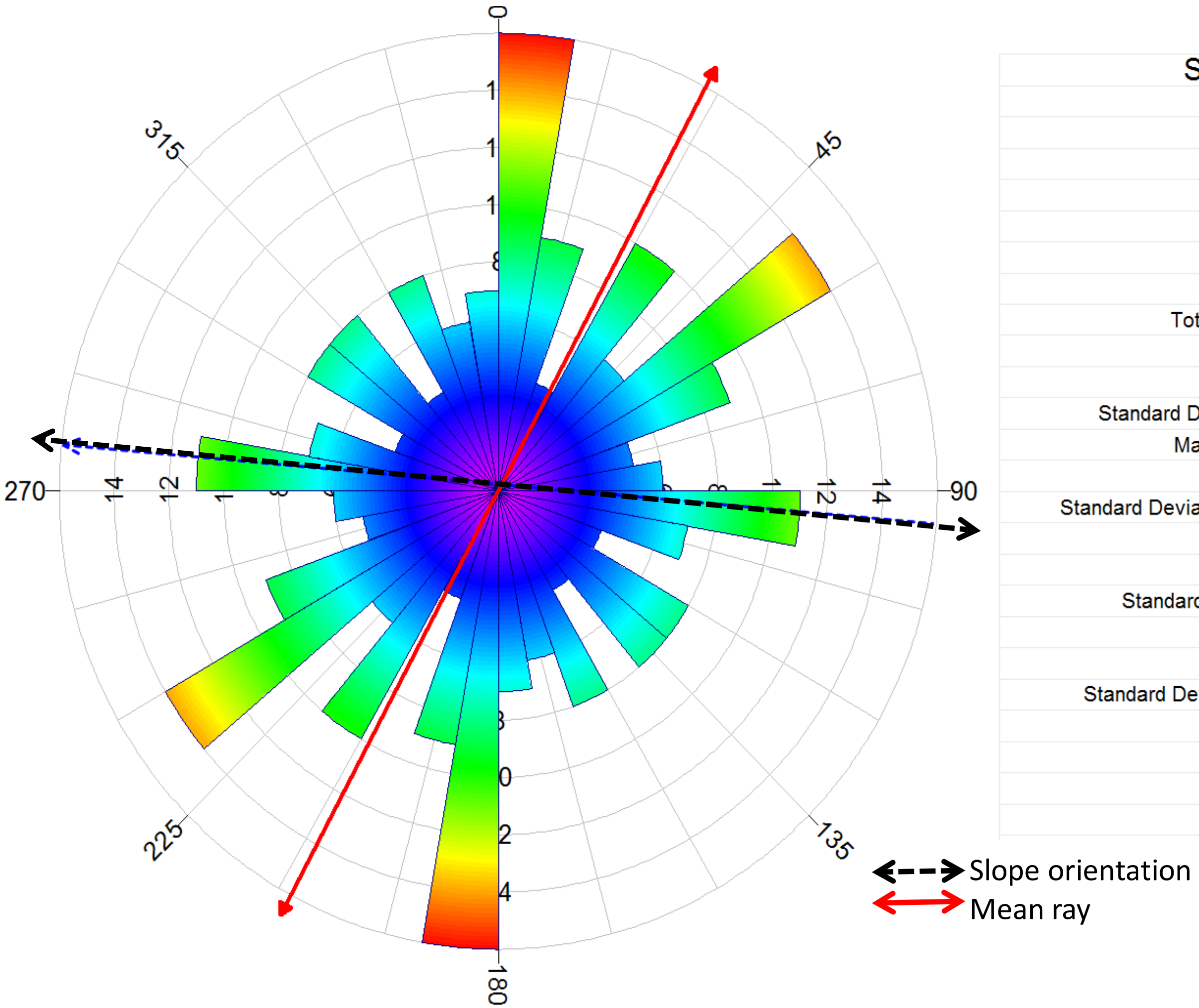

Statistical Summary	
Calculation Method:	Frequency
Class Interval:	10.0 Degrees
Azimuth Filtering:	Activated
Minimum Azimuth #1:	0.0 Degrees
Maximum Azimuth #1:	360.0 Degrees
Data Type:	Bidirectional
Population:	142
Total Length of All Lineations:	284.0
Maximum Bin Population:	16.0
Mean Bin Population:	7.89
Standard Deviation of Bin Population:	3.26
Maximum Bin Population (%):	5.63
Mean Bin Population (%):	2.78
Standard Deviation of Bin Population (%):	1.15
Maximum Bin Length:	16.0
Mean Bin Length:	7.89
Standard Deviation of Bin Lengths:	3.26
Maximum Bin Length (%):	5.63
Mean Bin Length (%):	2.78
Standard Deviation of Bin Lengths (%):	1.15
Vector Mean:	28.2 Degrees
	208.21 Degrees
Confidence Interval:	75.1 Degrees
	(95 Percent)
R-mag:	0.09

Figure 47: Rose diagram showing the mean orientation of 141 rockfalls (mean ray) measured at the Molteno Fm. ground-truthed site.

Chapter 6 - Multiple linear regression modelling results

Table 11 summarises the results of the multiple linear regression models using the calibrated dataset. The calibrated sample consisted of a population of 305 rockfalls (n_{All}). Of n_{All}, 47 samples were proportionately Clarens rockfalls ($n_{Clarens}$), 146 were proportionately Elliot rockfalls (n_{Elliot}), and 112 were proportionately Molteno rockfalls ($n_{Molteno}$). The results of the multiple linear regression models (Table 11) are reported by the TEGP, adjusted R^2, RMSE, and p-value. The TEGP column shows the independent TEGP which were significant in the model. The adjusted R^2 column is reported as a percentage and describes the relationship between the variations in the dependent rockfall characteristic with the independent TEGP. In addition, the adjusted R^2 reflects accuracy. An adjusted R^2 with a value of 100% implies that the independent TEGP describe the dependent rockfall characteristic perfectly. Hence, the fitted regression line would conform to the normal distribution and there would be zero residual error (Figure 48). The RMSE column reports on the precision of the residuals to determine whether or not they appear to fit the assumption of a normal distribution. The p-value column reports on whether or not the multiple linear regression model produced a significant result. Modelled results which produced no significant difference between rockfall characteristic and TEGP were excluded from validation.

Table 12 summarises the results of the multiple regression models applied to the validation dataset using the predict function in R. The validation sample consisted of a population of 136 rockfalls (n_{All}). Of n_{All}, 15 samples were proportionately Clarens rockfalls ($n_{Clarens}$), 44 were proportionately Elliot rockfalls (n_{Elliot}), and 29 were proportionately Molteno rockfalls ($n_{Molteno}$). The n_{Elliot} was excluded from validation as it failed to produce significant multiple linear regression models. The predict function anticipates what the values would be at each validation point, based on the multiple linear regression model. The results of the multiple linear regression models were used to calculate the predicted values and the validation sample was input as the observed dataset. Figure 49 shows the plotted regression line for the LA $n_{Clarens}$. The normal distribution is highlighted in red. The Y axis maps predicted values using the multiple regression model and the X axis maps the validation value. The R^2 column reports accuracy as a percentage. The closer R^2 is to 1 or 100%, the closer the predicted values correlate with the validation values. The RMSE reports on the precision of the validation. The lower the RMSE values, the closer the validation fits to a normal distribution. Hence, a good validation is one where the R^2 is high and the RMSE is as close to zero as possible. If all the plotted points were to fall on the plotted 1:1 line, defining the normal distribution, the multiple linear regression model would have 100% validation.

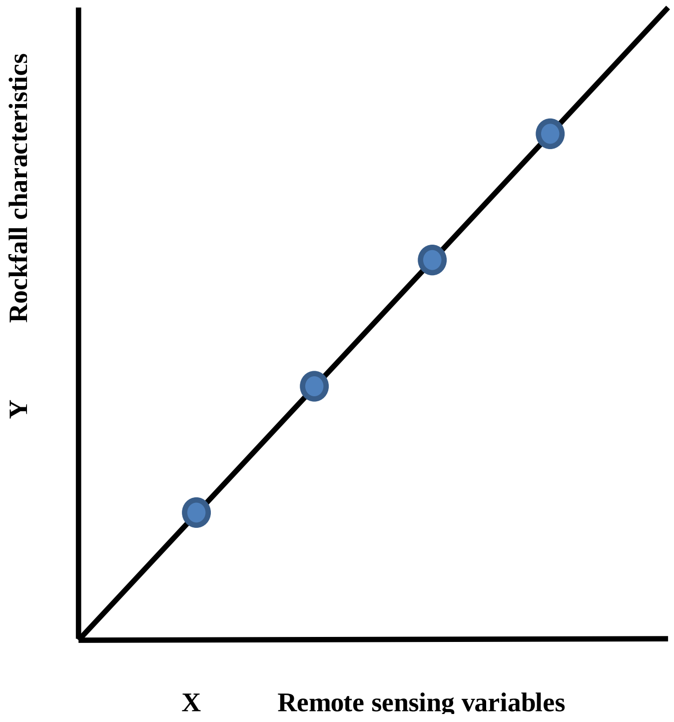

Figure 48: Hypothetical regression line assuming perfect fit with the normal distribution.

	Step-wise Linear Regression	TEGP Variables*	Adjusted R^2	RMSE	p-value**
LA	n_{all}	A,C,P,S,E,B1,B2,B3	34%	0.51m	HS
	$n_{Clarens}$	B2,B3	62%	0.59m	HS
	n_{Elliot}	NSV		0.3m	NP
	$n_{Molteno}$	B1,B3	10.3%	0.56	HS
PA	n_{all}	A,C,P,S,E,B2,B3	27%	0.33m	HS
	$n_{Clarens}$	C,P,B1,B2,B3	46%	0.45m	HS
	n_{Elliot}	B1,B2	0.31%	0.21m	NS
	$n_{Molteno}$	C,B1	5.8%	0.32m	S
Bearing of LA	n_{all}	A,C,P,R,E,TC,B1,B3	85%	118.4°	HS
	$n_{Clarens}$	A,B2,B3	7.9%	126°	NS
	n_{Elliot}	B1	0.9%	118.3°	NS
	$n_{Molteno}$	A,C	0.11	114.7°	HS
Circumference	n_{all}	A,C,P,S,E,B1,B2,B3	31%	1.34m	HS
	$n_{Clarens}$	B2,B3	60%	1.6m	HS
	n_{Elliot}	B1,B2	0.45%	0.86m	NS
	$n_{Molteno}$	B1,B3	9%	1.39m	HS
Area	n_{all}	S,E,B1,B2,B3	16%	1.28m	HS
	$n_{Clarens}$	B2,B3	39%	2.51m	HS
	n_{Elliot}	NSV		0.33m	NP
	$n_{Molteno}$	B1,B3	98%	0.74m	S

Calibration sample size:
n_{All} = 408 ; $n_{Clarens}$ = 47 ; n_{Elliot} = 146 ; $n_{Molteno}$ = 112

* TEGP
A – Aspect, S – Slope, C – Curvature, P – Plan, Pr – Profile, R – Roughness, E – Elevation, TC – Total curvature, TPI – Topographic position index, TRI – Topographic roughness index, B1 – Band 1 (red), B2 – Band 2 (green), B3 – Band 3 (blue), NSV – No significant variables.

** P-value confidence level

Highly significant (HS) = 99%	Significant (S) = 95%
Not significant (NS) = less than 95%	No probability value (NP)

Table 11: Tabulated results of the multiple linear regression models of rockfall characteristics with Topographic Environmental GIS Proxies (TEGP).

	Correlation	**R^2**	**RMSE**
LA	n_{all}	26%	0.59m
	$n_{Clarens}$	0.01%	1.37m
	$n_{Molteno}$	5.50%	0.48m
PA	n_{all}	30%	0.53m
	$n_{Clarens}$	0.00%	1.33m
	$n_{Molteno}$	5.90%	0.25m
Bearing of LA	n_{all}	0.10%	132.58°
	$n_{Clarens}$	27%	123.76°
	$n_{Molteno}$	0.30%	120.83°
Circumference	n_{all}	26%	1.55m
	$n_{Clarens}$	2.10%	3.94m
	$n_{Molteno}$	6.20%	1.14m
Area	n_{all}	12%	1.82m
	$n_{Clarens}$	0.61%	4.81m
	$n_{Molteno}$	11%	0.41m

Validation sample size:

$n_{All} = 136$; $n_{Clarens} = 15$; $n_{Molteno} = 29$

Table 12: Tabulated results of the multiple regression models applied to the validation dataset using the predict function in R.

6.1. LA multiple linear regression model results

The results of the multiple linear regression model for the rockfall characteristic LA shows that for the entire calibration sample (n_{All}), TEGP of aspect, curvature, plan, slope, elevation, band 1, band 2, and band 3 are highly significant in describing 34% (adjusted R^2) of the variation in the LA, however, the validation of this model using the independent validation dataset shows that only 26% of the variation was described by this model. The results of the LA multiple linear regression model for the Clarens Fm. sample ($n_{Clarens}$) shows that TEGP of band 2 and band 3 are highly significant in describing 62% (adjusted R^2) of the variation in the longest axis, however, the validation of this model using the independent validation dataset shows that only 0.01% of the variation was described by this model. The results of the LA multiple linear regression model for the Elliot Fm. sample (n_{Elliot}) shows that TEGP could not be used to describe the rockfall characteristic LA. The results of the LA multiple linear regression model for the Molteno Fm. sample ($n_{Molteno}$) shows that TEGP band 1 and band 3 are highly significant in describing 10.3% (adjusted R^2) of the variation in the longest axis, however, the validation of this model using the independent validation dataset shows that only 5.5% of the variation was described by this model.

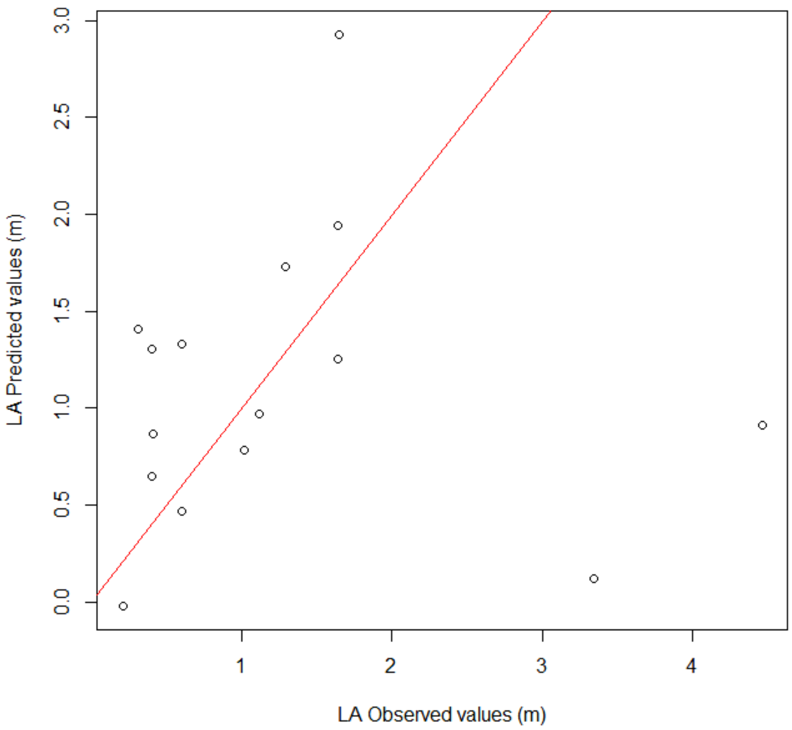

Figure 49: Plot of the $n_{Clarens}$ showing correlation between LA predicted values vs. LA validated values (i.e. observed values). The plotted red line represents the normal distribution of the regression.

The overall results of the multiple linear regression models show that the rockfall characteristic LA at the Clarens and Molteno ground-truthed sites can be modelled using independent TEGP, albeit to a very low extent. In summary, the TEGP produce a validated accuracy of 0.01% and 5.5% for the rockfall characteristic LA at the Clarens and Molteno Fm. ground-truthed sites respectively. The TEGP could not model the rockfall characteristic LA for the Elliot Fm. ground-truthed site. The $n_{Clarens}$ multiple linear regression model was rejected due to its poor validation accuracy.

6.2. PA multiple linear regression model results

The results of the multiple linear regression model for the rockfall characteristic PA show that for the entire calibration sample (n_{All}), TEGP of aspect, curvature, plan, slope, elevation , band 2, and band 3 are highly significant in describing 27% (adjusted R^2) of the variation in the PA, however, the validation of this model using the independent validation dataset shows that only 30% of the variation was described by this model. The results of the PA multiple linear regression model for the Clarens Fm. sample ($n_{Clarens}$) shows that TEGP of curvature, plan, band 1, band 2, and band 3 are highly significant in describing 46% (adjusted R^2) of the variation in the PA, however, the validation of this model using the independent validation dataset shows that 0% of the variation was described by this model. The results of the PA multiple linear regression model for the Elliot Fm. sample (n_{Elliot}) shows that TEGP could not be used to describe the rockfall characteristic PA. The results of the PA multiple linear regression model for the Molteno sample ($n_{Molteno}$) shows that TEGP of curvature and band 1 are significant in describing 5.8% (adjusted R^2) of the variation in the PA, however, the validation of this model using the independent validation dataset shows that only 5.9% of the variation was described by this model.

The overall results of the multiple linear regression models show that the rockfall characteristic PA for the Clarens and Molteno Fm. ground-truthed site can be modelled using independent TEGP, albeit to a very limited extent. In summary, the TEGP produce a validated accuracy of 0%, and 5.9% for the rockfall characteristic PA of the Clarens and Molteno Fm. ground-truthed sites respectively. The TEGP could not model the rockfall characteristic PA for the Elliot Fm. ground-truthed site. The $n_{Clarens}$ multiple linear regression model was rejected due to its poor validation accuracy.

6.3. Bearing of LA multiple linear regression model results

The results of the multiple linear regression model for the rockfall characteristic LA of bearing shows that for the entire calibration sample (n_{All}), TEGP of aspect, curvature, plan, roughness, elevation, total curvature, band 1 and band 3 are highly significant in describing 8% (adjusted R^2) of the variation in the bearing of LA, however, the validation of this model using the independent validation dataset shows that only 0.1% of the variation was described by this model. The results of the bearing of LA multiple linear regression model for the Clarens Fm. sample ($n_{Clarens}$) shows that TEGP of aspect, band 2 and band 3 were not significant in describing 7.9% (adjusted R^2) of the variation in the bearing of LA. The results for the bearing of LA multiple linear regression model for the Elliot Fm. sample (n_{Elliot}) shows that remote sensing variable band 1 was not significant in describing 0.9% of the rockfall characteristic bearing of LA. The results of the bearing of LA multiple linear regression model for the Molteno Fm. sample ($n_{Molteno}$) shows that TEGP of aspect, and curvature were highly significant in describing 11% (adjusted R^2) of the variation in the bearing of LA, however, the validation of this model using the independent validation dataset shows that 30% of the variation was described by this model.

The overall results of the multiple linear regression models show that the rockfall characteristic bearing of LA at the Clarens and Molteno Fm. ground-truthed sites can be modelled using independent TEGP, albeit to a very limited extent. In summary, the TEGP produce a validated accuracy of 27% and 0.3% for the rockfall characteristic bearing of LA at the Clarens and Molteno Fm. ground-truthed sites respectively. The TEGP could not model the rockfall characteristic bearing of LA for the Elliot Fm. ground-truthed site. The

$n_{Molteno}$ multiple linear regression model was rejected due to its poor validation accuracy.

6.4. Circumference multiple linear regression model results

The results of the multiple linear regression model for the rockfall characteristic circumference shows that for the entire calibration sample (n_{All}), the TEGP of aspect, curvature, plan, slope, elevation, band 1, band 2 and band 3 are highly significant in describing 31% (adjusted R^2) of the variation in the circumference, however, the validation of this model using the independent validation dataset shows that only 26% of the variation was described by this model. The results of the circumference multiple linear regression model for the Clarens Fm. sample ($n_{Clarens}$) shows that TEGP of band 2 and band 3 are highly significant in describing 60% (adjusted R^2) of the variation in the circumference, however, the validation of this model using the independent validation dataset shows that only 2.1% of the variation was described by this model. The results of the circumference multiple linear regression model for the Elliot Fm. sample (n_{Elliot}) shows that TEGP of band 1 and band 3 could not produce a significant result for describing the rockfall characteristic circumference. The results of the circumference multiple linear regression model for the Molteno Fm. sample ($n_{Molteno}$) shows that TEGP of band 1 and band 3 are highly significant in describing 9% (adjusted R^2) of the variation in the circumference, however, the validation of this model using the independent validation dataset shows that only 6.2% of the variation was described by this model.

The overall results of the multiple linear regression models show that the rockfall characteristic circumference at the Clarens and Molteno Fm. ground-truthed sites can be modelled using independent TEGP, albeit to a very low extent. In summary, the TEGP produce a validated accuracy of 2.1% and 6.2% for the rockfall characteristic circumference at the Clarens and Molteno Fm. ground-truthed sites respectively. The TEGP could not model the rockfall characteristic circumference for the Elliot Fm. ground-truthed site.

6.5. Area multiple linear regression model results

The results of the multiple linear regression model for the rockfall characteristic area shows that for the entire calibration sample (n_{All}), the TEGP of slope, elevation, band 1, band 2 and band 3 are highly significant in describing 16% (adjusted R^2) of the variation in the area, however, the validation of this model using the independent validation dataset shows that only 12% of the variation was described by this model. The results of the area multiple linear regression model for the Clarens Fm. sample ($n_{Clarens}$) shows that TEGP band 2 and band 3 are highly significant in describing 39% (adjusted R^2) of the variation in the area, however, the validation of this model using the independent validation dataset shows that only 0.6% of the variation was described by this model. The results of the area multiple linear regression model for the Elliot Fm. sample (n_{Elliot}) shows that TEGP could not be used to describe the rockfall characteristic area. The results of the area multiple linear regression model for the Molteno Fm. sample ($n_{Molteno}$) shows that TEGP band 1 and band 3 are highly significant in describing 98% (adjusted R^2) of the variation in the area, however, the validation of this model using the independent validation dataset shows that only 11% of the variation was described by this model.

The overall results of the multiple linear regression models show that the rockfall characteristic area at the Clarens and Molteno Fm. ground-truthed site can be modelled using independent TEGP, albeit to a very limited extent. In summary, the TEGP produce a validated accuracy of 0.61% and 11% for the rockfall characteristic bearing of LA at the Clarens and Molteno Fm. ground-truthed sites respectively. The TEGP could not model the rockfall characteristic area for the Elliot Fm. ground-truthed site. The $n_{Clarens}$ multiple linear regression model was rejected due to its poor validation accuracy.

6.6. Discussion: Multiple linear regression models

The multiple linear regression models for the rockfall characteristics LA, PA, bearing of LA, circumference, and area, produced low accuracies. The models show that rockfall characteristics can be modelled using independent TEGP, however, these models are not ideal for characterising rockfall from the imagery used. The major limitation with the multiple linear regression models is likely due to the difference in resolution or scale between the ground-truthed rockfall measurements and the independent TEGP used. The extent of difference between the resolution or scale of the independent variables and ground-truthed rockfalls appears to be too high, hence the poor validation results. The PA multiple linear regression model produced the most accurate result for characterising a rockfall characteristic for the entire calibration sample (nAll). The bearing of LA multiple linear regression model produced the most accurate result for characterising a rockfall characteristic for the Clarens Fm. calibration sample ($n_{Clarens}$). The area multiple linear regression model produced the most accurate result for characterising a rockfall characteristic for the Molteno Fm. calibration sample ($n_{Molteno}$). Future linear regression modelling using TEGP's derived from a higher resolution DEM could possibly yield better results.

Chapter 7 - Object-oriented approach for mapping rockfalls in the GGHNP

The OBIA approach was used to classify Clarens and Molteno Fm. rockfalls in the study area. The maximum circumference measurements for the Clarens and Molteno Fm. rockfalls in the calibration sample of the calval were used as threshold values in the OBIA. The OBIA of Elliot Fm. rockfalls was excluded as the results for the multiple linear regression models showed no significance for characterising Elliot Fm. rockfalls from TEGP. In addition to this, the box plots for the Elliot ground-truthed sample showed that all the mean values for the Elliot Fm. rockfall measurements fell well below the threshold value for the spatial resolution of the aerial imagery. The physical reason that rockfalls originating from the Elliot Formation sandstone are not discernible in the aerial imagery is likely attributable to the fact that this Formation breaks down easily with mudstones and siltstones to weather down rapidly to a poor soil (Groenewald, 1986). In contrast, the light coloured Clarens and Molteno Formation sandstones are more detectable in the aerial imagery as they form larger more resilient rockfalls.

7.1. OBIA of rockfalls

Figure 50 shows the flow diagram for the OBIA and validation approach used for classifying Clarens and Molteno Fm. rockfalls. The extents of the sampling grids for the Clarens and Molteno Fm. ground-truthed sites were used to create subsets of the mosaicked aerial imagery (Figure 51). The subsets were created to test and develop the OBIA rulesets for deriving rockfalls. The OBIA was performed using the software package, “eCognition Developer 8”.

7.1.1. Multi-resolution segmentation

Segmentation of the imagery is the first and main step in an OBIA and affects the overall success of the classification to a large extent (Burnett & Blaschke, 2003). The heterogeneity criterion of the imagery is thresholded by choosing a scale factor and by fixing the weights of the RGB image bands, and adjusting the shape and compactness factors. One of the main limitations observed with the aerial imagery is homogeneity. The aerial imagery contains a red, green, and blue band only, which makes the segmentation of image objects by means of spectral diversity a challenge. In addition, the rockfalls in the aerial imagery share very similar spectral characteristics with other image features (e.g. bare soils, dirt roads, and built-up areas). Although multispectral imagery would have been advantageous in extracting image objects using spectral information, only a red, green, and blue band were available in the aerial imagery. The limited spectral resolution of the aerial imagery makes OBIA techniques ideal for identifying rockfalls based on other criterion. OBIA was chosen over traditional supervised and unsupervised pixel-based techniques as it mimics the human cognitive interpretation process and has the potential to identify meaningful geomorphic processes, such as landsliding, using criteria based on shape, colour, texture and context, and produces results that are verifiable and that can easily be converted to GIS data (Benz et al., 2004; Blaschke, 2010; Martha et al., 2012). Measurements from the ground-truthed rockfalls were used as threshold inputs in the segmentation step.

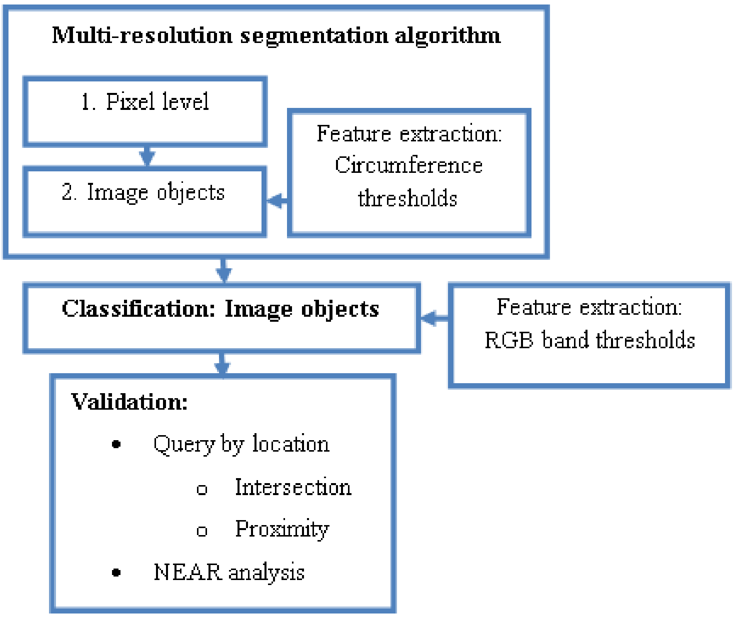

Figure 50: Flow diagram of OBIA and validation approach.

Figure 52 shows the results of the pixel level multi-resolution segmentation applied on the Clarens and Molteno subsets. The multi-resolution image segmentation algorithm was used to segment image pixels into image objects. eCognition's multi-resolution segmentation algorithm is a bottom up region-merging technique starting with one-pixel objects and through numerous subsequent steps, smaller image objects are merged into bigger ones (Benz et al., 2004). A scale parameter of 1 was used to segment the pixels into image objects. A scale parameter of 1 is the most sensitive for segmenting image objects. The default shape and compactness factors were used. The resulting image objects were made up of 1 to 2 pixels. The first segmentation or pixel level segmentation in the OBIA was necessary for creating image objects which could be refined with further segmentation. The lower the shape factor and compactness factor, the more sensitive the segmentation is to variations between pixel values (small image objects), and the larger the scale parameter, the more objects that can be fused and the larger the objects grow (Baatz and Schape, 1999). Segmentation can be subjective and in OBIA is usually a reiterative process that involves changing parameters until the best segmentation result is achieved. The ground-truthed measurements for the circumference of rockfalls were incorporated into a second multi-resolution segmentation in order to minimise the subjectivity of the scale parameter. In this instance, the geometry of ground-truthed rockfalls was used to contextualise image objects.

Figure 53 shows the results of the second multi-resolution segmentations applied on the Clarens and Molteno subsets. The circumference of measured rockfalls is similar to the border length of segmented image objects. Hence, the feature object ('border length') was used to refine image pixels into meaningful image objects by substituting the maximum circumference values for rockfalls in the calibration sample of the calval. The second multi-resolution segmentation allowed for the refinement of image objects produced during the first pixel level multi-resolution segmentation. For the refined multi-resolution segmentation, a scale parameter of 10 was used. Shape and compactness factors were left on their default setting of 0.1 and 0.5 respectively. The threshold conditions were defined as:

- For the Clarens subset, create image objects which have a border length that is less than or equal to 15.14 m (~30 pixels).
- For the Molteno subset, create image objects which have a border length that is less than or equal to 7.32 m (~15 pixels).

Figure 54 shows the areas of the mosaicked aerial image that were constrained for segmentation using a buffer layer based on the Clarens and Molteno Fm. sandstone lithologies. The segmentation of the mosaicked aerial image was constrained to a 500 m radius around the Clarens and Molteno Fm. lithologies. The buffer was derived using the 1:250,000 geological vector layer for the study area. The reason for constraining segmentation to a 500 m buffer was that potential rockfall depositing areas had to be defined in the mosaicked aerial imagery. One would expect Clarens and Molteno Fm. rockfalls to occur within a certain proximity to their respective lithologies or rockfall source areas. This was also done to avoid segmentation of areas that were not likely to contain Clarens and Molteno Fm. rockfalls.

Areas where the Molteno Fm. buffer overlapped with the Clarens Fm. buffer were subtracted using the GIS tool ERASE. The GIS tool ERASE creates a feature class by overlaying the Input Features with the polygons of the Erase Features and only those portions of the input features falling outside the erase features beyond boundaries are copied to the output feature class (ESRI, 2011).

7.1.2. Rockfall feature extraction and classification

Before proceeding with the classification of rockfalls, it was important to begin with defining a *rockfall*. When referring to rockfalls classified from the aerial imagery, it is of utmost importance to consider spatial resolution. Each pixel in the aerial imagery represents a 0.5 m by 0.5 m surface area. Figure 55 shows a schematic of the relationship between spatial resolution and rockfall image objects. It is incorrect to assume that each image object is representative of a single rockfall. In some instances the image object represents a single feature and in others a grouping or cluster of rockfalls.

This relationship can be understood through the Shannon sampling theorem (sometimes called Nyquist-Shannon sampling theorem), which states that an object should be in the order of one tenth of the dimension of the sampling scheme (the pixel) so as to ensure that it will be completely independent of its random position and its orientation, relative to the sampling scheme (Blaschke, 2010). Thus, the relationship between the spatial resolution of the image and the proximity and orientation of real world features plays a role in how they are represented as image objects. A classified rockfall derived through the OBIA can be representative of either a single rockfall or grouping (cluster) of rockfalls deposits.

Figure 56 shows the results of the OBIA for the Clarens and Molteno subsets. As already mentioned before, eCognition segments pixels into homogenous image objects. Once image objects are determined, image object information such as the mean and standard deviation of the spectral bands, shape, size, texture, and context become available. In eCognition, feature objects can be used to determine and define the upper and lower limits of a range of image object characteristics. Limits or thresholds can be defined and assigned to specific classes. This was done to define the Clarens and Molteno Fm. rockfall classes.

The feature objects' border length (i.e. length of the image object in pixels), mean red (i.e. average of red spectral pixel values for the image object), mean green, and mean blue were used to extract rockfalls from the subsets. Border length was thresholded using the maximum circumference values for rockfalls in the calibration sample of the calval. The thresholds for the mean red, mean green, and mean blue were determined by averaging the mean spectral values of image objects identified as rockfalls. The aerial imagery is not a multispectral image in the sense of satellite imagery, however as the aerial imagery is an RGB image, the mean red, mean green and mean blue could be ascertained. These mean pixel values were calculated to help further distinguish image objects identified as rockfall. In order to identify segmented image objects which might represent rockfalls, the digitised bounding containers vector was overlayed with the aerial image subsets and segmented image objects (Figure 57). The following thresholds were used to create the classification rulesets for classifying rockfalls in the Clarens and Molteno subsets:

- Clarens classification ruleset:
    - Classify image objects which have a border length that is less than or equal to 15.14 m as *Clarens rockfalls*.
    - Mean red ≥ 127, Mean green ≥ 131, Mean blue ≥ 136
- Molteno classification ruleset:
    - Classify image objects which have a border length that is less than or equal to 7.29 m as *Molteno rockfalls.*
    - Mean red ≥ 120, Mean green ≥ 122, Mean blue ≥ 130

The OBIA rulesets developed for the Clarens and Molteno subsets were then applied to the mosaicked aerial image of the study area so that classified Clarens and Molteno Fm. rockfalls could be derived. The Clarens and Molteno Fm. rockfalls were output as polygon and point features (i.e. centroids of the polygon features).

7.2. Validating the OBIA rockfall points

Using GIS query by attributes, Clarens rockfall points assigned the validation attribute within the calval, were selected. Then, using GIS query by location, Clarens rockfall points intersecting the Clarens rockfall polygons extracted from the OBIA were queried. Only 1 Clarens validation rockfall point out of 15 Clarens validation rockfall points intersected with 1 Clarens rockfall polygon extracted from the OBIA (Figure 58). This means that only 6.67 % of the Clarens validation rockfalls in the calval could be validated with Clarens rockfall polygons derived from the OBIA, assuming validation by intersecting ground-truthed rockfall points. The reasoning behind the Clarens validation rockfall points not intersecting with Clarens rockfall polygons derived from the OBIA may be attributable to a number of factors. The first consideration is the difference between the resolution of ground-truthed rockfalls and rockfalls classified in the aerial imagery. The second factor pertains to the orthorectification accuracy of the aerial imagery (i.e. 11 m to 1 m accuracy range for a 10.5 m DEM bias resulting from 20 m vectorised contours). These are factors which could likely cause misalignment between the ground-truthed rockfalls and rockfalls extracted from the aerial imagery during the OBIA. A further query by location was performed using a proximity factor. The mean LA value for rockfalls measured at the Clarens Fm. ground-truthed site was used to define the proximity factor. Figure 59 shows that 5 of the 9 Clarens rockfalls derived from the OBIA occur within 0.97 m of the Clarens validation rockfall points.

Using the same query by location procedure, 0 of 29 Molteno validation rockfall points could be validated by assuming intersection within Molteno rockfalls derived from the OBIA (Figure 60). Thus, 0% of Molteno rockfall polygons derived from the OBIA could be validated assuming validation by intersection. However, 9 of 15 Molteno rockfall polygons derived from the OBIA fall within 0.71 m (i.e. the mean LA value for rockfalls measured at the Molteno Fm. ground-truthed site) of the Molteno validation rockfall points (Figure 61). The same limitations experienced in validating the Clarens Fm. rockfalls would also apply to the Molteno Fm. rockfalls.

In order to provide a measure of the plainimetric accuracy between Clarens and Molteno Fm. rockfalls extracted from the OBIA, with Clarens and Molteno Fm. validation rockfall points, a NEAR ANALYSIS was performed. The NEAR ANALYSIS was performed using the points of the rockfalls extracted from the OBIA as the input features and the validation rockfall points as the near features. The NEAR ANALYSIS GIS tool determines the distance from each feature in the input features to the nearest feature in the near features (ESRI, 2011).

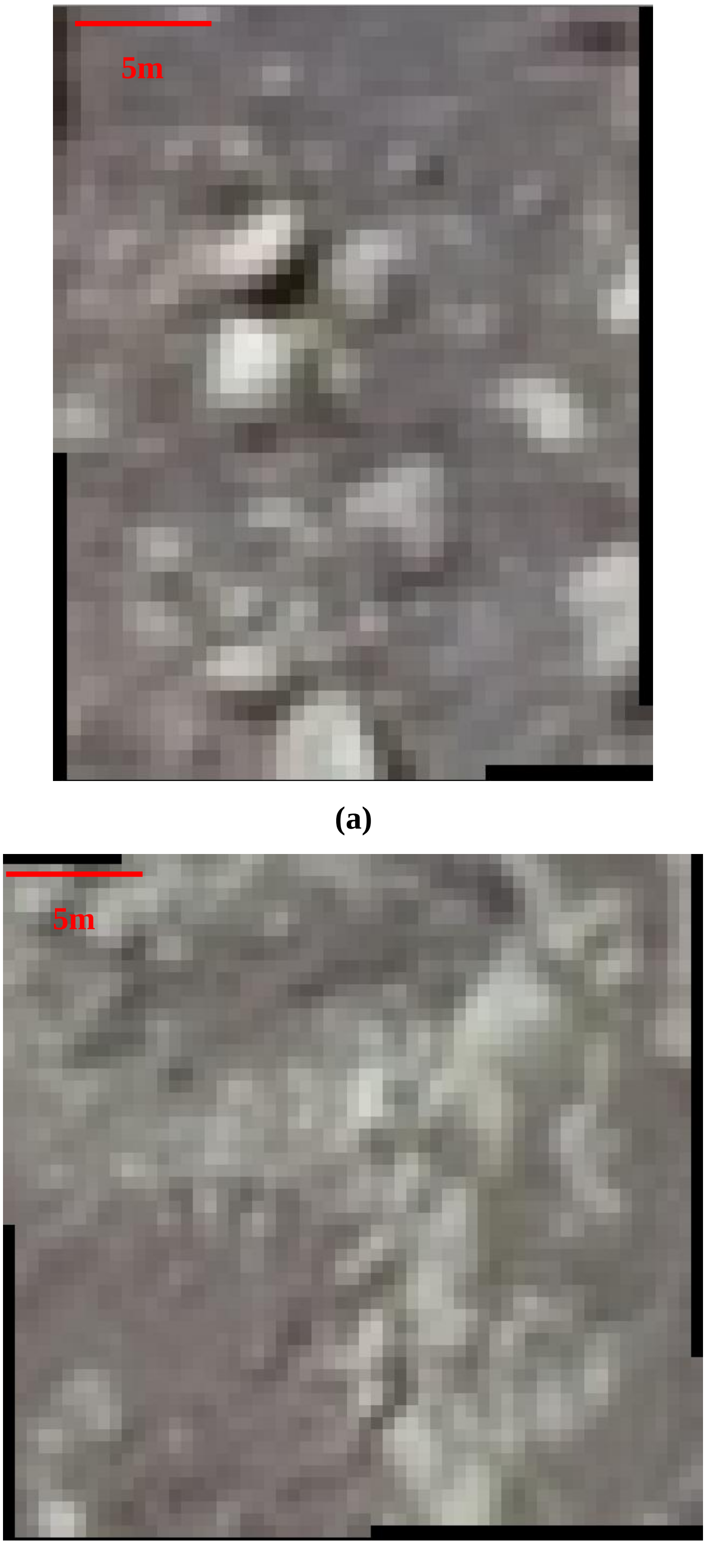

(a)

(b)

Figure 51: (a) Clarens subset and (b) Molteno subset.

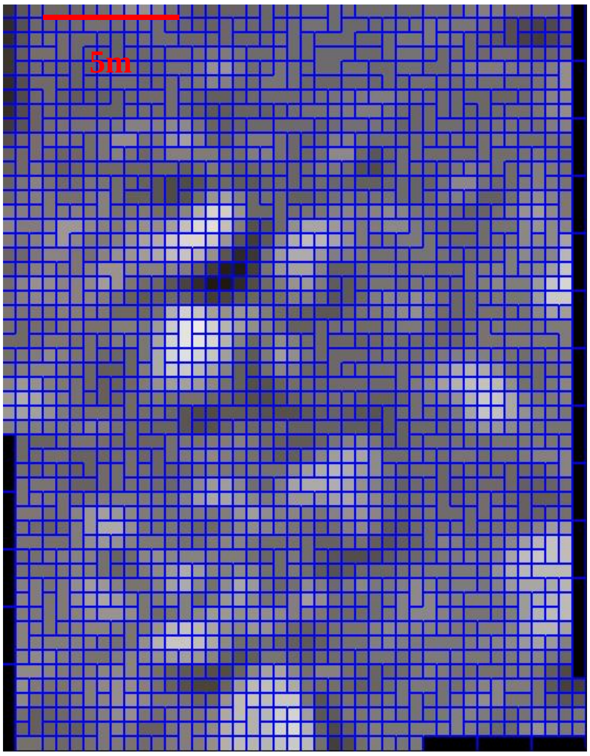

(a)

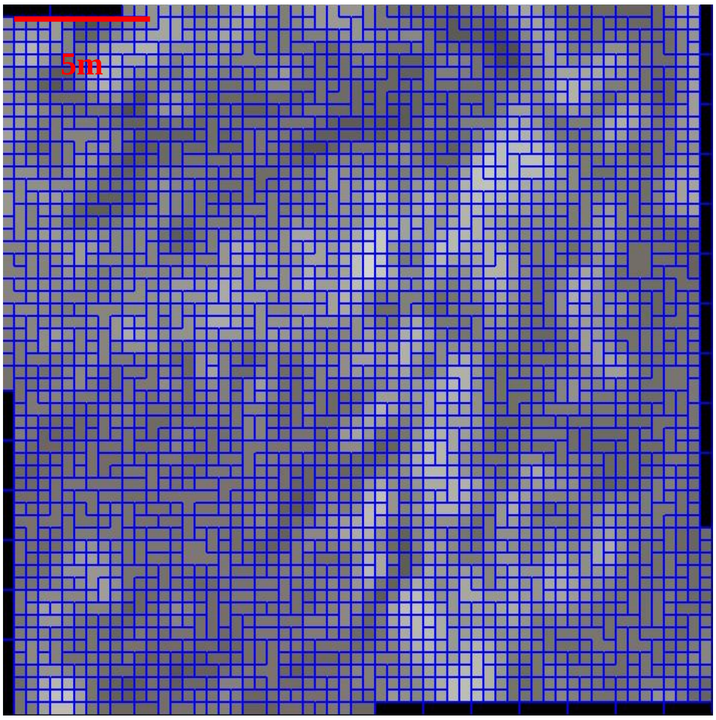

(b)

Figure 52: (a) Results of the initial multi-resolution segmentations for the Clarens subset and (b) Molteno subset.

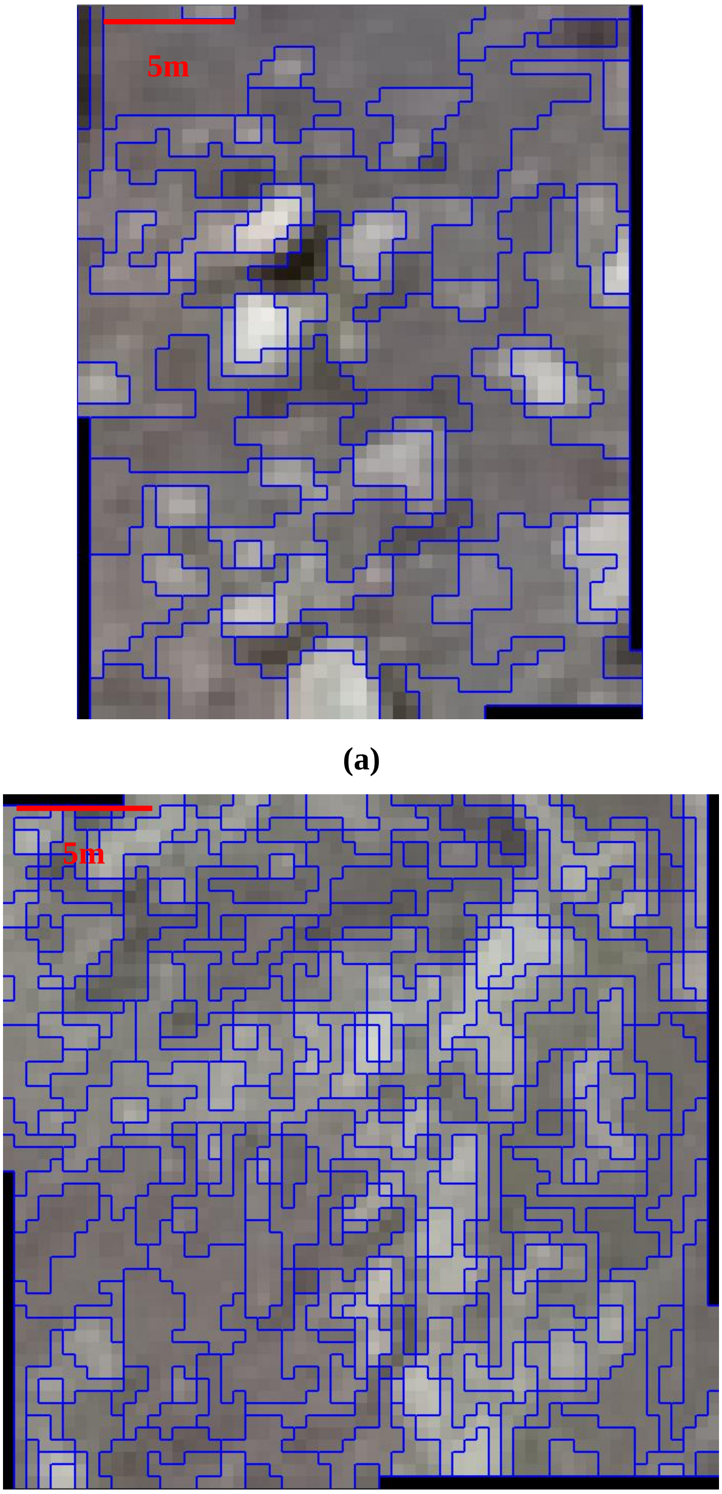

(a)

(b)

Figure 53: (a) Results of the second multi-resolution segmentations for the Clarens subset and (b) Molteno subset.

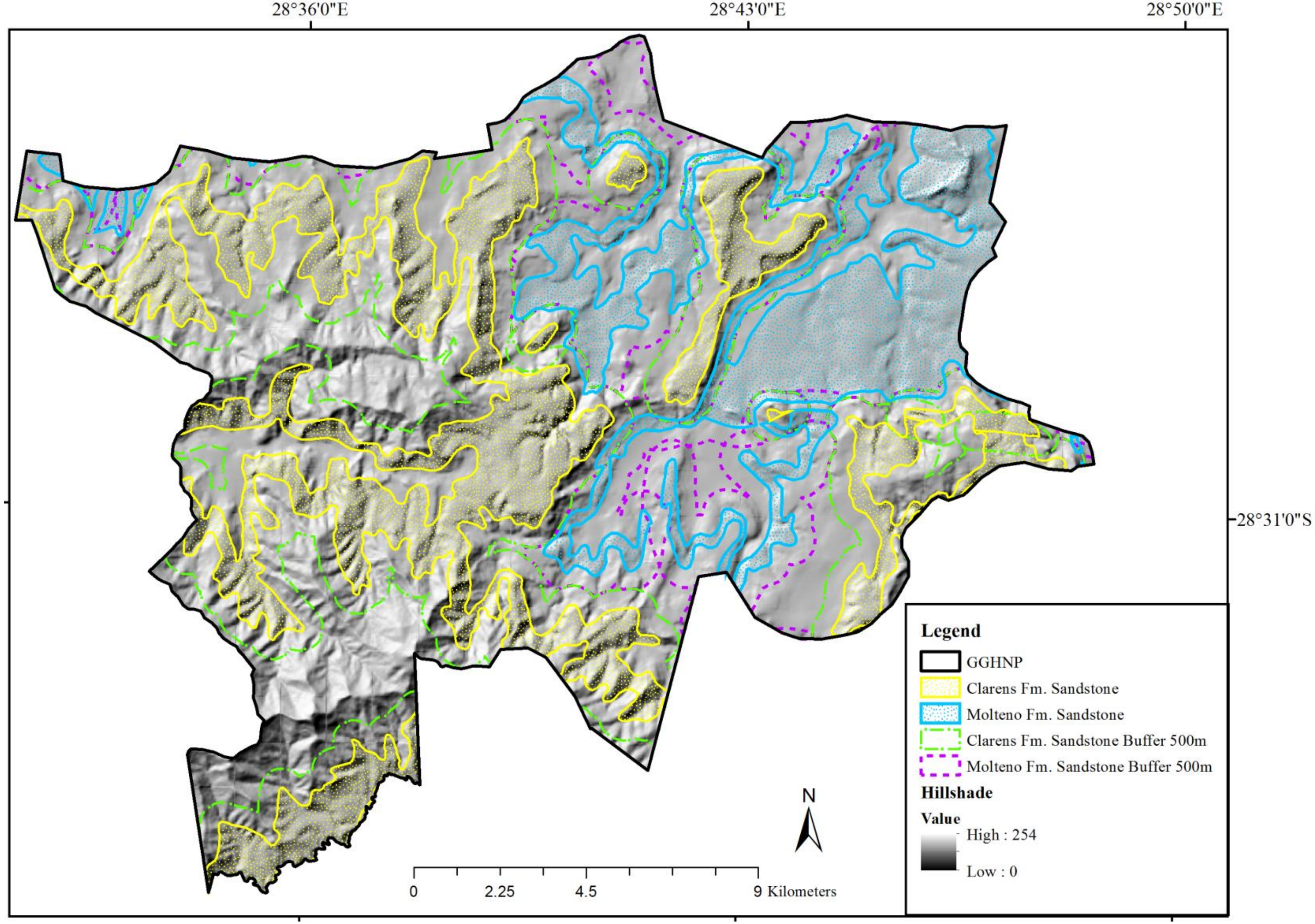

Figure 54: 500 m buffer areas defined for constraining the segmentation of Clarens and Molteno Fm. rockfalls.

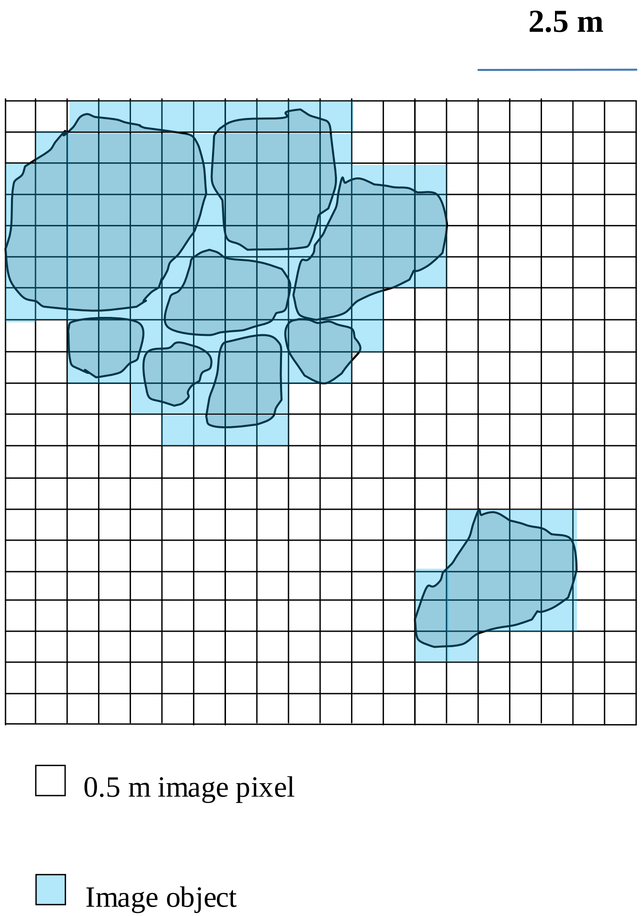

Figure 55: Schematic representation of the relationship between spatial resolution and rockfall image objects.

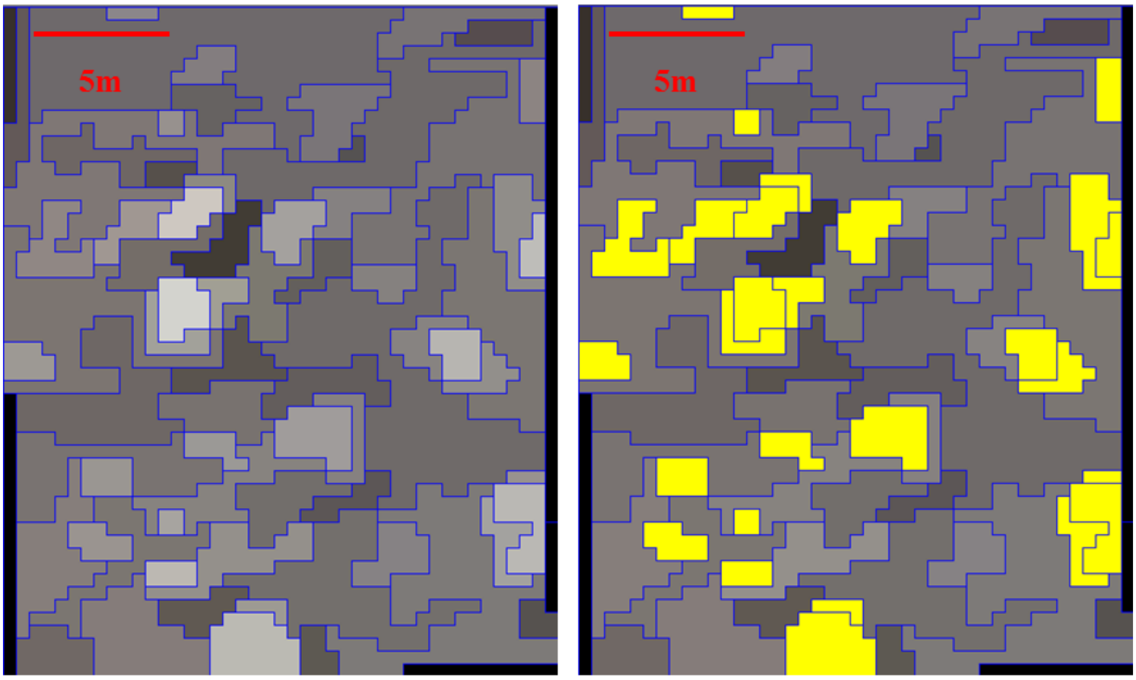

Mean feature view Classification

(a)

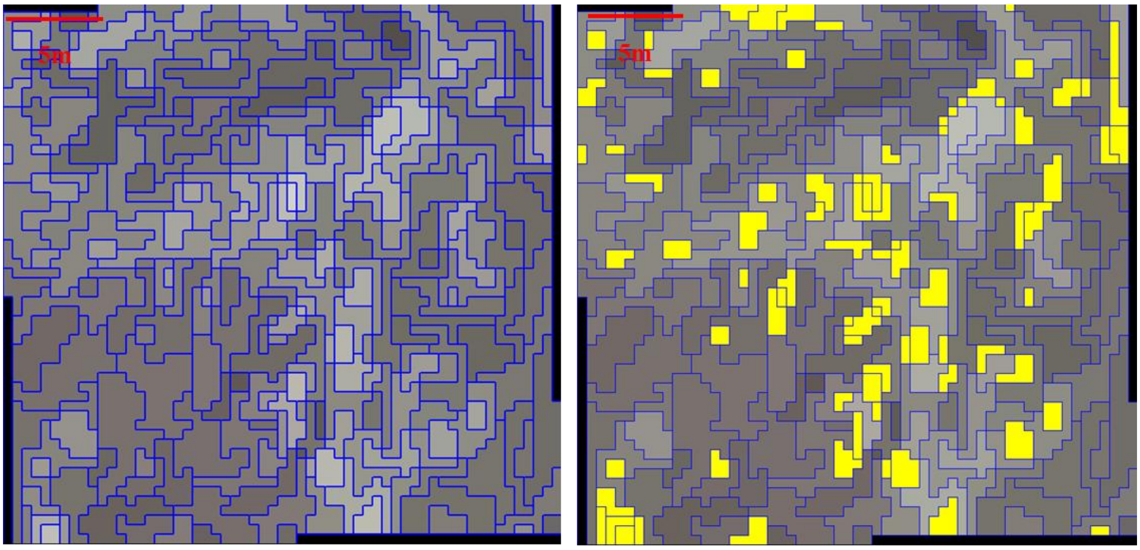

Mean feature view Classification

(b)

Figure 56: (a) Results of the OBIA classification for the Clarens subset and (b) Molteno subset.

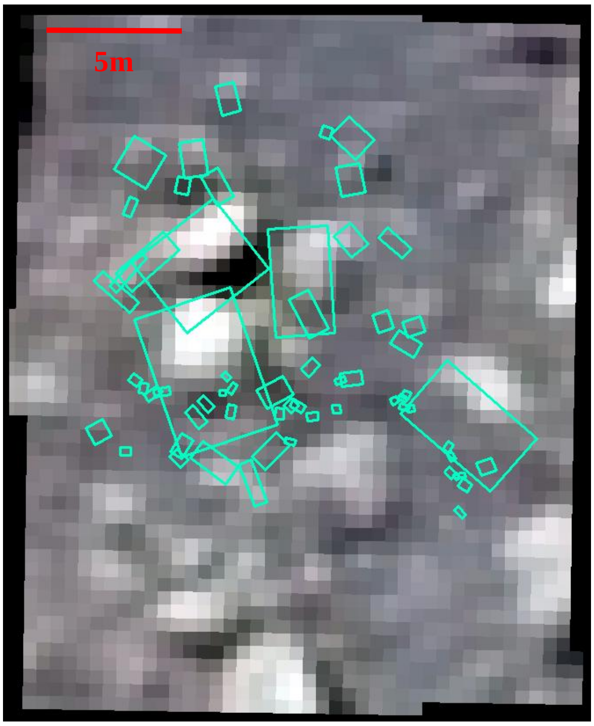

(a)

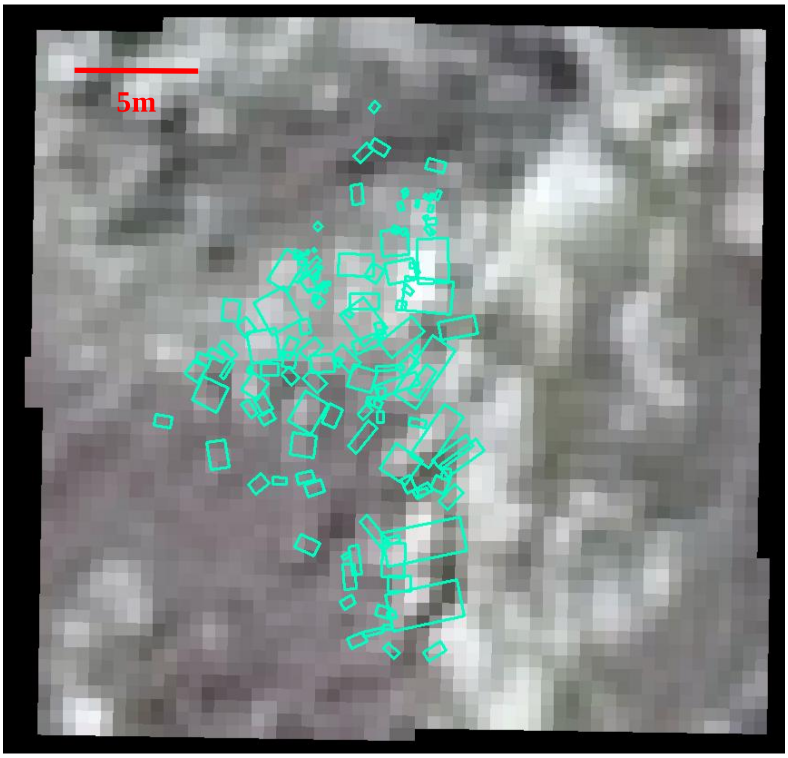

(b)

Figure 57: (a) Bounding containers overlayed on Clarens subset and (b) Molteno subset.

The results of the NEAR ANALYSIS for the Clarens Fm. ground-truthed site show that on average, the centroids for 11 Clarens rockfalls extracted from the OBIA fall within a distance of 2.11 m of the 62 Clarens validation rockfall points collected in the field. The nearest Clarens validation rockfall point fell within 0.84 m of Clarens rockfalls extracted from the OBIA, and the furthest within 4.96 m. Thus, the plainimetric accuracy between Clarens rockfalls extracted from the OBIA and Clarens validation rockfall points is on average 2.11 m and ranges between 0.84 m and 4.96 m. Using the horizontal and vertical extent of the Clarens Fm. ground-truthed site sampling grid (i.e. 15 m by 20 m) as a tolerance, the plainimetric accuracy falls within the tolerances of the sampling grid.

The results of the NEAR ANALYSIS for the Molteno Fm. ground-truthed site show that on average, the centroids for 30 Molteno rockfalls extracted from the OBIA fall within a distance of 1.32 m of the 141 Molteno validation rockfall points collected in the field. The nearest Molteno validation rockfall point fell within 0.13 m of Molteno rockfalls extracted from the OBIA, and the furthest within 7.21 m. Thus, the plainimetric accuracy between Molteno rockfalls extracted from the OBIA and Molteno validation rockfall points is on average 1.32 m and ranges between 0.13 m and 7.21 m. Using the horizontal and vertical extent of the Molteno Fm. ground-truthed site sampling grid (i.e. 15 m by 20 m) as a tolerance, the plainimetric accuracy falls within the tolerances of the sampling grid.

7.3. Filtering OBIA misclassification

The OBIA produced much misclassification between rockfalls and image objects with similar spectral and geometric characteristics. Misclassified features include Clarens and Molteno Fm. sandstone outcrops and ridgetops, built-up areas, tarred and dirt roads, and bare ground exposed in gullies and flat to near flat fields. In order to remove misclassified image objects, DEM derivatives, TPI and TRI, digitised vector layers, built up areas and tarred and dirt roads were used to filter out image objects falling within unlikely rockfall areas.

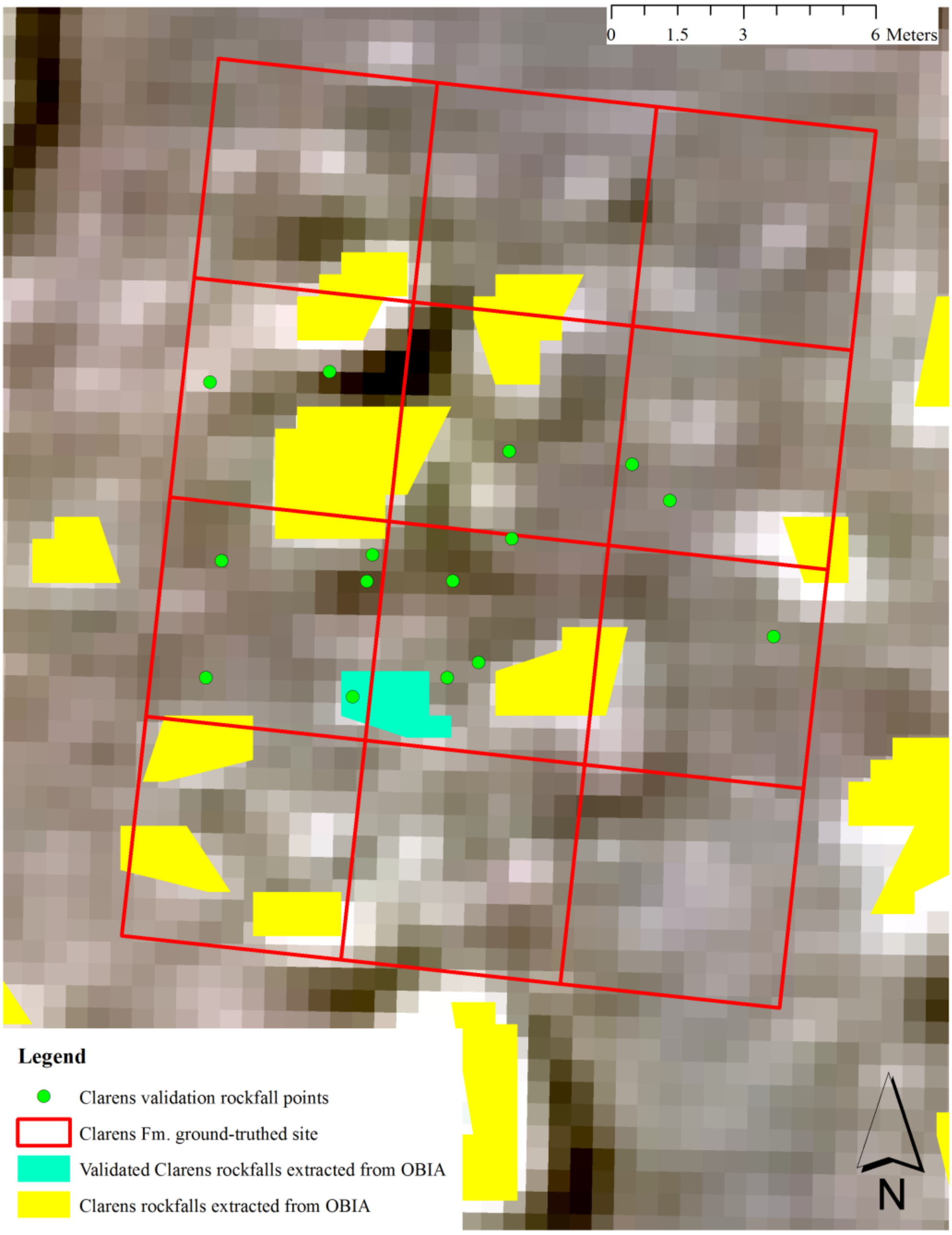

Figure 58: Clarens validation rockfall points intersecting with Clarens rockfalls extracted from the OBIA.

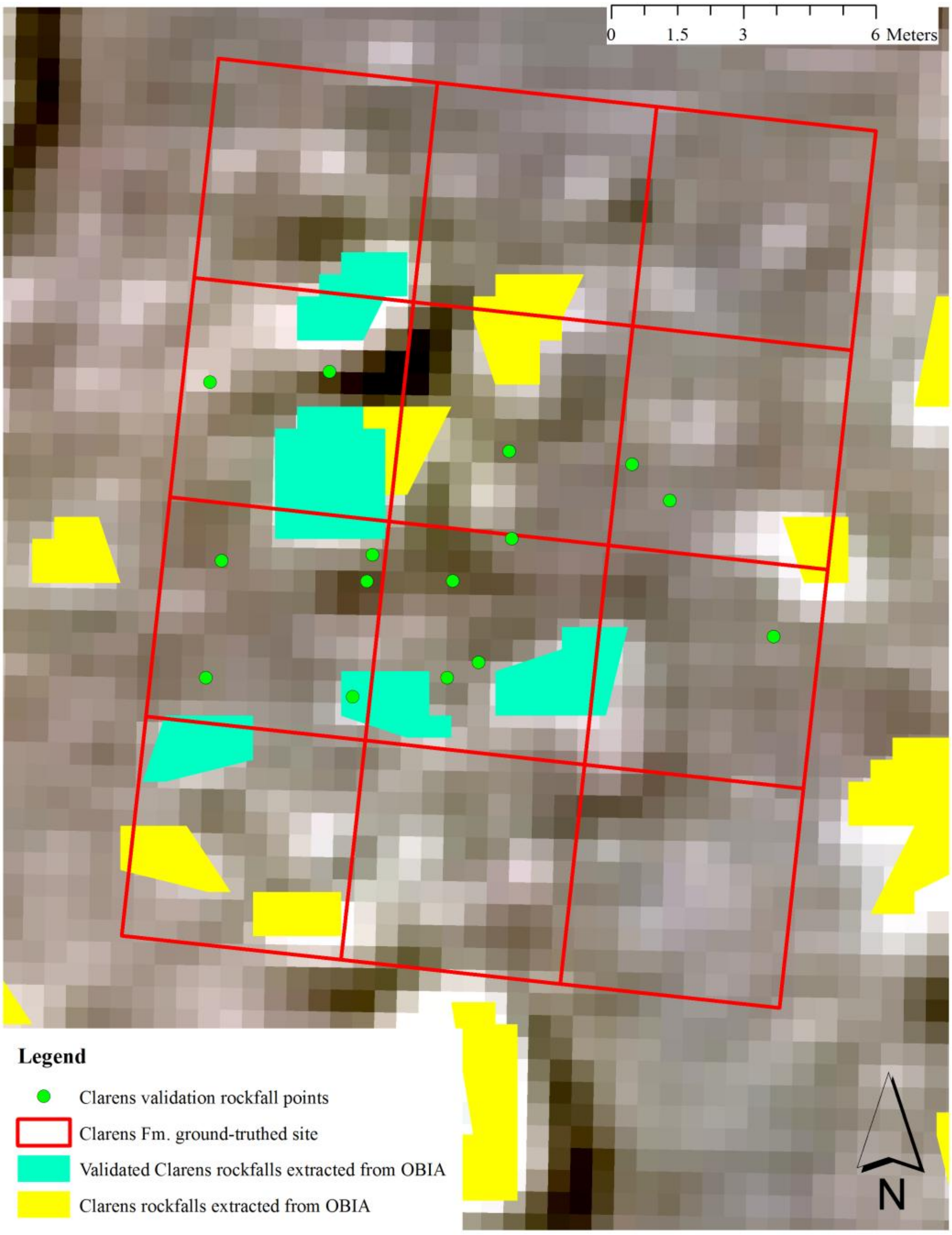

Figure 59: Clarens rockfalls extracted from the OBIA that fall within 0.97 m of Clarens validation rockfall points.

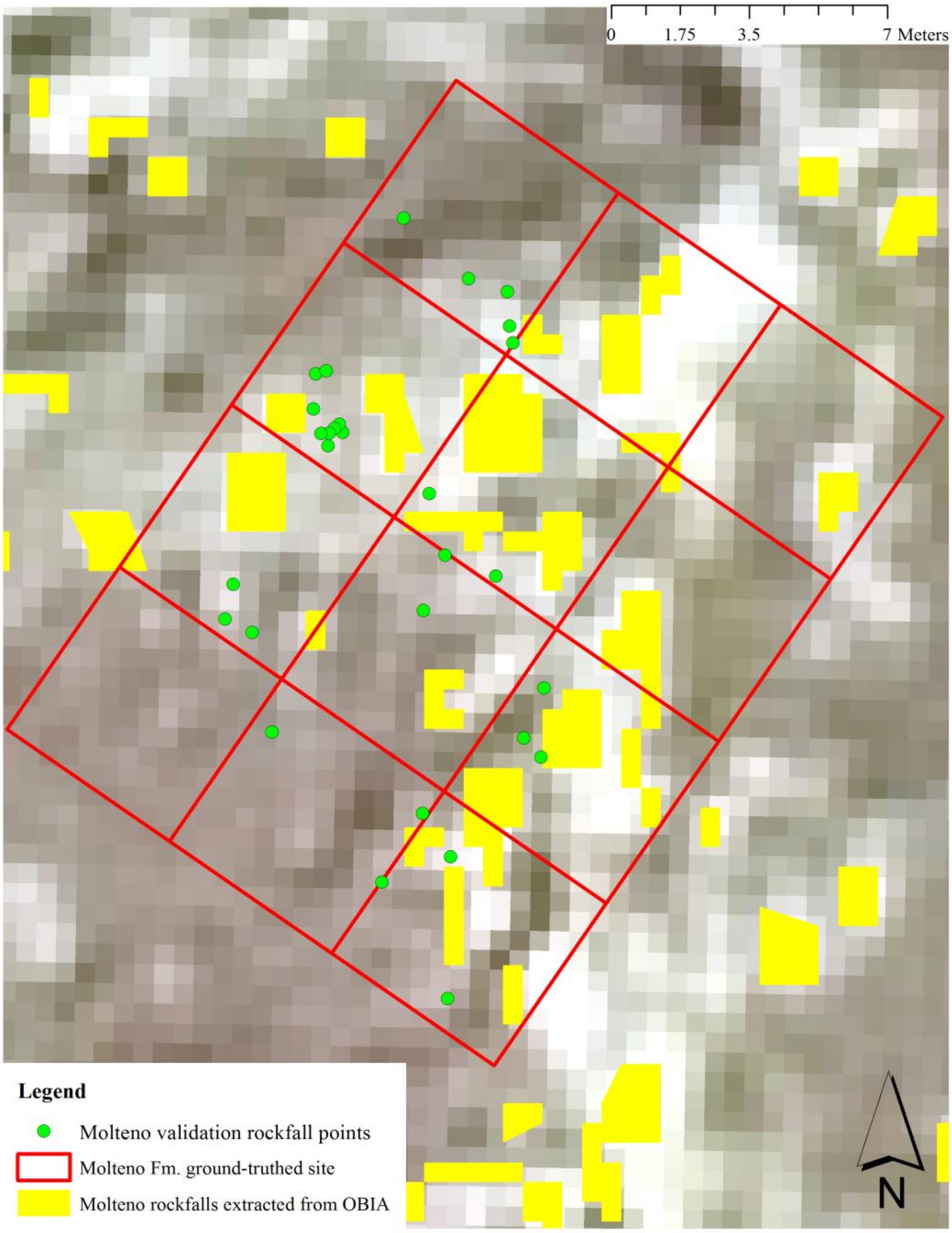

Figure 60: Molteno validation rockfall points intersecting with Molteno rockfalls extracted from the OBIA.

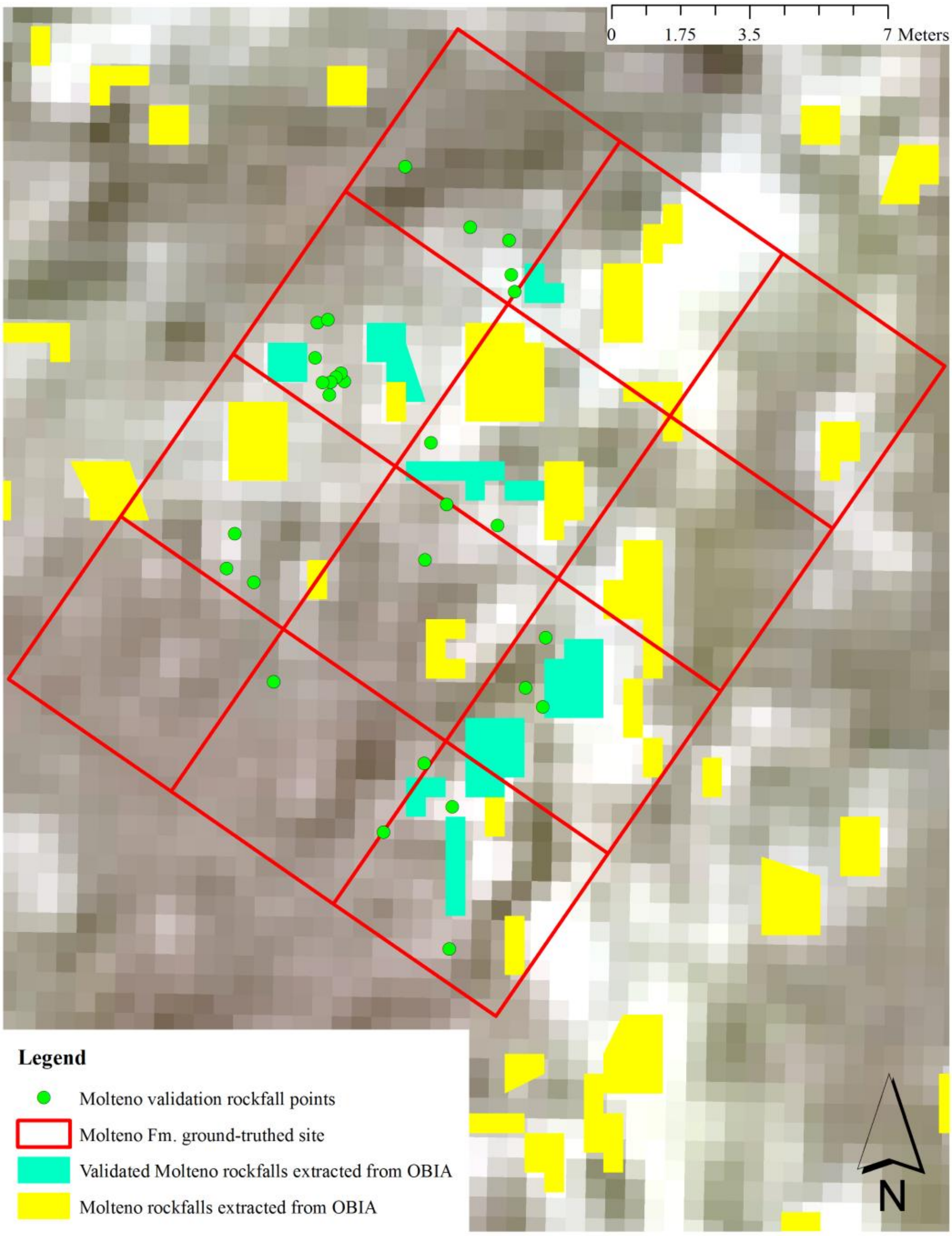

Figure 61: Molteno rockfalls extracted from the OBIA that fall within 0.71 m of the Molteno validation rockfall points.

The first filter used the GIS tool ERASE to remove misclassified rockfall points falling within the built-up areas, and tarred and dirt road polygon vector layers (Figure 15). The TPI was used to filter out misclassified image objects on ridgetops. The OBIA produced considerable misclassified image objects at ridgetops. The ridgetops represent the hilltops and cliff face of the terrain in the study area. Visual interpretation of the aerial imagery and field observations indicate rockfalls on the slopes adjacent to ridgetops. Hence, one would not expect to find rockfall deposition at ridgetops (interfluves). The ground-truthed rockfall sites confirm this, located on slopes adjacent to ridgetops. The TPI thematic layer was then vectorised to a polygon layer and the ridgetop polygon features were used to filter out misclassified image objects using the GIS function ERASE (Figure 62). The TRI was used to filter out misclassified image objects on flat to near flat terrain such as fields. The TRI was vectorised to a polygon feature and misclassified image objects falling within level and nearly level polygons were removed using the GIS function ERASE. Rockfalls are expected to occur within rockfall source areas which is characterised by rugged terrain (Figure 63). Visual interpretation of the mosaicked aerial imagery and the location of the ground-truthed sites within rugged terrain polygons confirm this.

7.4. Uni- and bi-variate statistical analyses of rockfalls with environmental variables.

Figure 64 presents the final results of the Clarens and Molteno Fm. rockfall points derived through the OBIA after filtering misclassified image objects with the TPI, TRI, digitised vector layers, built up areas, and tarred and dirt roads. A total of 419,518 Clarens Fm. rockfall points and 330,635 Molteno Fm. rockfall points were computed after filtering. The filtered Clarens and Molteno Fm. rockfall points contain some bias which stems from the OBIA.

They represent image objects which were defined as rockfalls in the OBIA using limited ground-truthed rockfall circumference measurements as a guide for thresholding the multi-resolution segmentation step. As such, the resulting rockfall points layer defines Clarens rockfalls which have a circumference that is less than or equal to 15.14 m (max. circumference value in calval), and Molteno rockfalls which have a circumference that is less than or equal to 7.29 m (max. circumference value in calval).

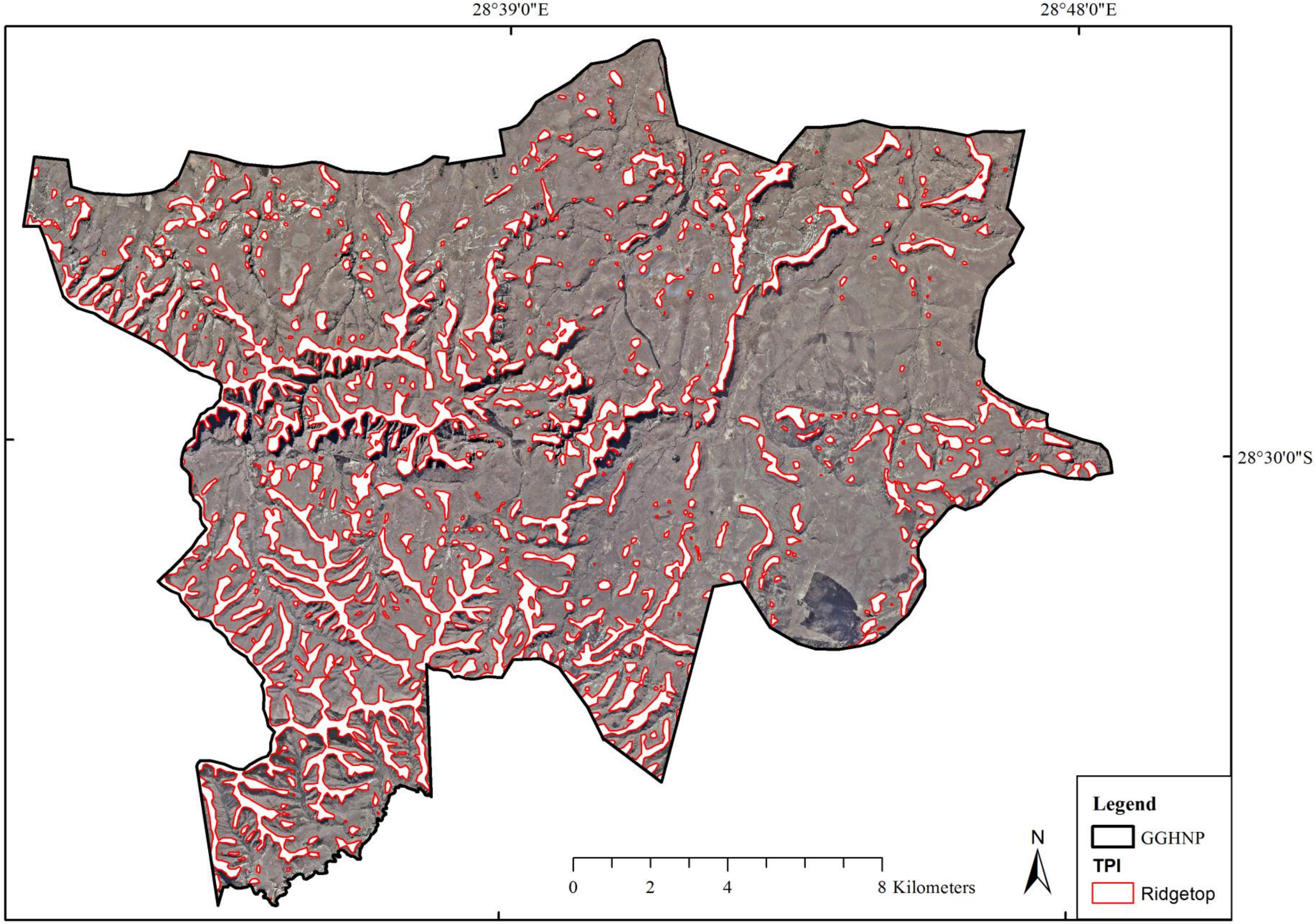

Figure 62: Ridgetop vector for the GGHNP.

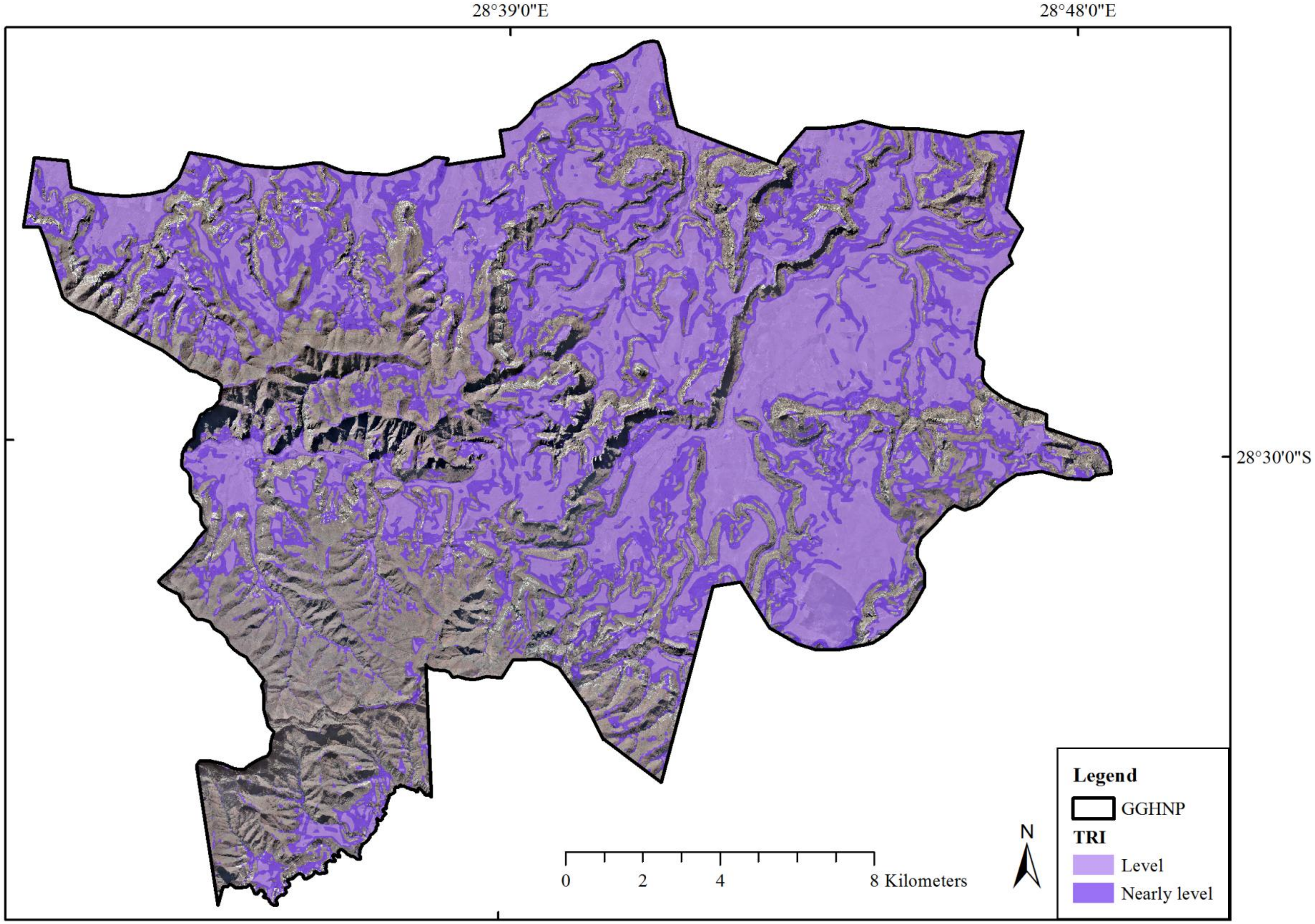

Figure 63: Level and nearly level vectors for the GGHNP.

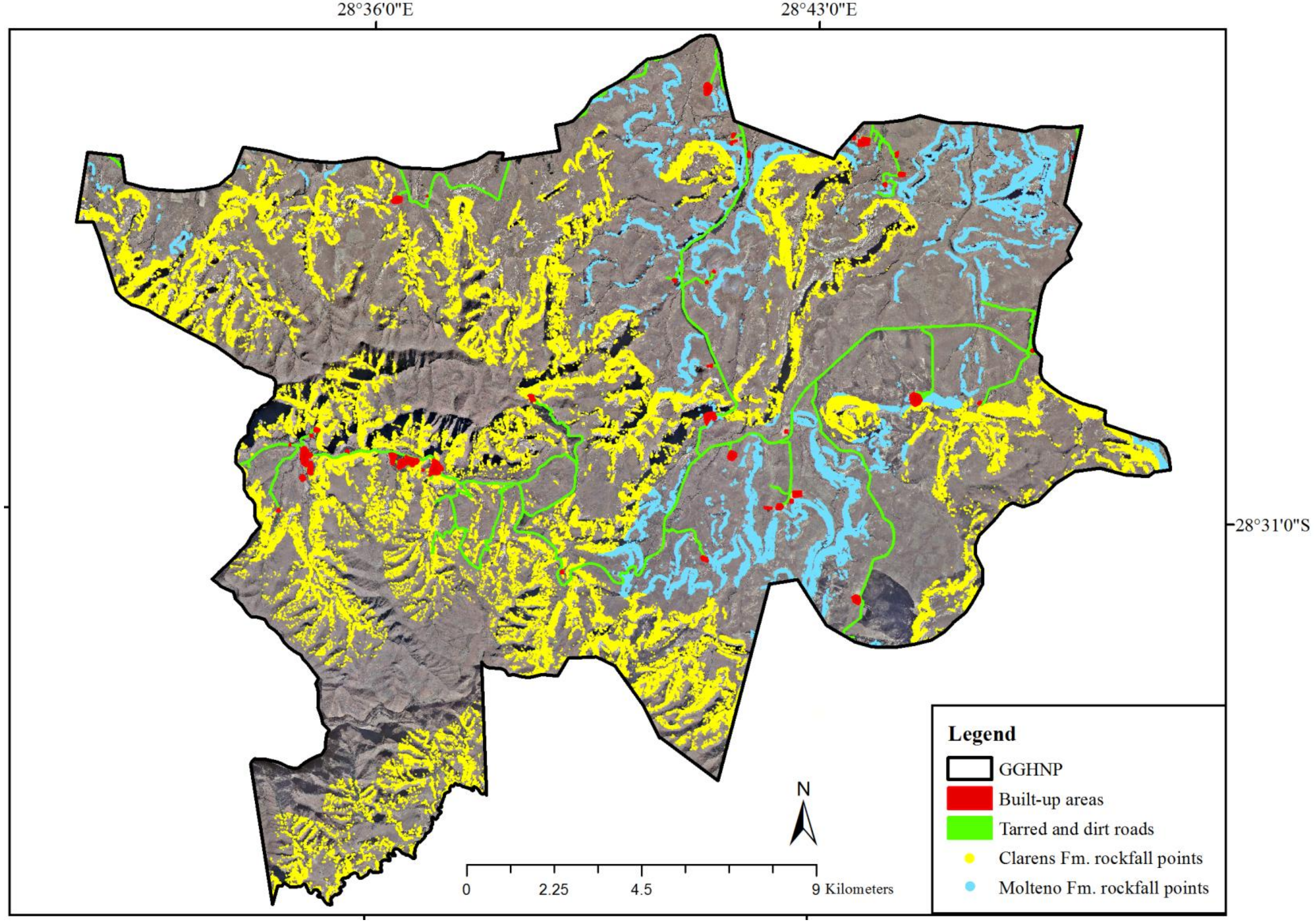

Figure 64: Results of the Clarens and Molteno Fm. rockfall points derived through the OBIA after filtering with the TPI, TRI, and digitised vector layers for built up areas and tarred and dirt roads.

Figure 65 shows the altitude frequency histogram for individual Clarens and Molteno Fm. rockfall points. The average altitude for 419,518 Clarens Fm. rockfall points and 330,635 Molteno Fm. rockfall points is 1,953.52 m a.s.l and 1,792.83 m a.s.l respectively. The Clarens Fm. rockfall points are distributed at higher altitudes in comparison to the Molteno Fm. rockfall points. This is expected as the Clarens Fm. is known to overlay the Elliot Fm., which has an upper contact with the Molteno Fm. Figure 66 shows the slope gradient frequency histogram for individual Clarens and Molteno Fm. rockfall points. The average slope gradient for 419,518 Clarens Fm. rockfall points and 330,635 Molteno Fm. rockfall points is 24.63° and 20.14° respectively. The majority of Clarens and Molteno Fm. rockfall points are distributed on slope gradients between 20° – 30°.

The following section describes the distribution of the Clarens and Molteno Fm. rockfall points derived through the OBIA, with univariate frequency histograms in relation to thematic classes defined for the environmental variables which include altitude, slope aspect, slope, slope unit, distance to lithology, and distance to drainage lines. In addition to this, ANN spatial pattern analysis of the Clarens and Molteno Fm. rockfall points is described for the whole study area and per thematic classes defined within the environmental variables. The frequency distribution and ANN spatial pattern analysis results are then compared to Hardwick's (2012) analyses of rock movement deposits in the Bushman's Nek region of the southern Drakensberg, and are also discussed within a global context to other rockfall studies.

7.4.1. Defining the distance to lithology and drainage lines

It was necessary to define the environmental variables for distance to lithology and drainage lines. Distance to lithology and drainage lines were not previously defined in section 4.3, as the results from the OBIA were required to establish which of the Fm. sandstones would be included for the frequency distribution and ANN spatial pattern analyses. The environmental variables distance to drainage lines and lithology were established by creating proximity bands of varying distance using the GIS BUFFER tool.

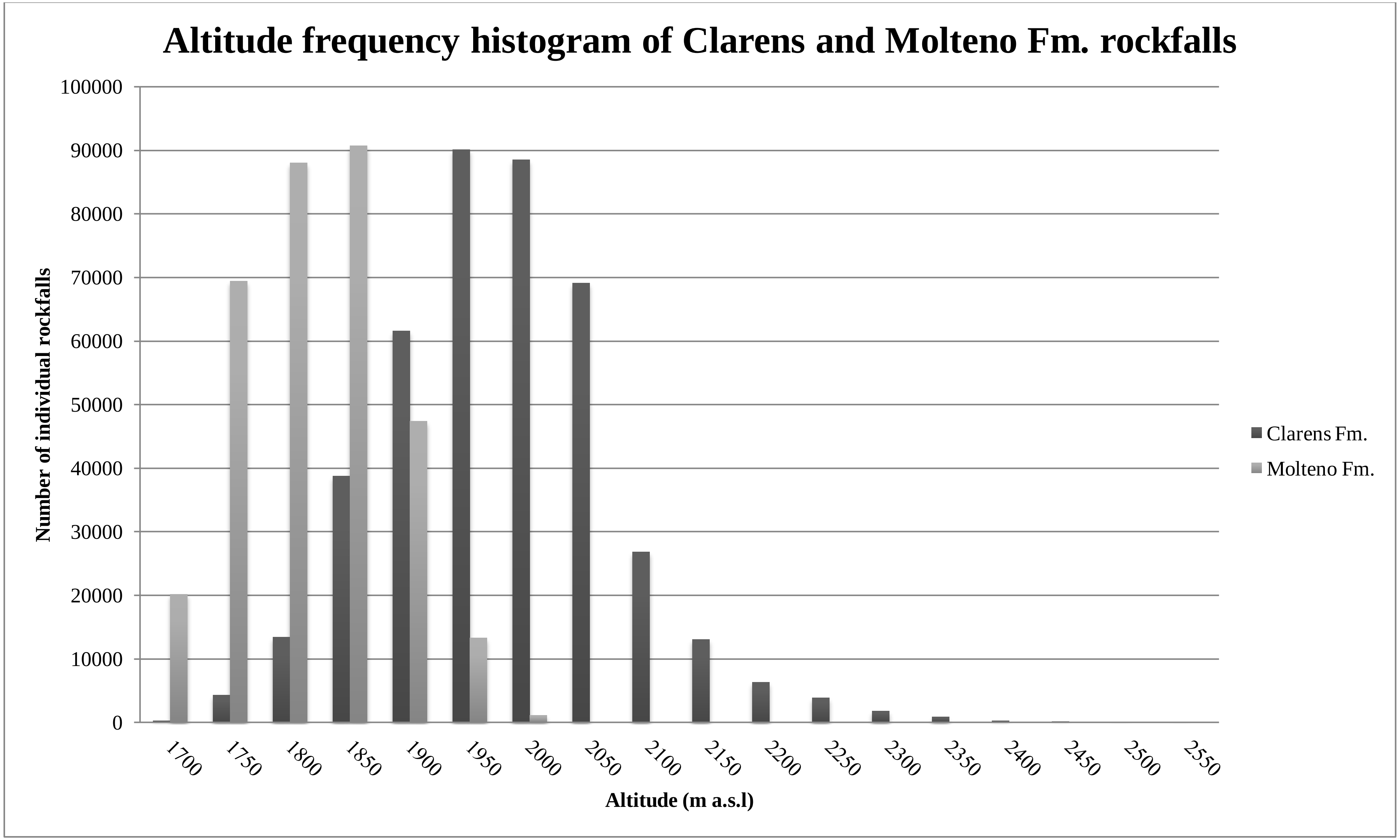

Figure 65: Altitude frequency histogram of Clarens and Molteno Fm. rockfall points.

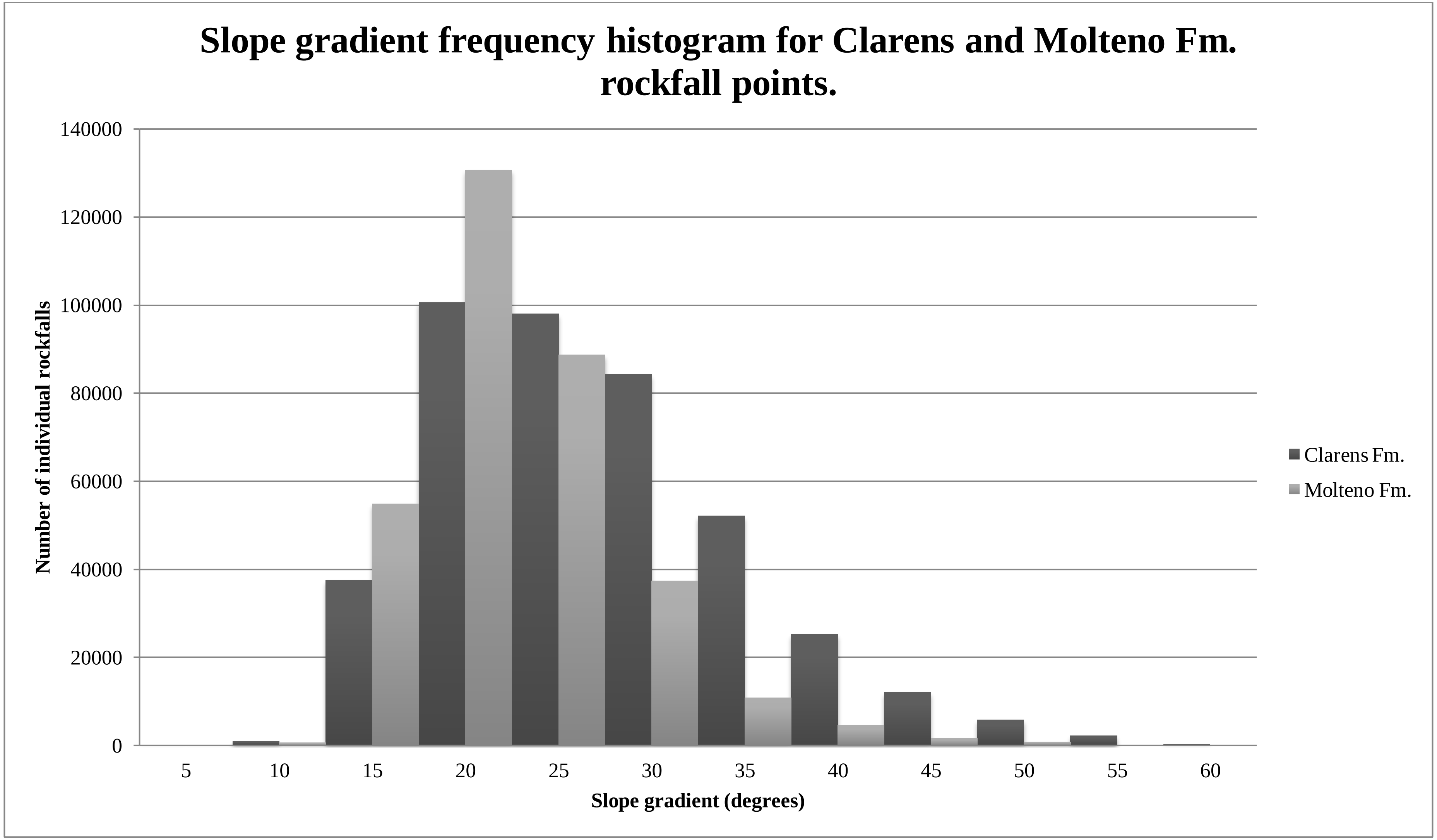

Figure 66: Slope gradient frequency histogram of Clarens and Molteno Fm. rockfall points.

The thematic classes for distance to drainage lines are defined as follows (Figure 67):

0 – 25 m
25 – 50 m
50 – 75 m
75 – 100 m
100 – 150 m
150 – 300 m
300 m >

Figure 68 and Figure 69 show the thematic classes for distance to Clarens and Molteno Fm. sandstone lithology, respectively. The environmental variable, distance to lithology is defined as the proximity of rockfalls points to Clarens/Molteno Fm. sandstone rock exposures. These rock exposures were taken from the 1:250,000 geological vector layer of the study area. In essence, the rock exposures are representative of rockfall source areas. The thematic classes for distance to lithology are defined as follows:

0 – 25 m
25 – 50 m
50 – 75 m
75 – 100 m
100 – 150 m
150 – 300 m
300 – 500 m

7.4.2. Frequency distribution, information value, average nearest neighbour and point density

Figures 70 and 71 show the frequency histograms for the environmental variables of the Clarens and Molteno Fm. rockfall points respectively. Frequency histograms of the environmental variables were created to show the frequency distribution of Clarens and Molteno Fm. rockfall points as a percentage of each thematic class. The frequency histograms were calculated by querying in ArcMap 10.1, the count of rockfall points (dependent variable) falling within each thematic class (independent environmental variable). The rockfall point count for each thematic class was then calculated as a percentage of the total number of rockfall points within each thematic layer.

Table 13 shows the comparison of the frequency distributions and Information Value (InfoVal) weights for the Clarens and Molteno Fm. rockfall points. The interpretation of univariate techniques, such as frequency histogram which are used to predict or weight independent variables, is complicated, and can only provide information on one of the independent variables, failing to show the influence of a range of input variables (Hardwick, 2012). The InfoVal is a data driven weighting approach which determines the ratio of the number of mass movement features (such as landslides) within a thematic class to the area of that particular thematic class (Yin & Yan, 1988; van Westen, 1997; Zezere, 2002; Saha et al., 2005; Vijith et al., 2009; Hardwick, 2012; Bhandary et al., 2013; Hua-xi & Kun-long, 2014). InfoVal is a bivariate statistical method which has been used as an indirect approach for assessing landslide susceptibility in an objective way (Vijith et al., 2009). Hardwick (2012) used the InfoVal to weight independent variables, thus showing the influence of a range of input variables, noting that although this method better represents the distribution of mass movement features than a frequency distribution, it cannot be used to describe causality between the variables.

The InfoVal for each thematic class of the independent variables was calculated using the following equation adapted to represent rockfalls instead of landslides (after van Westen, 1997; Saha et al., 2005; Vijith et al., 2009; Kundu et al., 2011; Hardwick, 2012; Hua-xi & Kun-long, 2014):

$$Wi = \ln\left(\frac{Rockfalls\ per\ class}{Rockfalls\ in\ layer}\right) = \ln\left[\left(\frac{N\text{pix(Si)}}{N\text{pix(Ni)}}\right)/\left\{\sum_{i=1}^{n} N\text{pix(Si)}/\sum_{i=1}^{n} N\text{pix(Ni)}\right\}\right]$$

where, *Wi* is the weight for the *i*th thematic class of a particular thematic layer (i.e., environmental variable), *Rockfalls per class* is the rockfall density within a thematic class, *Rockfalls in layer* is the rockfall density within the entire

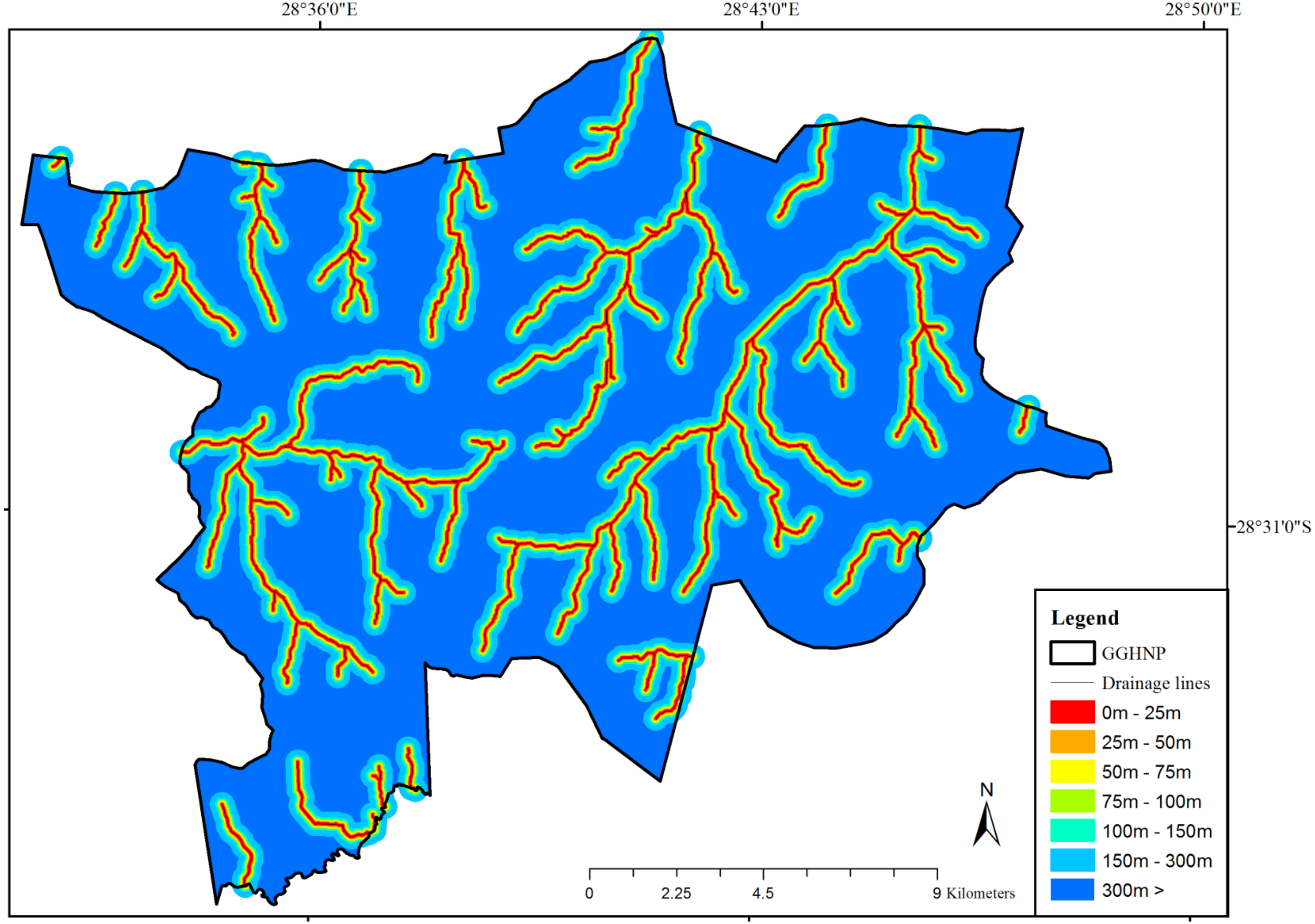

Figure 67: Distance to drainage lines vector layer for the GGHNP.

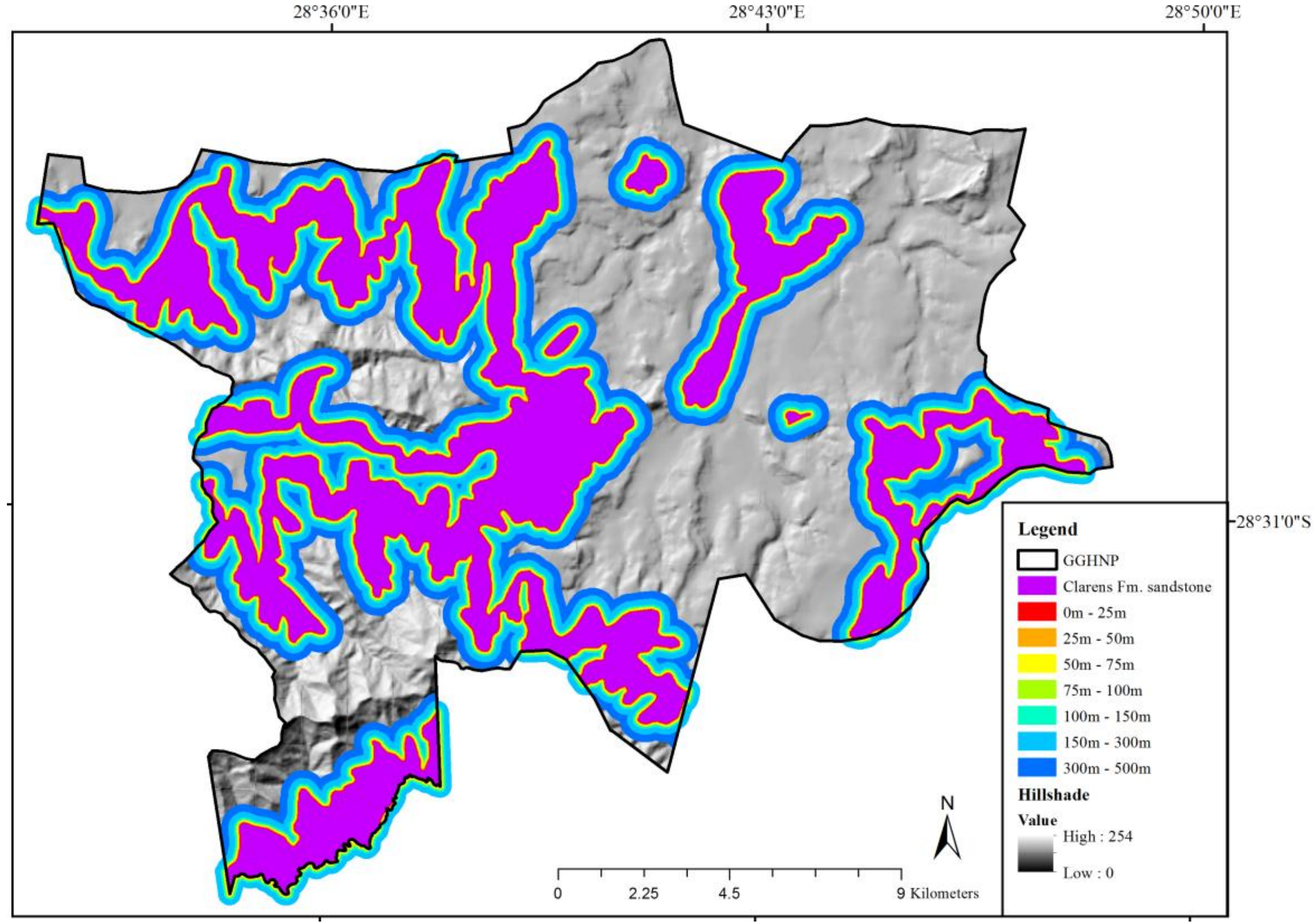

Figure 68: Distance to Clarens Fm. sandstone vector layer for the GGHNP.

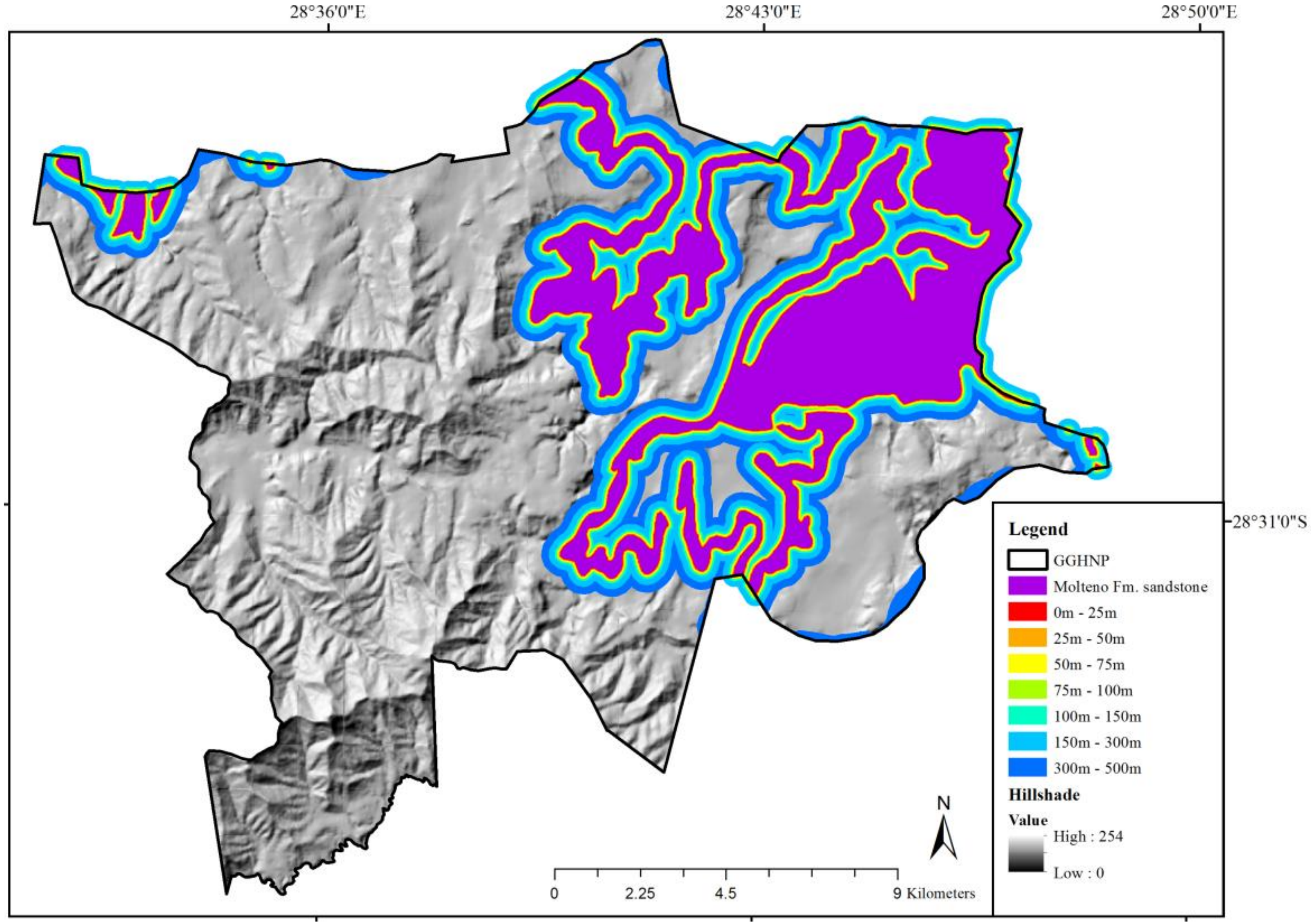

Figure 69: Distance to Molteno Fm. sandstone vector layer for the GGHNP.

thematic layer, *N*pix (Si) is the number of rockfall pixels in a certain thematic class, Npix (Ni) is the total number of pixels in a certain thematic class, and n is the number of classes in the thematic layer. The natural logarithm (ln) is used to take care of the large variation in the weights (Saha et al., 2005). The frequency distributions and InfoVal were ranked according to their highest values and then compared.

ANN was used to analyse the spatial pattern of the Clarens and Molteno Fm. rockfall points (i.e. clustered or dispersed). ANN calculates a nearest neighbour index based on the average distance from each feature to its nearest neighbouring feature (ESRI, 2011). The ANN ratio is given as:

$$ANN = \frac{\bar{D}_O}{\bar{D}_E}$$

Where $\bar{D}_O$ is the observed mean distance between each feature and their nearest neighbour, and $\bar{D}_E$ the expected mean distance for the features given a random pattern. When the $\bar{D}_O$ is less than the $\bar{D}_E$ (i.e. < 1), the pattern exhibits clustering. When the $\bar{D}_O$ is greater than the $\bar{D}_E$ (i.e. > 1), the trend is toward dispersion (ESRI, 2011) (Figure 72). The ANN was calculated using Euclidean distance (i.e. the straight line distance between 2 points). Figure 73 shows graphs of the observed mean distance for Clarens Fm. rockfalls at each of the classes defined in the environmental variables. Figure 74 shows graphs of the observed mean distance for Molteno Fm. rockfalls at each of the classes defined in the environmental variables. The observed mean distance was graphed to observe the relationship between the average distances of Clarens/Molteno Fm. rockfalls in relation to the different classes defined for each of the environmental variables.

The POINT DENSITY GIS tool produces a surface density raster which is the calculated density of point features around each output raster cell. Density surface rasters show where points are concentrated. The neighbourhood is defined around each raster cell center, and the number of points that fall within

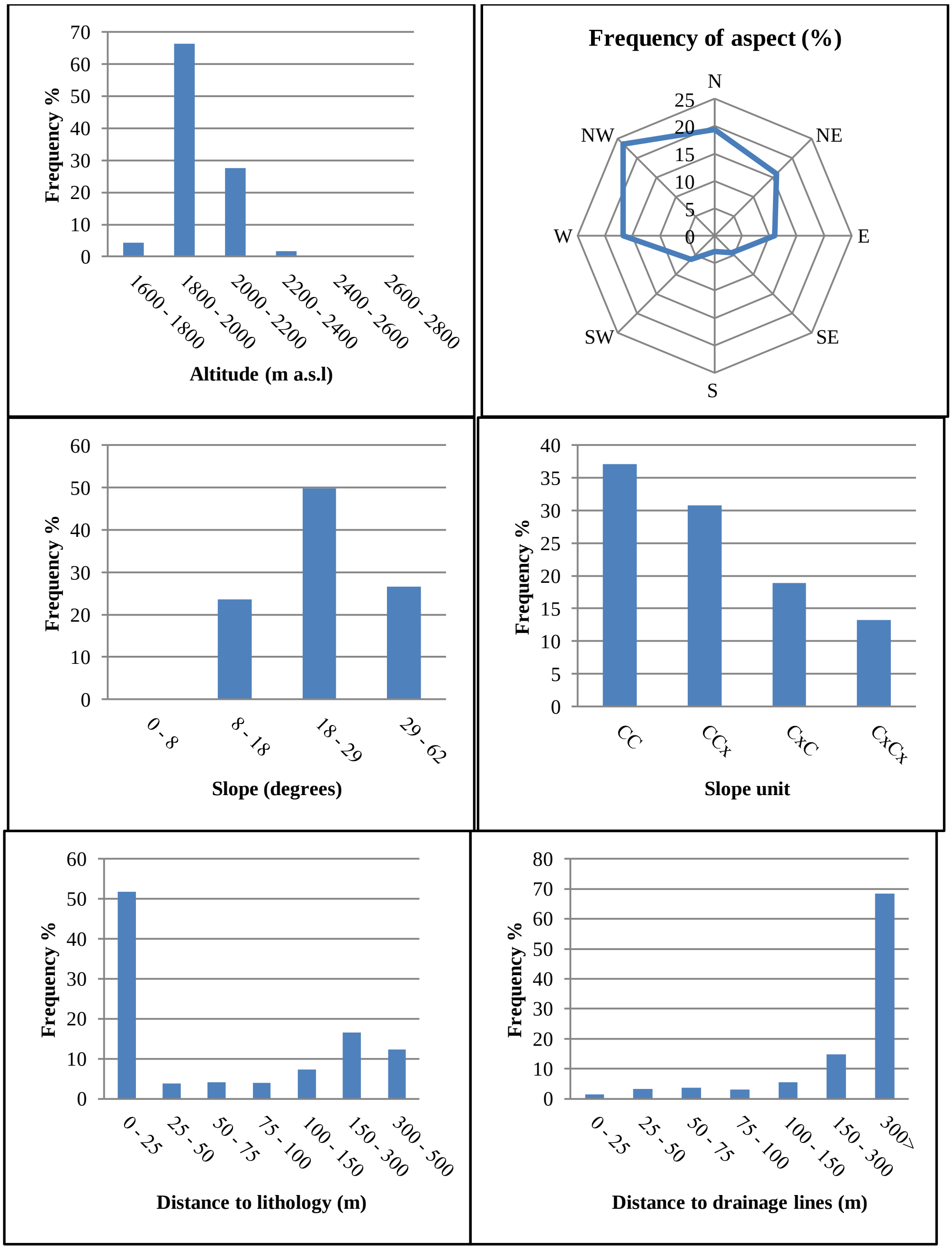

Figure 70: Histograms of the environmental variables for the Clarens Fm. rockfalls derived through the OBIA.

the neighbourhood is totalled and divided by the area of the neighbourhood (ESRI, 2011). The neighbourhood radius determines the shape of the area around each cell that is used to calculate the density value. The default circular neighbourhood radius was used and is defined as the shortest of the width or height of the extent of the input point features, in the output spatial reference, divided by 30. The larger the value of the neighbourhood radius, the more generalised the surface density raster and the smaller the value of the

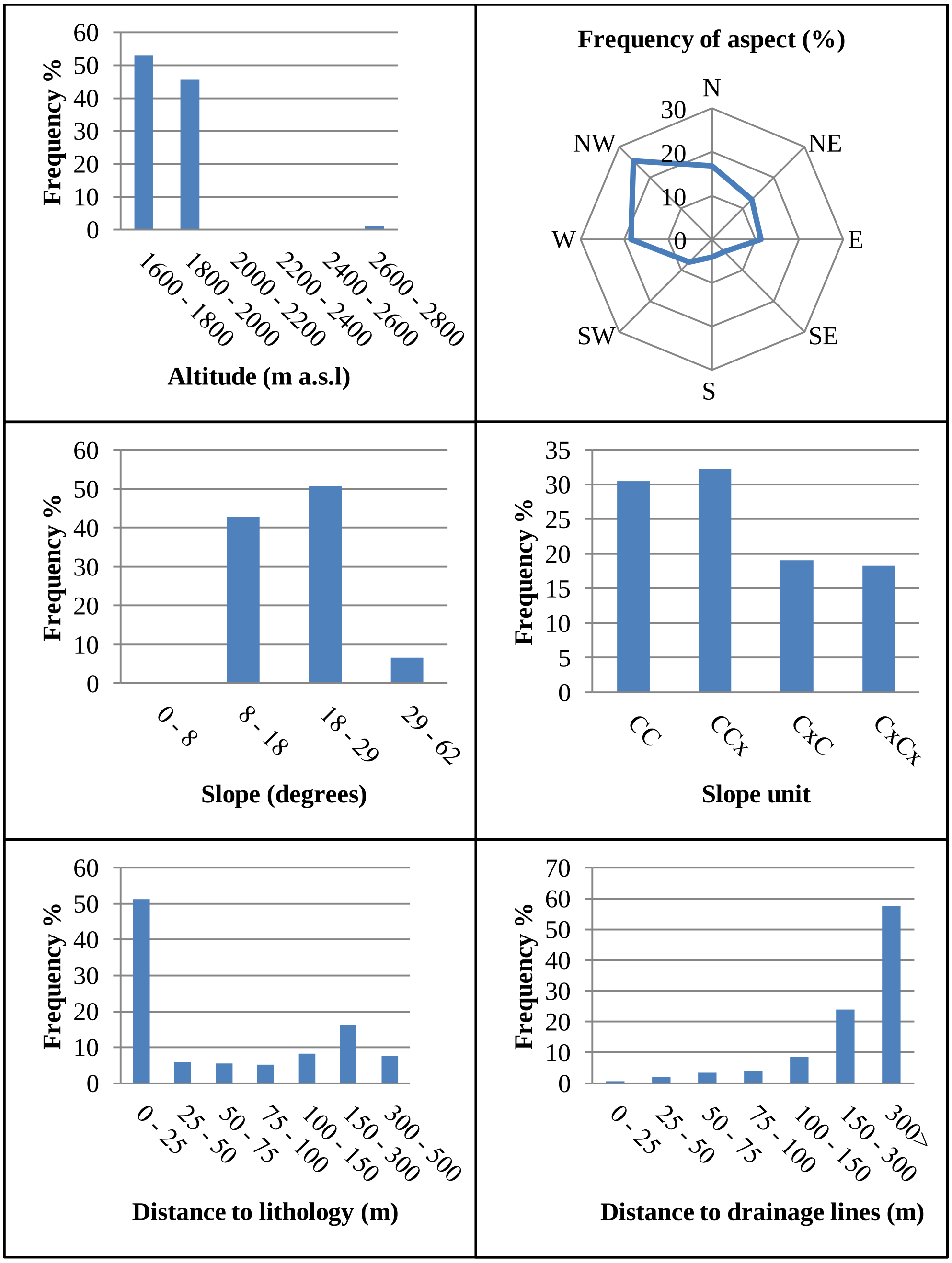

Figure 71: Histograms of the environmental variables for the Molteno Fm. rockfalls derived through the OBIA.

neighbourhood radius the more detail that will be produced in the surface density raster. An area unit scale factor was selected for the output density values as the rockfall points were defined in a meter projection (UTM 35 south).

Thematic layer (Env. Variable)	Class	Clarens Fm. rockfalls			Molteno Fm. rockfalls		
		Area (%)	Frequency of rockfalls (%)	InfoVal	Area (%)	Frequency of rockfalls (%)	InfoVal
Altitude (m)	**1600 - 1800**	24.47	4.29	-1.74	24.47	**53.05**	0.77
	1800 - 2000	41.27	**66.46**	**0.48**	41.27	45.62	0.10
	2000 - 2200	24.56	27.61	0.12	24.56	0.00	$
	2200 - 2400	7.44	1.60	-1.53	7.44	0.00	$
	2400 - 2600	1.99	0.04	-4.04	1.99	0.00	$
	2600 - 2800	0.26	0.00	$	0.26	1.32	**1.61**
Aspect (degrees)	**N**	15.11	19.42	0.25	15.11	16.83	0.11
	NE	15.52	15.98	0.03	15.52	12.90	-0.19
	E	14.83	10.97	-0.30	14.83	11.24	-0.28
	SE	10.50	4.34	-0.88	10.50	3.91	-0.99
	S	6.93	2.87	-0.88	6.93	4.08	-0.53
	SW	7.54	6.15	-0.20	7.54	7.29	-0.03
	W	12.41	16.67	0.30	12.41	18.45	**0.40**
	NW	17.15	**23.60**	**0.32**	17.15	**25.30**	0.39
Slope (degrees)	**0 - 8**	37.84	0.09	-6.03	37.84	0.11	-5.85
	8 - 18	29.47	23.59	-0.22	29.47	42.73	0.37
	18 - 29	21.87	**49.77**	0.82	21.87	**50.63**	**0.84**
	29 - 62	10.82	26.55	**0.90**	10.82	6.53	-0.50
Slope unit	**CC**	23.74	**37.07**	**0.45**	23.74	30.45	**0.25**
	CCx	28.78	30.79	0.07	28.78	**32.28**	0.11
	CxC	29.72	18.93	-0.45	29.72	19.04	-0.45
	CxCx	17.75	13.21	-0.30	17.75	18.23	0.03
Distance to Clarens/Molteno lithology (m)	**0 - 25**	45.80	**51.78**	0.12	44.64	**51.28**	0.14
	25 - 50	3.60	3.87	0.07	3.70	5.91	**0.47**
	50 - 75	3.59	4.17	**0.15**	3.73	5.54	0.39
	75 - 100	3.56	4.01	0.12	3.75	5.19	0.32
	100 - 150	6.94	7.35	0.06	7.33	8.20	0.11
	150 - 300	18.94	16.49	-0.14	19.10	16.32	-0.16
	300 - 500	17.56	12.33	-0.35	17.62	7.56	-0.85
Distance to drainage lines (m)	**0 - 25**	3.02	1.40	-0.77	3.02	0.65	-1.54
	25 - 50	3.00	3.33	0.11	3.00	2.06	-0.37
	50 - 75	2.98	3.68	**0.21**	2.98	3.33	0.11
	75 - 100	2.98	3.07	0.03	2.98	3.98	0.29
	100 - 150	5.93	5.49	-0.08	5.93	8.51	**0.36**
	150 - 300	17.59	14.69	-0.18	17.59	23.86	0.31
	300>	64.51	**68.34**	0.06	64.51	**57.61**	-0.11

Table 13: Comparison of the frequency distributions and InfoVal weights for the Clarens and Molteno Fm. rockfall points. Bold values indicate the highest value in class, and colour indicates variables with the greatest frequency.

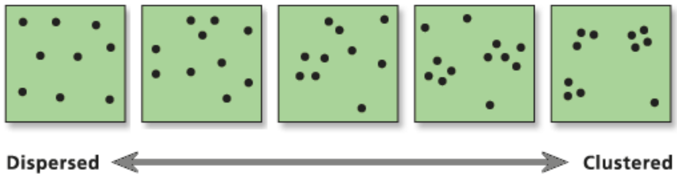

Figure 72: Graphic showing the difference between dispersed and clustered point features (ESRI, 2011).

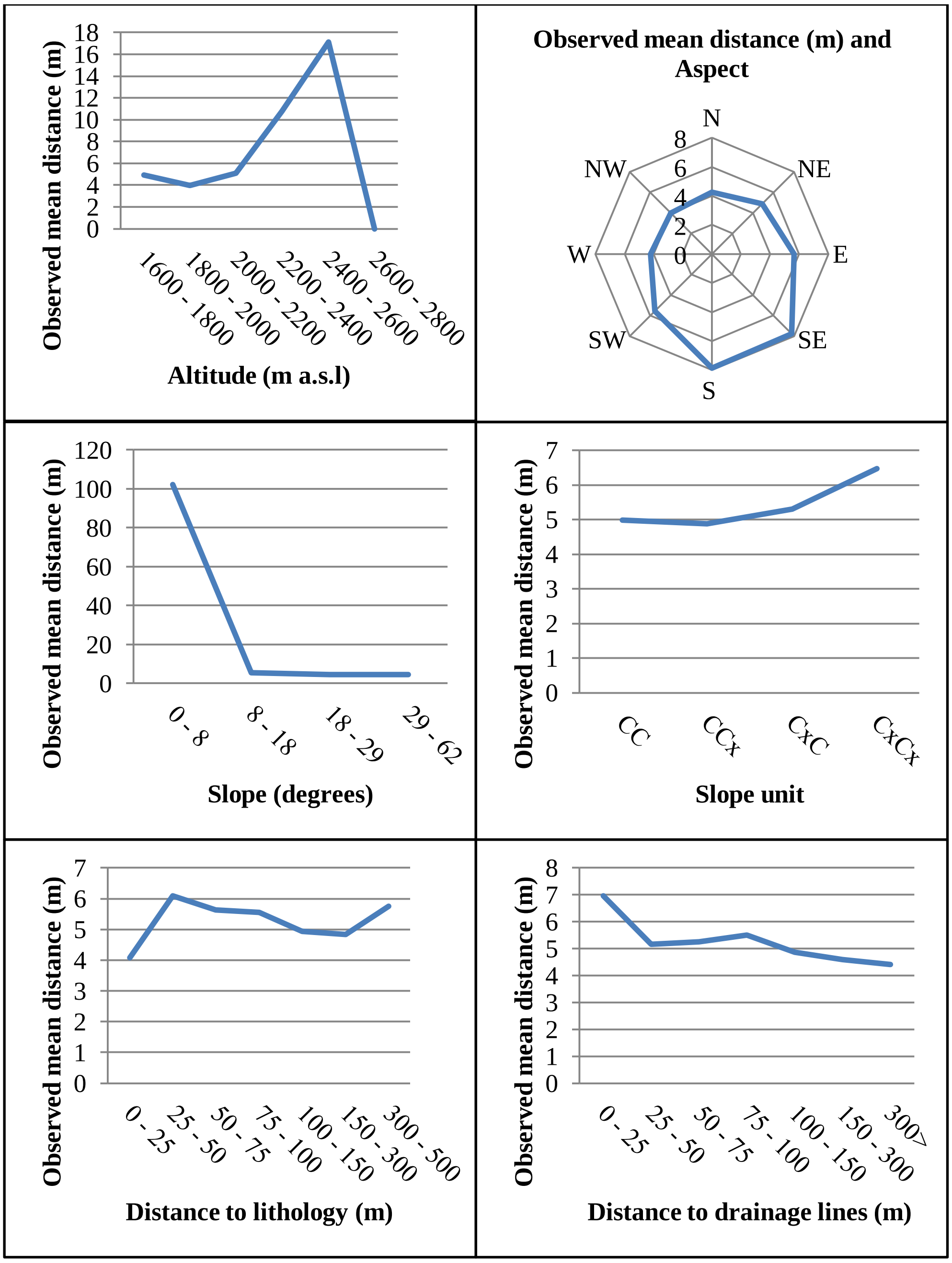

Figure 73: Observed mean distance of Clarens Fm. rockfalls in relation to the classes defined for the environmental variables.

Figure 75 and 76 show the results of the surface density rasters for the Clarens and Molteno Fm. rockfall points respectively. Table 14 describes the count and average number per Km² of Clarens and Molteno Fm. rockfall points occurring in each of the density classes in the study area. For this study, the density of Clarens and Molteno Fm. rockfall points per Km² was determined.

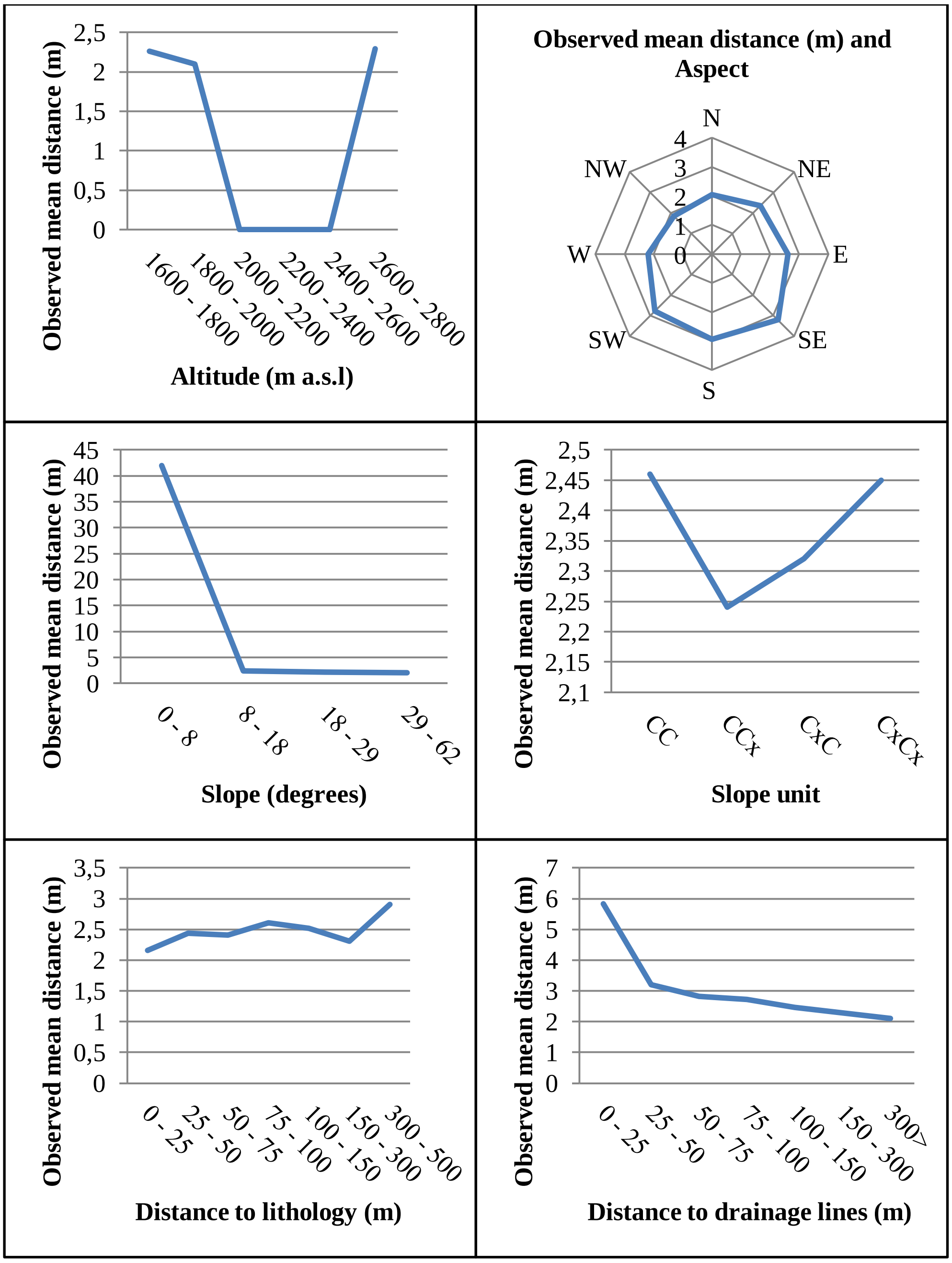

Figure 74: Observed mean distance of Molteno Fm. rockfalls in relation to the classes defined for the environmental variables.

A neighbourhood radius value of 1,000 m was used to produce surface density rasters of rockfall point density per Km². The resulting surface density rasters were then reclassified into low, moderate, high and very high rockfall point density classes using the standard deviation values of the surface density raster. The number of Clarens and Molteno Fm. rockfall points for each of the density classes was then calculated and divided by the area of each density class to determine the number of rockfalls occurring within a Km² (i.e. hypothetical perfect square with equal lengths of 31.62278 m) using the following population density equation:

$$Rockfalls\ per\ Km^2 = \frac{Number\ of\ rockfalls\ in\ thematic\ class}{Area\ of\ thematic\ class\ in\ Km^2}$$

In order to determine the location of the study area where rockfall points are on average most densely distributed, the mean center was determined. The mean center for the Clarens and Molteno Fm. rockfall points was calculated using the MEAN CENTER GIS tool, which identifies the geographic center (or the center of concentration) for a set of point features.

7.4.2.1. Results and discussion: Average nearest neighbour

The ANN for the 419,518 Clarens Fm. rockfall points using Euclidean distance is 0.259409 (z-score: -917.665639). An ANN value of less than 1 suggests that the data exhibit clustering and the z-score suggests that there is less than 1% likelihood that clustering is the result of random chance. It is therefore likely that the Clarens Fm. rockfall points are clustered in response to various environmental variables. The observed mean distance between each Clarens Fm. rockfall point and its neighbour (N=1) is 4.41 m. The ANN for the 330,635 Molteno Fm. rockfall points using Euclidean distance is 0.121624 (z-score: -966.241371). It is therefore likely that the Molteno Fm. rockfall points are clustered in response to various environmental variables. The observed mean distance between each Molteno Fm. rockfall point and its neighbour (N=1) is 2.18 m. The ANN results for the rockfall points in this study relate to the ANN results observed for rockfall points digitized in the Bushmen’s Nek region of the southern Drakensberg which also found rockfall points to be clustered in response to various environmental variables (Hardwick, 2012).

Altitude classes where Clarens and Molteno Fm. rockfall points were observed, show that the rockfalls points have a clustered spatial pattern. The observed mean distance for Clarens Fm. rockfalls was observed to show a positive relationship with altitude. This suggests that Clarens Fm. rockfalls cluster more closely in relation to each other as altitude increases. A relationship between the observed mean distance of Molteno Fm. rockfalls and altitude could not be established as rockfalls were not present at the altitude classes between 2000 and 2200 m a.s.l, 2200 and 2400 m a.s.l, and 2400 and 2600 m a.s.l.

The ANN results for the Clarens and Molteno Fm. rockfall points at all of the slope aspect classes show a clustered spatial pattern. The observed mean distance between each Clarens/Molteno Fm. rockfall point and its neighbour was observed to increase towards south-facing slopes (135° - 180°). Hence, the distances between clustered rockfalls is higher on south-facing slopes and lower on north-facing slopes. This is possibly attributable to more active slope weathering processes on the north-facing slopes.

The Clarens and Molteno Fm. rockfall points possess a clustered spatial pattern for all slope gradient classes. The observed mean distance for Clarens and Molteno Fm. rockfall points at the different slope gradient classes were found to be highly correlated (0.99) and decreases with an increase in slope gradient. This suggests that the Clarens and Molteno Fm. rockfalls are more closely clustered on the steeper slopes.

The ANN results for Clarens and Molteno Fm. rockfall points show a clustered spatial pattern at all slope units (i.e. CC, CCx, CxC CxCx). The observed mean distance for Clarens Fm. rockfall points is observed to be lowest at the CC slope unit, and highest at the CxCx slope unit. The observed mean distance for Molteno Fm. rockfall points was observed to be highest at the CC slope unit and lowest at the CCx slope unit. This suggests that Clarens and Molteno Fm. rockfalls are clustered more closely on the slope units where they occur most frequently, and further apart on slope units where they occur less frequently.

The ANN results for the Clarens and Molteno Fm. rockfall points show that there is clustered spatial patterning at all distances to lithology classes and an increase in the observed mean distance is observed as the distance to lithology increases. This suggests that the Clarens and Molteno Fm. rockfalls closest to their respective lithology (or ‘rock exposures’) cluster more closely in relation to one another.

The ANN results for the Clarens and Molteno Fm. rockfall points show that there are clustered spatial patterns at all distance to drainage line classes. The observed mean distance for the Clarens and Molteno Fm. rockfall points was observed to decrease with an increase in the distance to drainage lines.

7.4.2.2. Results and discussion: Frequency distribution

The highest frequency of Clarens and Molteno Fm. rockfall points are distributed between 1800 and 2000 m a.s.l (66%), and 1600 and 1800 m a.s.l (53%) respectively. No Clarens Fm. rockfall points were found distributed between 2200 and 2400 m a.s.l, and 2600 and 2800 m a.s.l. This is most likely due to the presence of Drakensberg Basalt ridges capping the Clarens Formation. Clarens Fm. rockfall points are distributed at higher altitudes (1800 - 2400 m a.s.l) in comparison with Molteno Fm. rockfalls (1600 - 2000 m a.s.l). This is expected as the Clarens Fm. sandstone is known to have an upper contact with the Molteno Fm. sandstone. There was no significant correlation observed between the frequency distribution of Clarens and Molteno Fm. rockfall points in relation to altitude. The high frequency distribution of the Clarens Fm. rockfall points between 1800 and 2000 m a.s.l compares well with the frequency distribution results of rockfalls in the Bushmen’s Nek region of the southern Drakensberg (~40%) (Hardwick, 2012).

Altitude has a very important influence on rockslopes globally, especially in mountainous regions where the difference in altitude is highly significant to the types of slope weathering experienced and the geomorphic landforms that result. In southern Africa, particularly the Drakensberg and Lesotho Highlands, a considerable amount of work has been devoted to understanding slope weathering processes and landforms in these mountainous regions (Grab, 1999; Boelhouwers & Meiklejohn, 2002; Boelhouwers & Sumner, 2003; Grab et al., 2009; Mills et al., 2009; Sumner et al., 2009; Grab, 2010). The High Drakensberg, Lesotho mountains, and Western Cape mountains are present day examples of frost environments. The strength of freeze-thaw cycles and humidity from rain or snowfall will cause rock disintegration and fragment detachment on rocky slopes to increase especially at higher altitudes (Gardner, 1983).

Amongst the environmental factors affecting rockfall, those related to climate are especially relevant. For instance, the role of climate change in the distribution and incidence of rockfalls is becoming increasingly relevant. Temporal analyses of rockfalls at 56 sites with slope failures between 1900 and 2007 in the central European Alps, show an increase in frequency within the last decades, fuelling ongoing debate on the effects of changes in the high-mountain cryosphere on rockfall and rock avalanche activity (Fischer et al., 2012). With regards to mapping rockfall distributions in relation to altitude, rockfall susceptibility mapping at the Cantabrian Mountains of northern Spain have shown that the maximum frequency distribution of rockfalls is on slopes of between 1500 and 1700 m a.s.l, and that increases in rockfall activity with elevation can be correlated mainly with climatic factors (Menéndez Duarte & Marquinez, 2002). In Val di Fassa (Italy), rockfall modelling has shown that areas more prone to rockfall activity are those located in correspondence with the highest portions of the region, proving aspect and elevation parameters to be important indicators of micro-climatic conditions (Frattini et al., 2008). Similar findings in the Colorado Front Range show that slope height and aspect are significant parameters for a rapid, preliminary indication of rockfall potential (Santi et al., 2009).

The highest frequency of Clarens and Molteno Fm. Rockall points are distributed on northwest-facing slopes (24% and 25% respectively). The frequency distribution of Clarens and Molteno Fm. rockfall points in relation to slope aspect was observed to be highly correlated (0.97) with one another. The high correlation value observed for the rockfall frequency distributions of Clarens and Molteno Fm. rockfall points with regards to slope aspect, shows a strong trend toward north-facing slopes, which are known to receive more solar radiation than other slope aspects in the southern hemisphere, leading to more active slope weathering processes (Mills et al., 2009; Grab & Mills, 2011).

Slope aspect is strongly determined by the dominant geological structure of a region. Rockfall susceptibility mapping at the Cantabrian Mountains of northern Spain has shown the Salience Syncline to be the main determinant for the high frequency of slopes with north-east or south-west orientations (Menéndez Duarte & Marquinez, 2002). The wealth of evidence for slope aspect as a significant indicator of micro-climatic conditions is abundant. Evidence from studies of rockfalls in the northern hemisphere have shown slope aspect to play an important role in rockfall susceptibility, as south-facing slopes experience far more freeze-thaw cycles annually than north-facing slopes (Flatland, 1993; Watters, 1998). For instance, studies on rockfall events in the Central European Alps have found evidence linking an increase in rockfall events to extremely warm periods (Ravanel & Deline, 2011; Fischer et al., 2012; Huggel et al., 2012) and it is thought unlikely that these events were a consequence of earthquakes. The opposite is of course true for the southern hemisphere where north-facing slopes receive more solar radiation. Studies for mountainous regions in the southern hemisphere have shown the evolution of geomorphic landforms and processes to be more pronounced on south-facing slopes (Mulder & Grab, 2002; Grab, 2007; Grab et al., 2009; Mills et al., 2009; Grab, 2010). For instance, an analysis of rock temperatures measured in Lesotho found significant variations in temperature between north- and south-facing slopes such that north-facing slopes experience 35 times fewer freezing days than south-facing slopes (Grab, 2007).

The highest frequency of Clarens and Molteno Fm. rockfall points are distributed on slope gradients of 18° - 29°. The frequency distribution of rockfall points at the steepest slope gradient class, 29° - 62°, was observed to be Clarens Fm. sandstone. This could, in part, be attributed to the fact that the Clarens Fm. sandstone overlies the Molteno Fm. sandstone. In general, steeper slopes exhibit more frequent rockfalls, as a consequence of gravity effects (Antoniou & Lekkas, 2010). Slopes of ~30° and ~85° are known to produce rockfalls with the largest runout distances (Maerz et al., 2005). This is due to the fact that steeper slope gradients generate higher levels of rock slope instability (Roering & Kirchner, 2001). The high frequency distribution of rockfalls on slope gradients between 18º - 29º compares well with the frequency distribution of rockfalls on slope of 20º - 30º in Bushmen's Nek (~38%). In addition to this, the results for the frequency distribution of rockfalls on slope gradients between 18º - 29º compares well with values for shadow angles of rockfalls in Sol`a d'Andorra la Vella, Central Pyrenees (Copons et al., 2009). The shadow angle is defined as the dipping of the energy line which connects the apex of the talus slope to the furthest fallen boulder (Evans & Hungr, 1993). The slope gradient of the Clarens and Molteno Fm. rockfall points exemplify the shadow angle as the rockfall points represent the furthest runout distance of the rockfalls.

The frequency distribution of Clarens Fm. rockfall points was observed to be highest at CC (33%) or sloping closed basins which have a concave lateral and vertical profile. The frequency distribution of Molteno Fm. rockfall points was observed to be highest at CCx (32%) or sloping recessing hills which have a concave lateral profile and convex vertical profile. Clarens and Molteno Fm. rockfall points were observed to be least distributed on CxCx (13% and 18% respectively) or sloping inflated hills which have a convex lateral and vertical profile. The frequency distribution of Clarens and Molteno Fm. rockfall points on CC, CCx, CxC, and CxCx slope units was highly correlated (0.93).

Studies analysing landforms such as rockfalls in relation to slope units are very limited in southern Africa. However, Hardwick (2012) has shown the frequency distribution of rockfalls in the Bushmen's Nek region of southern Africa to be highest on CxCx or sloping inflated hills. The CxCx slope unit is usually associated with slope failures which involve a mixture of landslides and rock falls, and have biconcave slip surfaces (Ayalew & Yamagishi, 2004).

In contrast, Clarens and Molteno Fm. rockfall points were observed to be least distributed on CxCx slope units. The Molteno Fm. rockfall points were found to be most highly distributed on CCx slope units which are commonly adjacent to their CxCx counterparts.

The Clarens Fm. rockfall points were found to be most highly distributed on CC slope units closely followed by CCx slope units. CC slope units are characteristic of landscapes where many retrogressive upward-propagating landslides can be found occurring (Ayalew & Yamagishi, 2004). The differences observed in the frequency distributions for rockfalls of the southern Drakensberg and GGHNP in relation to slope units, might be varied due to the differences between the landscapes of the regions which are largely determined by the underlying geology.

The frequency distribution of Clarens and Molteno Fm. rockfall points was observed to be highest at a distance of 0 – 25 m to Clarens and Molteno Fm. sandstone lithologies and highly correlated (0.99) with one another. The frequency of Clarens and Molteno Fm. rockfalls was observed to be highest where there are exposed Clarens and Molteno Fm. sandstone outcrops. The lithologies mapped in the 1:250,000 geological vector layer were not only representative of the outcrops, but also included the slopes adjacent to exposed outcrops. Hence, the high frequency distribution of Clarens and Molteno Fm. rockfall points at the distance to lithology class, 0-25 m.

The high frequency distribution of Clarens and Molteno Fm. rockfalls within 0 – 25 m of the Clarens and Molteno sandstone lithologies or rock exposures suggests that most rockfalls do not travel far from their source areas. This result compares well with the frequency distribution of rockfalls in Bushmen's

Nek which was found to be highest at 0 - 25 m of a rock exposure (~53%) (Hardwick, 2012).

The frequency distribution of Clarens and Molteno Fm. rockfall points was observed to be greatest at distances greater than 300 m to drainage lines (68% and 58% respectively). The frequency distribution results for Clarens and Molteno Fm. rockfall points in relation to distance to drainage lines were found to be highly correlated (0.98) with one another. In contrast Hardwick (2012) found ~36% of rockfalls to be within 25 m of drainage lines, suggesting that the drainage lines function as topographic lows collecting displaced material. This contrast may suggest that drainage lines play less of a role in influencing rockfall distribution in the GGHNP as compared to the rockfalls in the Bushmen's Nek region of the southern Drakensberg.

7.4.2.3. Results and discussion: Information value

Finally, the comparison of the frequency distribution and InfoVal weights for the rockfall points were examined to infer the relationship between the thematic class with the highest frequency distribution of rockfalls, and the thematic class with the most influence on the frequency distribution of rockfalls. The comparison of the frequency distribution and InfoVal weights for the Clarens Fm. rockfalls indicate that rockfalls are most frequent at distances greater than 300 m to drainage lines and most greatly influenced by very steep slope gradients between 29° – 62°. The comparison of the frequency distribution and InfoVal weights for the Molteno Fm. rockfalls indicate that rockfalls occur most frequently at distances greater than 300 m to drainage lines and are most greatly influenced by high altitudes of between 2600 and 2800 m a.s.l. This result may be unlikely as Drakensberg Basalt is typically found occurring at 2600 and 2800 m a.s.l. In contrast, the InfoVal results for rockfalls in the Bushmen's Nek region of the southern Drakensberg were found to be most attributable to distances of 0 – 25 m of rock exposures.

7.4.2.4. Results and discussion: Point density

The mean center of the Clarens Fm. rockfall points shows that rockfalls are concentrated at UTM coordinates X: 660935.184823 Y: 6847357.7548 (mean center of rockfall concentration) near Wonderhoek. The population density equation of Clarens Fm. rockfall points found that there are an average of 0.77 rockfalls per Km² in the low surface density class, 1.8 rockfalls occurring per Km² in the moderate surface density class, 3.13 rockfalls occurring per Km² in the high surface density class, and 4.55 rockfalls occurring per Km² in the very high surface density class. On average, ~2 Clarens Fm. rockfalls are found per Km² of the entire study area. There are a number of regions in the study area where Clarens Fm. rockfalls occur at very high densities (~5 Clarens Fm. rockfalls per Km²). The very high density polygons for Clarens Fm. rockfalls were named according to the overlapping historical farm names inherited in the study area. The names of the farms were captured from 1:50,000 topographic maps of the study area. The very high Clarens Fm. rockfall density regions include:

- Bos en Dal, Suikerboorand, Waterval, and Witkop in the north-west region of the GGHNP (Figure 77).
- Wilgerhof, and Noordbrabant in the western region of the GGHNP (Figure 77).
- Avondrust in the northern region of the GGHNP (Figure 78).
- Wonderhoek in the central part of the GGHNP. (Figure 77, 78 & 79).
- Twijfel Hoek (or Silasberg), and Klipfontein in the eastern part of the GGHNP (Figure 78, 79).
- General Will, Doncaster, Toss Line, and Highlands in the southern part of the GGHNP (Figure 77).

The Wonderhoek region was found to possess the largest area of very high density rockfalls. A near analysis of the very high density regions with park infrastructure was calculated to infer the region of the study area most vulnerable to Clarens Fm. rockfalls. The near analysis for buildings in the park found that the distances to very high density rockfall regions range from

0 to 3.8 Km. The average near distance of buildings to very high density rockfall regions is 1.37 Km. The near analysis for tarred and dirt roads in the park found that the distances to very high density rockfall regions range from 0 to 3.12 Km. The average near distance of buildings to very high density rockfall regions is 1.1 Km. Buildings and roads located at or near Wilgerhof were found to have the greatest potential risk to Clarens Fm. rockfalls (Figure 78). Overall, the average near distance of buildings to very high density rockfall regions suggests that the buildings of the park are in no real danger of Clarens Fm. rockfalls. Although tourist accommodation sites such as the Brandwag hotel and Glen Reenen camp possess no real threat to Clarens Fm. rockfalls, anthropogenic outdoor activities could potentially be impacted by infrequent rockfall hazards. Footpaths or hiking trails located within or near very high density Clarens Fm. rockfall regions should consider potential rockfall threat.

The mean center of the Molteno Fm. rockfall points shows that rockfalls are concentrated at UTM coordinates X: 667278.241286 Y: 6849663.78046 (mean center of rockfall concentration), near Riet Spruit. The population density equation of Molteno Fm. rockfall points found that there are an average of 2.13 rockfalls per Km^2 in the low surface density class, 4.12 rockfalls per Km^2 in the moderate surface density class, 7.47 rockfalls per Km^2 in the high surface density class, and 14.55 rockfalls per Km^2 in the very high surface density class. On average, 4 Molteno Fm. rockfalls are found per Km^2 for the entire study area. Only one region in the study area was found to have very high densities of Molteno Fm. rockfalls (~15 Clarens Fm. rockfalls per Km^2). The very high density polygon for Molteno Fm. rockfalls was named according to the overlapping historical farm name inherited in the study area. The name of the farm was captured from a 1:50,000 topographic map of the study area and is namely:

- Schuinskop or the Skuinskop Mountain, located in the north-eastern part of the GGHNP (Figure D).

Schuinskop is located in a very remote region of the park and no anthropogenic activities such as camping and hiking is permitted there. A near analysis shows that the closest infrastructure to Schuinskop is 585.31 m.

Surface density class	Clarens Fm. rockfall points			Molteno Fm. rockfall points		
	Count	Area (Km²)	Ave. Rockfalls per Area Km²	Count	Area (Km²)	Ave. Rockfalls per Area Km²
Low	58393.00	76150.68	0.77	97483.00	45865.23	2.13
Moderate	112283.00	62451.03	1.80	114284.00	27750.58	4.12
High	151716.00	48457.57	3.13	82624.00	11056.24	7.47
Very high	96309.00	21165.51	**4.55**	35590.00	2446.10	**14.55**
Total	418701.00	208224.79	2.01	329981.00	87118.15	3.79

Table 14: Count, and average number per Km² of Clarens and Molteno Fm. rockfall points occurring in each of the density classes for the study area. Bold values indicate the density class with the highest occurrence of rockfall points per Km² and colour indicates the Formation with the greatest occurrence of rockfall points per Km² for the entire study area.

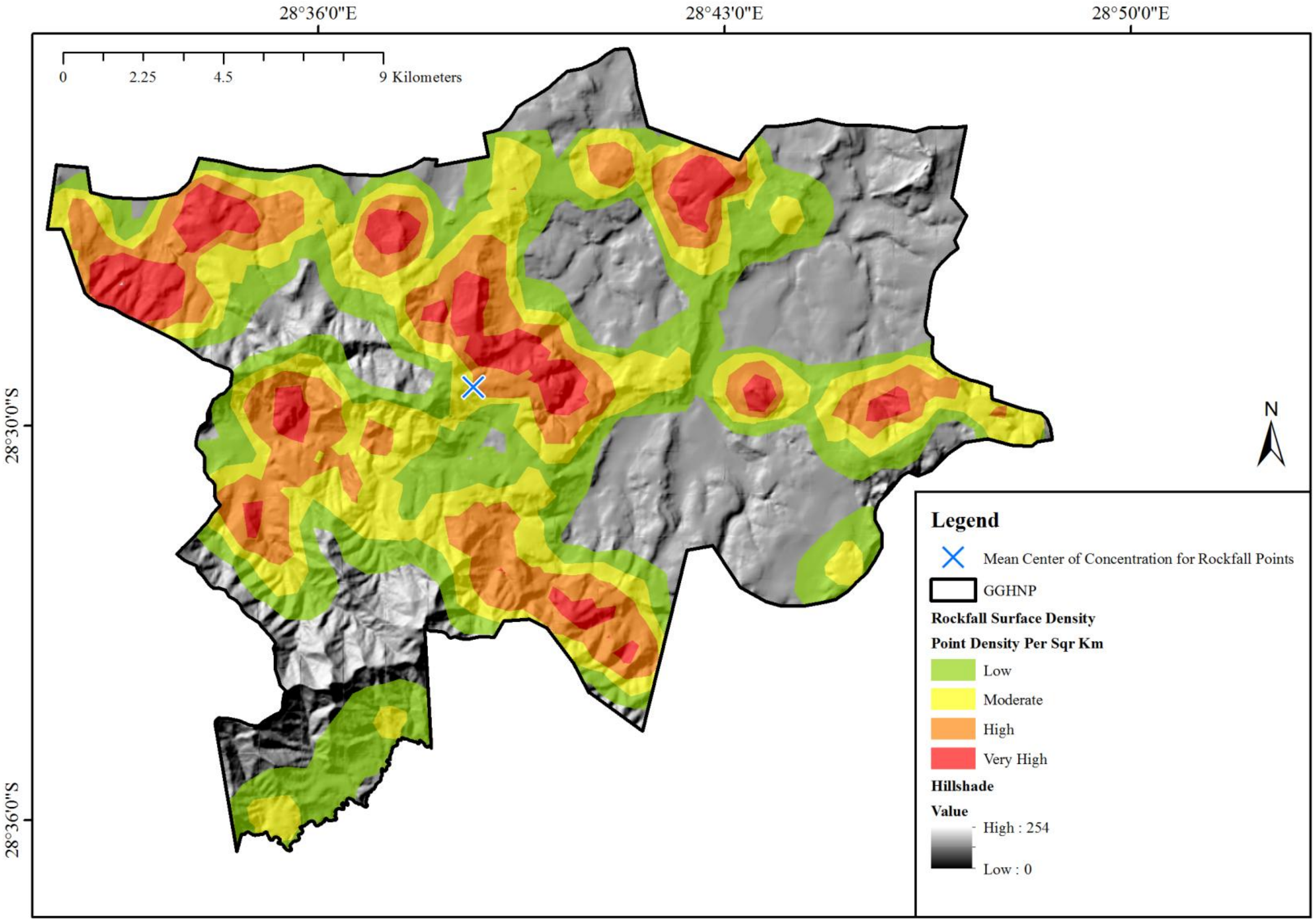

Figure 75: Surface density raster for Clarens Fm. rockfall points.

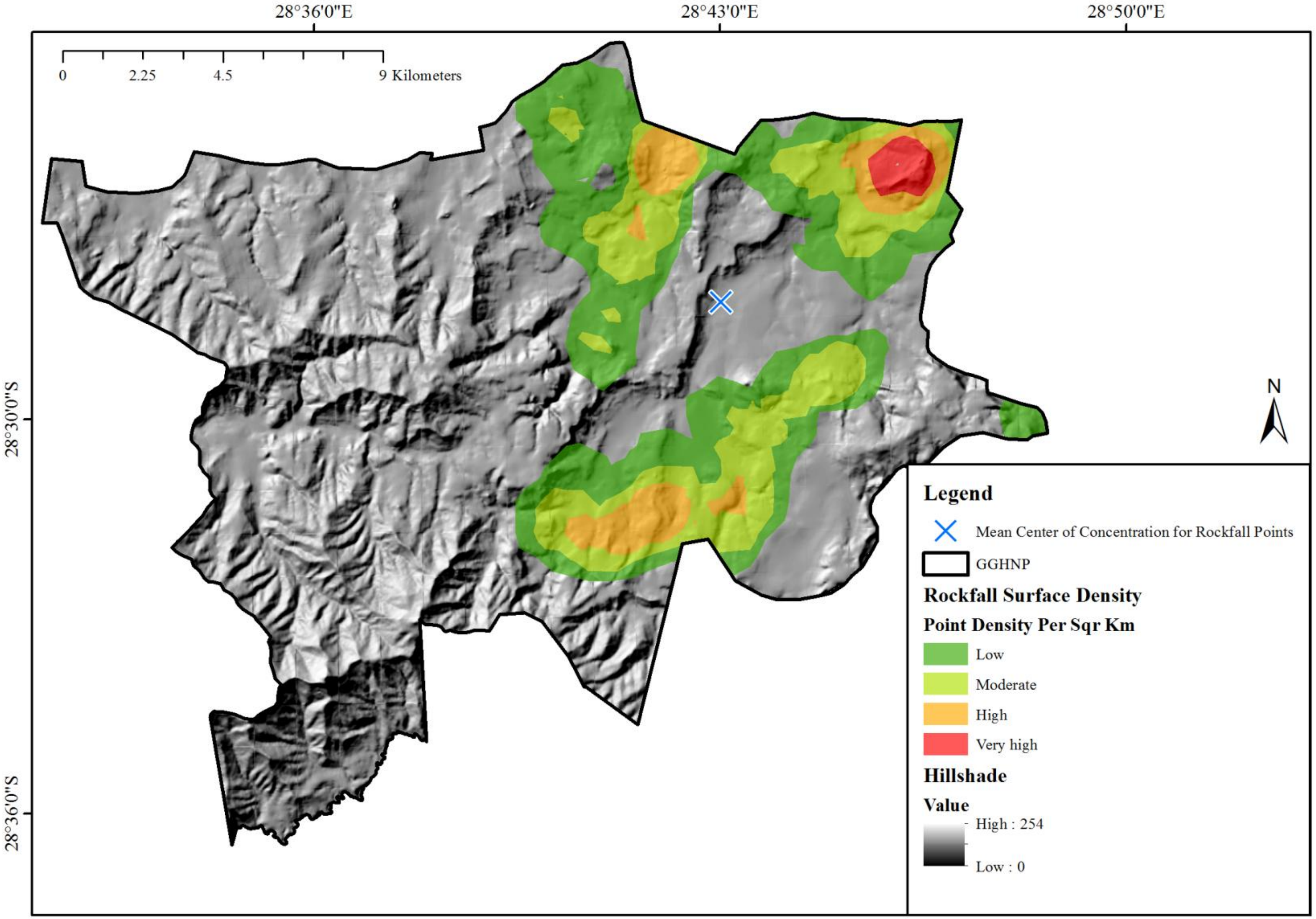

Figure 76: Surface density raster for the Molteno Fm. rockfall points.

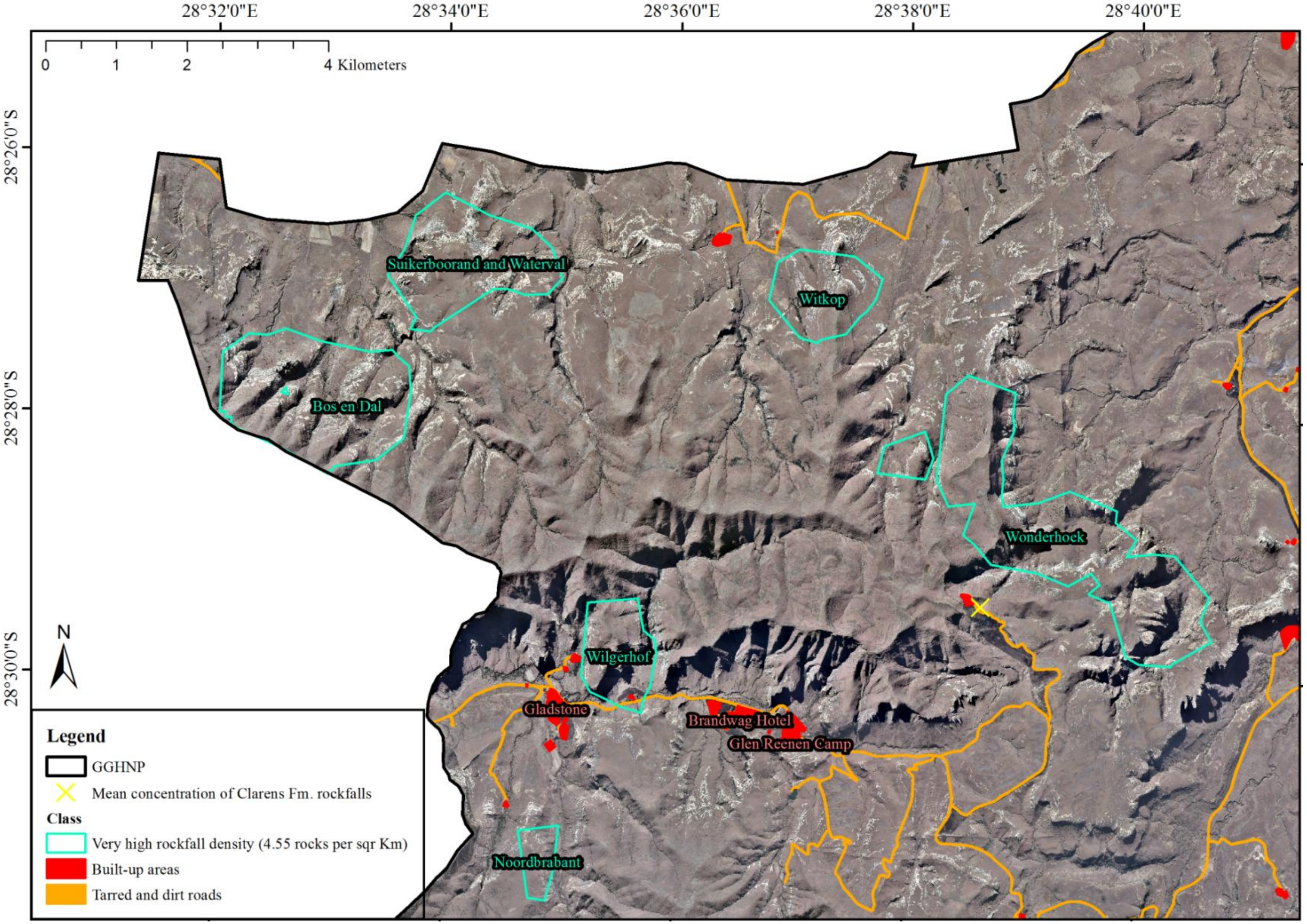

Figure 77: Very high density Clarens Fm. rockfall regions for the GGHNP, which include: Bos en Dal, Suikerboorand, Waterval, Witkop, Wonderhoek, Wilgerhof, and Noordbrabant.

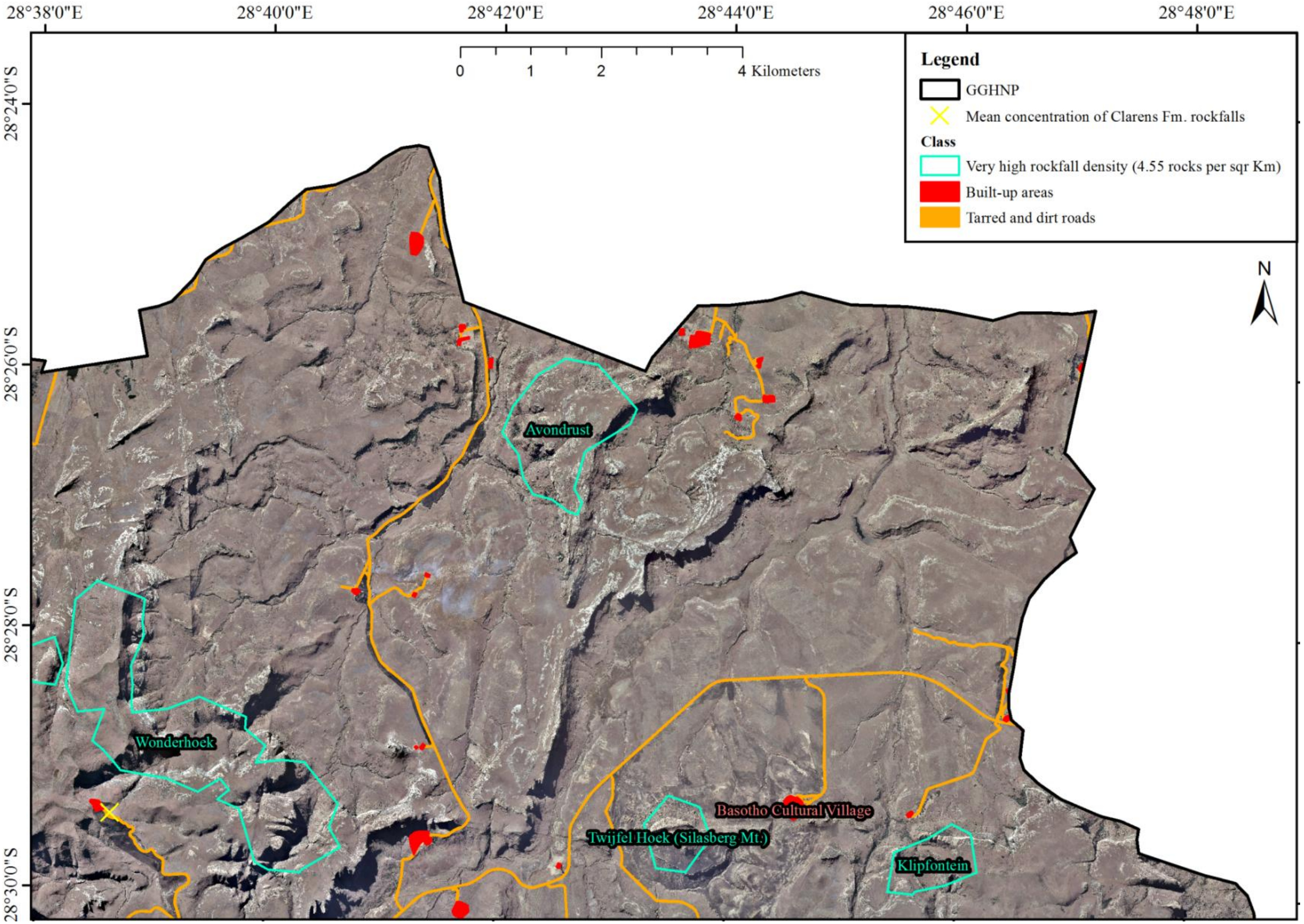

Figure 78: Very high density Clarens Fm. rockfall regions for the GGHNP, which include: Avondrust, Wonderhoek, Twijfel Hoek (or the Silasberg), and Klipfontein.

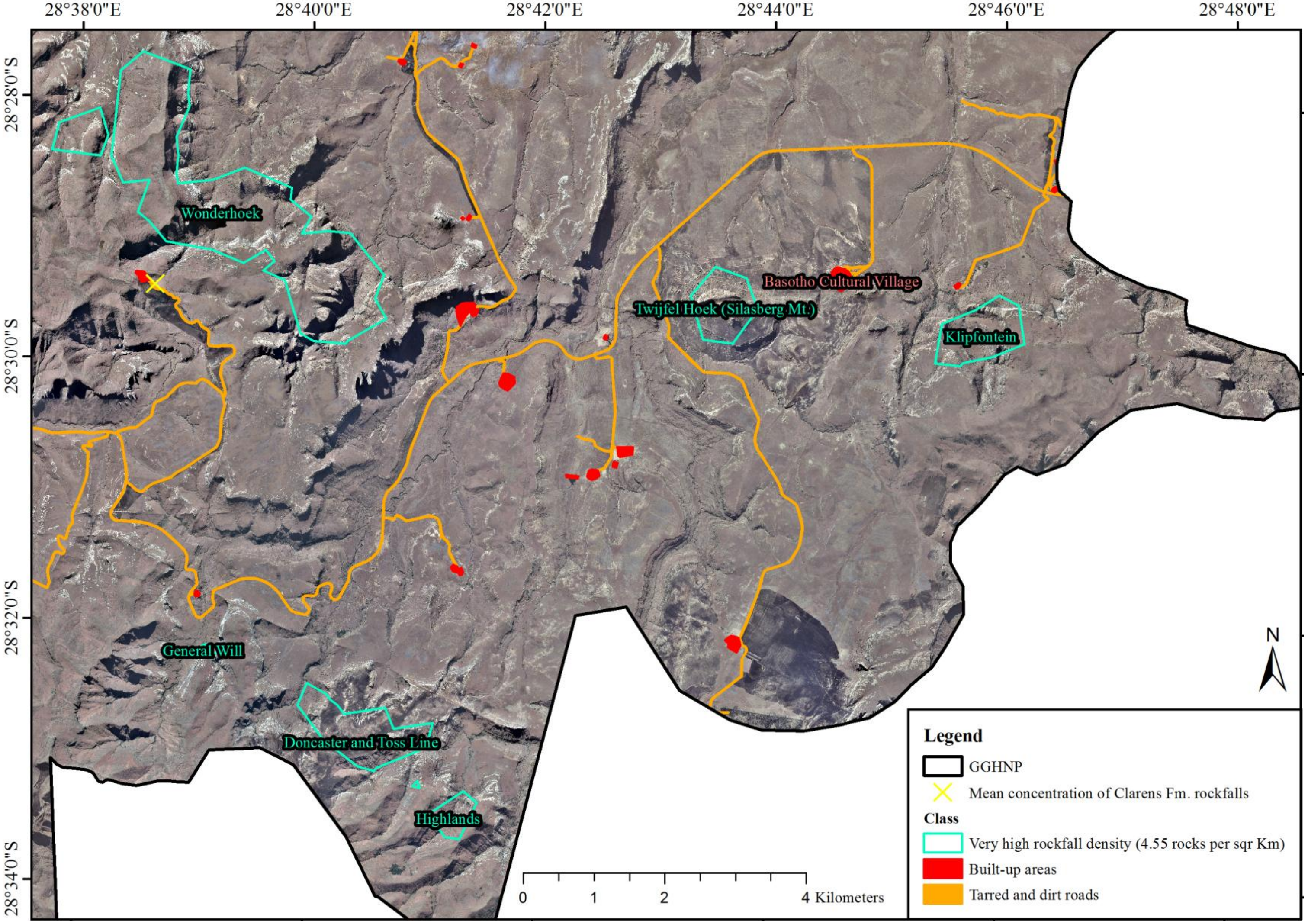

Figure 79: Very high density Clarens Fm. rockfall regions for the GGHNP, which include: Wonderhoek, General Will, Twijfel (or the Silasberg), Klipfontein, Doncaster, Toss Line, and Highlands.

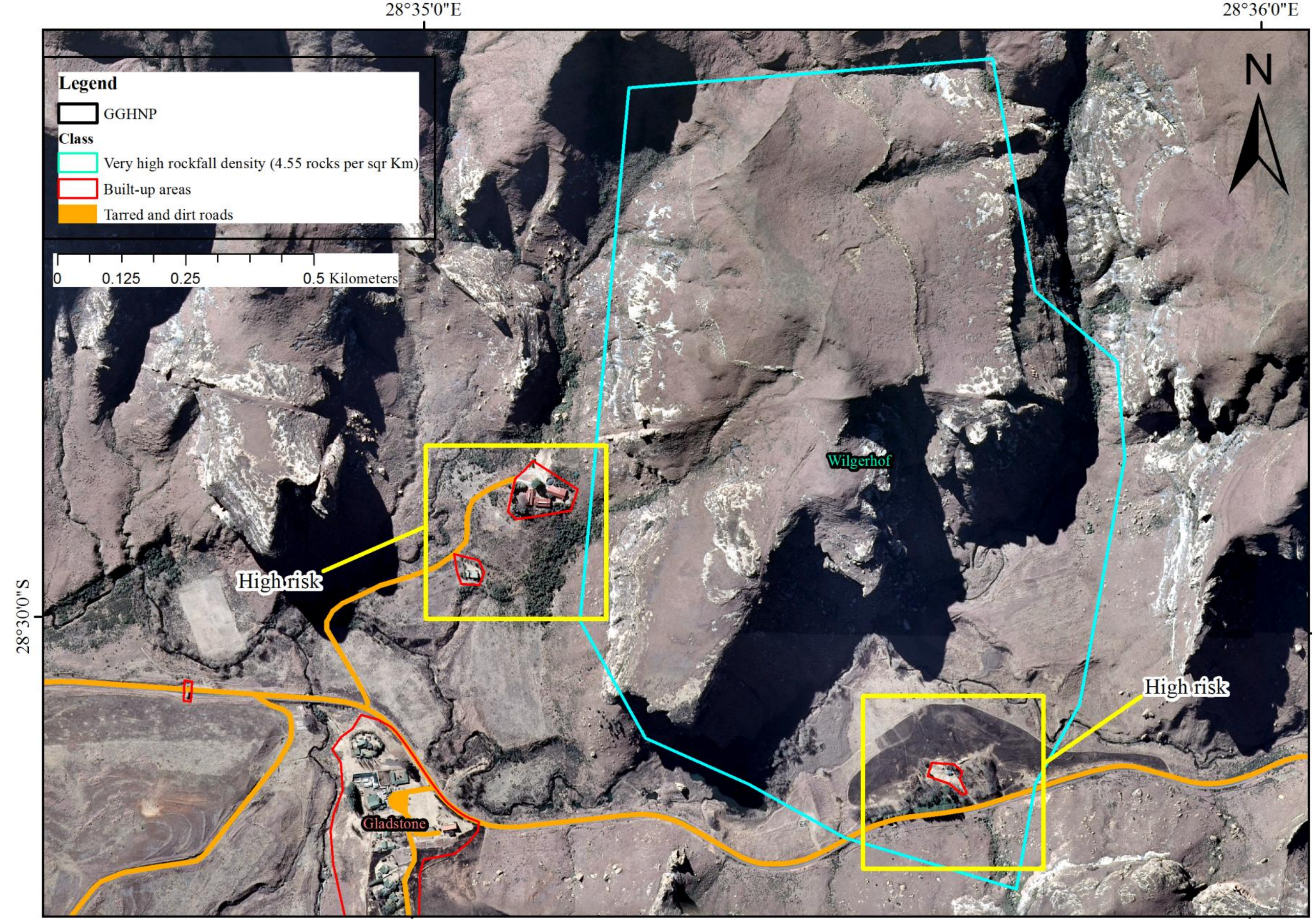

Figure 80: Potential very high risk Clarens Fm. rockfall areas at Wilgerhof, GGHNP.

Chapter 8 - Conclusion

This study on rockfalls in the GGHNP shows the potential of remote sensing and GIS techniques to be used for extracting rockfall characteristics from remotely sensed imagery and analysing them in relation to topographic variables derived from remotely sensed imagery. The validation of ground-truthed rockfalls with classified rockfalls proved challenging given the differences in resolution between field measurements and the remotely sensed imagery. One of the major constraints experienced with validating classified rockfalls was that many of the ground-truthed rockfall samples had LA or PA measurements that were less than or equal to the spatial resolution of the aerial imagery (i.e. 0.5 m). The validation of rockfalls derived in further OBIA with ground-truthed rockfalls could be improved in future by increasing the scale of sampling sites and the amount of rockfalls sampled. In addition to this, canonical analysis or multivariate multiple regression analysis could be used to interpret the extent of similarity between image objects representing rockfalls with the extents of actual ground-truthed rockfalls.

Another major limitation noted in this study is that the use of environmental variables derived through a 20 m DEM is not ideal for the assessment of micro-scale rockfall features and is more ideally suited to the analysis of macro-scale landforms. The creation of a very high spatial resolution DEM would provide a more accurate and representative analysis of micro-scale rockfalls in relation to environmental variables.

The use of multiple linear regression modelling to examine whether or not ground-truthed rockfalls in the GGHNP can be validated with remotely sensed imagery shows that rockfall characteristics LA, PA, bearing of LA, area, and circumference can be modelled using independent TEGP, albeit to a very limited extent. The major constraint for these models is likely consequential to the difference between the coarse resolution of the remotely sensed imagery and the ground-truthed rockfalls. The extent of difference between the resolution of the independent variables and ground-truthed rockfalls appears to be too high, hence the poor validation results. The PA multiple linear regression model produced the most accurate result for characterising a rockfall characteristic for the entire calibration sample (nAll). The bearing of LA multiple linear regression model produced the most accurate result for characterising a rockfall characteristic for the Clarens Fm. calibration sample ($n_{Clarens}$). The area multiple linear regression model produced the most accurate result for characterising a rockfall characteristic for the Molteno Fm. calibration sample ($n_{Molteno}$). The multiple linear regression results for the Elliot Fm. calibration sample were found to be inconclusive and as a result this meant that the Elliot Fm. was excluded from the OBIA.

OBIA of Clarens and Molteno Fm. rockfalls was developed for the GGHNP using the circumference measurements of ground-truthed rockfalls to guide the segmentation of rockfalls into meaningful image objects. Univariate statistics such as the frequency distribution of Clarens and Molteno Fm. rockfall points were analysed in conjunction with environmental variables (thematic layers) derived from a 20 m DEM and 1:250,000 geological vector layer of the study area which include altitude, slope aspect, slope gradient, slope units, distance to drainage lines and lithology (rock exposure).

Frequency histogram univariate statistical techniques were originally intended to compare the distribution of Clarens and Molteno Fm. rockfalls in relation to the different environmental variables. However, when the frequency of rockfalls within a thematic class was normalised using the area of the environmental variable, it became apparent that the frequency distributions were not reliable. InfoVal was therefore used to effectively compare the weights of each environmental variable and to compare the thematic classes within each environmental variable.

The frequency distribution of Clarens and Molteno Fm. rockfalls in the GGHNP was found to compare well with the frequency distribution of rockfalls in the Bushmen's Nek region of the southern Drakensberg for rockfalls:

- 0 – 25 m of rock exposures
- on slopes with an altitude between 1800 and 2000 m a.s.l
- with slope gradients of 18° - 29°

However, the frequency distribution of Clarens and Molteno Fm. rockfalls in the GGHNP was found to contrast with the frequency distribution results of rockfalls in the Bushmen’s Nek region of the southern Drakensberg in terms of slope unit, slope aspect and distance to drainage lines. These observed differences might be attributable to the differences between the topography of the study area which falls within the northern Drakensberg and the topography of the Bushmen’s Nek region which falls within the southern Drakensberg.

The InfoVal weights for the Clarens Fm. rockfalls indicate that rockfalls are most greatly influenced by very steep slope gradients between 29° – 62° and Molteno Fm. rockfalls are most greatly influenced by very high altitudes of 2600 and 2800 m a.s.l. In contrast, the InfoVal results for rockfalls in the Bushmen’s Nek region of the southern Drakensberg were found to be most attributable to distances of 0 – 25 m of rock exposures (Hardwick, 2012).

Previous macro-scale geomorphological studies on the Drakensberg-Maluti Mountains suggested that the massive basalt and Clarens Fm. sandstone boulders on the scree slopes below the cliffs formed owing to the resilient Basalt-Clarens Formation scarps and are thus lithologically controlled (Moore & Blenkinsop, 2006). The analysis of the topographic/lithological variables and their frequency distribution, hydrological variables, and InfoVal weights provided in this dissertation, support previous suggestions that the macro-scale geomorphological forms, and in this case local- (mirco-) scale forms (rock fall deposits) are primarily controlled through topography and lithology. The high frequency of rockfalls occurring in close proximity to rock exposures (0 – 25 m) and the strong InfoVal weighs for steep slope gradients (29° – 62°) and high altitudes (2600 and 2800 m a.s.l) may be supporting evidence that lithology in the southern and northern Drakensberg is largely responsible for the presence of rockfalls. However, whilst the spatial distribution of rockfalls may be topographically/lithologically controlled, the temporal/frequency dynamics are more likely climate controlled through various climate-temporal scales, as has been found for other regions, such as those controlled by permafrost (e.g. Rabatel et al., 2008).

ANN analysis was performed to analyse the spatial pattern of rockfalls in relation to the environmental variables. The results for the ANN show that rockfalls in the study area relate to the ANN results observed for rockfall points digitized in the Bushmen's Nek region of the southern Drakensberg, which also found rockfall points to be clustered in response to various environmental variables (Hardwick, 2012). The observed mean distance between Clarens and Molteno Fm. rockfalls was observed to:

- increase with a decrease in altitude
- increase with a decrease in slope gradient
- increase with a decrease in distance to rock exposures
- increase with a decrease in drainage lines

The observed mean distance between Clarens and Molteno Fm. rockfalls was also noted to be higher on south-facing slopes and lower on north-facing slopes.

In terms of slope units, the observed mean distance for Clarens and Molteno Fm. rockfalls was found to be lower on slope units where rockfalls occur more frequently and higher on slope units where rockfalls occur less frequently.

Surface density rasters created using point density analysis are useful for not only identifying and classifying the geographic locations of rockfall density but also assist in calculating average rockfalls per specified area unit. The point density analysis found that an average of ~2 Clarens Fm. rockfalls occur per Km^2 of the entire study area and ~5 Clarens Fm. rockfalls occur per Km^2 at very high density rockfall classes. On average ~4 Molteno Fm. rockfalls occur per Km^2 of the entire study area and ~15 Molteno Fm. rockfalls occur per Km² at the very high density rockfall class. The difference in the number of Clarens and Molteno Fm. rockfalls suggests that the Molteno Fm. rockfalls are more abundant per Km² of the study area. This is likely as the Clarens Fm. is more resilient sandstone which produces fewer but larger blocks. The identification of very high density rockfall regions can be used to assist park management in planning tourist activities, and infrastructure planning. Park infrastructure and anthropogenic activities at Wilgerhof show potential risk to Clarens Fm. rockfalls. Overall, infrastructure at the GGHNP possesses no real danger from Clarens and Molteno Fm. rockfalls, however anthropogenic outdoor activities such as hiking, which are more difficult to measure, could be more highly susceptible to rockfall hazards, especially in very high density Clarens Fm. rockfall regions. The inclusion of footpath captured in the field using GPS tracking for inclusion in further studies could provide a solution for measuring vulnerability to high density rockfalls.

The use of hierarchical partitioning and classification and regression trees could prove useful for identifying environmental variables associated with rockfalls. The findings of this study could be taken further to develop predictive mapping using logistic regression models to map and quantify the proportion of area in the GGHNP most likely to experience rockfall activity. Furthermore, precipitation data and multi-temporal imagery could potential insight for measuring the effects of climate change on rockfall distributions, density and probability over time.

Reference List

Boelhouwers, J.C., Sumner, P.D., 2003: The paleoenvironmental significance of southern African blockfields and blockstreams, in M. Phillips, S.M. Springman, L.U. Arenson (Eds.), Permafrost, Swets and Zeitlinger, Lisse, 73-78.

Agliardi, F., Crosta, G. B., Sosio, R., Rivolta, C., Mannucci, G., 2013: In situ and remote long term real-time monitoring of a large alpine rock slide. In *Landslide Science and Practice* , Springer Berlin Heidelberg, 415-421.

Aguilar, F. J., Agüera, F., Aguilar, M. A., & Carvajal, F. (2005). Effects of terrain morphology, sampling density, and interpolation methods on grid DEM accuracy. Photogrammetric Engineering & Remote Sensing, 71(7), 805-816.

Antoniou, A. A., & Lekkas, E., 2010: Rockfall susceptibility map for Athinios port, Santorini island, Greece. *Geomorphology*, 118(1), 152-166.

Antoniou, A. A., 2013: GIS-based evaluation of rockfall risk along routes in Greece. *Environmental Earth Sciences*, 70(5), 2305-2318.

Van Asselen, S., & Seijmonsbergen, A. C., 2006: Expert-driven semi-automated geomorphological mapping for a mountainous area using a laser DTM. *Geomorphology*, 78(3), 309-320.

Ayalew, L., & Yamagishi, H., 2004: Slope failures in the Blue Nile basin, as seen from landscape evolution perspective. *Geomorphology*, 57(1), 95-116.

Ayalew, L., Yamagishi, H., Ugawa, N., 2004: Landslide susceptibility mapping using GIS-based weighted linear combination, the case in Tsugawa area of Agano River, Niigata Prefecture, Japan, Landslides, 1 (1), 73-81.

Baatz, M., & Schäpe, A., 1999: Object-oriented and multi-scale image analysis in semantic networks. In *2nd international symposium: operationalization of remote sensing*, 16-20.

Baillifard, F., Jaboyedoff, M., Sartori, M., 2003: Rockfall hazard mapping along a mountainous road in Switzerland using a GIS-based parameter rating approach. *Natural Hazards and Earth System Science*, 3(5), 435-442.

Barlow, J., Martin, Y., & Franklin, S. E. (2003). Detecting translational landslide scars using segmentation of Landsat ETM+ and DEM data in the northern Cascade Mountains, British Columbia. *Canadian Journal of Remote Sensing*,*29*(4), 510-517.

Barlow, J., Franklin, S., Martin, Y., 2006: High spatial resolution satellite imagery, DEM derivatives, and image segmentation for the detection of mass wasting processes. *Photogrammetric Engineering and Remote Sensing*, 72(6), 687-692.

Barredo, J., Benavides, A., Hervás, J., van Westen, C. J., 2000: Comparing heuristic landslide hazard assessment techniques using GIS in the Tirajana basin, Gran Canaria Island, Spain. *International Journal of Applied Earth Observation and Geoinformation*, 2(1), 9-23.

Basson, F. R. P., 2012: Rigid body dynamics for rock fall trajectory simulation. In *46th US Rock Mechanics/Geomechanics Symposium*. American Rock Mechanics Association.

Bell, R., Glade, T., Granica, K., Heiss, G., Leopold, P., Petschko, H., Schweigl, J., 2013: Landslide susceptibility maps for spatial planning in Lower Austria. In *Landslide Science and Practice* . Springer Berlin Heidelberg, 467-472.

Benz, U. C., Hofmann, P., Willhauck, G., Lingenfelder, I., Heynen, M., 2004: Multi-resolution, object-oriented fuzzy analysis of remote sensing data for GIS-ready information. *ISPRS Journal of photogrammetry and remote sensing*, 58(3), 239-258.

Beukes, N.J., 1969: *Die sedimentologie van die Etage Holkranssandsteen, Sisteem Karoo.* M.S.c thesis, University of the Orange Free State, Bloemfontein.

Beukes, N.J., 1970: Stratigraphy and sedimentology of the Cave Sandstone Stage, Karoo System. *Proc. Gondwana Simposium* 1970: 321-341.

Bhandary, N. P., Dahal, R. K., Timilsina, M., Yatabe, R., 2013: Rainfall event-based landslide susceptibility zonation mapping. *Natural hazards*, 69(1), 365-388.

Bigarella, J.J & van Eden, O.R., 1970: Mesozoic paleowind patterns and the problem of continental drift. *Bol. Parana. Geoscienc.,* (28-29), 115-144.

Bijker, H.J., 2001: *A Hydrological-Slope Stability Model for Shallow Landslide Prediction in the Injisuthi Valley, KwaZulu-Natal Drakensberg*, MSc dissertation, University of Pretoria, Pretoria.

Bijukchhen, S. M., Kayastha, P., Dhital, M. R., 2012: A comparative evaluation of heuristic and bivariate statistical modelling for landslide susceptibility mappings in Ghurmi–Dhad Khola, east Nepal. *Arabian Journal of Geosciences*, 1-17.

Blais-Stevens, A., Behnia, P., Kremer, M., Page, A., Kung, R., Bonham-Carter, G., 2012: Landslide susceptibility mapping of the Sea to Sky transportation corridor, British Columbia, Canada: comparison of two methods. *Bulletin of Engineering Geology and the Environment*, 71 (3), 447-466.

Blaschke, T., Lang, S., Lorup, E., Strobl, J., Zeil, P., 2000: Object-oriented image processing in an integrated GIS/remote sensing environment and perspectives for environmental applications. *Environmental information for planning, politics and the public*, 2, 555-570.

Blaschke, T., Burnett, C., Pekkarinen, A., 2004: Image segmentation methods for object-based analysis and classification. In *Remote sensing image analysis: Including the spatial domain.* Springer Netherlands, 211-236.

Blaschke, T., 2010: Object based image analysis for remote sensing. *ISPRS journal of photogrammetry and remote sensing*, 65 (1), 2-16.

Blight, G.E., Van Heerden, A., Brackley, I.J., 1970: *Landslides at Amsterdamhoek and Bethlehem: an examination of the mechanics of stiff fissured clays, Civil Engineer in South Africa,* 129-140.

Boelhouwers, J.C. & Meiklejohn, K.I., 2002: Quaternary periglacial and glacial geomorphology of southern Africa: review and synthesis, *South African Journal of Science*, 98, 47-55.

Boelhouwers, J.C. & Sumner, P.D., 2003: The palaeoenvironmental significance of southern African blockfields and blockstreams, in M. Phillips, S.M. Springman, L.U. Arenson (Eds.), *Permafrost, Swets and Zeitlinger,* Lisse, 73-78.

Bordy, E. M., John Hancox, P., Rubidge, B. S., 2004: Fluvial style variations in the Late Triassic–Early Jurassic Elliot Formation, main Karoo Basin, South Africa. *Journal of African Earth Sciences*, 38 (4), 383-400.

Borghuis, A.M., Chang, K., Lee, H.Y., 2007: Comparison between automated and manual mapping of typhoon-triggered landslides from SPOT-5 imagery, *International Journal of Remote Sensing*, 28 (8), 1843-1856.

Botha, B.J.V., 1968: The stratigraphy of the red beds stage, Karroo System at Elliot, Cape Province. *Transvaal geological society of South Africa*, 71, 110-117.

Brand, R. F., Brown, L. R., & Preez, P. J. D., 2010: A floristic analysis of the vegetation of Platberg, eastern Free State, South Africa. *koedoe*, 52(1), 1-11.

Brardinoni, F., Slaymaker, O., Hassan, M.A., 2003: Landslide inventory in a rugged forested watershed: a comparison between air-photo and field survey data, *Geomorphology*, 54 (3–4), 179-196.

Büdel, B., Weber, B., Kühl, M., Pfanz, H., Sültemeyer, D. & Wessels, D., 2004: Reshaping of sandstone surfaces by cryptoendolithic cyanobacteria: bioalkalization causes chemical weathering in arid landscapes, *Geobiology* 2, 261−268. doi:10.1111/ j.1472-4677.2004.00040.x

Burnnett, C. & Blaschke, T., 2003: A multi-scale segmentation/object relationship modelling methodology for landscape analysis. *Ecological Modelling*, 168, 233–249.

Carrara, A., Cardinali, M., Detti, R., Guzzetti, F., Pasqui, V., Reichenbach, P., 1991: GIS techniques and statistical models in evaluating landslide hazard, *Earth Surface Processes and Landforms*, 16 (5), 427-445.

Carrara, A., Crosta, G., Frattini, P., 2003: Geomorphological and historical data in assessing landslide hazard, *Earth Surface Processes and Landforms*, 28 (10), 1125-1142.

Carrara, A., 1983: Multivariate models for landslide hazard evaluation, *Mathematical Geology*, 15 (3), 403-426.

Casadei, M., Dietrich, W.E., Miller, N.L., 2003: Testing a model for predicting the timing and location of shallow landslide initiation in soil-mantled landscapes, *Earth Surface Processes and Landforms*, 28 (9), 925-950.

Casals-Carrasco, P., Kubo, S., & Madhavan, B. B., 2000: Application of spectral mixture analysis for terrain evaluation studies. *International Journal of Remote Sensing*, 21(16), 3039-3055.

Catani, F., Lagomarsino, D., Segoni, S., & Tofani, V. (2013, April). Sensitivity analysis and scale issues in landslide susceptibility mapping. In *EGU General Assembly Conference Abstracts*, 15, 7855.

Chau, K. T., Sze, Y. L., Fung, M. K., Wong, W. Y., Fong, E. L., Chan, L. C. P., 2004: Landslide hazard analysis for Hong Kong using landslide inventory and GIS. *Computers & Geosciences*, 30 (4), 429-443.

Chiessi, V., D'Orefice, M., Scarascia Mugnozza, G., Vitale, V., Cannese, C., 2010: Geological, geomechanical and geostatistical assessment of rockfall hazard in San Quirico Village (Abruzzo, Italy). *Geomorphology*, 119 (3), 147-161.

Chung, C. J. F., & Fabbri, A. G., 2003: Validation of spatial prediction models for landslide hazard mapping. *Natural Hazards*, 30(3), 451-472.

Cirella, G. T., Semenzin, E., Critto, A., Marcomini, A., 2014: Natural Hazard Risk Assessment and Management Methodologies Review: Europe. In *Sustainable Cities and Military Installations*. Springer Netherlands, 329-358.

Cooks, J., & Pretorius, J. R. (1987). Weathering basins in the Clarens Formation sandstone, South Africa. *South African journal of geology*, 90 (2), 147-154.

Copons, R., & Vilaplana, J. M., 2008: Rockfall susceptibility zoning at a large scale: from geomorphological inventory to preliminary land use planning. *Engineering geology*, 102 (3), 142-151.

Copons, R., Vilaplana, J.M., Linares, R., 2009: Rockfall travel distance analysis by using empirical models, *Natural Hazards and Earth System Sciences*, 9, 2107-2118.

Cordes, S. E., Stock, G. M., Schwab, B. E., Glazner, A. F., 2013: Supporting Evidence for a 9.6±1 ka Rock Fall Originating from Glacier Point in Yosemite Valley, California. *Environmental & Engineering Geoscience*, 19 (4), 345-361.

Dahal, R. K., Hasegawa, S., Yamanaka, M., Bhandary, N. P., Yatabe, R., 2010: Statistical and deterministic landslide hazard assessment in the Himalayas of Nepal. In *IAEG 2010 conference, Geologically active. Taylor & Francis Group, London* , 1053-1060.

Dai, F.C. & Lee, C.F., 2002: Landslide characteristics and slope instability modeling using GIS, Lantau Island, Hong Kong, *Geomorphology*, 42 (3–4), 213-228.

Dalrymple, J.B., Blong, R.J., Conacher, A.J., 1968: A hypothetical nine-unit landsurface model, *Zeitschrift für Geomorphologie*, 12, 60-76.

Das, I., Sahoo, S., van Westen, C., Stein, A., Hack, R., 2010: Landslide susceptibility assessment using logistic regression and its comparison with a rock mass classification system, along a road section in the northern Himalayas (India). *Geomorphology*, *114* (4), 627-637.

Day, R.W. 1997: Case studies of rockfall in soft versus hard rock. *Environmental and Engineering, Geoscience*, 3(1), 133–40.

Deng, Y., 2007: New trends in digital terrain analysis: landform definition, representation, and classification. *Progress in Physical Geography*, 31(4), 405-419.

Department: Rural Development and Land Reform Republic of South Africa. (2009A, August 16). *Accuracy of Orthorectified Imagery provided by the Chief Directorate: National Geo-spatial Information*. Cape Town, DC: Duesimi, R. G.

Department: Rural Development and Land Reform Republic of South Africa. (2009B, August 16). *Accuracy of Digital Elevation Model Data (DEM) provided by the Chief Directorate: National Geo-spatial Information.* Cape Town, DC: Duesimi, R. G.

Dias, A. V., & Gunathilake, A. A. J. K., 2012: A Comparative Analysis of Landslide Susceptibility by WAA and SINMAP Model. In *IPL Symposium*, 69.

Dikau, R., 1989: The application of a digital relief model to landform analysis in geomorphology. Three dimensional applications in geographical information systems, 51-77.

Diop, S., Forbes, C., Chiliza, G., 2010: Landslide inventorization and susceptibility mapping in South Africa, *Landslides*, 7 (2), 207-210.

Dong, J., Tung, Y., Chen, C., Liao, J., Pan, Y., 2011: Logistic regression model for predicting the failure probability of a landslide dam, *Engineering Geology*, 117 (1–2), 52-61.

Dorn, R. L., 2004: Case hardening. Encyclopedia of Geomorphology. London: Loutledge, 118-119.

Dorren, L. K., & Seijmonsbergen, A. C., 2003: Comparison of three GIS-based models for predicting rockfall runout zones at a regional scale. *Geomorphology*, 56(1), 49-64.

Dorren, L. K., 2003: A review of rockfall mechanics and modelling approaches.*Progress in Physical Geography*, 27 (1), 69-87.

Drăguţ, L., & Eisank, C., 2011: Object representations at multiple scales from digital elevation models. *Geomorphology*, 129 (3), 183-189.

Du Toit, A.L., 1981: The zones of the Karroo system and their distribution. Proc. Geol. Soc. S. Afr., 21, 17-36.

Erener, A., & Düzgün, H. S. B., 2010: Improvement of statistical landslide susceptibility mapping by using spatial and global regression methods in the case of More and Romsdal (Norway). *Landslides*, 7 (1), 55-68.

Eriksson, P.G., 1979: *A paleoenvironmental study of the Clarens Formation in the Natal Drakensberg.* M.S.c thesis, University of Natal, 115.

Eriksson, P.G., 1981: A paleoenvironmental analysis of the Clarens Formation in the Natal Drakensberg. *Trans. Geol. Soc. S. Afr*., 84, 7-17.

Eriksson, P.G., 1983: *A Paleaoenvironmental Study of the Molteno, Elliot and Clarens Formations in the Natal Drakensberg and the Northeastern Orange Free State,* PhD thesis, University of Natal, Pietermaritzburg.

Ericksson, P.G., 1984: A paleoenvironmental analysis of the Molteno Formation in the Natal Drakensberg. *Trans. Geol. Soc. S. Afr*., 87, 237-244.

Eriksson, P. G., 1985: The depositional palaeoenvironment of the Elliot Formation in the Natal Drakensberg and northeastern Orange Free State. *South African Journal of Geology*, 88 (1), 19-26.

ESRI, 2011: ArcMap, *Environmental Systems Resource Institute 9.3.*

Esterhuizen, G.S. and Streuders, S.B., 1998: Rockfall hazard evaluation using probilbilistic keyblock analysis, *Journal of the South African Institute of Mining and Metallurgy* (2), 59-64.

Evans, S. G., & Hungr, O., 1993: The assessment of rockfall hazard at the base of talus slopes. *Canadian Geotechnical Journal*, 30 (4), 620-636.

Filipello, A., & Mandrone, G., 2013: A Ready to Use GRASS GIS Workbench for Rockfall Analysis. In *Landslide Science and Practice* (pp. 231-238). Springer Berlin Heidelberg.

Fischer, L., Purves, R. S., Huggel, C., Noetzli, J., & Haeberli, W., 2012: On the influence of topographic, geological and cryospheric factors on rock avalanches and rockfalls in high-mountain areas. *Natural Hazards & Earth System Sciences*, 12 (1), 241-254.

Flanders, D., Hall-Beyer, M., & Pereverzoff, J. (2003). Preliminary evaluation of eCognition object-based software for cut block delineation and feature extraction. *Canadian Journal of Remote Sensing*, *29*(4), 441-452.

Flatland, 1993Flatland, R., 1993: *Application of the Rockfall Hazard Rating System to the Rock Slopes Adjacent to U.S. 50 and State Route 28 on the East Side of Lake Tahoe,* M.S. Thesis, University of Nevada, Reno, 318 p.

Fleming, A., Summerfield, M. A., Stone, J. O., Fifield, L. K., & Cresswell, R. G., 1999: Denudation rates for the southern Drakensberg escarpment, SE Africa, derived from in-situ-produced cosmogenic 36C1: initial results. Journal of the Geological Society, 156(2), 209-212.

Frattini, P., Crosta, G., Carrara, A., Agliardi, F., 2008: Assessment of rockfall susceptibility by integrating statistical and physically-based approaches, *Geomorphology,* 94 (3–4), 419-437.

García-Rodríguez, M. J., & Malpica, J. A. (2010). Assessment of earthquake-triggered landslide susceptibility in El Salvador based on an Artificial Neural Network model. *Natural Hazards and Earth System Science*, *10*(6), 1307-1315.

Gardner, J.S., 1983: Rockfall frequency and distribution in the Highwood Pass area, Canadian Rocky Mountains. *Zeitschrift für Geomorphologie*, 27 (3), 311–24.

Garland, G., Olivier, M.J., 1993: Predicting landslides from rainfall in a humid, sub-tropical region. *Geomorphology,* 8:165–173.

SANParks., 2012: Golden Gate Highlands National Park Management Plan, South Africa, Draft 4.4, 1-87.

Gomez, H., & Kavzoglu, T., 2005: Assessment of shallow landslide susceptibility using artificial neural networks in Jabonosa River Basin, Venezuela. *Engineering Geology,* 78 (1), 11-27.

Grab, S. W., & Mills, S. C., 2011: Quaternary slope processes and morphologies in the upper Sehonghong Valley, eastern Lesotho. *Proceedings of the Geologists' Association*, 122 (1), 179-186.

Grab, S.W., Mulder, N.A., Mills, S.C., 2009: Spatial associations between longest-lasting winter snow cover and cold region landforms in the High Drakensberg, southern Africa , Geografiska Annaler: Series A, *Physical Geography,* 91 (2), 83-97.

Grab, S. W., Goudie, A. S., Viles, H. A., & Webb, N., 2011: Sandstone geomorphology of the Golden Gate Highlands National Park, South Africa, in a global context. *Koedoe,* 53 (1), 1-14.

Grab, S., 1999: Block and debris deposits in the high Drakensberg, Lesotho, southern Africa: implications for high altitude slope processes. Geografiska Annaler: Series A, *Physical Geography*, 81(1), 1-16.

Grab, S.W., 2007: Near-surface rockwall temperatures in the high Drakensberg basalt: spatio-temporal differences and possible implications for weathering, *Zeitschrift für Geomorphologie, Supplement*, 51, 103-113.

Grab, S. W., 2010: Alpine turf exfoliation pans in Lesotho, southern Africa: Climate–process–morphological linkages. *Geomorphology*, 114(3), 261-275.

Green, R.W.E. and Bloch, S., 1971: The Ceres, South Africa, earthquake of September 29, 1969: Report on some aftershocks, *Bulletin of the Seismological Society of America*, 61 (4), 851-859.

Groenewald, G.H., 1986: Geology of the Golden Gate Highlands National Park, *Koedoe*, 29, 165-181.

Guisan, A., Weiss, S. B., & Weiss, A. D., 1999: GLM versus CCA spatial modeling of plant species distribution. *Plant Ecology*, 143 (1), 107-122.

Gumede, H., & Stacey, T. R., 2007: Measurement of typical joint characteristics in South African gold mines and the use of these characteristics in the prediction of rock falls. *Journal of the South African Institute of Mining & Metallurgy*, 107(5), 335.

Guzzetti, F., Carrara, A., Cardinali, M., Reichenbach, P., 1999: Landslide hazard evaluation: a review of current techniques and their application in a multi-scale study, Central Italy, *Geomorphology*, 31 (1–4), 181-216.

Guzzetti, F., Malamud, B. D., Turcotte, D. L., & Reichenbach, P., 2002: Power-law correlations of landslide areas in central Italy. Earth and Planetary Science Letters, 195(3), 169-183.

Guzzetti, F., Reichenbach, P., Cardinali, M., Galli, M., Ardizzone, F., 2005: Probabilistic landslide hazard assessment at the basin scale, *Geomorphology*, 72 (1–4), 272-299.

Hagos, A. A., 2013: Remote sensing and GIS-based mapping on landslide phenomena and landslide susceptibility evaluation of Debresina Area (Ethiopia) and Rio San Girolamo basin (Sardinia). UNICA, Italy.

Haneberg, W. C., 2000: Deterministic and probabilistic approaches to geologic hazard assessment. *Environmental & Engineering Geoscience*, 6 (3), 209-226.

Haneberg, W. C., 2000: Deterministic and probabilistic approaches to geologic hazard assessment. *Environmental & Engineering Geoscience*, 6(3), 209-226.

Hardwick, D., 2012: *A mass movement classification for the southern Drakensberg, South Africa*. PhD thesis. University of the Witwatersrand, Johannesburg.

Hayakawa, Y. S., Oguchi, T., & Lin, Z. 2008: Comparison of new and existing global digital elevation models: ASTER G-DEM and SRTM-3. *Geophysical Research Letters*, 35(17)

Henderson, Z., Scott, L., Rossouw, L. & Jacobs, Z., 2006: Dating, paleoenvironments, and archaeology: a progress report on the Sunnyside 1 site, Clarens, South Africa, Archaeological Papers of the American Anthropological Association 16, 139–149. doi:10.1525/ap3a.2006.16.1.139

Hengl, T., & Reuter, H. I., 2009: Geomorphometry: concepts, software, applications, vol. 33, Elsevier.

Hengl, T., & Reuter, H. 2011: How accurate and usable is GDEM? A statistical assessment of GDEM using LiDAR data. *Geomorphometry*, 2, 45-48.

Herath, S., Wang, Y., 2009: Case Studies and National Experiences. In: Sassa, K., Canuti, P. (Eds.), *Landslides — Disaster Risk Reduction*. Springer Verlag, Berlin Heidelberg, 475–497.

Höhle, J., & Höhle, M. 2009: Accuracy assessment of digital elevation models by means of robust statistical methods. *ISPRS Journal of Photogrammetry and Remote Sensing*, 64(4), 398-406.

Hua-xi, G., & Kun-long, Y. (2014). Study on spatial prediction and time forecast of landslide. *Natural Hazards*, 1-14.

Huggel, C., Clague, J. J., & Korup, O., 2012: Is climate change responsible for changing landslide activity in high mountains?. *Earth Surface Processes and Landforms*, 37(1), 77-91.

Hutchinson, J.N., 1968: Mass movement, in R.W. Fairbridge (Ed.), *Encyclopaedia of Earth Sciences*, Reinhold, New York, 688-695.

Intergovernmental Panel on Climate Change (IPCC). 2007. Climate change 2007: the physical science basis. In *Contribution of Working Group I to the Fourth Assessment Report of the Intergovernmental Panel on Climate Change*, Solomon S, Qin D, Manning M, Chen Z, Marquis M, Averyt KB, Tignor M, Miller HL (eds). Cambridge University Press: Cambridge http://www.ipcc.ch/ipccreports/assessments-reports.htm

Iverson, R. M., 2014: Debris flows: behaviour and hazard assessment. *Geology Today*, *30*(1), 15-20.

Ives, J. D., & Messerli, B., 1981: Mountain Hazards Mapping in Nepal Introduction to an Applied Mountain Research Project. *Mountain Research and Development*, 223-230.

Jaboyedoff, M., & Derron, M. H., 2005). A new method to estimate the infilling of alluvial sediment of glacial valleys using a sloping local base level. In *Geophysical Research Abstracts*, 7, 05810.

Jaboyedoff, M., & Labiouse, V., 2003: Preliminary assessment of rockfall hazard based on GIS data. In *10th International Congress on Rock Mechanics ISRM*, 575-578.

Jaboyedoff, M., & Labiouse, V., 2011: Technical Note: Preliminary estimation of rockfall runout zones. *Natural Hazards and Earth System Science*, 11(3), 819-828.

Jaboyedoff, M., Oppikofer, T., Abellán, A., Derron, M. H., Loye, A., Metzger, R., Pedrazzini, A., 2012a: Use of LIDAR in landslide investigations: a review. *Natural Hazards*, 61(1), 5-28.

Jaboyedoff, M., Choffet, M., Derron, M. H., Horton, P., Loye, A., Longchamp, C., Pedrazzini, A., 2012b: Preliminary Slope Mass Movement Susceptibility Mapping Using DEM and LiDAR DEM. In *Terrigenous Mass Movements* (pp. 109-170). Springer Berlin Heidelberg.

Jenness, J., Brost, B., Beier, P., 2010: *Land facet corridor designer*. www.jennessent.com.

Jenness, J., 2006: Topographic Position Index (tpi_jen.avx) extension for ArcView 3.x, v. 1.2. Jenness Enterprises. Available at: http://www.jennessent.com/arcview/tpi.htm.

Jiménez-Perálvarez, J. D., Irigaray, C., El Hamdouni, R., & Chacón, J., 2011: Landslide-susceptibility mapping in a semi-arid mountain environment: an example from the southern slopes of Sierra Nevada (Granada, Spain). *Bulletin of Engineering Geology and the Environment*, *70*(2), 265-277.

Jubb, R.A., 1973: Brief synthesis of present information on the geographical and stratigraphical distribution of fossil fish within the Stormberg Series, South Africa. *Palaeont. Afr*. 16, 17-23.

Kayastha, P., Dhital, M. R., De Smedt, F., 2012: Landslide susceptibility mapping using the weight of evidence method in the Tinau watershed, Nepal. *Natural hazards*, *63* (2), 479-498.

Kellerer-Pirklbauer, A., Lieb, G. K., Avian, M., Carrivick, J., 2012: Climate change and rock fall events in high mountain areas: Numerous and extensive rock falls in 2007 at Mittlerer Burgstall, Central Austria. *Geografiska AANNler: Series A, Physical Geography*, *94* (1), 59-78.

Kenner, R., Phillips, M., Danioth, C., Denier, C., Thee, P., Zgraggen, A., 2011:Investigation of rock and ice loss in a recently deglaciated mountain rock wall using terrestrial laser scanning: Gemsstock, Swiss Alps. *Cold Regions Science and Technology*, *67*(3), 157-164.

Keylock, C., & Domaas, U., 1999: Evaluation of topographic models of rockfall travel distance for use in hazard applications. *Arctic and alpine research*, 31(3), 312-320.

King, L. C., 1953: Canons of landscape evolution. *Geological Society of America Bulletin*, 64(7), 721-752.

King, L.C., 1963: *South African Scenery*. Oliver and Boyd, London, United Kingdom.

King, L.C., 1972: *The Natal monocline: explaining the origin and scenery of Natal, South Africa.* Geology Department, University of Natal, South Africa.

Kirkby, M. J., & Statham, I., 1975: Surface stone movement and scree formation. The Journal of Geology, 349-362.

Kitching, J.W & Raath, M.A., 1984: Fossils from the Elliot and Clarens Formation (Karoo Sequence) of the northeastern Cape, Orange Free State and Lesotho, and a suggested biozonation based on tetrapods. *Palaeont. Afr*, 25, 11-125.

Kitching, J.W., 1977: *The distribution of the Karroo vertebrate fauna*. Bernard price institute of Paleontological research, University of the Witwatersrand, Johannesburg, 131.

Kitching, J.W., 1979: Preliminary report on a clutch of six dinosaurian eggs from the Upper Triassic Elliot Formation, Northern Orange Free State. *Palaeont. Afr.*, 22, 41-45.

Kundu, S., Sharma, D.C., Saha, A.H., Pant, C.C., Mathew, J., 2011: GIS-BASED STATISTICAL LANDSLIDE SUSCEPTIBILITY ZONATION: A CASE STUDY IN GANESHGANGA WATERSHED, THE HIMALAYAS. 12th Esri India User Conference, 1-9.

Kurtz Jr, H. D., & Netoff, D. I., 2001: Stabilization of friable sandstone surfaces in a desiccating, wind-abraded environment of south-central Utah by rock surface microorganisms. *Journal of Arid Environments*, 48(1), 89-100.

Lan, H., Derek Martin, C., Lim, C.H., 2007: RockFall Analyst: A GIS extension for three-dimensional and spatially distributed rockfall hazard modeling, *Computers & Geosciences*, 33 (2), 262-279.

Le Roux, J.S., 1974: *Die paleogeologiese en paleogeografiese aspekte van die Etage Rooilae van die Sisteem Karoo*. PhD, University of the Orange Free State, 295.

Liu, J.G., Mason, P.J., Clerici, N., Chen, S., Davis, A., Miao, F., Deng, H., Liang, L., 2004: Landslide hazard assessment in the Three Gorges area of the Yangtze river using ASTER imagery: Zigui–Badong, *Geomorphology*, 61 (1–2), 171-187.

Loye, A., Jaboyedoff, M., Pedrazzini, A., 2009: Identification of potential rockfall source areas at a regional scale using a DEM-based geomorphometric analysis. *Natural Hazards & Earth System Sciences*, 9(5), 1643-1653.

Lu, P., Stumpf, A., Kerle, N., Casagli, N., 2011: Object-oriented change detection for landslide rapid mapping. *Geoscience and Remote Sensing Letters, IEEE*, 8(4), 701-705.

Luckman, B. H., 1976: Rockfalls and rockfall inventory data: some observations from Surprise Valley, Jasper National Park, Canada. Earth Surface Processes, 1(3), 287-298.

Maerz, N. H., Youssef, A., Fennessey, T. W., 2005: New risk–consequence rockfall hazard rating system for Missouri highways using digital image analysis. *Environmental & Engineering Geoscience*, 11 (3), 229-249.

Martha, T. R., Kerle, N., Jetten, V., van Westen, C. J., Kumar, K. V., 2010: Characterising spectral, spatial and morphometric properties of landslides for semi-automatic detection using object-oriented methods. *Geomorphology*, 116(1), 24-36.

Martha, T. R., Kerle, N., van Westen, C. J., Jetten, V., Vinod Kumar, K., 2012: Object-oriented analysis of multi-temporal panchromatic images for creation of historical landslide inventories. *ISPRS journal of photogrammetry and remote sensing*, 67, 105-119.

Martin, Y. E., & Franklin, S. E., 2005: Classification of soil-and bedrock-dominated landslides in British Columbia using segmentation of satellite imagery and DEM data. International Journal of Remote Sensing, 26 (7), 1505-1509.

Matsuoka, N., & Sakai, H., 1999: Rockfall activity from an alpine cliff during thawing periods. *Geomorphology*, 28(3), 309-328.

McCarroll, D., Shakesby, R.A. and Matthews, J.A., 1998: Spatial and temporal patterns of late Holocene rockfall activity on a Norwegian talus slope: a lichenometric and simulation modelling approach. *Arctic and Alpine Research*, 30 (1), 51–60.

McKechnie, C., Grab, S., Drennan, G., 2007: Documenting lichen-induced mechanical weathering of quartzitic sandstone at Kaapsehoop, Mpumalanga: research in action. *South African Journal of Science*, 103(3 & 4), 117-120.

Meissl, G., 1998: Modellierung der Reichweite von Felsstürzen. Fallbeispeile zur GISgestützten Gefahrenbeurteilung aus dem Beierischen und Tiroler Alpenraum. Innsbrucker Geografischen Studien 28. Ph.D. Thesis, Universität Innsbruck, Innsbruck, p-249

Mellor, A., Short, J., Kirkby, S. J., 1997: Tafoni in the El Chorro area, Andalucia, southern Spain. *Earth Surface Processes and Landforms*, 22(9), 817-833.

Melzner, S., Lotter, M., Koçiu, A., 2009: Development of an efficient methodology for mapping and assessing potential rock fall source areas and run-out zones. In *EGU General Assembly Conference Abstracts*, 11, p-8029.

Menéndez Duarte, R., & Marquínez, J., 2002: The influence of environmental and lithologic factors on rockfall at a regional scale: an evaluation using GIS. *Geomorphology*, *43* (1), 117-136.

Mergili, M., Schratz, K., Ostermann, A., Fellin, W., 2011: A GRASS GIS implementation of the Savage-Hutter avalanche model and its application to the 1987 Val Pola event. In *Proceedings of the Second World Landslide Forum* , 3, 7.

Mills, S. C., Grab, S. W., & Carr, S. J., 2009: Late Quaternary Moraines Along the Sekhokong Range, Eastern Lesotho: Contrasting the Geomorphic History of North- and South-Facing Slopes. *Geografiska Annaler: Series A, Physical Geography*, *91*(2), 121-140.

Minár, J., & Evans, I. S., 2008: Elementary forms for land surface segmentation: The theoretical basis of terrain analysis and geomorphological mapping. Geomorphology, 95(3), 236-259.

Mol, L., & Viles, H. A., 2012: The role of rock surface hardness and internal moisture in tafoni development in sandstone. Earth Surface Processes and Landforms, 37(3), 301-314.

Mol, L., 2013: Investigations into the relationship between changes in internal moisture regimes and rock surface deterioration in cavernous sandstone features. Earth Surface Processes and Landforms. DOI: 10.1002, 6-14.

Moore, A., & Blenkinsop, T., 2006: Scarp retreat versus pinned drainage divide in the formation of the Drakensberg escarpment, southern Africa. South African Journal of Geology, 109(4), 599-610.

Mulder, N., & Grab, S. W., 2002: Remote sensing for snow cover analysis along the Drakensberg escarpment: research in action. South African journal of science, 98 (5 & 6), p-213.

Multiple linear regression, 1997. Retrieved 1 March 2013, from http://www.stat.yale.edu/Courses/1997-98/101/linmult.htm

Nefeslioglu, H.A., Gokceoglu, C., Sonmez, H., 2008: An assessment on the use of logistic regression and artificial neural networks with different sampling strategies for the preparation of landslide susceptibility maps, *Engineering Geology*, 97 (3–4), 171-191.

Norstrom, E., Scott, L., Partridge, T.C., Risberg, J., Holmgren, K., 2009: Reconstruction of environmental and climate changes at Braamhoek wetland, eastern escarpment South Africa, during the last 16,000 years with emphasis on the Pleistocene-Holocene transition. *Palaeogeography, Palaeoclimatology, Palaeoecology*, 271 (3–4), 240–258.

Ollier, C. D., & Marker, M. E. (1985). The great escarpment of southern Africa. Z. *Geomorph. Suppl*, 54, 37-56.

Paige-Green P & Croukamp, L., 2004: A revised landslide susceptibility map of Southern Africa. *Geoscience Africa*, p-508.

Paige-Green, P. & Leyland, R., 2009: Structural Failures of the Road Environment, *PG Technical Report*, CSIR, Pretoria.

Paige-Green, P., 1985: The development of a landslide susceptibility map for Southern Africa. In: *Proceedings Annual Transportation Convention*, Pretoria vol. FB

Paige-Green, P., 1989: Landslides: extent and economic significance in southern Africa, in E.E. Brabb, B.L. Harrod (Eds.), *Landslides: Extent and Economic Significance*, Balkema, Rotterdam, 261-269.

Pandey, A., Dabral, P. P., Chowdary, V. M., Yadav, N. K., 2008: Landslide hazard zonation using remote sensing and GIS: a case study of Dikrong river basin, Arunachal Pradesh, India. *Environmental geology*, 54(7), 1517-1529.

Park, N. W., & Chi, K. H., 2008: Quantitative assessment of landslide susceptibility using high-resolution remote sensing data and a generalized additive model. *International Journal of Remote Sensing*, 29 (1), 247-264.

Partridge, T.C. & Maud, R.R., 1987: Geomorphic evolution of southern Africa since the Mesozoic, *South African Journal of Geology*, 90 (2), 179-205.

Peila, D., Patrucco, M., Falanesca, M., 2011: Quantification and management of rockfall risk in opencast quarrying activities. *Environmental & Engineering Geoscience*, *17*(1), 39-51.

Petley, D.N., 2010: On the impact of climate change and population growth on the occurrence of fatal landslides in South, East and SE Asia, *Quarterly Journal of Engineering Geology and Hydrogeology*, 43 (4), 487-496.

Pradhan, B., 2010: Remote sensing and GIS-based landslide hazard analysis and cross-validation using multivariate logistic regression model on three test areas in Malaysia. *Advances in Space Research*, 45(10), 1244-1256.

Pradhan, B., Lee, S., Buchroithner, M. F., 2009: Use of geospatial data and fuzzy algebraic operators to landslide-hazard mapping. *Applied Geomatics*, *1*(1-2), 3-15.

Pradhan, B., & Lee, S., 2010: Landslide susceptibility assessment and factor effect analysis: backpropagation artificial neural networks and their comparison with frequency ratio and bivariate logistic regression modelling. *Environmental Modelling & Software*, *25*(6), 747-759.

Pradhan, B., 2010: Remote sensing and GIS-based landslide hazard analysis and cross-validation using multivariate logistic regression model on three test areas in Malaysia. *Advances in Space Research*, *45*(10), 1244-1256.

Rabatel, A., Deline, P., Jaillet, S., & Ravanel, L. (2008): Rock falls in high-alpine rock walls quantified by terrestrial lidar measurements: A case study in the Mont Blanc area. *Geophysical Research Letters, 35*(10).

Ravanel, L., & Deline, P., 2011: Climate influence on rockfalls in high-Alpine steep rockwalls: The north side of the Aiguilles de Chamonix (Mont Blanc massif) since the end of the 'Little Ice Age'. The Holocene, 21(2), 357-365.

Reisz, R. R., Scott, D., Sues, H. D., Evans, D. C., Raath, M. A., 2005: Embryos of an Early Jurassic prosauropod dinosaur and their evolutionary significance. Science, 309 (5735), 761-764.

Reuter, H. I., Nelson, A., Strobl, P., Mehl, W., & Jarvis, A. (2009, July). A first assessment of Aster GDEM tiles for absolute accuracy, relative accuracy and terrain parameters. In Geoscience and Remote Sensing Symposium, 2009 IEEE International, IGARSS 2009 (Vol. 5, pp. V-240). IEEE.

Roering, J. J., Kirchner, J. W., & Dietrich, W. E., 1999: Evidence for nonlinear, diffusive sediment transport on hillslopes and implications for landscape morphology. Water Resources Research, 35(3), 853-870.

Riley, S. J., 1999: Index That Quantifies Topographic Heterogeneity. http://www.osgeo.org

Riley, S. J., S. D. DeGloria, Elliot, R., 1999: A terrain ruggedness index that quantifies topographic heterogeneity. *Intermountain Journal of Sciences,* 5(1–4),23–27.

Roberts, B.R., 1969, The vegetation of the Golden Gate Highlands National Park, *Koedoe*, 12, 15–28.

Rossi, M., Guzzetti, F., Reichenbach, P., Mondini, A. C., Peruccacci, S., 2010: Optimal landslide susceptibility zonation based on multiple forecasts.*Geomorphology*, 114(3), 129-142.

Rowbotham, D. N., & Dudycha, D., 1998: GIS modelling of slope stability in Phewa Tal watershed, Nepal. *Geomorphology*, 26(1), 151-170.

Ruff, M., & Czurda, K., 2008: Landslide susceptibility analysis with a heuristic approach in the Eastern Alps (Vorarlberg, Austria). *Geomorphology*, 94(3), 314-324.

Rust, B.R., 1962: *On the sedimentation of the Molteno sandstones in the vicinity of Molteno*, C. P. Annale. Univ. Stellenbosch, 37, 165-236.

Saha, A.K., Gupta, R.P., Sarkar, I., Arora, M.K., Csaplovics, E., 2005: An approach for GIS-based statistical landslide susceptibility zonation—with a case study in the Himalayas, *Landslides*, 2 (1), 61-69.

Santacana, N., Baeza, B., Corominas, J., De Paz, A., Marturiá, J., 2003: A GIS-Based Multivariate Statistical Analysis for Shallow Landslide Susceptibility Mapping in La Pobla de Lillet Area (Eastern Pyrenees, Spain), *Natural Hazards*, 30 (3), 281-295.

Santi, P. M., Russell, C. P., Higgins, J. D., & Spriet, J. I. (2009). Modification and statistical analysis of the Colorado rockfall hazard rating system. *Engineering Geology*, *104* (1), 55-65.

Sappington, J., Longshore, K. M., Thompson, D. B., 2007: Quantifying landscape ruggedness for animal habitat analysis: a case study using bighorn sheep in the Mojave Desert. *The Journal of wildlife management*, 71(5), 1419-1426.

Schneevoigt, N. J., van der Linden, S., Thamm, H. P., Schrott, L., 2008: Detecting Alpine landforms from remotely sensed imagery. A pilot study in the Bavarian Alps. Geomorphology, 93(1), 104-119.

Schopper, E, Lang, S., Strobl, J., 2010: Segmentation and Object-Based Image Analysis. In: Rashed, T. – Jürgens, C. (Eds): *Remote Sensing of Urban and Suburban Areas*. Springer, Dordrecht. 181 – 192.

Schuster, R.L., 1996: Introduction, In R.L. Schuster, R.J. Krizek (Eds.), *Landslides: Anaylsis and Control*, *Transportation Research Board*, Washington, 1-10.

Shapiro, L. G., & Stockman, G. C., 2000: *Computer Vision*, March 2000.

Shirzadi, A., Saro, L., Joo, O. H., Chapi, K., 2012: A GIS-based logistic regression model in rock-fall susceptibility mapping along a mountainous road: Salavat Abad case study, Kurdistan, Iran. *Natural hazards*, 64 (2), 1639-1656.

Šilhán, K., Pánek, T., & Hradecký, J., 2013: Implications of spatial distribution of rockfall reconstructed by dendrogeomorphological methods. *Natural Hazards & Earth System Sciences*, 13 (7), 174-184.

Singh, L., van Westen, C., Champati Ray, P., Pasquali, P., 2005: Accuracy assessment of InSAR derived input maps for landslide susceptibility analysis: a case study from the Swiss Alps, *Landslides*, 2 (3), 221-228.

Singh, R.G., 2008: *Landslide Classification, Characterization and Susceptibility Modeling in KwaZulu-Natal*, MSc dissertation, University of the Witwatersrand, Johannesburg.

Soomro, A. S., Rajput, A. Q. K., & Solangi, S. H. GIS-Based Fast Moving Landslide Risk Analysis Model Using Qualitative Approach: A Case Study of Balakot, Pakistan. *Mehran University Research Journal of Engineering & Technology*, 30 (2), 335-342.

Spies, J.J., 1969: Die geologiese en geomorfologiese geskiedenis van Golden Gate Hoogland Nasionale Park. *Koedoe*, 12, 184-198.

Statham, I. 1976: A scree slope rockfall model. *Earth Surface Processes* 1, 43–62.

Stock, G. M., Bawden, G. W., Green, J. K., Hanson, E., Downing, G., Collins, B. D., Leslar, M., 2011: High-resolution three-dimensional imaging and analysis of rock falls in Yosemite Valley, California. *Geosphere*, *7*(2), 573-581.

Stock, G. M., Martel, S. J., Collins, B. D., Harp, E. L., 2012: Progressive failure of sheeted rock slopes: the 2009–2010 Rhombus Wall rock falls in Yosemite Valley, California, USA. *Earth Surface Processes and Landforms*, 37(5), 546-561.

Stoffel, M., & Huggel, C., 2012: Effects of climate change on mass movements in mountain environments. *Progress in Physical Geography*, 36(3), 421-439.

Stoffel, M., Wehrli, A., Kühne, R., Dorren, L. K., Perret, S., Kienholz, H., 2006: Assessing the protective effect of mountain forests against rockfall using a 3D simulation model. *Forest ecology and management*, 225 (1), 113-122.

Stoffel, M., Tiranti, D., Huggel, C., 2014: Climate change impacts on mass movements—case studies from the European Alps. *Science of The Total Environment*. http://dx.doi.org/10.1016/j.scitotenv.2014.02.102.

Strahler, A.N., 1952: Hypsometric (area-altitude) analysis of erosional topography, Geological Society of America Bulletin, 63 (11), 1117-1142.

Straub, D. & Schubert, M., 2008: Modeling and managing uncertainties in rock-fall hazards, *Georisk: Assessment and Management of Risk for Engineered Systems and Geohazards*, 2 (1), 1-15.

Stumpf, A., & Kerle, N., 2011: Object-oriented mapping of landslides using Random Forests. *Remote Sensing of Environment*, 115 (10), 2564-2577.

Sumner, P.D., Hall, K.J., van Rooy, J.L., Meiklejohn, K.I., 2009: Rock weathering on the eastern mountains of southern Africa: Review and insights from case studies, *Journal of African Earth Sciences*, 55 (5), 236-244.

Tanarro, L. M., & Muñoz, J., 2012: Rockfalls in the Duraton canyon, central Spain: Inventory and statistical analysis. *Geomorphology*, 169, 17-29.

Taru, P., Chingombe, W., & Mukwada, G., 2013: South Africa's Golden Gate Highlands National Park management plan: Critical reflections. South African Journal of Science, 109 (11-12), 1-3.

Telfer, M. W., Thomas, Z. A., Breman, E., 2012: Sand ramps in the Golden Gate Highlands National Park, South Africa: Evidence of periglacial aeolian activity during the last glacial. *Palaeogeography, Palaeoclimatology, Palaeoecology*, 313, 59-69.

Temesgen, B., Mohammed, M. U., & Korme, T. (2001). Natural hazard assessment using GIS and remote sensing methods, with particular reference to the landslides in the Wondogenet area, Ethiopia. *Physics and Chemistry of the Earth, Part C: Solar, Terrestrial & Planetary Science*, *26*(9), 665-675.

Van Westen, C. J & Terlein, M.T., 1996: An approach towards deterministic landslide hazard analysis in GIS - a case study from Manizales (Colombia). *Earth Surface Processes and Landforms*, 21, 853-868.

Thomas, M.A. & van Schalkwyk, A., 1993: Geological hazards associated with intense rain and flooding in Natal, *Journal of African Earth Sciences (and the Middle East)*, 16 (1–2), 193-204.

Van der Beek, P., Summerfield, M.A., Braun, J., Brown, R. W. Fleming, A., 2002: Modelling post breakup landscape development and denudational history across the southeastern African (Drakensberg Escarpment) margin. *Journal of Geophysical Research*, 107, B12 DOI 10.1029/2001JB000744.

Van Dijke, J. J., & Van Westen, C. J., 1990: Rockfall hazard, a geomorphological application of neighbourhood analysis with ILWIS. *ITC Journal*, 1, 40-44.

Van Eeden, O.R., 1937: The geology of the country around Bethlehem and Kestell with special reference to oil indications. *Mem. Geol. Surv. S. Afr.*, 33, 1-68.

Van Westen, C. J., 2000: The modelling of landslide hazards using GIS. *Surveys in Geophysics*, 21(2-3), 241-255.

Van Westen, C.J., 1997: *Statistical landslide hazard analysis. In: Application guide, ILWIS 2.1 for Windows*. ITC, Enschede, the Netherlands, 73-84.

Varnes, D.J., 1978: Slope movement types and processes, in R.L. Schuster, R.J. Krizek (Eds.), *Landslides: Analysis and Control, Transportation Research Board*, Washington, 11-33.

Vijith, H., Rejith, P. G., Madhu, G., 2009: Using InfoVal method and GIS techniques for the spatial modelling of landslide susceptibility in the upper catchment of River Meenachil in Kerala. *Journal of the Indian Society of Remote Sensing*, 37 (2), 241-250.

Visser, D.J.L. & van Riet Lowe, C., 1956: Die geologie en argeologie van die Klein-Caledon rivier valley. *Mem. Geol. Surv. S. Afr.*, 47, 1-66.

Vogt, D., Brink, V. Z., Brink, S., Price, M., Kagezi, B., 2010: New technology for improving entry examination, thereby managing the rockfall risk in south african gold and platinum mines. *Proceedings Science real and relevant conference,* CSIR, Pretoria, 1-11.

Volkwein, A., Melis, L., Haller, B., Pfeifer, R., 2005: Protection from Landslides and High Speed Rockfall Events: Reconstruction of Chapmans Peak Drive. In *IABSE Symposium Report* , 90(6), 47-54).

Volkwein, A., Schellenberg, K., Labiouse, V., Agliardi, F., Berger, F., Bourrier, F., Mölk, M., 2011: Rockfall characterisation and structural protection--a review. Natural Hazards & Earth System Sciences, 11 (9), 2617-2651.

Watters, R.J., 1998. Modification to the Rockfall Hazard Rating System for successful mitigation in mountainous terrain as a result of climate and slope aspect considerations. Association of Engineering Geologists 41st Annual Meeting, Programs with Abstracts, 41, p-134.

Wessels, D. C. J., & Büdel, B., 1995: Epilithic and cryptoendolithic cyanobacteria of Clarens sandstone cliffs in the Golden Gate Highlands National Park, *South Africa. Botanica Acta*, 108(3), 220-226.

Wessels, D. C. J. & Wessels, L.-A., 1991: Erosion of Biogenically Weathered Clarens Sandstone by Lichenophagous Bagworm Larvae (Lepidoptera; Pyschidae). *The Lichenologist*, 23, 283-291.

Wessels, D., Venter, D., Wessels, W., Wessels, L., 1995: Experimental strain analysis of Clarens Sandstone colonised by endolithic lichens, *Koedoe* 38, 35−47.

Wieczorek, G. F., Morrissey, M. M., Iovine, G., & Godt, J., 1999: Rock-fall potential in the Yosemite Valley, California. *US Geological Survey Open-File Report*, 99-578.

Wilson, M. F., O'Connell, B., Brown, C., Guinan, J. C., Grehan, A. J., 2007: Multiscale terrain analysis of multibeam bathymetry data for habitat mapping on the continental slope. *Marine Geodesy*, 30 (1-2), 3-35.

Xu, C., Xu, X., Yao, Q., Wang, Y., 2013: GIS-based bivariate statistical modelling for earthquake-triggered landslides susceptibility mapping related to the 2008 Wenchuan earthquake, China. *Quarterly Journal of Engineering Geology and Hydrogeology*, *46* (2), 221-236.

Yalcin, A., Reis, S., Aydinoglu, A. C., Yomralioglu, T., 2011: A GIS-based comparative study of frequency ratio, analytical hierarchy process, bivariate statistics and logistics regression methods for landslide susceptibility mapping in Trabzon, NE Turkey. *Catena*, 85(3), 274-287.

Yilmaz, I., & Yildirim, M., 2006: Structural and geomorphological aspects of the Kat landslides (Tokat—Turkey) and susceptibility mapping by means of GIS. *Environmental Geology*, 50 (4), 461-472.

Yilmaz, I., 2009: Landslide susceptibility mapping using frequency ratio, logistic regression, artificial neural networks and their comparison: A case study from Kat landslides (Tokat—Turkey), *Computers & Geosciences*, 35 (6), 1125-1138.

Yilmaz, I. (2010). Comparison of landslide susceptibility mapping methodologies for Koyulhisar, Turkey: conditional probability, logistic regression, artificial neural networks, and support vector machine.*Environmental Earth Sciences*, *61*(4), 821-836.

Yin, K.L, Yan, T.Z., 1988: Statistical prediction model for slope instability of metamorphosed rocks. In: *Landslides-Glissements de Terrain. Proceedings V international Symposium on Landslides,* 2, Lausanne, Switzerland, 1269-1272.

Zezere, J.L., 2002: Landslide susceptibility assessment considering landslide typology. A case study in the area north of Lisbon (Portugal*). Natural Hazards and Earth System Sciences* 2, 73-82.

Zimmer, V.L., Collins, B.D., Stock, G.M., Sitar, N., 2012: Rock fall dynamics and deposition: an integrated analysis of the 2009 Ahwiyah Point rock fall, Yosemite National Park, USA, *Earth Surface Processes and Landforms*, 37 (6), 680-691.